VU VRIJE UNIVERSITEIT AMSTERDAM

VU Research Portal

Beauty and a Search for Pentaquarks at HERA-B

Sbrizzi, A.

2006

document version
Publisher's PDF, also known as Version of record

Link to publication in VU Research Portal

citation for published version (APA)
Sbrizzi, A. (2006). *Beauty and a Search for Pentaquarks at HERA-B*. [PhD-Thesis - Research and graduation internal, Vrije Universiteit Amsterdam].

General rights
Copyright and moral rights for the publications made accessible in the public portal are retained by the authors and/or other copyright owners and it is a condition of accessing publications that users recognise and abide by the legal requirements associated with these rights.

- Users may download and print one copy of any publication from the public portal for the purpose of private study or research.
- You may not further distribute the material or use it for any profit-making activity or commercial gain
- You may freely distribute the URL identifying the publication in the public portal ?

Take down policy
If you believe that this document breaches copyright please contact us providing details, and we will remove access to the work immediately and investigate your claim.

E-mail address:
vuresearchportal.ub@vu.nl

Download date: 04. May. 2023

Beauty and a Search for Pentaquarks at HERA-B

Cover picture: **Beauty and the beast,** an artwork of Frank Frazetta.

Printed by Ponsen & Looijen BV, Wageningen.
Copyright © 2006 by Antonello Sbrizzi. All rights reserved.

The work presented in this thesis is part of the research programme of the "Nationaal Instituut voor Kernfysica en Hoge-Energie Fysica" (NIKHEF) in Amsterdam, the Netherlands. The author was financially supported by the "Stichting voor Fundamenteel Onderzoek der Materie" (FOM).

VRIJE UNIVERSITEIT

Beauty and a Search for Pentaquarks at HERA-B

ACADEMISCH PROEFSCHRIFT

ter verkrijging van de graad Doctor aan
de Vrije Universiteit Amsterdam,
op gezag van de rector magnificus
prof.dr. T. Sminia,
in het openbaar te verdedigen
ten overstaan van de promotiecommissie
van de faculteit der Exacte Wetenschappen
op vrijdag 16 juni 2006 om 13.45 uur
in de aula van de universiteit,
De Boelelaan 1105

door

Antonio Sbrizzi

geboren te Napels, Italië

promotor: prof.dr.ing. J.F.J. van den Brand
copromotor: dr. Th.S. Bauer

Alla mia famiglia

Mi piace far risalire
all’attenzione per mia madre,
e per il suo ingegno domestico,
large parte della mia
curiosità scientifica.

Contents

Introduction

"[...] As I said at the beginning, you are all a bunch of particles,
but with this I don't want to say that you are not important
for the person you are. Each of you is a unique person!
But each of you is also a unique combination of particles
and I see a lot of poetry in it! [...] "
Pippi D'Angelo

The work presented in this thesis is the result of a study performed in the field of elementary particles physics. The expression "elementary particles" is used to indicate the smallest constituents of matter, those which presumably do not have any internal structure, thus are considered indivisible. The idea, which roots back in the history of ancient greek philosophy, is that the wide complexity of the different forms of matter which appear in the universe, can be interpreted in terms of a few fundamental entities. During the course of history, the dimensions and the number of such fundamental entities changed many times. The atoms inside the molecule, the nuclei inside the atoms and the quarks inside the nucleus are some of the last steps of this process, which might well be a never ending story.

The physics of elementary particles is also known as high energy physics, since the study of microscopic phenomena is only possible when a large amount of energy is concentrated in a small region of space. The instruments used to produce such a large energy are called particle accelerators. These accelerators are complex machines, up to many kilometers long, in which bunches of charged particles, usually protons or electrons, are accelerated by electric fields and are bent and focused by magnetic fields. Particles are forced into collisions in order to explore the details of their internal structure. The limit which might be reached nowaday in the investigation of the fine structure of matter is 10^{-16} cm, which means about $1/1,000$ the proton diameter.

The study of elementary particles has revealed that the forces which are exchanged by particles have a large degree of similarity. In particular, there is a relation between electromagnetism, which governs electrons and nuclei inside atoms and molecules, and the weak force, which governs the radioactivity (beta decay). In a next step, theoretical physicists successfully worked to unify them with the strong force, which describes the interaction of particles inside the nuclei. Gravity, which is important at macroscopic level, governing for instance the motion of the galaxies, is not yet included in this unified theory.

The theory which currently describes most of the phenomena occurring in elementary particle physics at a large degree of accuracy is the Standard Model (SM). The particles which make up matter are called quarks and leptons[1], those which carry the interaction are called bosons. The boson which carries the electromagnetic force is the photon (γ). The weak force is carried by $W^{\pm}$ and Z bosons, while the strong force is mediated by gluons (g) (see table 1). For each particle an anti-particle with the same mass and opposite charge exists.

Quarks	Q	M	**Leptons**	Q	M	**Bosons**	Q	M
u, up	$+2/3$	$1.5-4.0$	e	-1	0.5	γ	0	0
d, down	$-1/3$	$4.0-8.0$	ν_e	0	0	g	0	0
c, charm	$+2/3$	$1.15-1.35$	μ	-1	105	$W^{\pm}$	±1	80
s, strange	$-1/3$	$80-130$	ν_μ	0	0	Z	0	91
t, top	$+2/3$	$178,100$	τ	-1	1780			
b, beauty	$-1/3$	$4,100-4,400$	ν_τ	0	0			

Table 1. Standard Model particles, charges Q and approximate masses M (in MeV) [2].

The ordinary matter observed in every day life is made of the lightest quarks (u and d), which form protons (uud) and neutrons (udd) in the atomic nucleus, and electrons, which orbit around the nucleus. The different kinds of matter have just a different composition of these basic ingredients. Quarks with a larger mass (s, c, b and t) do not form ordinary matter since they are unstable. As soon as they are created, they disintegrate into fragments of matter containing the lighter quarks. This process is also called decay. Protons and electrons are stable particles, while neutrons live in average for 15 minutes before decaying, when they are not captured inside a nucleus.

The study of particles made of heavier quarks is done in a laboratory equipped with a particle accelerator, which provide the energy sufficient to create them. Once they are created in a high energetic collision, heavy quarks live for an extremely short time before decaying. Their instability and the features of their decays are experimentally used as a signature to separate them from ordinary matter. From the experimental point of view, quarks are not observed directly, since the strong force keeps them confined into hadrons. At the moment, two types of hadrons are known: mesons, which are made of quark-antiquark pairs ($q\bar{q}$), and baryons, which are made of three quarks (qqq). The most common baryons are protons (uud) and neutrons (udd).

[1] In 1964 M. Gell-Mann and G. Zweig suggested that most of the particles known at that time could be explained as combinations of just 3 particles, called quarks. It was certainly revolutionary the idea that quarks had to carry a fraction of the proton charge, something which had never been observed before. The name 'quark' was inspired by James Joyce's novel Finnegans Wake (by the phrase "three quarks for Muster Mark"). The name 'lepton' was used by L. Rosenfeld in 1948: "*Following a suggestion of Prof. C. Möller, I adopt as a pendant to 'nucleon' the denomination 'lepton' (in greek small, thin, delicate) to denote a particle of small mass"* [1].

The identification of the different particles created in a high energetic collision is achieved with particle detectors. A detector is itself made of ordinary matter. It is placed in the proximity of the point where the collision takes place and serves to keep track of the processes originating from the collision. The study presented in this thesis was made at the HERA proton-electron accelerator in Hamburg. Along the proton beam, the HERA-B detector was placed to study the phenomena occurring in the collision of protons with wire targets of different materials.

The main topic of this thesis is the measurement of the abundance of b quarks produced in hadronic collisions. Quantum ChromoDynamics (QCD) [3], which is the theory of the strong interaction between quarks and gluons, is the theoretical framework of this study. At high energies, the prediction of the physical quantities, such as cross sections and lifetimes, is done in perturbative QCD (pQCD) [4] by expanding them in powers of the strong coupling constant α_s. The smaller α_s, the faster the series converges and the higher is the predictive power of the theory. The value of α_s decreases with the energy scale of the physics process under study. For heavy quark production the energy scale is fixed by the quark mass. Even though α_s is sufficiently small at the b quark mass ($\alpha_s \sim 0.1$), the convergence of the series is spoiled at HERA-B by the presence of logarithmic coefficients which are large when the centre of mass energy ($\sqrt{s} = 41.6$ GeV) is close to the kinematic limit for b quark production ($2m_b \sim 10$ GeV). In the last years, theoretical physicists improved the accuracy of the b cross section prediction, including higher order QCD processes, which are dominated by the emission of soft gluons and become relevant near the kinematic threshold. In conclusion, the measurement of beauty production at HERA-B offers the possibility to test pQCD in a peculiar kinematic range.

At HERA-B, the beauty cross section is measured relatively to J/ψ mesons (which are $c\bar{c}$ bound states). Therefore, it is crucial to have a clear understanding of the J/ψ production mechanism as well. The study of beauty production is also interesting for heavy ion collider experiments, where the suppression of J/ψ production, with respect to that in nucleon-nucleon collisions, is considered to be a signature of a new, deconfined state of matter, called Quark Gluon Plasma (QGP). A large fraction of J/ψ in these experiments is expected from beauty decays. The production of b relatively to c quarks increases from 0.0014 at $\sqrt{s} = 63$ GeV, which is close to the HERA-B energy, up to 0.072 at $\sqrt{s} = 5500$ GeV, which is the energy of ion collisions at LHC [5]. Therefore, a deep understanding of beauty production is needed in order to estimate correctly the J/ψ suppression. Other experiments will benefit of an increased knowledge in beauty production for the study of top physics.

Previously, two measurements of the b cross section in fixed target pA collisions were performed at Fermilab (E771 [6] and E789 [7]) but the results are inconsistent. However, due to the large theoretical uncertainties, the results are both consistent with the theoretical predictions. Compared to the previous experiments, HERA-B has a similar centre of mass energy but a larger kinematical acceptance. The larger the acceptance, the smaller is the systematic uncertainty due to the cross section extrapolation over the full phase space.

QCD successfully accounts for many fundamental properties observed in high energy experiments. One of these is the quark configuration of hadrons. In QCD, a quantum number called colour is assigned to all quarks and gluons. Quarks carry colour, antiquarks carry anticolour, while gluons carry colour-anticolour. The colour can be red (r), green (g) or blue (b). The fact that only hadrons with two quark configurations are experimentally observed, baryons (qqq) and mesons ($q\bar{q}$), is accounted for by requiring hadrons to be colourless objects (colour confinement). Two different kinds of colourless objects are in fact obtained by combining three quarks (rgb) or a quark and an antiquark ($r\bar{r}$, $g\bar{g}$ or $b\bar{b}$), which correspond to baryons and mesons. However, the existence of colourless objects with a quark configuration different from $q\bar{q}$ and qqq, which are known as exotic hadrons, is not excluded in QCD. Therefore, exotic hadrons, such as glue-balls (gg, ggg), hybrid mesons ($q\bar{q}g$) and others ($q\bar{q}q\bar{q}$, $qqqq\bar{q}$ and so on), have been searched for since the early days of QCD, but their existence has never been established beyond any doubt (see for instance reference [8]). This thesis aims also to search for experimental proofs of the existence of an exotic particle, the Θ^+ pentaquark, which is hypothetically made of four quarks and an antiquark ($uudd\bar{s}$). The period between 2002 and 2003, after the observation of such exotic state claimed by the LEP collaboration in Japan, was characterised by an intense worldwide activity of research in this field and the HERA-B collaboration participated providing relevant results.

This thesis is organised as follows. In chapter 1 we give an overview of the theory of heavy quark production and subsequent formation of bound states in pA collisions, with short paragraphs dedicated to theoretical models of exotic quark configurations. An overview of the status of the experimental search for the Θ^+ pentaquark is also presented. Chapter 2 gives a description of the detector and a summary of the main physics topics covered by the experiment. In chapter 3 the first level trigger is described in more details and its performance is studied in terms of track efficiency for leptons produced in J$/\psi$ decays. A measurement of the beauty production cross section is reported in chapter 4. Finally, in chapter 5, the results of a search for the Θ^+ exotic particle is presented.

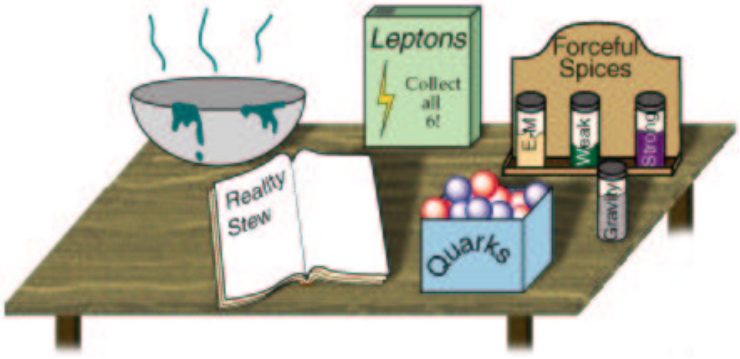

Figure 1. Ingredients of the Standard Model (taken from reference [9]).

Chapter 1

Theory

Nothing left to do but cry (1985) - R. Benigni and M. Troisi

We overview the theory of heavy quark production and subsequent formation of bound states in pA collisions, emphasising different aspects of beauty production and charmonium formation. We also introduce two models proposed to describe pentaquarks and give an overview of the status of the experimental search for the Θ^+ pentaquark.

1.1 Kinematics of nucleon-nucleon collisions

In the parton model, nucleons (protons and neutrons) are made of three valence quarks and a sea of low momentum partons (quarks, antiquarks and gluons). A collision between two nucleons is sketched in figure 1.1.

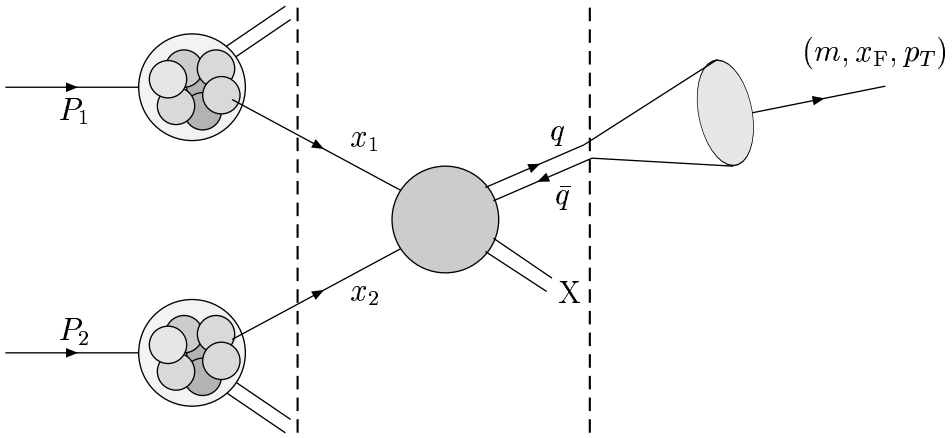

Figure 1.1. Production of a $q\bar{q}$ bound state in nucleon-nucleon collisions. The vertical dashed lines indicate an ideal separation in three subprocesses.

The parton four-momenta, p_1 and p_2, are the fractions x_1 and x_2 of the nucleon four-momenta (P_1 and P_2), with $p_1 = x_1 P_1$ and $p_2 = x_2 P_2$. The energy in the nucleon-nucleon centre of mass system is $\sqrt{s}$, with

$$s = (P_1 + P_2)^2. \tag{1.1}$$

At HERA-B, we have $\sqrt{s} = 41.6$ GeV. The centre of mass energy in the partonic system is given by

$$(p_1 + p_2)^2 \approx x_1 x_2 s. \tag{1.2}$$

In order to create a particle of mass m, we must have $x_1 x_2 s > m^2$. The kinematics of the final state particles in fixed target collisions is usually described in terms of the p_T and $x_{\rm F}$ (Feynman-x) variables, which are defined as

$$p_T \equiv \sqrt{p_x^2 + p_y^2} \quad \text{and} \quad x_{\rm F} \equiv \frac{2p_{z,cm}}{\sqrt{s}} \approx x_1 - x_2, \tag{1.3}$$

where p_x and p_y are the momentum components perpendicular to the momenta of the colliding nucleons and $p_{z,cm}$ is the longitudinal momentum, in the nucleon-nucleon centre of mass frame. An alternative to $x_{\rm F}$ is the rapidity y, defined as

$$y \equiv \frac{1}{2} \log \left(\frac{E + p_{z,cm}}{E - p_{z,cm}} \right), \tag{1.4}$$

where E is the energy of the produced particle. The shape of the rapidity distribution is invariant under a Lorentz transformation along the beam axis.

1.2 Factorisation theorem

The cross section of the process in figure 1.1 is calculated under the assumption that the initial state, the hard scattering process and the final state can be factorised. The factorisation is allowed only when the processes have different energy scales. The energy scale of the initial state is $\Lambda_{\rm QCD}$ ($\sim$ 200 MeV), since it is dominated by the dynamics of the partons inside the nucleons. The energy scale of the hard scattering is given by the heavy quark mass (m_Q), which is larger than $\Lambda_{\rm QCD}$. The factorisation of the initial state and hard parton scattering is known as factorisation theorem [10], while the factorisation of the final state is not yet proven (section 1.6).

The formula used to calculate the heavy quark production cross section is

$$\sigma_{H_1 H_2 \to q\bar{q}}(s) = \int_{4m_Q^2/s}^{1} {\rm d}x_1 \int_{4m_Q^2/x_1 s}^{1} {\rm d}x_2 \sum_{i,j} f_i^{H_1}(x_1) f_j^{H_2}(x_2) \times \hat{\sigma}_{ij \to q\bar{q}}(x_1 x_2 s), \tag{1.5}$$

where i and j run over the light quarks and gluons, $f_i^{H_1}$ and $f_j^{H_2}$ are the parton density functions (PDFs) in the colliding nucleons (H_1 and H_2) and $\hat{\sigma}_{ij \to q\bar{q}}$ is the hard parton scattering cross section.

1.3 Hard parton scattering

The cross section $\hat{\sigma}_{ij\to q\bar{q}}$ describes the probability to create a heavy quark pair $q\bar{q}$ in the interaction of two partons (i and j) of the colliding nucleons. In pQCD, $\hat{\sigma}$ is evaluated as a series in the strong coupling constant α_s, truncating the series to a certain power of α_s,

$$\hat{\sigma} = \sum_{l=\xi}^{\infty} a_l \alpha_s^l. \tag{1.6}$$

The lowest order ξ at which calculations can be performed is called leading-order. Calculations performed up to $\xi + 1$ are indicated as next-to-leading-order (NLO), those up to $\xi + 2$ as next-to-next-to-leading-order (NNLO), and so on. The smaller α_s, the faster the series converges and the perturbative approach provides more accurate results already at the lowest orders. At LO, the Feynman diagrams for heavy quark production are $q\bar{q}$ annihilation and gluon-gluon fusion (figure 1.2).

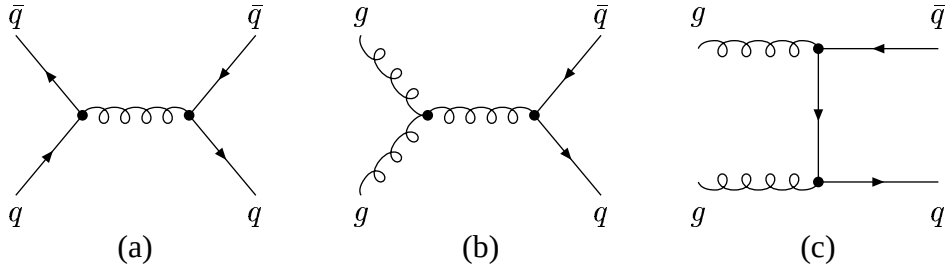

Figure 1.2. LO Feynman diagrams for $q\bar{q}$ production: $q\bar{q}$ annihilation (a) and gluon-gluon fusion (b), (c). Diagram (c) also contributes with a permutation of the gluon lines.

Leading order cross section calculations are finite in pQCD. At higher orders, however, divergences appear in the calculations. The diagrams that contribute to the cross section at higher orders are gluon emission and loop diagrams (figure 1.3).

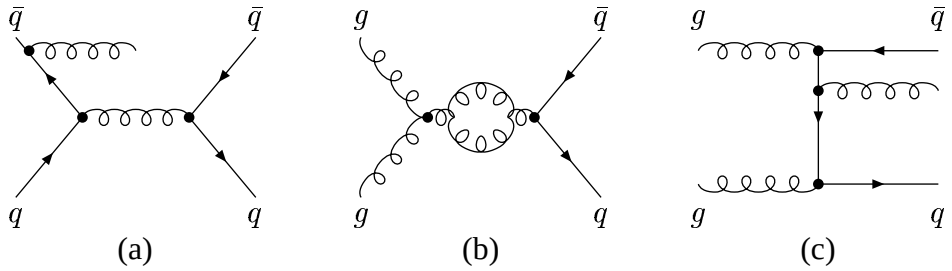

Figure 1.3. Examples of higher order Feynman diagrams for $q\bar{q}$ production: gluon emission in the initial (a) and final state (c) and loop diagram (b).

The divergences are classified in three types: ultraviolet, infrared and collinear.

The ultraviolet divergence arises when internal loops are taken into account. The momentum running around the loop goes to infinity and the calculations performed to predict physical quantities lead to indeterminate results. The predictive power of the theory is recovered by renormalising the coupling constant, which means to incorporate all terms responsible for ultraviolet divergences in the definition of the coupling constant. This procedure leads to a dependence of the coupling constant with the renormalisation scale μ,

$$\alpha_s(\mu^2) \sim \frac{12\pi}{(33-2n_f)\ln(\mu^2/{\Lambda_{\rm QCD}}^2)}, \tag{1.7}$$

where n_f is the number of quark flavours running around in the loop. The scale dependence of α_s exhibits two important features of QCD: asymptotic freedom and colour confinement. At large energy scales, α_s is small and quarks and gluons behave as free particles (asymptotic freedom) which allows to use pQCD for theoretical predictions. At low energy scales, α_s becomes large, resulting in confinement of quarks and gluons in colourless objects, called hadrons, as it is experimentally observed (colour confinement).

The infrared divergences appear when the emission of soft gluons are included in the calculation. These divergences cancel when the contributions of real and virtual gluons are summed.

The collinear divergences are due to the emission of gluons at small angles with respect to the quark momentum. In a procedure similar to renormalisation, the collinear divergences are absorbed in the definition of the parton density functions (PDFs). As a consequence, a factorisation scale μ_F appears in equation (1.5), where $f(x,\mu_F)$ takes the place of $f(x)$. The hard parton scattering cross section thus depends on two scales, which are arbitrary parameters needed to perform finite calculations in pQCD. For the sake of simplicity, they are frequently chosen to be equal ($\mu = \mu_F$). Although the physical cross section does not depend on the renormalisation scale, a scale dependence might appear in finite order calculations. The higher the order of the calculation, the weaker is the scale dependence. In heavy quark production, μ is the heavy quark mass and the variation of the result with μ is taken as an estimate of the theoretical uncertainty. The value of the coupling constant at the beauty and charm masses ($\alpha_s(m_c) = 0.33$, $\alpha_s(m_b) = 0.21$ [11]) suggests that for beauty production pQCD calculations are reliable, while for charm production non-perturbative effects might play a more important role.

1.4 Parton density functions

In the parton model, a beam of hadrons is equivalent to a beam of partons with longitudinal momentum distribution given by the PDFs $f(x,\mu)$. Specifically, $f(x,\mu)\mathrm{d}x$ is the probability to find a parton with momentum between xp and $(x+\mathrm{d}x)p$. The

analytical form of the PDFs cannot be calculated in pQCD because they are determined by low energy processes (the dynamics of partons inside the nucleon). However, QCD is able to predict their scale dependence (DGLAP equations [12]). If the factorisation theorem is valid, then the PDFs can be considered as universal functions and the value at HERA-B can be extrapolated from that obtained in other experiments at different energy scales (deep inelastic proton-electron scattering). The fits to the data are performed with different methods by several groups, such as the CTEQ5 (Coordinated Theoretical Experimental project on QCD) [13], the MRST (Martin, Roberts, Stirling, Thorne) [14] and the GRV98 (Glück, Reya, Vogt) [15]. The variation of the cross section with the set of parton density functions gives an estimate of the theoretical uncertainty.

1.5 The beauty cross section

The beauty production mechanism at HERA-B is dominated by gluon-gluon fusion (see figure 1.2(c)), which accounts for about 70% of the total cross section [16]. The contribution of quark-gluon scattering is at the level of a few percent [17]. NLO calculations in pQCD of the beauty cross section exist (see reference [17, 18]) but they are not sufficiently accurate since the correction factors at NLO with respect to LO are large (almost a factor 2). Therefore, calculations at higher order are necessary. A complication arises when the production takes place near the kinematic threshold ($x_1 x_2 s \approx 4m_b^2$), as it happens for beauty at HERA-B. The coefficients of the series in equation (1.6), in fact, can be written as

$$a_l = \sum_{k=0}^{l-2} a_l^{(l-2-k)} \log^{l-2-k}\left(1 - \frac{4m_b^2}{x_1 x_2 s}\right). \tag{1.8}$$

where the logarithmic terms, which we shall label L, are associated with the emission of soft gluons. The logarithmic terms become large near the kinematic threshold, where the convergence of the series is slowed down [16, 19]. The predictive power of the theory is recovered by keeping only some of the logarithmic terms in equation (1.8), and rearranging the series in equation (1.6) in such a way that it can be summed. This procedure is called "*resummation*", which is a short-hand for all order summation of potentially large terms in perturbation theory [20]. The meaning of resummation becomes clear when one rewrites schematically the cross section as a function of α_s and the potentially large logarithmic terms L [20],

$$\hat{\sigma} = 1 + \alpha_s(L^2 + L + 1) + \alpha_s^2(L^4 + L^3 + L^2 + L + 1) + \cdots . \tag{1.9}$$

The presence of L^2 corresponds to the simultaneous emission of soft and collinear gluons. The resummed form of the cross section can be written as

$$\hat{\sigma} = C(\alpha_s) \times \exp[Lg_1(\alpha_s L) + g_2(\alpha_s L) + \alpha_s g_3(\alpha_s L) + \cdots] + R(\alpha_s). \tag{1.10}$$

The terms g_i are functions of $\alpha_s L$ and can be computed. The terms $C(\alpha_s)$ and $R(\alpha_s)$ are series in α_s without logarithmic terms, which means, presumably, better behaviour [20]. Calculations up to g_1 are indicated as leading-logarithm (LL), those up to g_2 as next-to-leading-logarithm (NLL), and so on. An advantage of resummation is that the dependence on the logarithm moves into the exponent, as a series in $(\alpha_s L)$, which is under better control compared to equation (1.6). The exponential form appearing in the resummation formula reflects the fact that independent gluon emissions follow a Poisson statistics. The bottleneck of this procedure is that singularities, which are not present in finite order calculations, might appear in all-order resummation. However, these singularities can be usually handled.

At the moment two methods have been used to improve the NLO calculation of the heavy quark production cross section. Bonciani *et al.* [19] calculated NLL corrections at all orders of perturbation theory and added the result to the NLO cross section. Kidonakis *et al.* performed the calculation including terms up NLO order and adding corrections at NNLL-NNLO [16] and NNNLL-NNLO [21]. The scale dependence of the beauty cross section, as calculated by Bonciani *et al.*, shows that the theoretical prediction becomes less dependent on the choice of the scale when NLL contributions are included into the calculations (figure 1.4).

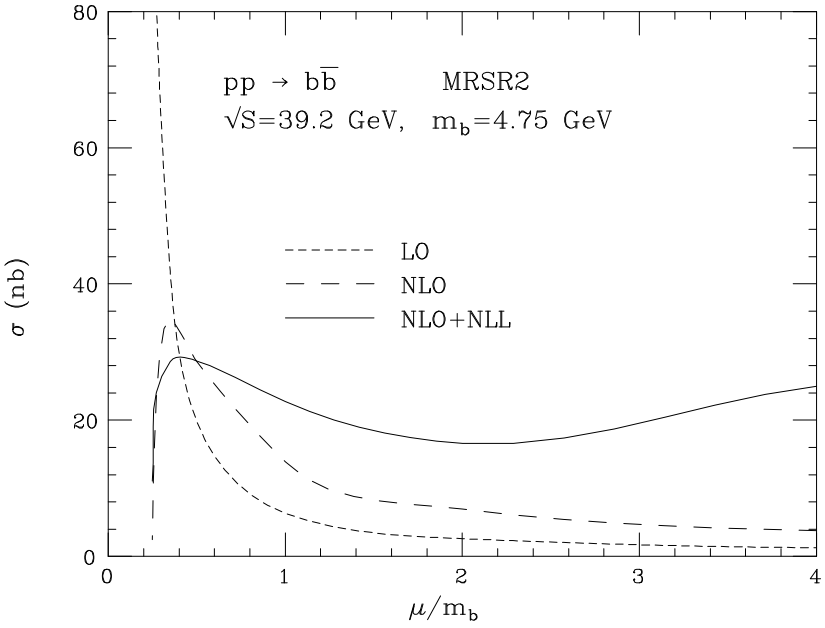

Figure 1.4. Beauty cross section dependence on the energy scale μ (from reference [19]) for LO, NLO and NLO+NLL calculations when the centre of mass energy of the pp collision is close to that of HERA-B and the MRSR2 PDFs are taken. Including NLL contributions, the theoretical prediction becomes less dependent on the choice of the energy scale.

After resummation, the theoretical prediction is still affected by a large uncertainty, due to the unknown b quark mass and the scale dependence (figure 1.5).

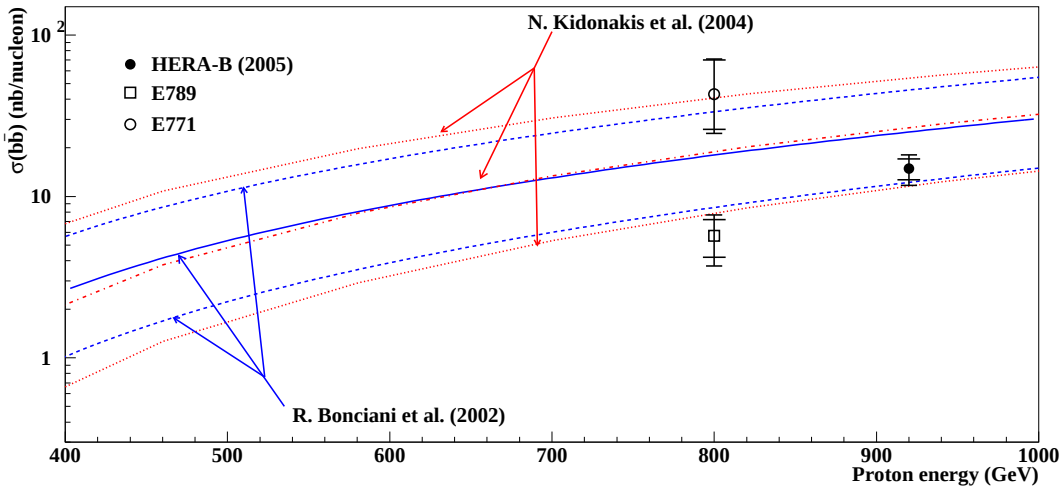

Figure 1.5. Beauty cross section per nucleon as a function of the proton energy in fixed target pA collisions, as predicted by Bonciani *et al.*[19] and Kidonakis *et al.*[21]. The predicted curves are accompanied by an upper and a lower curve accounting for the uncertainty in the calculations. The three available experimental results are superimposed.

The theoretical predictions of $\sigma_{b\bar{b}}$ at the HERA-B energy ($\sqrt{s} = 41.6$ GeV) are

$$\sigma_{b\bar{b}} = 25^{+20}_{-13} \text{ nb/nucleon } [19], \tag{1.11}$$

$$\sigma_{b\bar{b}} = 30 \pm 13 \text{ nb/nucleon } [16], \tag{1.12}$$

$$\sigma_{b\bar{b}} = 28 \pm 15 \text{ nb/nucleon } [21], \tag{1.13}$$

$$\sigma_{b\bar{b}} = 25 \pm 13 \text{ nb/nucleon } [21]. \tag{1.14}$$

The value (1.11) is obtained at NLO+NLL order, with the updated MRST parton distributions. The value (1.12) is obtained at NLLO+NNLL order, with the CTEQ5 parton distributions. The values (1.13) and (1.14) are obtained at NLLO+NNNLL order, with the MRST and GRV98 parton distributions. Three measurements on $\sigma_{b\bar{b}}$ are available from fixed target pA collisions (Tab.1.1). Those at the same energy are incompatible with each other [7, 6]. The measurement provided by the HERA-B collaboration is in agreement with the theoretical prediction.

Experiment	Year	Target	Proton Energy [GeV]	$\sigma_{b\bar{b}}$ [nb/nucleon]
E789 [7]	1995	Au	800	$5.7 \pm 1.5 \pm 1.3$
E771 [6]	1999	Si	800	$43^{+27}_{-17} \pm 7$
HERA-B[22]	2002/5	C/Ti/W	920	$14.9 \pm 2.2 \pm 2.4$

Table 1.1. Measurements of $\sigma_{b\bar{b}}$ at HERA-B and Fermilab experiments in pA collisions.

1.6 Hadronisation

Hadronisation is the mechanism by which quarks and gluons form the hadrons observed in the final state. Due to the low energy scale involved, pQCD cannot be used to describe the transition from quarks and gluons to hadrons. Therefore, the hadronisation process is parameterised with phenomenological models. We will discuss the methods used to describe the hadronisation in two cases: open beauty and charmonium production (with special focus on J/ψ).

1.6.1 Fragmentation of b quarks

In the hadronisation process, quarks lose part of their energy in fragmentation. The fragmentation function $f_p^H(z)$ is the probability to create a hadron (H) with a fraction z of the energy of the parton p. Two proposed parameterisations are the Peterson and Kartvelshvili functions,

$$f_p^H(z) = z^\alpha(1-z) \quad \text{and} \tag{1.15}$$

$$f_p^H(z) = \frac{1}{z}\left(1 - \frac{1}{z} - \frac{\varepsilon}{1-z}\right) \tag{1.16}$$

respectively, where α and ε are parameters extracted from the fit to the data. The b fragmentation function extracted from e^+e^- collisions is shown in figure 1.6 [23].

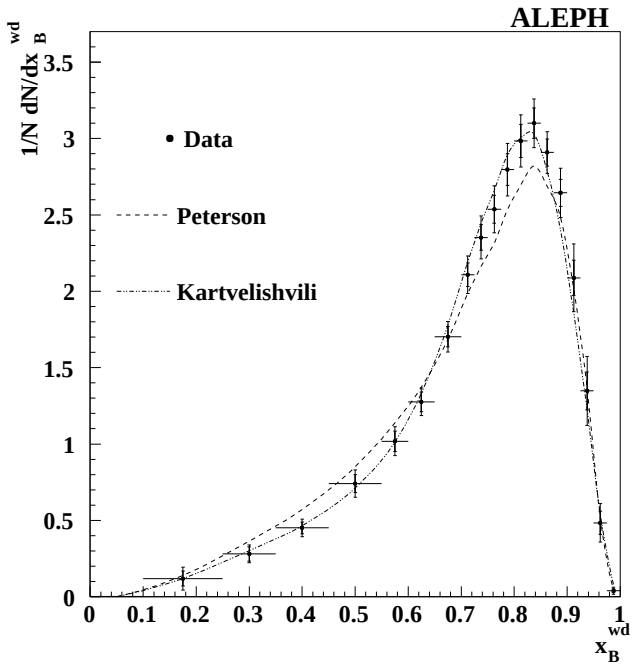

Figure 1.6. ALEPH results on b fragmentation as a function of the B meson energy ($\approx z$). The data and the fits with the Peterson and Kartvelshvili functions are shown.

1.6.2 Charmonium production

Most of the $c\bar{c}$ pairs produced in hard scattering hadronise into open charm mesons. Only a small fraction of $c\bar{c}$ pairs will form a bound state (charmonium). The different charmonium states are characterized by their quantum numbers: the radial number n, the orbital angular momentum L, the spin S and the total momentum J. The orbital angular momentum is usually denoted with letters, namely $\mathrm{S}, \mathrm{P}, \mathrm{D}$, for $L = 0, 1, 2$ respectively. The angular momentum determines the eigenvalues under parity and charge conjugation symmetry,

$$C = (-1)^{L+S} \qquad P = (-1)^{L+1}. \tag{1.17}$$

The names used to refer to the charmonium states are listed in table 1.2.

State	$\eta_c(n\mathrm{S})$	$\psi(n\mathrm{S})$	$h_c(n\mathrm{P})$	$\chi_{cJ}(n\mathrm{P})$
J^{PC}	0^{-+}	1^{--}	1^{+-}	J^{++}

Table 1.2. Names and quantum numbers of charmonium states. The $\psi(1\mathrm{S})$ is usually denoted by J/ψ, whereas the $\psi(2\mathrm{S})$ is also known as ψ'.

The charmonium cross section has an expression similar to equation (1.5),

$$\sigma_{H_1 H_2 \to H}(s) = \int_{4m_Q^2/s}^{1} \mathrm{d}x_1 \int_{4m_Q^2/x_1 s}^{1} \mathrm{d}x_2 \sum_{i,j} f_i^{H_1}(x_1) f_j^{H_2}(x_2) \times \hat{\sigma}_{ij\to H}(x_1 x_2 s). \tag{1.18}$$

The hadronic cross section $\hat{\sigma}_{ij\to H}$ is the probability to create the final state hadron H, starting from the partons i and j. It is calculated factorising the hard parton scattering and the hadronisation processes. Since the hadronisation energy scale is close to that of the hard parton scattering, the validity of the factorisation is not obvious. The energy scales involved in the formation of heavy quark bound states (quarkonia) are the quark mass (m), momentum (mv) and kinetic energy ($\frac{1}{2}mv^2$), where v is the velocity of the quarks in the quarkonium rest frame ($v^2 \approx 0.3$ for charmonium [11]). In order to describe the hadronisation, different phenomenological models have been proposed with different hypothesis on the factorisation. We introduce three models used to describe the production of charmonium, which are of interest for the work presented in this thesis.

1.6.3 The colour evaporation model

The first colour evaporation model (CEM) [24] was proposed in 1977, right after the discovery of the J/ψ. A more recent review can be found in reference [25]. In this model, the hadronic production cross section is factorised in the product of

the coloured $q\bar{q}$ quark pair and the subsequent evolution into a colour-singlet bound state. The transition probability is independent of the colour and the spin of the primary quark pair since it takes place by emission of soft gluons, which neutralize the initial colour configuration. If the hadronic final state H is charmonium, than the hadronic cross section ($\hat{\sigma}_{ij\to H}$) is obtained by integrating the hard parton scattering cross section ($\hat{\sigma}_{ij\to q\bar{q}}$ in equation (1.5)) from the kinematic limit $4m_c^2$ to the threshold for open charm production $4m_D^2$,

$$\hat{\sigma}_{ij\to H} = \mathcal{V}^H \int_{4m_c^2}^{4m_D^2} \mathrm{d}m^2 \frac{\hat{\sigma}_{ij\to q\bar{q}}(m)}{\mathrm{d}m^2}, \tag{1.19}$$

where $\mathcal{V}^H$ is a constant. Many predictions of the CEM disagree with the results obtained in $p\bar{p}$ collisions at the Tevatron. The basic prediction of the CEM is that the ratio of cross sections for two charmonium states should be constant for all production processes. This is in contrast with the observation that the ratio of cross sections for J/ψ and χ_c in photo-production and hadro-production are different [26]. Another prediction contradicted by experiments is the polarisation. The CEM predicts that the inclusive charmonium production does not depend on the spin of the $q\bar{q}$ pair. Therefore, charmonium should be unpolarised, which is in contrast with the observation of J/ψ polarisation [26].

1.6.4 The colour singlet model

In the colour singlet model (CSM) [27, 28] it is assumed that the hadron, which is a colour-singlet, can be formed only when the $q\bar{q}$ pair is created in a colour-singlet state with the correct angular momentum quantum numbers. For the conservation of C-parity in the strong process, the J/ψ must be accompanied by a gluon in the final state. Therefore, the leading order diagram for J/ψ production is $\mathcal{O}(\alpha_s^3)$ (see figure 1.7). A Feynman diagram with a third gluon in the initial state, rather than in the final state, is still leading order in α_s but is suppressed by the requirement of another gluon originating from the colliding nucleons (power suppressed).

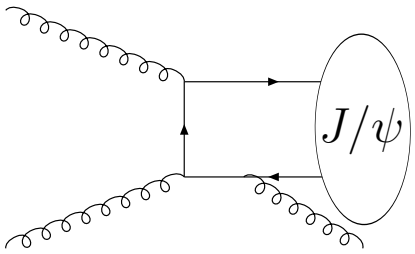

Figure 1.7. Leading order diagram for J/ψ production in CSM.

The hadronic cross section is obtained as product of the cross section for the production of a quark pair $q\bar{q}$ with quantum numbers n ($\hat{\sigma}_{ij\to q\bar{q}[n]}$) and the square of the radial wave function at the origin,

$$\hat{\sigma}_{ij\to H} = \left| \frac{\mathrm{d}^l}{\mathrm{d}r^l} R_{nl}(0) \right|^2 \hat{\sigma}_{ij\to q\bar{q}[n]}. \tag{1.20}$$

This is a factorisation formula, obtained under the assumption that the binding of the $q\bar{q}$ pair at low energy can be treated separately from the production mechanism at high energy. The radial wave function at the origin can be obtained either from the Schrödinger equation with a potential model, or from the measurement of the decay width into leptons. Contrary to the CEM, the CSM is able to predict the production cross section. Leading order calculations of the J/ψ cross section in the CSM disagree with the data provided by CDF [29]. As it can be seen in figure 1.8, higher order processes, such as gluon fragmentation, are needed to make the shape of the CSM prediction compatible with the data.

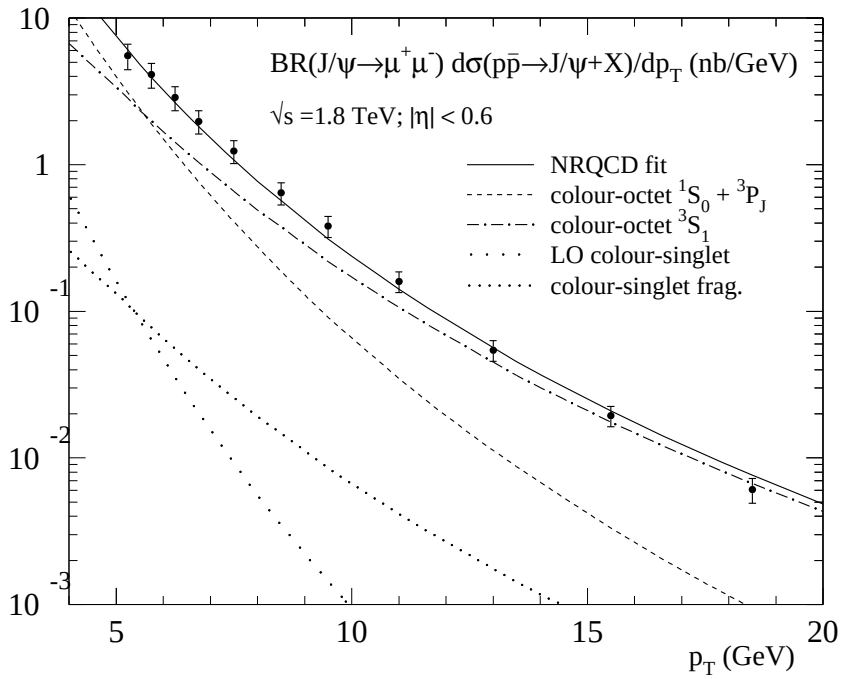

Figure 1.8. Differential J/ψ production cross section as a function of p_T[26]. The data points are CDF measurements, the dotted curve represents the prediction of the CSM model, the solid curve is a NRQCD fit (see next section), while the other curves are individual colour-octet contributions.

The absolute value of the cross section is still underestimated. A better description is obtained including contributions from colour-octet states. Such states are produced at the time scale of heavy quark production ($1/m_q$) and become colourless later, at the time scale of quarkonium production ($1/m_q v$), giving a substantial contribution to the total quarkonium production cross section.

1.6.5 Non-relativistic QCD

In order to include contributions from colour-octet states, a more formal approach was proposed in 1985, in the framework of a non relativistic quantum field theory, known as Non Relativistic QCD (NRQCD) [30]. It is an effective field theory in which quarks move at non-relativistic velocities v in the quarkonium rest frame (potential model calculations give $v^2 \approx 0.3$ for charmonium). In the NRQCD factorisation approach, the hadronic cross section is written as

$$\hat{\sigma}_{ij\to H} = \sum_n \hat{\sigma}_{ij\to q\bar{q}[n]} \langle \mathcal{O}^H[n] \rangle, \tag{1.21}$$

where $\hat{\sigma}_{ij\to q\bar{q}[n]}$ is the hard parton scattering cross section already defined in equation (1.20) and $\langle \mathcal{O}^H[n] \rangle$ are matrix elements which describe the probability that the quark pair forms a bound state. A formal proof of the NRQCD factorisation does not exist, but it has been recently shown that it holds up to two loops for high-p_T quarkonium production [31]. The matrix elements cannot be computed in pQCD and they are considered to be universal. The predictive power of NRQCD is due to the fact that the matrix elements obey a velocity scaling rule [32],

$$\langle \mathcal{O}^H[n] \rangle \propto v^{f(n,H)}, \tag{1.22}$$

where f is a function of the quantum numbers n and the final state H [33]. This allows to evaluate the hadronic cross section as a double series in α_s and v,

$$\hat{\sigma}_{ij\to H} = \sum_{l,m} a_{l,m} \alpha_s^l v^m, \tag{1.23}$$

providing a similar framework as pQCD for the evaluation of the quark production cross section. For charmonium production, this is a slowly convergent series due to the fact that the mass of the c quark is not too large and the velocity v is not so small. Therefore, one has to add many matrix elements in order to have an accurate cross section calculation (some of them can be expressed in terms of the others by using heavy quark spin symmetry [34]). As for the calculation of $\sigma_{b\bar{b}}$ in pQCD, the occurrence of large logarithms can make the series to converge even slower.

Despite the success of NRQCD in describing the CDF data on charmonium production (figure 1.8), the validity of this theory is still debated. The fact that matrix elements are extracted from fits to data implies that the uncertainties are quite large and are affected by the choice of a specific set of PDFs of the colliding particles. Furthermore, NRQCD is not able to account for some experimental results. The assumption of universality is contradicted by the fact that different values of the colour-octet matrix elements are extracted in $p\bar{p}$ collisions at the Tevatron and in pe collisions at HERA. NRQCD predicts the polarisation of J/ψ at high-p_T, which was not observed in CDF data [35].

1.7 Nuclear effects

We have described the kinematics of nucleon-nucleon collisions treating the nucleons as independent objects. However, the target nucleons in HERA-B are part of nuclei, and one has to take into account possible effects of the surrounding nuclear matter on the bare nucleon-nucleon cross section. The proton-nucleus cross section (σ_{pA}) is usually factorised in the product of the cross section per proton-nucleon interaction (σ_{pN}) and a power law of the atomic weight (A^{α}),

$$\sigma_{pA} = \sigma_{pN} \cdot A^{\alpha}. \tag{1.24}$$

The probability that processes with large cross sections occur is expected to grow with the surface of the nucleus. Since the dependence of the surface on the number of nucleons is $A^{2/3}$, the same dependence is expected for the cross section. This expectation is confirmed by the observation that the inelastic cross section grows as $A^{0.71}$. Rare processes, such as quarkonium production, are expected to grow with the volume of the nucleus. Since the volume is proportional to the number of nucleons, the cross section for rare processes is expected to grow with A.

For J/ψ production, the value of α has been measured with high precision as a function of x_{F} and p_T by the E866 collaboration at a centre of mass energy similar to that of HERA-B but in a smaller acceptance ($0.0 < x_{\mathrm{F}} < 0.2$),

$$\alpha = 0.96 \pm 0.01 [36]. \tag{1.25}$$

Nuclear effects are usually separated into initial and final state effects. A description of nuclear effects in nucleon-nucleon interactions can be found in reference [37, 38]. Initial state effects concern the parton density functions inside the target and the incident nucleons. Deep inelastic scattering experiments show that partons in a single proton have a different distribution when the proton is inside the nucleus (nuclear shadowing). Incident partons can also be affected by the nuclear environment. Multiple scattering in the nuclear matter, in fact, leads to energy loss and broadening of the transverse momentum distribution of the projectile partons. Final state effects take place after the hard scattering process. Once the $q\bar{q}$ pair is formed, the evolution into a bound state can be affected by the presence of nuclear matter. At HERA-B, most of the J/ψ are formed outside the nuclear matter [38]. Inside the nuclear matter, the pre-meson $q\bar{q}$ pair is subject to interactions similar to those affecting the incident partons which can lead to a dissociation of the quark pair and a subsequent reduced probability to form the J/ψ (nuclear suppression). Once the J/ψ is formed, the interactions with other particles produced in the interaction can cause a dissociation of the bound state (co-mover suppression).

The study of nuclear effects is interesting since theoretical models on charmonium formation give different predictions. Furthermore, the understanding of nuclear effects in nucleon-nucleon collisions is the basis for the study of nuclear effects in nucleus-nucleus collisions, where quarks are expected to form a deconfined state of matter called the Quark-Gluon-Plasma (QGP).

1.8 The J/ψ cross section in NRQCD

The colour-octet matrix elements extracted from the CDF data [39] and the colour-singlet matrix elements taken from potential models [40, 41] have recently been used to perform a global fit to all data available in charmonium production in pp collisions and fixed target experiments [42]. The result of the fit as a function of the centre of mass energy for J/ψ production is reported in figure 1.9, when the value of α_s presented in the previous section ($\alpha = 0.96 \pm 0.01$) is used.

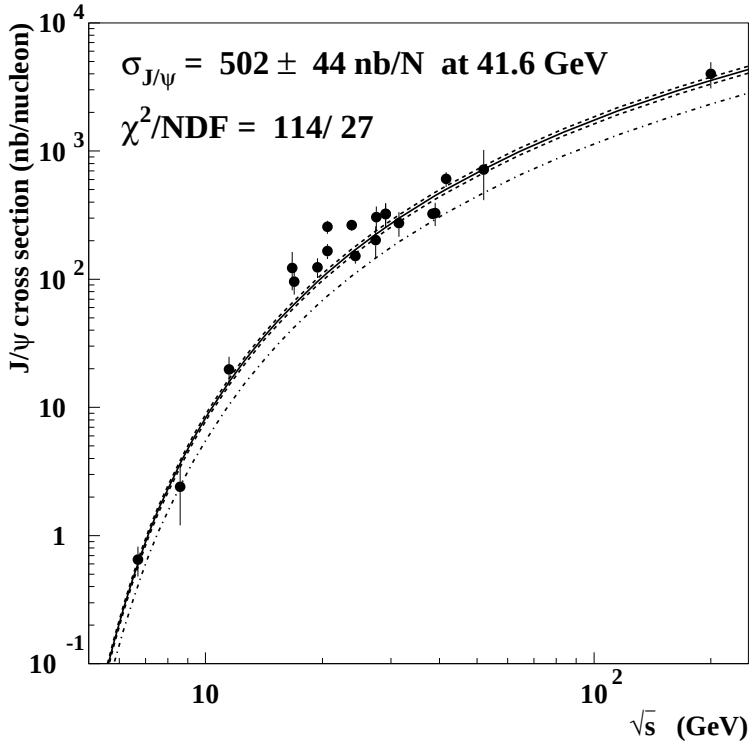

Figure 1.9. Experimental values of the J/ψ cross section as a function of the centre of mass energy. A fit performed on the basis of NRQCD calculations is superimposed [42]. The dot-dashed line indicates the NRQCD prediction without any colour-octet. The continuous line is the result of a fit including colour-octet contributions. The two dotted lines refer to the uncertainty in the fit.

The J/ψ cross section per nucleon at HERA-B ($\sqrt{s} = 41.6$ GeV) results in

$$\sigma_{pN}(\mathrm{J}/\psi) = 502 \pm 44 \text{ nb/nucleon}. \tag{1.26}$$

The main uncertainty is systematic and has been evaluated by changing the set of fitted data points, the energy scale and the set of parton density functions. Within the HERA-B acceptance, the J/ψ cross section is

$$\sigma_{pN}(\mathrm{J}/\psi) = 417 \pm 37 \text{ nb/nucleon}. \tag{1.27}$$

1.9 Light hadrons

QCD successfully accounts for many fundamental properties observed in experiments (asymptotic freedom, colour confinement *etc.*). At high energy scales, QCD has been tested to a high level of accuracy in its perturbative version, while in the low energy regime, where QCD is non-perturbative, calculations can only be performed with lattice simulations. Since the application of lattice QCD is limited by the demand of computing power, hadron spectra, as well as other low energy processes, are often described with phenomenological models. One of the most successful is the quark model.

According to the quark model, hadrons are grouped in two families of colour singlet objects called mesons and baryons. Mesons have a $q\bar{q}$ quark configuration and integer spin. Baryons have a qqq quark configuration and half-integer spin. They are grouped in multiplets. The multiplets can be obtained by assuming that the Hamiltonian of the strong interaction is invariant under certain transformations, like rotations in the ordinary space or in the space of quark flavours [43]. For instance, asking that the Hamiltonian is invariant under a rotation in the space of the u, d, s flavours generates the multiplet containing protons, Σ and Ξ states, but with all states degenerate at the same mass. Introducing some degree of symmetry breaking, like a difference in mass between u, d and s, allows to reproduce the observed hadron spectrum. In figure 1.10 we show the octet ($J^P = \frac{1}{2}^+$) and decuplet ($J^P = \frac{3}{2}^+$) of baryons in the Y-I_3 plane, where Y is the hypercharge, which is defined as the sum of the baryon and strange quantum numbers, and I_3 is the third component of the isospin.

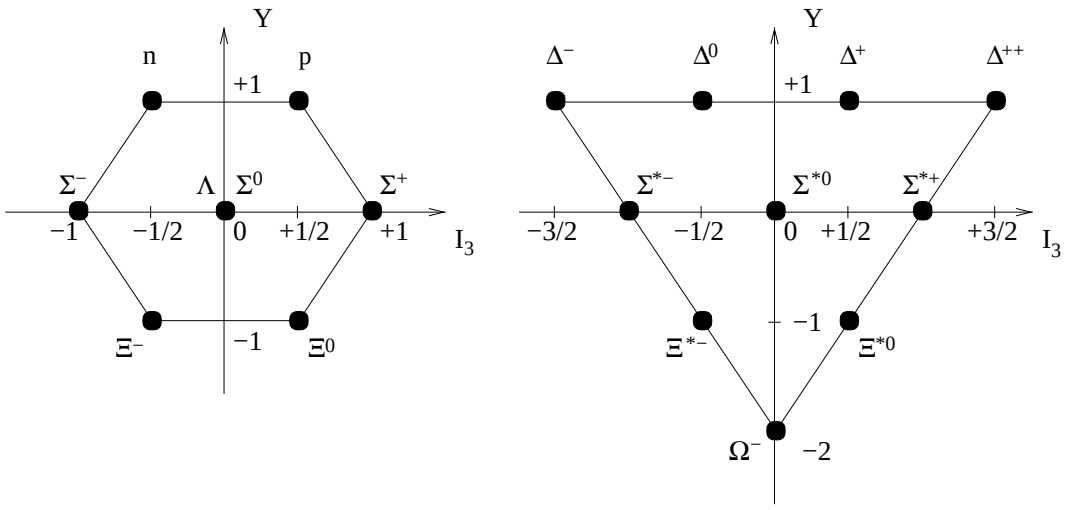

Figure 1.10. Octet and decuplet of baryons in the Y-I_3 plane.

1.10 Theoretical models for pentaquarks

The existence of hadrons with exotic quark configurations (those different from $q\bar{q}$ and qqq) is not excluded in QCD, under the condition that hadrons are colour singlets. Therefore, exotic hadrons, such as glue-balls (gg, ggg), hybrid mesons ($q\bar{q}g$) and others ($q\bar{q}q\bar{q}$, $qqqq\bar{q}$ and so on), have been searched for since the early days of QCD, but their existence has never been established beyond any doubt (see for instance reference [8]).

In 2002, the LEPS collaboration at SPring-8 claimed the observation of a state with the pentaquark configuration $uudd\bar{s}$, labelled $\Theta^+(1540)$[44]. Due to its positive strangeness ($S = 1$), this pentaquark should be copiously produced by scattering kaons on a proton or deuteron target and should undergo a strong kaon-nucleon decay, since it is energetically allowed. However, the hadron spectroscopy in kaon-nucleon scattering experiments has been subject of intense studies in the past and such state has never been observed [2]. Early theories were based on a straightforward extension of QCD and predicted the existence of pentaquarks at masses larger than $2\ \mathrm{GeV}/c^2$. It has been argued that the fact that all experimental efforts were concentrated at masses larger than $2\ \mathrm{GeV}/c^2$ diverted the attention from the detection of possible lower mass resonances [45].

Due to the renewed interest in this field, the first theoretical study of pentaquarks based on a lattice simulation have been recently reported [46]. The result is the absence of pentaquarks with $J^P = \frac{1}{2}^+$ and $I = 0, 1$. In the following, we discuss two theoretical models proposed to account for pentaquarks.

1.10.1 Chiral soliton model

In 1997, Diakonov *et al.*[47] predicted the existence of a pentaquark having a width smaller than $15\ \mathrm{MeV}/c^2$ and a mass of $1530\ \mathrm{MeV}/c^2$, within the framework of the chiral soliton model[1]. The predicted pentaquark has baryon number $B = 1$, strangeness $S = 1$, hypercharge $Y = 2$, third component of the isospin $I_3 = 0$ and spin-parity $J^P = \frac{1}{2}^+$.

Contrary to QCD, the chiral soliton model is an effective theory dominated by pseudoscalar mesons, the Goldstone modes of QCD. These allow topologically stable soliton solutions. The first model based on the idea of the solitons was proposed by Skyrme in 1963 [49]. After the introduction of quarks, the consistency of the soliton picture with QCD at low energy scale was proven [50] [51]. In the chiral soliton model, baryons are interpreted as different rotational states of the same physical object. The first two rotational states correspond to the octet and decuplet of the observed baryon mass spectrum. With only symmetry considerations, it relates the characteristics of the members of the octet and the decuplet.

[1] After the observation claimed by the LEPS collaboration, the state predicted by Diakonov has been named $\Theta^+(1540)$. In a recent note, Jaffe [48] pointed out that the estimate of the width by Diakonov *et al.* is not correct, due to an arithmetic error. The correct value is $\Gamma < 30\ \mathrm{MeV}/c^2$.

One of the most striking successes of the model is the Guadagnini formula [52] which relates the mass splitting inside the decuplet with that inside the octet,

$$8(m_{\Xi^\star + M_N}) + 3m_\Sigma = 11m_\Lambda + 8m_{\Sigma^\star}. \tag{1.28}$$

This formula is experimentally verified within 1% accuracy. Diakonov *et al.* proposed that the $\Theta^+(1540)$ is the lightest member of the antidecuplet corresponding to the third rotational state of the chiral soliton model (figure 1.11).

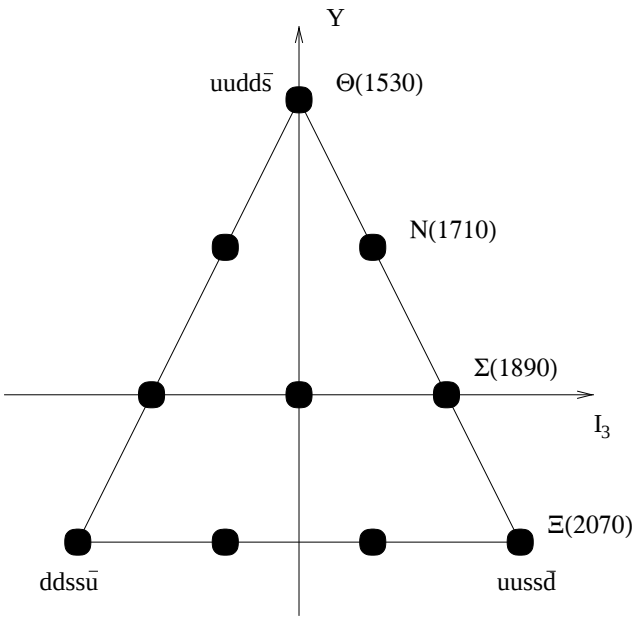

Figure 1.11. The antidecuplet of pentaquarks predicted by Diakonov *et al.* in the Y-I_3 plane [47]. The states at the corners of the triangle exhibit an exotic quark configuration. The state labelled Θ^+ has a $uudd\bar{s}$ configuration and has the lowest mass.

The only members with an exotic quark configuration are those on the corners of the antidecuplet. Following symmetry considerations, the value of the mass splitting in the antidecuplet can be obtained,

$$\Delta m = 180 \text{ MeV}. \tag{1.29}$$

The absolute value of the mass depends on the moment of inertia of the rotating object and is model dependent. Therefore, Diakonov *et al.* preferred to fix the mass by identifying one of the member of the multiplet with the conventional $N(1710)$ resonance. The narrow width of the $\Theta^+(1540)$ comes from the cancellation of the coupling constant in the LO, NLO and NNLO of the perturbative expansion in the number of quark colours (N_c). However, in reference [53], it was pointed out that the perturbative treatment in N_c cannot be used to predict the existence of the $\Theta^+(1540)$ while it can still be useful to describe the relations between the members of the antidecuplet, once their existence would be experimentally established.

1.10.2 Diquark model

In 2003, Jaffe and Wilczek [54] proposed that the $\Theta^+(1540)$ is a bound state of a strange antiquark and two highly correlated scalar ($J = 0$) ud quark pairs. They proposed that there exists a strong correlation between light quarks when they are in the antisymmetric flavour, colour, isospin and spin configuration [54]. The lighter the quarks, the stronger is the correlation. This helps the light quark pair to form a diquark. The pentaquark antidecuplet is accompanied by an almost degenerate octet, which also mixes with the antidecuplet. The resulting pentaquark antidecuplet and octet have $J^P = \frac{1}{2}^+, \frac{3}{2}^+$ (figure 1.12).

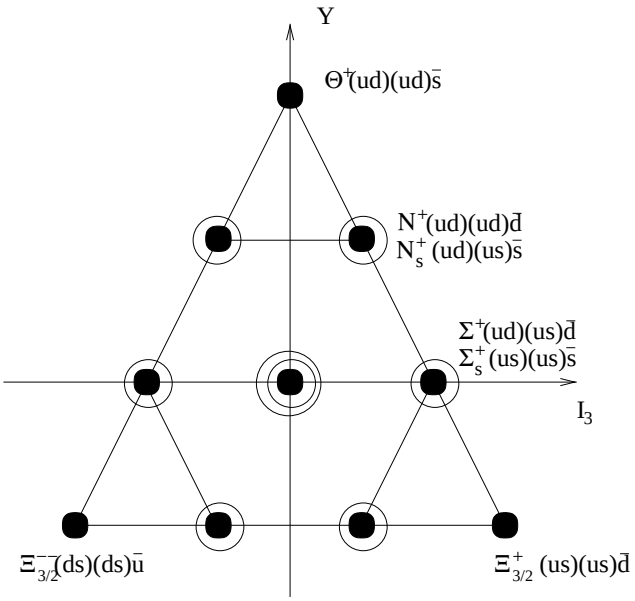

Figure 1.12. The antidecuplet and overlapping octet of pentaquark baryons predicted by Jaffe and Wilczek in the Y-I_3 plane [54].

Therefore, contrary to the chiral soliton model, the diquark model predicts the existence of pentaquark partners of the $J^P = \frac{1}{2}^+$ antidecuplet with a larger angular momentum and, as a consequence, a larger mass. In addition, the $\Theta^+(1540)$ does not result the lightest pentaquark. The mixing between the octet and the antidecuplet produces two states, one below and the other above the $\Theta^+(1540)$ mass (in figure 1.12 they are labelled N^+ and N_s^+, respectively). With the $\Theta^+(1540)$ mass as input, the N_s^+ mass is about $1710\ \mathrm{MeV}/c^2$, while the lighter N^+ is identified with the Roper resonance [54]. This is a well established "*four stars*" (****) state having a width of about $250\ \mathrm{MeV}/c^2$, which is much larger than the claimed width of the $\Theta^+(1540)$. No explanation is provided in reference [54] for the simultaneous existence of two pentaquarks with such different widths. Finally, both chiral soliton and diquark models predict pentaquarks with positive parity. However, in the diquark model there is room for additional states with negative parity. The experimental proof of the absence of such states would clearly invalidate the diquark model.

1.11 The claim for pentaquark

When the work of Diakonov in 1997 appeared [47], the experimental search for pentaquarks had a new life. He predicted the existence of an exotic strange particle with a mass of $1530\ \mathrm{MeV}/c^2$ and a width smaller than $15\ \mathrm{MeV}/c^2$, decaying into a kaon and a nucleon. He proposed to search for it in photo-production experiments, since the initial state photon already carries a portion of strange quark. The first observation of a narrow signal around $1.5\ \mathrm{GeV}/c^2$ in the kaon-nucleon system was claimed by the LEPS collaboration in 2002 [44], employing an electromagnetic probe on a carbon target ($E_{max} = 2.4$ GeV). The claimed signal at the invariant mass $1540 \pm 10_{stat} \pm 5_{syst}\ \mathrm{MeV}/c^2$, with an estimated significance of $4.6 \pm 1\sigma$ and a width less than $25\ \mathrm{MeV}/c^2$, is reported in figure 1.13(a).

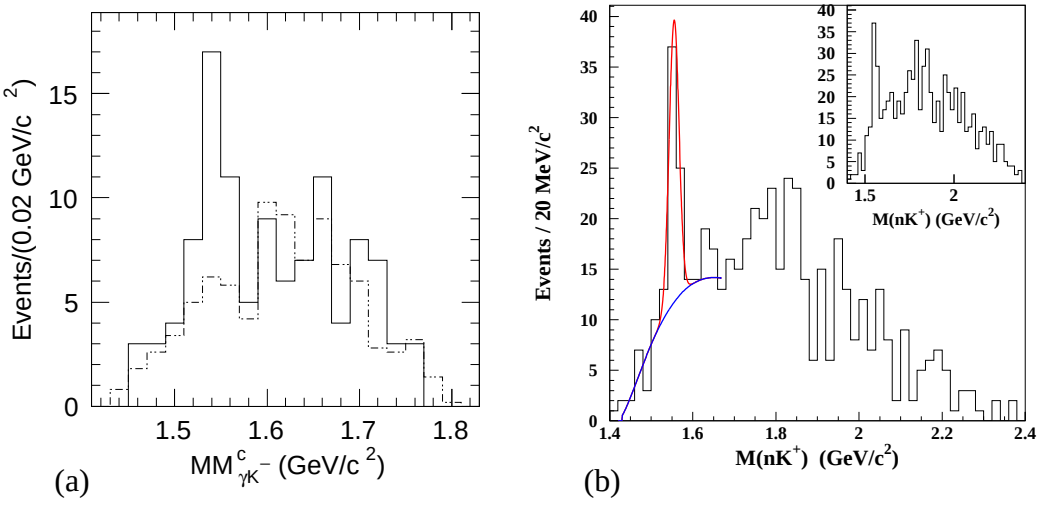

Figure 1.13. The left plot shows the n-K^+ invariant mass in $\gamma\,^{12}\mathrm{C} \to K^+K^-\ X$ reactions (solid histogram) at SPring-8. The dash histogram represents the background estimated with a hydrogen target. The right plot shows the n-K^+ invariant mass in $\gamma p \to K^+K^-\ \pi^+ n$ reactions at CLAS, when $\cos\theta^\star_{K^+} < 0.6$ and $\cos\theta^\star_{\pi^+} > 0.8$. The fits of signal and background are superimposed. The inset shows the same spectrum for all values of $\cos\theta^\star_{K^+}$.

Following the LEPS announcement, the CLAS collaboration searched for the reaction $\gamma p \to K^+K^-\ \pi^+(X)$ in photoproduction data taken with a photon energy between 4.8 and 5.4 GeV on a hydrogen target [55]. The claimed signal at the invariant mass $1555 \pm 7_{stat} \pm 10_{syst}\ \mathrm{MeV}/c^2$, with an estimated significance of 8σ and a width less than $35\ \mathrm{MeV}/c^2$, is reported in figure 1.13(b). The signal claimed by the CLAS collaboration looks interesting. However, the analysis cuts used to isolate the signal raise doubts. The angle between the K^+ and the photon beam in the centre of mass system is such that $\cos\theta^\star_{K^+} < 0.6$. A similar cut is also applied to the $\pi^+(\cos\theta^\star_{\pi^+} > 0.8)$. Since these angles might be correlated with the invariant mass, similar cuts could produce fake structures. In addition, a general concern in

the search for resonances in the Θ^+ mass region is the possibility that fake structures are produced either by kinematical reflections of low mass resonances [56] or by the presence of tracks clones [57].

After the claims of LEPS and CLAS, old data on kaon-nucleon scattering were reanalysed to shed some light on the low mass region [58]. The conclusion of these studies was that the existence of the reported $\Theta^+(1540)$ is excluded for widths larger than $1\ \mathrm{MeV}/c^2$, while the lack of statistics did not allow any conclusion for smaller widths. Since then, there was a shower of reports on the observation of narrow structures in the n-K^+ [59] and in the p-K^0_s mass spectrum [60, 61, 62, 63, 64, 65]. As a consequence, the $\Theta^+(1540)$ pentaquark was included in the PDG of 2004 as a "*three stars*" (***) resonance [2].

Two experiments reported about other possible candidates of the mass decuplet predicted by Diakonov. The NA49 collaboration claimed the observation of a doubly strange resonance at $1862\ \mathrm{MeV}/c^2$ [66] in pp collisions that was interpreted as the Ξ^{--} member of the pentaquark decuplet. However, old hyperon beam data produced to study Ξ spectroscopy, were reanalysed and no evidence of a new exotic resonance was reported [67, 68], even though they relied on a larger sample of the classical Ξ^0_{1530} state. The NA49 collaboration also reported the absence of exotic signals in the nK system. The H1 collaboration at HERA reported a narrow signal in the $pD^\star$ system [69], which was interpreted as a member of the charm pentaquark multiplet. However, the ZEUS experiment, which is installed on the same beam line and is to large extents similar to H1, did not observe the exotic charmed resonance. Another inconsistency between the two experiments was that ZEUS claimed a signal in the p-K^0_s channel, which H1 could not see. After that, many experiments with large statistics data in pp, pA and e^+e^- collisions did not confirm the existence of the $\Theta^+(1540)$ pentaquark [70, 71, 72, 73, 74][2].

Question of the mass and the width

The masses of the claimed signals is spread in a range of $12\ \mathrm{MeV}/c^2$, despite the accuracy with which some experiments are able to resolve masses. It could be that each experiment is looking at different particles of a pentaquark multiplet, but in this case one should understand why these particles prefer to appear in one experiments rather than the others. Another debated argument is the width. As all strong decays, Θ^+ is expected to have a large width as well. The model introduced in section 1.9 accounts for the small width with a small overlap between the initial and final wave functions. In this controversial context, the HERA-B collaboration also performed a search for narrow signals in the p-K^0_s system.

[2] Recently, the CLAS collaboration performed the first high statistics photoproduction experiment dedicated to the search for $\Theta^+ \to nK^+$ decays in the reaction $\gamma p \to \bar{K^0}K^+n$, with a high mass resolution detector ($\sigma < 2\ \mathrm{MeV}/c^2$) [75]. In contrast with their previous observation, no structure could be identified between 1.4 and $2.2\ \mathrm{GeV}/c^2$.

Chapter 2

The HERA-B Experiment

The legend of the holy drinker (1988) - E. Olmi

HERA-B was a fixed target experiment that used the 920 GeV proton beam of the HERA accelerator at DESY in Hamburg. We describe the detector and the main physics topics covered by the experiment.

2.1 A brief historic introduction

The HERA-B experiment was proposed in 1994 to study the violation of CP symmetry in neutral B meson decays $B^0 \to \mathrm{J}/\psi K^0_s$[76, 77]. Compared to inelastic pA collisions, the occurrence of such decays is suppressed by a factor 10^{-11}. Therefore, a highly selective trigger was built to identify dilepton decays of the J/ψ mesons. The commissioning of the detector was completed only in 2002. This was due to a prolonged effort required to improve the performance of the tracking system, strongly affecting the trigger [78]. By that time, it was clear that the two competitor experiments, Belle [79] and BaBar [80], were going to perform the same measurement in e^+e^- collisions at the $\Upsilon(4s)$ energy, where a clean and abundant production of B mesons could guarantee a larger accuracy.

The physics program of the experiment was modified to cover different aspects of heavy quark production in pA interactions. In particular, the large acceptance of the detector, the high spatial resolution for primary and secondary vertices, the selective dilepton trigger and the multi-target operation make the experiment suitable for the study of many interesting topics [81, 82].

Data-taking started in October 2002 and lasted only for 5 months, since a long shut-down of the accelerator was performed in order to improve the performance of the colliding beam experiments installed on the same beam line. After the long shut-down, the HERA-B experiment was terminated.

2.2 Accelerator

The HERA-B detector was installed in the HERA (Hadron Elektron RingAnlage) accelerator at DESY in Hamburg. The accelerator is a storage ring for protons of 920 GeV and electrons or positrons of 27.5 GeV with a circumference of about 6 km. Particles are injected after a series of pre-acceleration steps (figure 2.1).

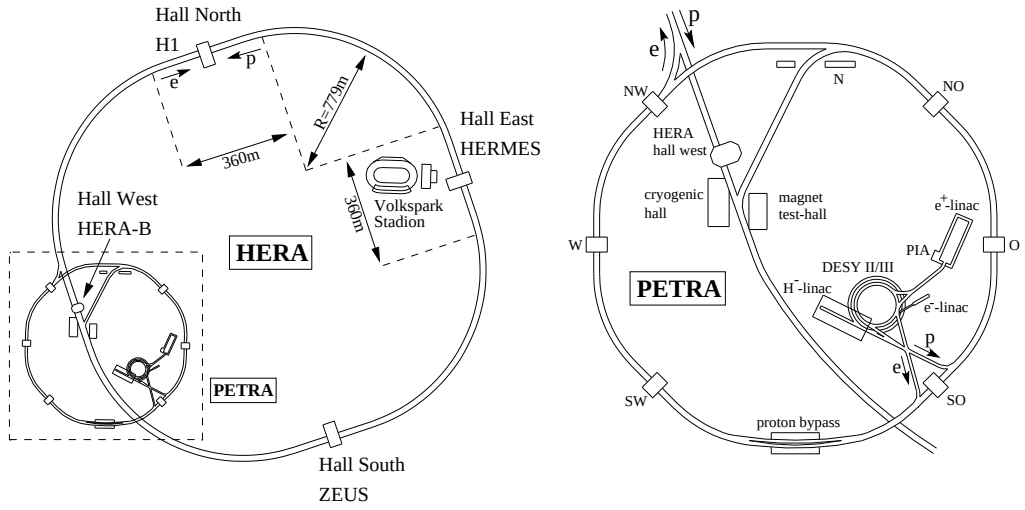

Figure 2.1. The HERA accelerator at DESY in Hamburg. The left picture shows the location of the four experiments installed at HERA. The right picture shows the pre-acceleration steps used to fill the main storage ring. Protons are guided by superconducting magnets while electrons are guided by normal conducting magnets.

The storage ring can accept 220 bunches of about 10^{11} protons. The filling scheme at HERA foresees that only 180 bunches are usually filled. Since the time between two bunches is 96 ns, the average rate of proton bunches crossing the HERA-B detector is about 10 MHz.

Four experiments are installed in the accelerator. Two colliding beam experiments, ZEUS [83] and H1 [84], explore deep inelastic scattering of protons and electrons in order to study the proton structure functions. One fixed target experiment, HERMES [85], studies the spin structure of the nucleons by scattering longitudinally polarised electrons on polarised hydrogen and deuterium gas targets. Finally, the HERA-B experiment [76] investigates the interaction of the proton beam halo with targets of different materials in order to study the production of beauty and charm hadrons at a centre of mass energy of $\sqrt{s} = 41.6$ GeV.

2.3 Detector layout

The HERA-B detector [77] is a forward spectrometer with large acceptance used to reconstruct charged particle tracks produced in the interaction of 920 GeV protons with fixed wire targets of different materials (figure 2.2).

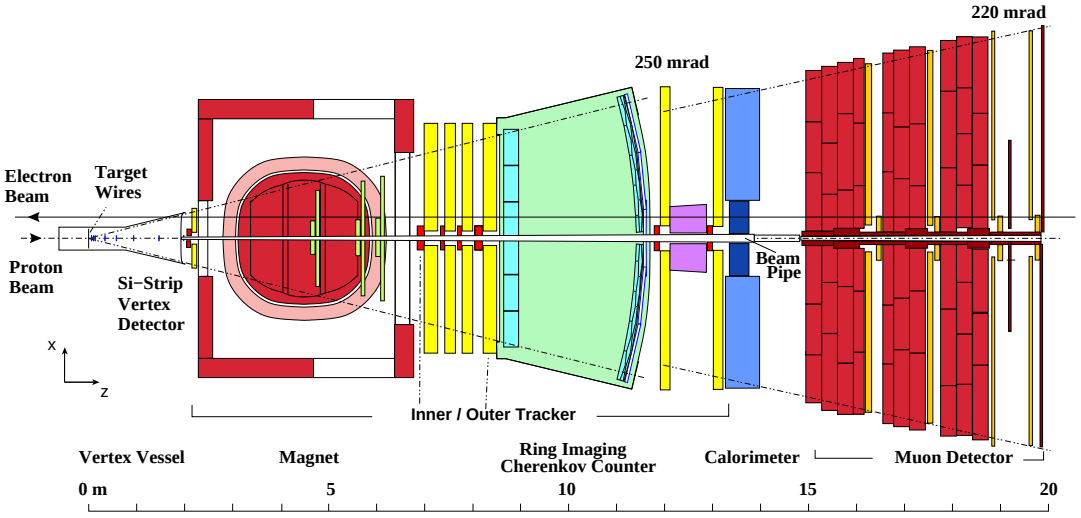

Figure 2.2. Plan view of the HERA-B detector.

The spectrometer is built around a dipole magnet. It consists of several tracking stations which are used to reconstruct particle trajectories and to evaluate their momenta. It is about 20 m long and covers the solid angle from 15 to 220 mrad in the bending plane (xz) and from 15 to 160 mrad in the yz plane. This angle in the laboratory frame approximately corresponds to 90% of the solid angle in the centre of mass system of the proton-nucleon interactions.

In front of the magnet, the silicon vertex detector (VDS) is used to reconstruct primary and secondary vertices with a high spatial resolution. Behind the magnet, the main tracking system consists of two subsystems with different granularity which are used to reconstruct particle tracks in the inner (ITR) and the outer (OTR) region of the detector with respect to the proton beam pipe. Particle identification is performed with three subsystems. A Čerenkov detector (RICH) is located between two sets of tracking stations and allows the identify protons and kaons over a large range of momenta. An electromagnetic calorimeter (ECAL) is located behind the tracking stations and is used to identify electrons and photons. Finally, at the very end of the detector, a sandwich of muon chambers (MUON) and iron absorbers are used for muon identification. The iron absorbers help to suppress background in the muon identification since they shield all particles but muons.

2.4 Target stations

The HERA-B detector is designed to reconstruct charged particle tracks produced in the interaction of a proton beam with fixed target wires. The targets are inserted in the proton beam halo of the HERA collider (see figure 2.3), in order to minimise the interference with the proton beam, which is used also in other experiments.

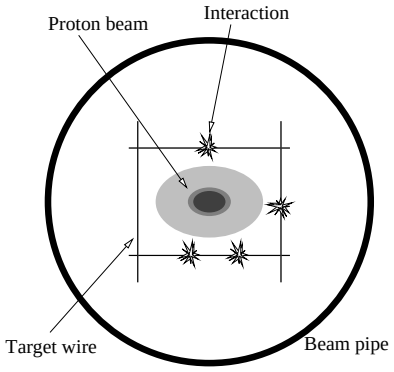

Figure 2.3. Schematic view of the target system. The diameter of the beam pipe cross section at the z position of the target system is about 10 cm.

The target consists of 8 wires made from different materials and shapes. They are mounted at relative angles of 90° on two stations which are located 4 cm apart along the direction of the proton beam. Their position is changed continuously during data taking in order to keep the interaction rate stable. The coasting beam, which is a continuous current of non bunched protons provided by accelerator [86], is a relevant source of background in the determination of the target luminosity. A list of target configurations available at HERA-B are reported in table 2.1.

Target	Name	Material	Atomic Weight	Shape	Cross section (μm)
Inner1	$i1$	Tungsten	184	Cylinder	50 (diameter)
Outer1	$o1$	Titanium	48	Cylinder	50 (diameter)
Below1	$b1$	Carbon	12	Ribbon	100×500
Above1	$a1$	Aluminum	27	Ribbon	50×500
Inner2	$i2$	Carbon	12	Ribbon	100×500
Outer2	$o2$	Tungsten	184	Ribbon	50×500
Below2	$b2$	Titanium	48	Cylinder	50 (diameter)
Above2	$a2$	Palladium	107	Cylinder	50 (diameter)

Table 2.1. Targets available at HERA-B in January 2003 [87]. Due to an accidental exposition to the proton beam, some wires were broken and replaced during detector operation.

The availability of different materials allows to study the nuclear dependence of the cross section with a reduced systematic uncertainty.

2.5 Vertex detector

The purpose of the **vertex detector system** (VDS) [88] is to reconstruct tracks in a high track density environment with sufficient accuracy to distinguish among tracks coming from the primary interaction and those coming from the decay of long living particles (with a decay length of a few mm). The VDS is located in a vacuum vessel equipped with Roman pots in order to minimise multiple scattering (figure 2.4).

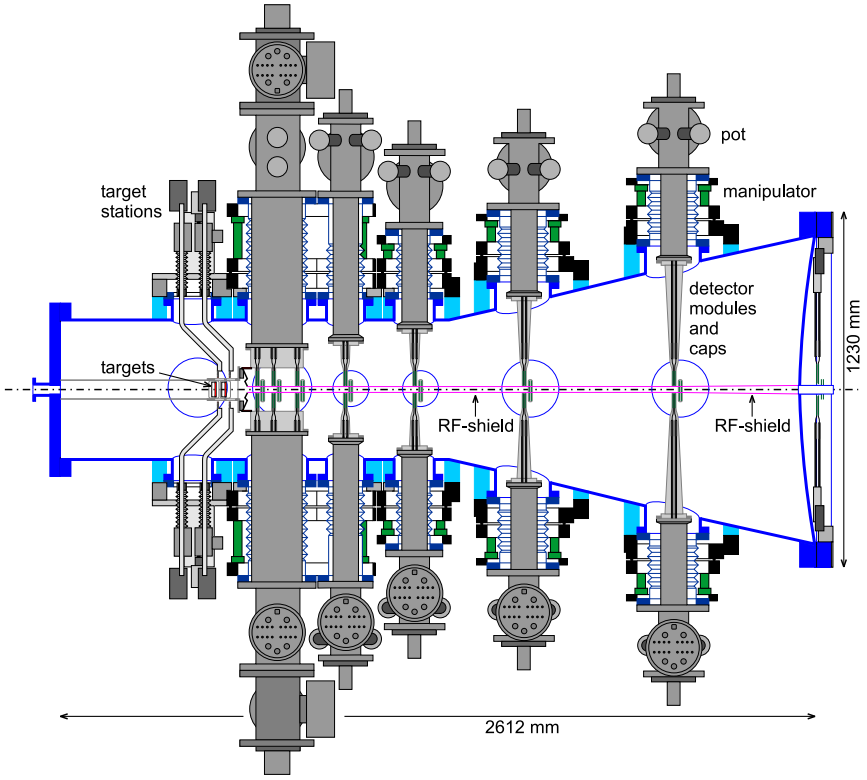

Figure 2.4. Schematic view of the VDS.

At the beginning of every proton fill, the VDS is moved towards the beam and, at the end of the operation, is retracted to avoid possible damage during the injection of the proton beam. The VDS consists of 8 modules of silicon microstrip detectors covering a magnetic field-free region of 2 m downstream of the target stations. Each module is segmented in 4 quadrants having 2 double-sided layers and a sensitive area of 50×70 mm^2. The modules are placed at increasing distance in the direction of the proton beam, in order to provide a uniform rapidity coverage. The read-out pitch of 50 μm guarantees an occupancy smaller than 5%. The spatial resolution for primary vertices in the plane perpendicular to the beam has been extracted from the Monte Carlo simulation of soft pA interactions and results in about 40 μm [89]. Along the beam, the decay length resolution has been extracted from a sample of $\mathrm{J}/\psi \to \mu^+\mu^-$ decays in data and results in 790 μm, which is significantly smaller than the average decay length (9 mm) of B mesons [89].

2.6 Tracking behind the magnet

The HERA-B spectrometer is equipped with a normal conductive dipole magnet providing an integrated vertical field of 2.2 T·m. The magnet is used to deflect charged particles and allows the measurement of particle momenta. The magnetic field outside the magnet is shielded by an iron yoke (figure 2.2). In order to preserve the polarisation of the electron beam, a combination of active and passive shield systems are placed around the electron beam pipe inside the magnet.

In front of the magnet, particles are tracked with the VDS. Behind the magnet, particles are tracked with the main tracker. The latter is divided into two subsystems of different granularity and radiation hardness: the inner and the outer tracker.

The **inner tracker** (ITR) covers the region around the beam pipe, between 5 and 25 cm, where the particle density is higher. It is built of Micro Strip Gaseous Chambers (MSGC) with Gas Electron Multiplier (GEM) foils (figure 2.5).

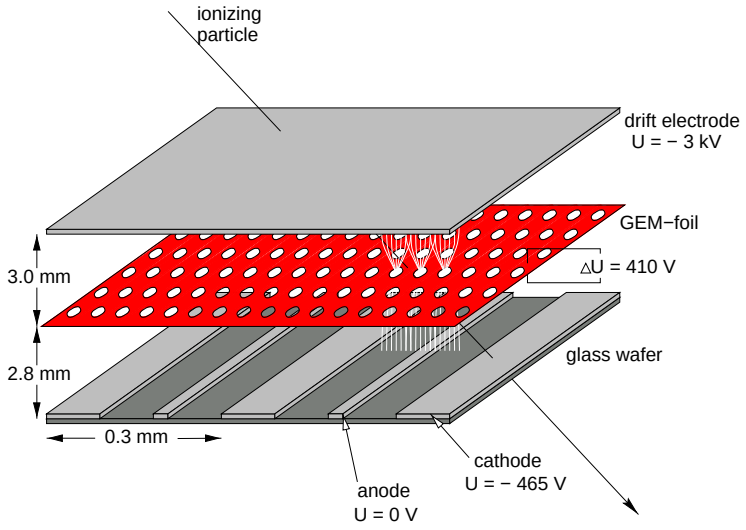

Figure 2.5. Schematic view of a MSGC-GEM chamber used in the ITR.

The electrode structure is built on a glass substrate. It consists of thin anodes ($\sim$ 10 μm), which are kept at ground potential, and broader cathodes, where a negative voltage ($\sim$ -500V) is applied. Opposite to the MSGC structure, a drift cathode is kept at a negative high voltage ($\sim$ -3kV), creating a strong electric field. Electrons deposited by the passage of ionising particles are forced to drift towards the MSGC plate. The electric field in the region close to the anode produces a gas amplification. The amplification gain needed to detect minimum ionising particles was too large and provoked serious damage at the anodes. Therefore, GEM foils were added to produce a pre-amplification step and reduce the gain at the anode. The chambers are arranged in layers at different angles with respect to the y axis $(0, \pm 5^\circ)$ in order to provide the space point information. A gas mixture of Argon and CO_2, in the volume ratio of Ar:CO_2=70:30, and a strip pitch of 300 μm allowed

to reach a spatial resolution of 110 μm and a hit efficiency of 90% [90]. Due to its unstable performance, the ITR was not used in the off-line track reconstruction.

The **outer tracker** (OTR) [91] covers the region between 25 cm and 3 m from the beam pipe. This area corresponds to an angular coverage that goes from the ITR border up to 160 mrad in the yz plane and 220 mrad in the bending plane (xz). An exhaustive study of the OTR can be found in the PhD thesis of W. Hulsbergen [92]. The outer tracker is made of honeycomb drift chambers mounted perpendicular to the beam and arranged in single and double layer systems (figure 2.6).

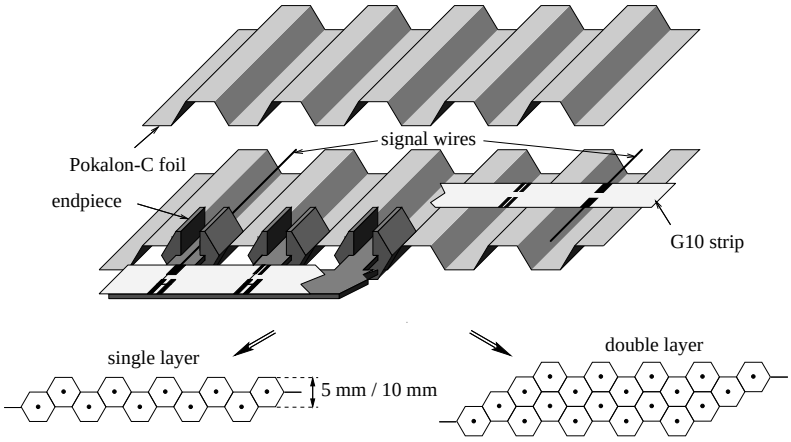

Figure 2.6. Schematic view of a honeycomb chamber used in the OTR.

The anode is a 25 μm gold-plated tungsten wire. The cathode is a 75 μm polycarbonate foil coated on the inside by a thin gold and copper layer. The modules are up to 4.5 m long and about 30 cm large. In order to have an efficient track reconstruction, keeping the load of the trigger network at a sufficient low level, the OTR segmentation is such that the hit occupancy does not exceed 20%. Therefore, the size of the drift cells is 5 mm, for radial distances smaller than 50 cm from the beam pipe, and 10 mm, in the outer region, where the hit occupancy is lower. Smaller cells would be too expensive. Larger cells cannot be used because otherwise the drift time would be too large. In order to avoid the overlap between adjacent events, the maximum drift times cannot exceed the time between two proton bunches (96 ns). The gas mixture contains CF_4. This gas has two advantages. It is fast and has a large ionisation density. However, the usage of CF_4 leads to the production of chemically aggressive radicals, which can damage the anode wires. It was found that aging effects were minimised by using a gas mixture of Argon, CF_4 and CO_2 in the volume ratio of Ar:CF_4:CO_2=65:30:5 [93]. The honeycomb modules are assembled in 6 super layers (figure 2.2). Each super layer is made of three stereo layers at different angles with respect to the vertical axis ($0, \pm 5^\circ$), in order to provide the space point information. The proton and electron beam pipes traverse the detector at a distance of 50 cm from each other (figure 2.7).

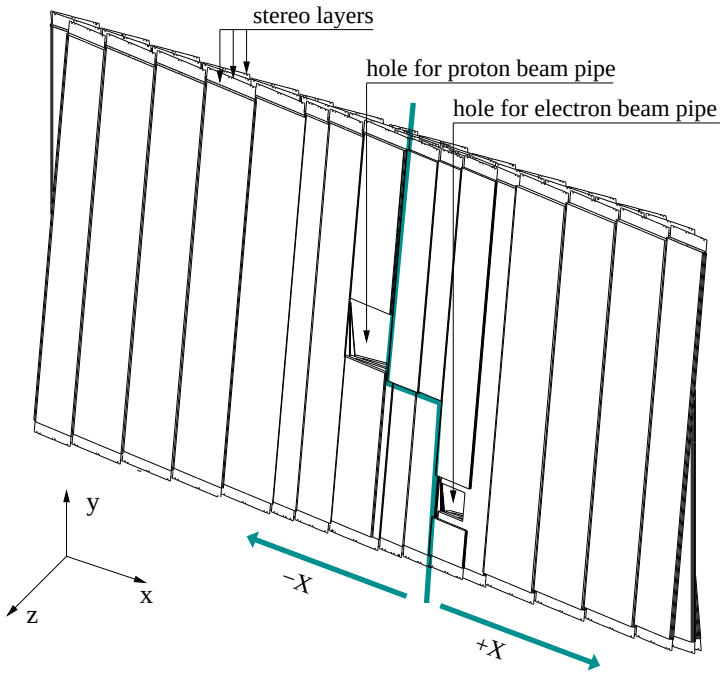

Figure 2.7. Honeycomb modules in an OTR super layer. In order to allow lateral movements, without interfering with the beam pipes, the super layer is divided in the $\pm$X stations.

Four Pattern Chambers (PC), between the magnet and the RICH, are used for track pattern recognition. Two Trigger Chambers (TC), between the RICH and the ECAL, are used by the first level trigger for track search behind the magnet, in combination with the first and the last PC stations. In order to increase the trigger efficiency, each stereo layer of the TC chambers is doubled (table 2.2) and the trigger requires only one out of the two possible hits along the beam axis.

OTR station	z_{min} [cm]	z_{max} [cm]	Stereo layers
PC1	702.1	730.7	$\circ - \circ \oplus \odot \ominus$
PC2	742.3	766.4	$\circ + \circ - \circ +$
PC3	777.9	802.0	$\circ + \circ - \circ +$
PC4	822.6	851.2	$\circ - \circ \oplus \odot \ominus$
TC1	1192.2	1211.7	$\oplus \odot \ominus$
TC2	1305.8	1325.3	$\oplus \odot \ominus$

Table 2.2. List of OTR stations. The positions along the beam axis (z) and the stereo layers are indicated: $+$, $\circ$, $-$ are single layers, while $\oplus$, $\odot$, $\ominus$ are double layers at $+5°$, $0°$, $-5°$.

During data taking, the efficiency of the inner cells was 94% (97% for the outer cells). The hit resolution for particle momenta larger than 20 GeV/c was 320 μm.

2.7 Particle identification

The **ring imaging Čerenkov detector** (RICH) [94] is used to separate kaons and protons from the large pion background over a wide momentum range by using the Čerenkov effect. When charged particles travel through a medium of refractive index n with velocity v larger than the speed of light in the medium (c/n), an emission of photons occur. The emission angle θ with respect to the particle direction of motion is given by

$$\cos\theta = \frac{c}{v \cdot n}. \tag{2.1}$$

The light emitted by charged particles is projected by spherical and planar mirrors into a ring image on the photon detector plane, as schematically depicted in figure 2.8(a). The gas used as radiator at HERA-B is C_4F_{10}.

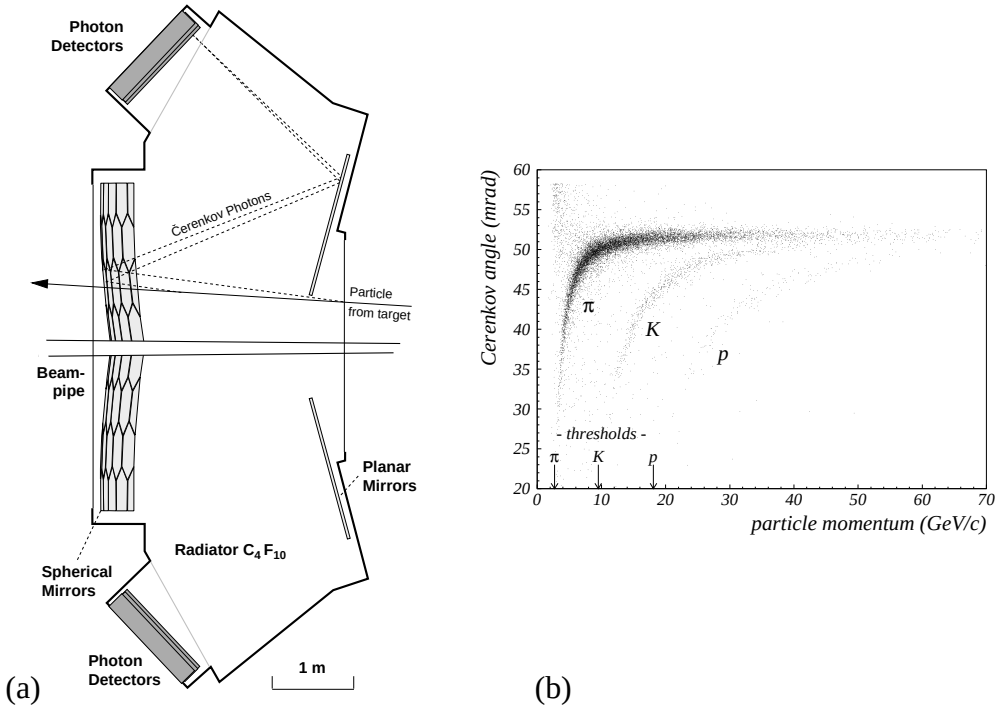

Figure 2.8. Schematic view of the RICH (a), and dependence of the Čerenkov angle on the particle momentum [94] (b). Bands corresponding to proton, kaons and pions are visible.

Since the refractive index n of the radiator is known, the velocity of the particle can be extracted by measuring the angle θ of the observed rings. With the momentum information provided by the tracking system, it is possible to determine the mass of the particle. The Čerenkov angle as a function of the particle momentum is shown in figure 2.8(b). The threshold momentum at which the emission of photons starts to occur is also indicated ($2.7\ \mathrm{GeV}/c$ for pions, $9.6\ \mathrm{GeV}/c$ for kaons, $18\ \mathrm{GeV}/c$ for protons).

The RICH performance was evaluated by studying the identification and mis-identification probability as a function of the particle momentum (figure 2.9).

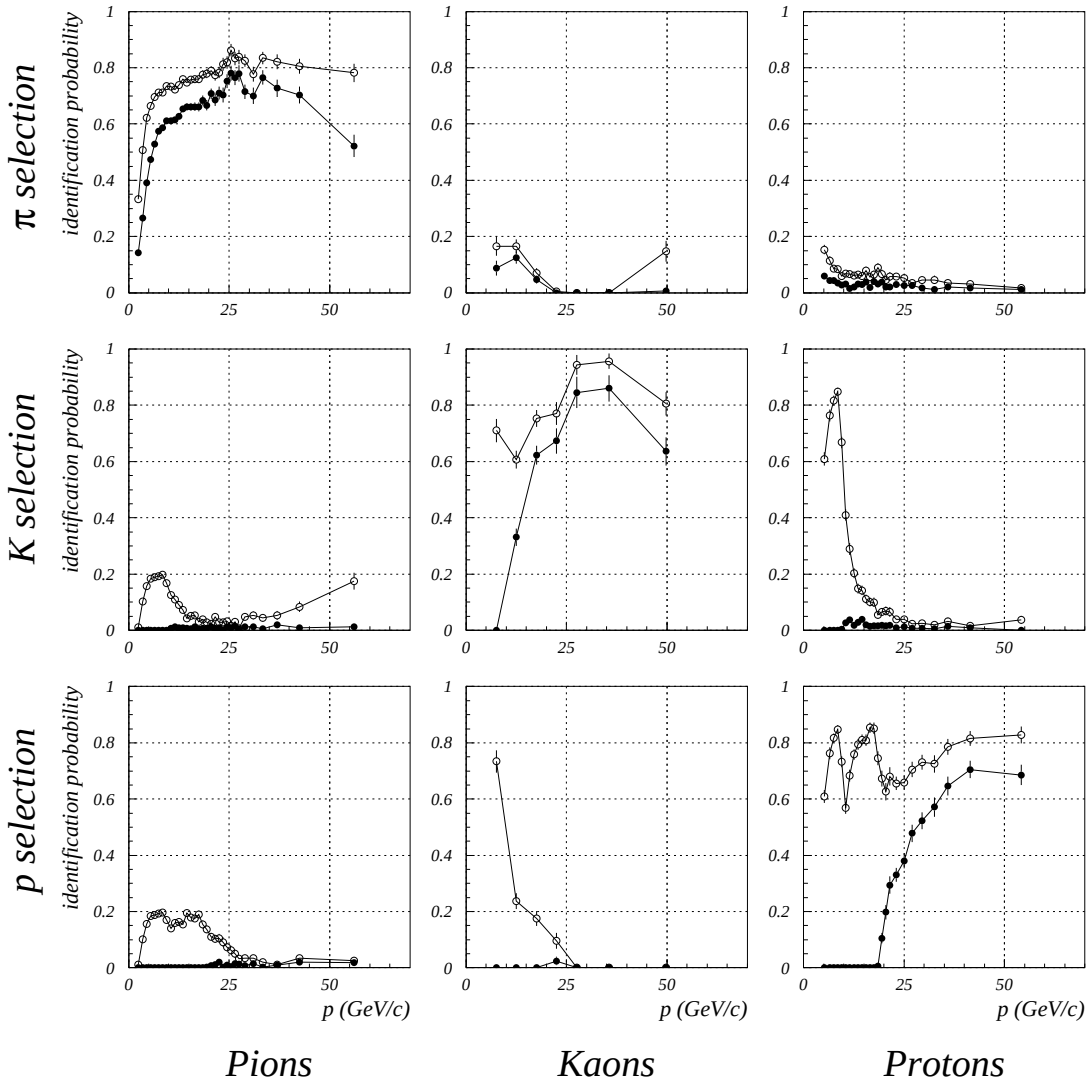

Figure 2.9. Momentum dependence of the RICH efficiency for medium (open circles) and hard (full circles) p, K and π selection. The efficiency is extracted from real data with pions and protons from Λ decays and kaons from ϕ decays. Diagonal plots shows the identification probability. The other plots show the mis-identification probability.

At medium selection criteria, kaon identification for momenta between 10 and 60 GeV/c is between 60% and 95%, with about 5% pion mis-identification. The proton identification for momenta between 20 and 60 GeV/c is between 60% and 80%, with about 5% pion mis-identification. Below 5 GeV/c, the performance is spoiled by multiple scattering, which affects the direction of motion of the particles, and by the small number of emitted photons for pion tracks.

The **electromagnetic calorimeter** (ECAL) [95] is used for electron and photon identification. It also provides information for electrons at the first level trigger. Whereas electrons deposit their full energy in the ECAL, hadrons deposit only part of it, since the produced neutrons escape the detection. Within the detector resolution, the electron energy E measured with the ECAL is equal to the momentum p provided by the main tracker. Therefore, an E/p ratio close to unity can be used to separate electrons from hadrons. Photons are identified by their energy deposited in the ECAL which is not associated with tracks in the main tracker. The ECAL consists of about 6000 shashlik sampling cells in which Pb and W absorbers are sandwiched between scintillator layers, as shown in figure 2.10(a).

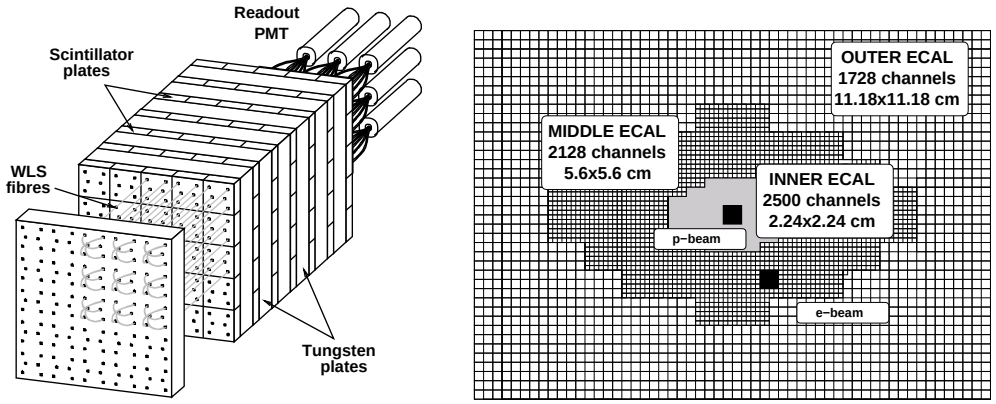

Figure 2.10. The ECAL cell (a) and the segmentation of the ECAL detector (b).

Electromagnetic showers are generated at the passage of electrons and photons through the absorbers. The showers consist of bremsstrahlung photons and electron-positron pairs which produce light in the scintillator layers. The light is collected by plastic wavelength-shifting (WLS) fibers inserted in the calorimeter parallel to the beam (shashlik architecture) and is read-out by photomultiplier tubes (PMTs) at the end of the calorimeter. Since a shower typically deposits energy in several neighbouring cells, in order to make particle identification, neighbouring cells are combined into clusters. The ECAL is divided in three sections with different granularity, as shown in figure 2.10(b), in order to adjust for the decreasing particle densities as the distance from the the proton beam pipe increases. The cell dimensions are 2.2×2.2 cm^2 in the inner part, 5.6×5.6 cm^2 in the middle part and 11.2×11.2 cm^2 in the outer part. The energy resolution, obtained from the width of the E/p distribution for electrons in the middle ECAL, is

$$\frac{\sigma_E}{E} = \frac{10.3\%}{\sqrt{E[\mathrm{GeV}]}} \oplus 6.1\%.$$

The **muon detector** (MUON) [96] is a tracking system used for muon identification (figure 2.11). It consists of four super layers (MU1-MU4) located behind the ECAL and separated from each other by 1 m thick walls of concrete and iron (except between MU3 and MU4, where there is no such absorber). Most hadrons stop in the absorbers, whereas muons with momenta larger than $5\ \mathrm{GeV}/c$ can penetrate.

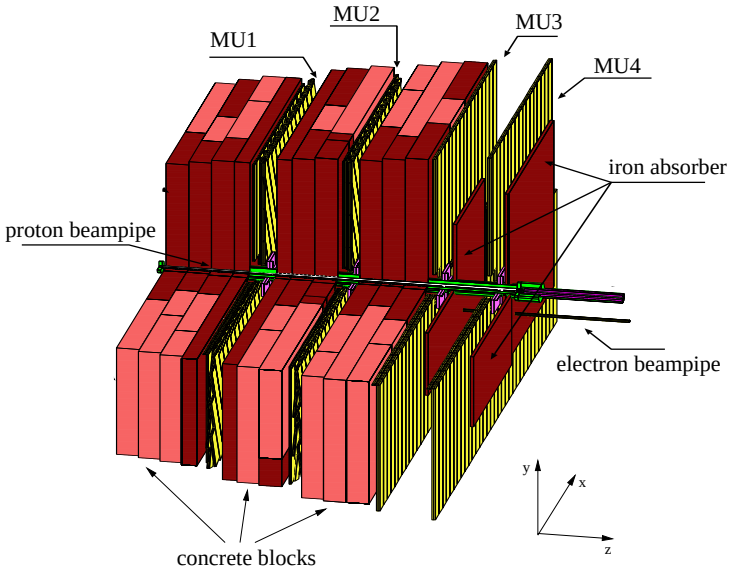

Figure 2.11. Schematic view of the MUON detector.

The sensitive area is divided into two parts. The inner region is covered by gaseous pixel chambers of 9×9 mm^2 in which the anode is a 30 mm long wire oriented along the beam. In order to reduce the number of read-out channels, matrices of 2×2 pixels, in MU1 and MU2, and columns of 4 pixels, in MU3 and MU4, are combined together when they are read-out. A gas mixture of Argon, CF_4 and CO_2 in the volume ratio of Ar:CF_4:CO_2=65:30:5 is sufficiently fast and resistant to aging effects [97]. The outer region is covered by super layers of multi-wire proportional tube chambers with a cross section of 14×12 mm^2. MU1 and MU2 provide the space point information by means of three double layers at different angles with respect to the y axis $(0, \pm 20^\circ)$. MU3 and MU4 have a single 0° layer and are segmented with cathode read-out pads of 12×10 cm^2, which are used to provide information for the first level trigger. The accuracy in the position determination is increased by removing the absorbers between MU3 and MU4. The detection efficiency is increased by a logic OR of adjacent pads in the read-out.

Muonic decays of kaons and pions within the detector volume spoil the identification of muons produced in the primary interaction. The mis-identification probability depends on the particle momentum and on the muon likelihood probability. In average, it is less than 4% for pions and less than 2% for kaons [98]. The average hit efficiency is 92% for pad and 99% for tube chambers [37].

2.8 Trigger and data acquisition systems

The trigger and Data AcQuisition (DAQ) systems [99] of HERA-B are built to process the information of about 0.5 M detector channels for every proton bunch crossing (96 ns). The trigger is designed to reduce an average primary interaction rate of 5 MHz to an output rate of 100 Hz, which can be written to tape. The required event rate reduction must be achieved keeping the highest efficiency for events in which J/ψ mesons are produced. The signature of such events is the presence of a pair of high p_T lepton tracks, which are used to trigger $\mathrm{J}/\psi \to l^+l^-$ decays. A block diagram of the data acquisition and trigger systems is shown in figure 2.12.

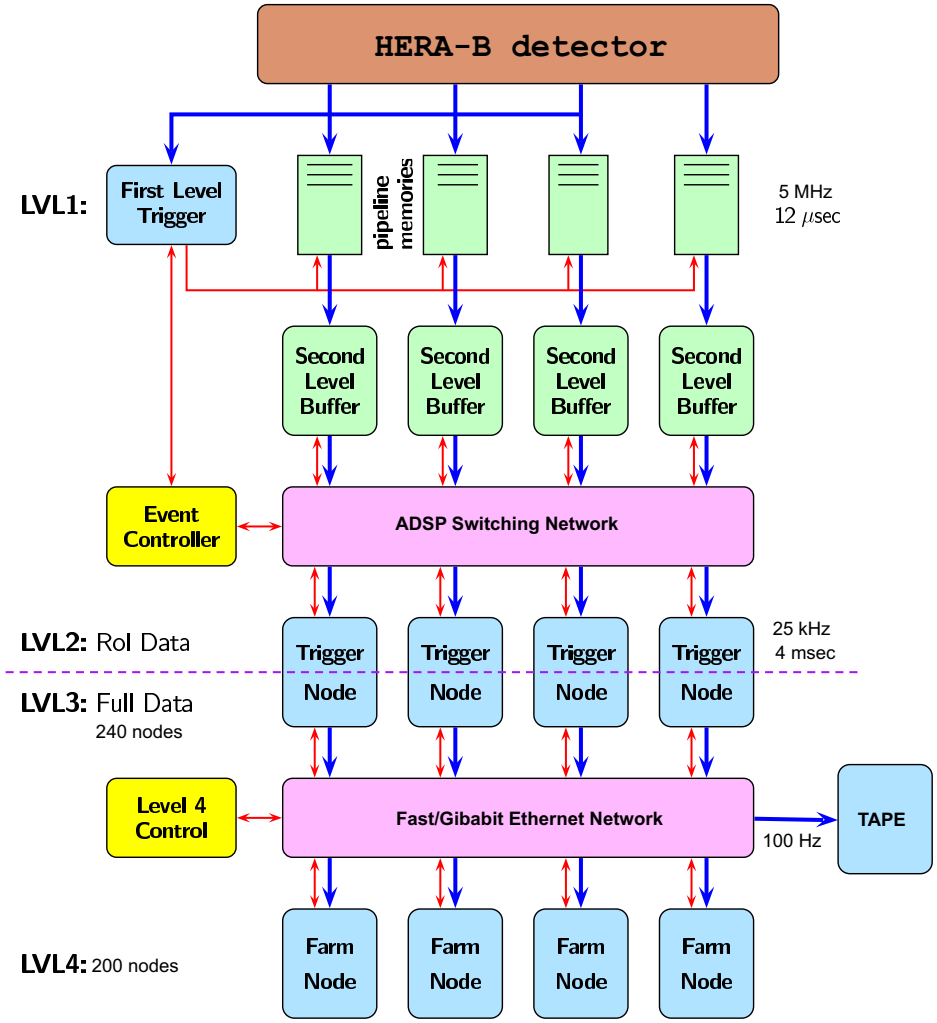

Figure 2.12. Block diagram of the data acquisition and trigger systems. The different trigger levels and relative latency and event rate reductions are indicated.

The trigger consists of four decision levels preceded by a pretrigger system. The pretrigger provides the starting point for the track search performed at higher trigger levels. Pretrigger signals are generated either by the occurrence of hit coincidences in the MUON pad chambers (for muons) or high energetic clusters in the ECAL (for electrons). No rate reduction is needed at pretrigger level.

The **First Level Trigger** (FLT) is a hardware trigger made of about 60 dedicated electronic units, interconnected and linked to the detector by a system of optical links. A system of buffers allows to store a maximum of 128 events while the FLT processes the events. This corresponds to a latency of 12 μs (96 ns$\times$128), which is the maximum decision time of the FLT. The FLT propagates the pretrigger seeds through the spectrometer by requiring a coincidence of hits in 12 layers for electrons and 17 layers for muons. When tracks are found, their momentum is estimated from the deflection in the magnet field, assuming that the track originates from the target. A p_T cut might be applied. Accepted events are stored in the Second Level Buffers (SLBs) and become available for the next trigger level.

The **Second Level Trigger** (SLT) is a software trigger running on a farm of 240 nodes (Linux PCs). The SLT refines the FLT decision by using hits from all tracking chambers and vertex detector layers. It searches for tracks in the detector regions defined either by the FLT or by the pretrigger. A vertex fit is performed to check that the trigger tracks have a common origin. This requirement helps to identify events in which two leptons originate from $\mathrm{J}/\psi \to l^+l^-$ decays. Since the requirement on the χ^2 probability of the vertex fit is soft ($\chi^2 < 20$), the trigger allows to select also events in which two B hadrons undergo simultaneously semileptonic decays. Each SLT node can access to each buffer, using a switching network placed between the SLB and the SLT processors. The switch and the buffers are built on Digital Signal Processors (DSPs). The communication between them is handled by an event controller process. During data taking, the maximum input rate of the SLT was 25 kHz and was limited by the performance of the switching network.

Once an SLT node accepts the event, it collects all detector informations from the SLB and 'builds' the event. The same node calls the **Third Level Trigger** (TLT). The TLT can select events on the basis of global properties, such as the occurrence of additional high p_T tracks or vertex detachment. During data taking, the TLT was not used.

Events accepted by the SLT and TLT algorithms are sent to the **Fourth Level Trigger** (4LT) via an Ethernet switch. The 4LT is a PC farm of about 200 CPUs, where events are fully reconstructed, classified and logged. In order to optimise the DAQ performance during data taking, the fraction of events reconstructed on-line was limited to 25%. The rest of the events were reconstructed off-line, when the detector was not active. The 4LT is also used as data quality monitor during the detector operation. Since the DAQ and the trigger performance strongly rely on the general run conditions (such as calibration and alignment of different subsystems, status of detector channels *etc.*), an on-line monitor was developed to stabilize the detector performance with a continuous update of the run conditions [100].

During data taking, two trigger configurations were usually employed.

The **minimum bias trigger** was achieved by requiring a minimal activity in the detector. Events corresponding to filled bunches, according to the HERA scheme, were triggered when at least 30 hits in the RICH and a total energy of 1 GeV in the ECAL were recorded. The FLT was not active in this configuration. The logging rate was 1 kHz.

The **dilepton trigger** was based on the combined action of FLT and SLT. The FLT issued a trigger when at least one track was reconstructed and two pretriggers of the same type (muon or electron) were found. The pretriggers were then used by the SLT to perform an independent track search. When two lepton tracks originating from a common vertex were found, the final positive (and negative if not found) trigger decision was issued. The logging rate in this configuration was 100 Hz.

2.9 Event reconstruction

The on- and off-line reconstruction at HERA-B is performed in ARTE [101]. The latter provides software tools for hit preparation, track and vertex reconstruction and particle identification. The "hit preparation" part translates the raw information on tape into the space points (hits) where particles crossed a specific subdetector.

Track reconstruction

In the VDS, hits are combined in track segments. These are used by CATS (Cellular Automaton for Tracking in Silicon) [102] to build the track candidates. The latter are fitted with a Kalman filter technique, which provides a fast, efficient, robust and accurate algorithm for the determination of the track parameters. In the main tracker, a similar approach [103] is used for pattern recognition in the PC chambers, while RANGER [104, 105] propagates tracks through the magnet and the TC chambers. However, the lower hit efficiency and the lower resolution compared to the vertex detector requires special tools to minimise the rate of ghost tracks and to maximise the track efficiency. The VDS segments are matched with track segments in the subdetectors behind the magnet by using MARPLE [106, 92], and from the deflection in the magnetic field the particle momentum is estimated.

Particle identification

The CARE algorithm [107] is used to search for clusters of cells with energy deposited in the ECAL. The energy, the position and the shape of electromagnetic showers in the clusters are determined by looking at groups of 3×3 cells. Particle identification in the RICH is performed with RITER [108, 109]. This is a track seeded algorithm, which assigns likelihoods to the electron, muon, pion, kaon and proton hypothesis of each reconstructed track. The likelihood of a mass hypothesis is determined by calculating the Čerenkov angles of all combinations of tracks in

the main tracker and rings in the RICH [110]. The muon identification is performed with MUREC-B [111], which implements a track following technique. Tracks in the main tracker are extrapolated to the MUON detector in order to search for confirmation hits. Many muon candidates can be assigned to the same track seed, each one having a likelihood determined by the distance between the extrapolated track and the MUON hits. The likelihood of the best candidate is assigned to the original track.

Vertex reconstruction

Once all tracks are reconstructed, primary and secondary vertices are found by GROVER [112]. The algorithm to search for primary vertices is based on a Kalman filter technique. In the first step, a search for clusters of tracks 3σ away from the target is performed, where σ is the uncertainty of the track position. These tracks are used to determine a first estimate of the vertex position. In the filtering procedure, the χ^2 contribution of each track to the total χ^2 of the vertex is calculated. Tracks with a χ^2 contribution larger than 20 are rejected and all vertex parameters are updated. The procedure is iterated until the desired accuracy is reached.

2.10 Physics topics

The physics program of the HERA-B collaboration after the HERA upgrade in 2001 is reported in reference [81, 82]. Since HERA-B could obtain only 10% of the requested and promised beam time, some of the topics described in the program could not be studied.

Heavy quark production

The main physics topic of HERA-B is the study of charmonium production (J/ψ, ψ' and χ_c) and the related influence of the nuclear medium. Since charmonium production is not completely understood, measurements of particle production ratios and differential cross sections in x_F, p_T and decay angles, can help to distinguish among the proposed models (CSM [28], CEM [25], NRQCD [34]). The acceptance of HERA-B extends to large negative values in x_F, down to -0.35, where no measurements are available. The possibility of multi-target operation allows to measure nuclear effects with reduced systematic uncertainty [37]. Furthermore, the study of charmonium production in pA interactions serves as a basis for the interpretation of heavy ion collisions in which the formation of a Quark Gluon Plasma (QGP) [113] is expected.

The measurement of the $b\bar{b}$ cross section provides a test of the predictive power of perturbative QCD. This measurement was performed by using inclusive J/ψ decays of $b\bar{b}$ pairs in the PhD thesis of H. Wahlberg [114]. The work presented in

this thesis provides an independent measurement of the $\sigma_{b\bar{b}}$ performed with double semi-muonic b decays.

The production of open charm mesons has also interesting features. For instance, a simple model predicts that the cross section ratio of charged and neutral D mesons is $\frac{1}{3}$ [115]. However, several experiments measured larger values. Since the experimental uncertainties are large, the question is still open.

A recent overview of the preliminary HERA-B results in heavy quark production can be found in reference [116].

Strangeness production

The production of strange particles is abundant in pA interactions and can be used as a calibration for the measurement of the strangeness enhancement in heavy ion collisions, which has been proposed as a possible signature of QGP formation. A recent measurement of the K^0_s, Λ and $\bar{\Lambda}$ production cross sections can be found in reference [117]. Differential distributions of K^* [118] and ϕ production have been measured, too. A measurement of the Λ polarisation has been performed [119], in a kinematic region where existing experimental results suffer from large statistical uncertainties. Contrary to the expectations, the Λ produced in unpolarised hadronic collisions are transversely polarised and the amplitude of the polarisation depends on the kinematic variables [120]. In particular, the polarisation increases with p_T and decreases as $|x_{\mathrm{F}}|$ approaches to zero.

Direct photon production

In perturbative QCD, direct photon production is dominated by the leading order hard quark-gluon scattering $qg \rightarrow q\gamma$. Therefore, the measurement of the high-p_T photon spectrum offers the possibility to probe the gluon structure of the nucleons. Previous experiments show significant deviations from results of next to leading order QCD calculations [121].

Exotic and rare processes

The occurrence of flavour-changing neutral current decays is forbidden at the lowest order and strongly suppressed at second order in the standard model. The sample of HERA-B dilepton triggered data has been used to extract the most stringent upper limit on the branching ratio for $D^0 \rightarrow \mu^+\mu^-$ decays [122].

In the last few years, following the theoretical work of Diakonov *et al.*[47], several experiments claimed evidence of an exotic strange baryon with five valence quarks ($uudd\bar{s}$) and a mass of $1540\ \mathrm{MeV}/c^2$, mostly in interactions of photons with nuclear targets. The search for pentaquarks in the sample of minimum bias data collected with HERA-B is one of the topics of this thesis and led to the publication of upper limits on pentaquark production in pA collisions [123].

Chapter 3

Efficiency of the First Level Trigger

La grande bouffe (1973) - M. Ferreri

We report on a study of the First Level Trigger (FLT) efficiency at HERA-B. We illustrate the procedure to extract the efficiency from data and study the dependence on several kinematic variables. The average track efficiency for leptons produced in J/ψ decays over the entire period of data taking is $\varepsilon_e = 58.74 \pm 0.12_{stat} \pm 1.0_{sys}$ % for electrons and $\varepsilon_\mu = 28.25 \pm 0.12_{stat} \pm 0.7_{sys}$ % for muons.

3.1 Introduction

The production of J/ψ mesons in pA interactions at $\sqrt{s} = 41.6$ GeV occurs in a small fraction of the events ($\sigma_{\mathrm{J}/\psi}/\sigma_{inel} \approx 10^{-5}$). The enrichment of the data sample is accomplished with a complex trigger chain which allows to identify J/ψ decays into two leptons. The clear signature of these events originates from the high mass of the charmonium that is transfered into kinetic energy of the light decay products and allows to distinguish them from the undesired low energetic background.

The core of the trigger chain is the FLT, a hardware trigger system which is used to perform on-line track reconstruction with a Kalman filter technique [124]. It is built with about 60 message-driven pipelined processors operating at a clock frequency of 50 MHz and aims to reduce the primary interaction rate of 5 MHz to 20 kHz, which is the maximum input rate of the second level trigger. Since the proton bunch crossing (BX) occurs every 96 ns and data are stored in a 128 BX deep pipeline on the front-end electronics, the dead time of the FLT is zero as long as the decision time does not exceed 96 ns $\times$ 128 = 12.3 μs. Due to the large amount of outer tracker hits (about 1 Tbit/s) and the short decision time, the FLT network is built to process 80 bit "messages" encoding the parameters necessary for track reconstruction.

3.2 Concept of the first level trigger

The FLT performs on-line track reconstruction with a Kalman filter technique. It uses pretrigger signals as seeds for its track search. A pretrigger signal is generated either by hit coincidences in the MU3 and MU4 chambers or by energetic clusters in the ECAL. The FLT uses the Regions Of Interests (ROIs) defined by the pretrigger to search for hits in the adjacent upstream tracking chambers (see figure 3.1).

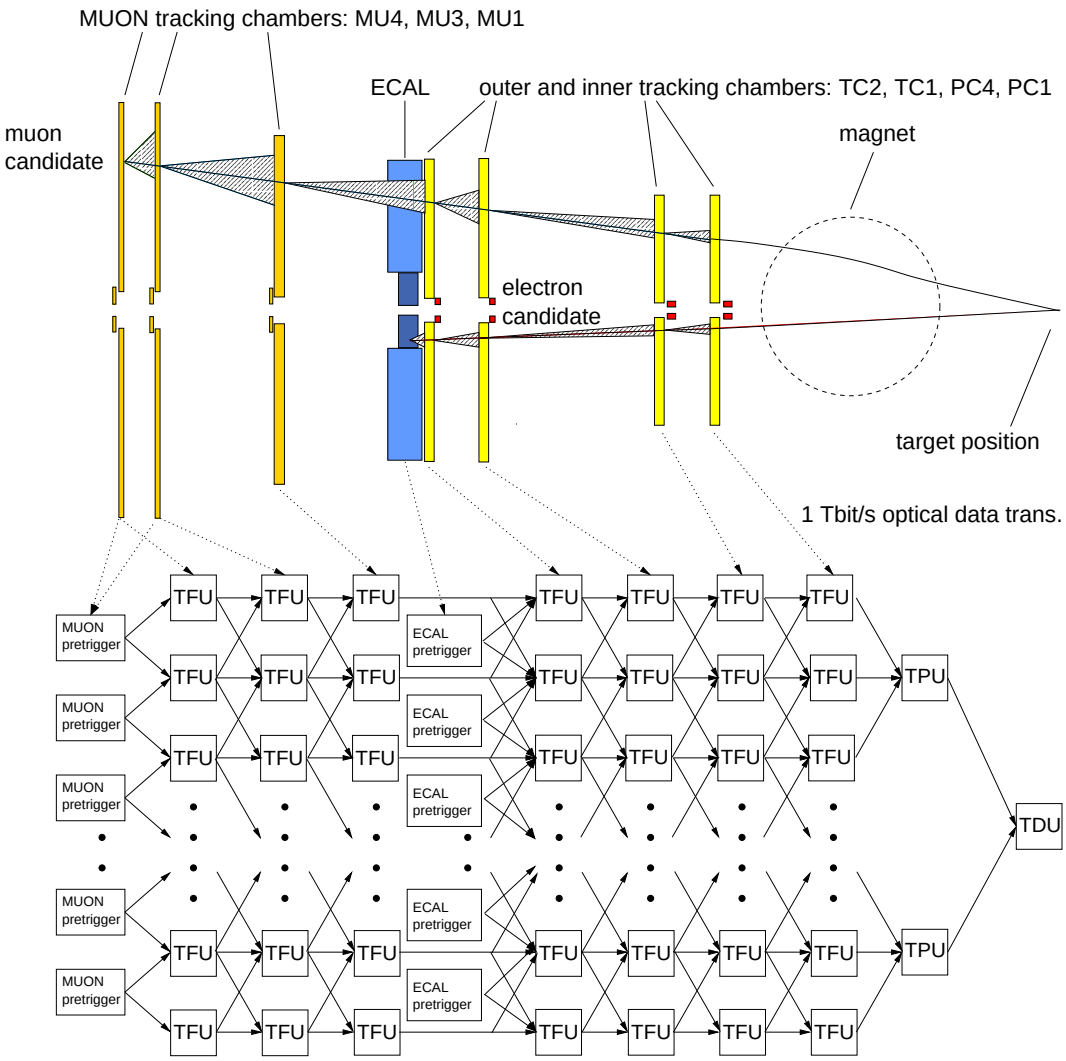

Figure 3.1. Illustration of the FLT hardware network. The picture indicates the correspondence between FLT processors and detector subsystems used by the trigger. The FLT is made of 55 TFUs (Track Finding Units). Each TFU scans for space points in a specific part of the tracking system. The tracks found by the TFUs are passed to the TPUs (Track Parameter Units), which are used to calculate the track momentum, and a TDU (Trigger Decision Unit), which take the final trigger decision.

The momentum of the track is estimated from the deflection in the magnetic field, under the assumption that the particle originates from the target position. The trigger decision is based on the number of found electrons or muons.

When a pretrigger signal is generated, track parameters are estimated and sent to the TFUs (Track Finding Units) covering the ROI where the particle is supposed to come from. If the TFU find a coincidence of hits in the ROI, then the ROI and the track parameters are updated and sent to the TFUs of the next super layer. The track search is performed in the direction opposite to the proton beam, until the last trigger chamber (PC1) is reached. The track parameters are then sent to the TPUs (Track Parameter Units), where the calculation of the track momentum allows a selection on p, p_T or E/p. All selected tracks are sent to the TDU (Trigger Decision Unit), where the invariant mass of the track pairs is determined and the final decision of the FLT is taken.

The hardware of the first level trigger consists of 59 electronic units of three types: 55 TFUs, which are used to find the particle trajectories within the detector, 3 TPUs, which calculate the track momentum, and 1 TDU, which issues the trigger decision. The hits from one trigger chamber are processed by several TFUs (see the FLT network in figure 3.1), each of them covering a rectangular region of the chamber. The segmentation of a trigger chamber in terms of TFUs is reported in figure 3.2.

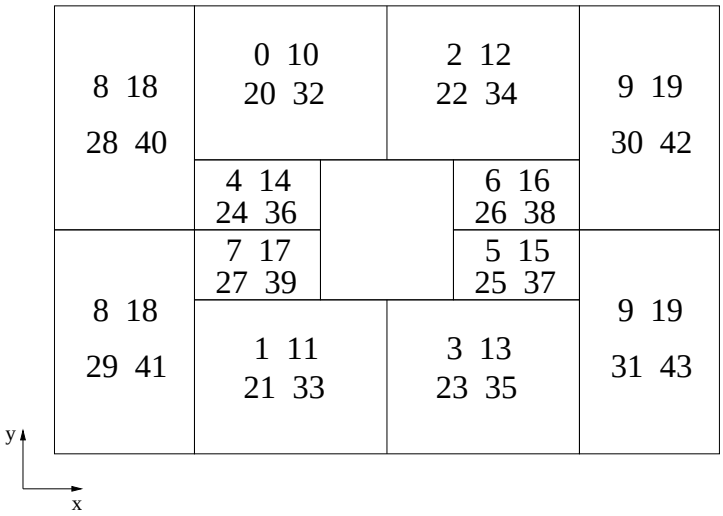

Figure 3.2. Typical segmentation of a trigger chamber in terms of TFUs. A number is assigned to each TFU depending on the sector and the chamber it belongs to: 0-9 (PC1), 10-19 (PC4), 20-31 (TC1) and 32-43 (TC2). The segmentation of the muons chambers (not reported in the picture) is: 65-66 (MU4), 67-68 (MU3) and 69-75 (MU1).

A detailed description of the first level trigger and its performance during the commissioning period can be found in the PhD thesis of M. Bruinsma [38].

3.2.1 Track seeding

The search for tracks at the first level trigger begins with the occurrence of either an electron or a muon pretrigger signal. An electron pretrigger signal is generated when an energetic cluster in the electromagnetic calorimeter (ECAL) is found. The cluster has a cross shape and contains 5 cells, as shown in figure 3.3(a).

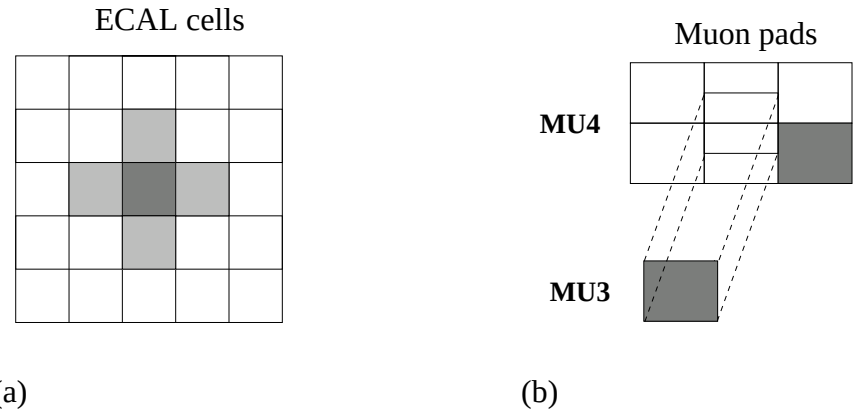

Figure 3.3. Scheme of the pretrigger configurations for electrons (a) and muons (b). The ECAL cluster is depicted in figure (a). The gray area indicates the five cells of the signal, the central one having the largest energy. A possible hit coincidence between MU3 and MU4 pads is reported in figure (b). The gray areas indicate the pads with signals and the dashed line is the projection of the MU3 pad on MU4.

Given a certain threshold energy (E_{th}), the electron pretrigger algorithm generates a signal when the central cell energy is larger than $E_{th}/2$ and the total energy of the five cells is larger than E_{th}. The energy threshold set in the experiment is the transverse energy (E_T), which is related to E_{th} by the formula

$$E_{th} = E_T \cdot \sqrt{\frac{x^2 + y^2 + z^2}{x^2 + y^2}}, \tag{3.1}$$

where x, y and z are the coordinates of the centre of gravity of the cluster [38]. The bending due to the magnetic field is neglected. During data taking, the value of E_T was set at 1 GeV.

A muon pretrigger signal is generated when a hit coincidence in the last two muon pad chambers (MU3 and MU4) occurs. The muon pretrigger algorithm searches for combinations of hits among each MU3 pad and six MU4 pads, according to the scheme in figure 3.3(b). This is done to account for multiple scattering in the thick iron walls placed between the muon chambers upstream of MU3.

3.2.2 Track reconstruction

The track reconstruction is performed by the TFUs. A block diagram of the main functions of a TFU is shown in figure 3.4.

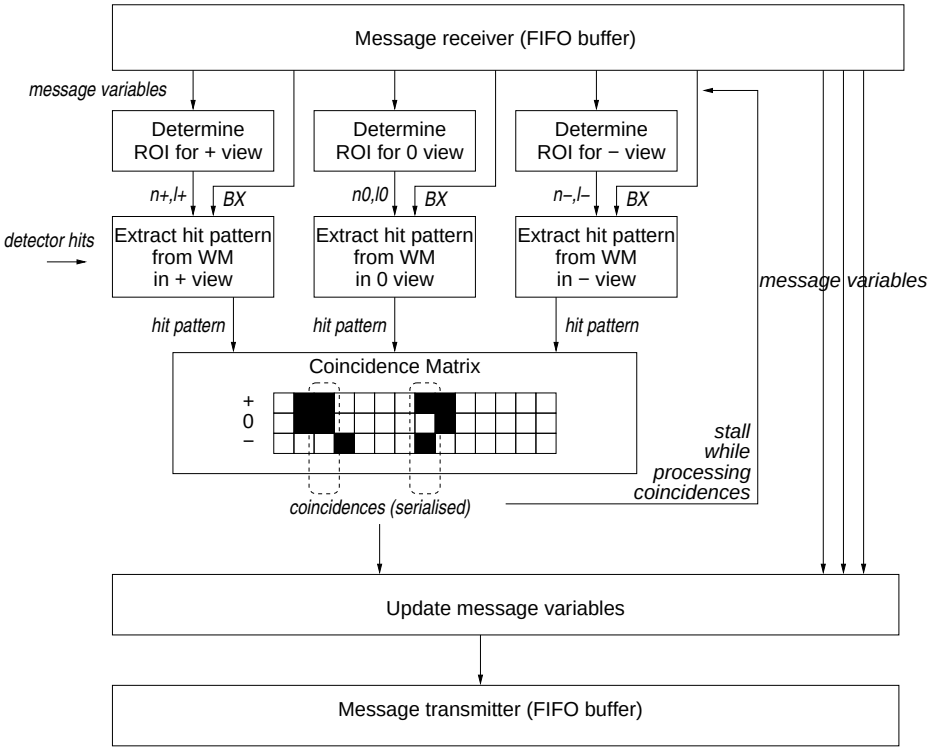

Figure 3.4. Block diagram of a TFU. The TFU receives hits from the trigger chambers and track parameters from the pretrigger or the previous super layer. When a triple hit coincidence is found, the track parameters are updated and sent to the next super layer.

The TFU receives an 80 bit message, either from the pretrigger or from the previous super layer. The message contains the current estimate of the track parameters and the information needed to determine the size and the position of the ROI in this super layer. The TFU receives also hit patterns from the trigger chambers. It stores them in three wire memories (WMs), one for each stereo layer forming an angle of $0°$ and $\pm 5°$ with the vertical axis. The WM is a dual ported memory. On one port, hits are constantly written at an address provided by the incoming hit pattern. The read address is given by the BX of the message. A region up to 32 wires wide, for each of the three projections, is determined with the track parameters of the incoming message. A Coincidence Matrix searches for coincidences of hits in the three projections. When a coincidence of hits is found, the track parameters and the ROI are updated with the position of the new hits. A new message is sent to the TFU of the next super layer, where other hits are expected to be found. The definition of hit coincidence can include one, two or three neighbourhood hits (figure 3.4), in

order to account for the uncertainty in the vertical slope of the track. Multiple coincidences of hits are processed serially. The TFU is stalled until all coincidences are processed. During that time, it is not possible to handle a new incoming message. The only parameters updated in the track fit are the x slope and the size of the ROI. The latter is reduced as the precision of the fit increases. All other parameters are transmitted unchanged, except for the y slope for muons, which is updated at MU1. This is due to the fact that the pretrigger estimate at MU4 suffers from multiple scattering in the iron absorbers [125].

The messages travel asynchronously through the network. The timing and the path of the messages is not determined a priori but depends on the detector occupancy. Most of the calculations are performed in parallel at 50 MHz with programmable Look Up Tables (LUTs). The LUTs allow a substantial reduction of the processing time. The TFU has 24 optical receivers, 8 for each WM. Since the optical link serves 48 channels, 384 channels per WM and 1152 channels per TFU are processed. The input rate of a TFU is 16 Gbit/s. The entire FLT network processes about 1 Tbit/s. Further details can be found in reference [125].

3.2.3 Trigger decision

All messages processed by the TFU of the last super layer (PC1) are sent to a TPU. The TPU uses LUTs to determine the momentum of the particle track from the bending in the magnetic field, under the assumption that the track originates from the target position. The LUTs can be programmed to apply cuts on p, p_T and E/p of the track. During data taking, we required:

- a momentum between 0 and $200\ \mathrm{GeV}/c$;
- a transverse momentum between 0.5 and $1000\ \mathrm{GeV}/c$;
- an E/p (energy over momentum) ratio between 0.2 and 2.

The first two cuts are in common for electrons and muons. The third cut rejects hadronic background in electron identification. The TPU can be used for clone removal by comparing the x and y components of the track momenta. A clone is generated by the occurrence of fake coincidences of hits inside the region of interest. In order to prevent an excessive load of the TDU, a maximum number of 23 processed tracks per BX is foreseen.

Tracks surviving the TPU selection are sent to the TDU, the final step of the FLT. The trigger decision can be based either on the number of track candidates of the same type (electrons or muons), or on the calculation of the invariant mass of the track pairs, which is also performed with LUTs. Track candidates accepted by the TDU are sent to the SLT, which can use them as a seed for a refined track search. In the final trigger configuration, events were accepted when a track of one type (electron or muon) was reconstructed by the FLT and a second pretrigger of the same type was found. In order to be independent from the FLT, the SLT was seeded by pretrigger messages rather than by the FLT track candidates.

3.3 Performance of the data transmission

We give an overview of the data stream from the outer tracker system to the input of the first level trigger and discuss the test performed to check the quality of the data transmission.

3.3.1 Outer tracker read-out

In figure 3.5 we show a scheme of the outer tracker power supply and read-out system [126].

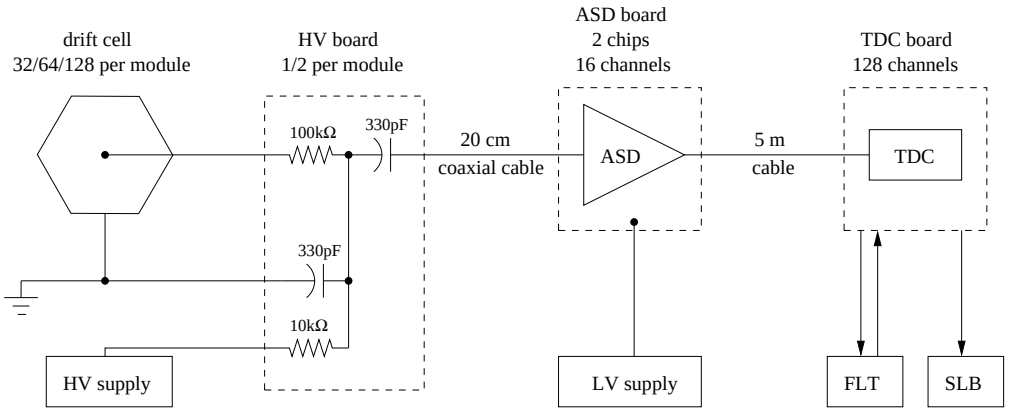

Figure 3.5. Scheme of the outer tracker power supply and read-out system.

One or two high voltage boards are mounted on each OTR module. The signal is carried out of the wire chambers by 20 cm coaxial cables, which connect the detector to the ASD (Amplifier Shaper Discriminator) boards. The ASD board contains two ASD chips, serving 8 channels each. The open collector single ended output is connected to a TDC (Time to Digital Converter) board via 5 m cables. The TDC uses 8 bits to encode the drift time of the particle hit and serves a maximum of 128 detector channels. On the TDC, 128 events are buffered for the FLT decision, allowing a maximum latency of about 12 μs. The hit pattern of the TDC, without the drift time information, is transfered to the Trigger Link Boards (TLBs). The TLBs map the OTR geometry into the geometry used by the FLT. In case of a positive trigger decision, the TDC information is passed to the Second Level Buffer (SLB), where the information becomes available for the higher level triggers.

The TDC also performs a logical OR between the hits of the two layers of a double layer along z (see figure 3.6). This operation allows to increase the track finding efficiency of the FLT and make it less dependent on the hit efficiency of the outer tracker cells. The read-out of the MUON chambers is similar, except for the TDC, since the drift time of the MUON hits is not evaluated.

3.3.2 Mapping of detector hits

The hit pattern from the TDC is transferred to the TLBs with flat cables of 34 wires (32 signals, 2 grounds). Inside the TLB, the geometrical mapping of the outer tracker hits to the TFU wire memory is performed with Programmable Logic Devices (PLDs). The mapping is needed to rearrange the outer tracker hits according to the simplified geometry used by the FLT. Despite the presence of 5 and 10 mm drift cells, in fact, the FLT memory is mapped assuming equal spacing between adjacent outer tracker cells (figure 3.6), in order to simplify the reconstruction of the space points from the raw hit information.

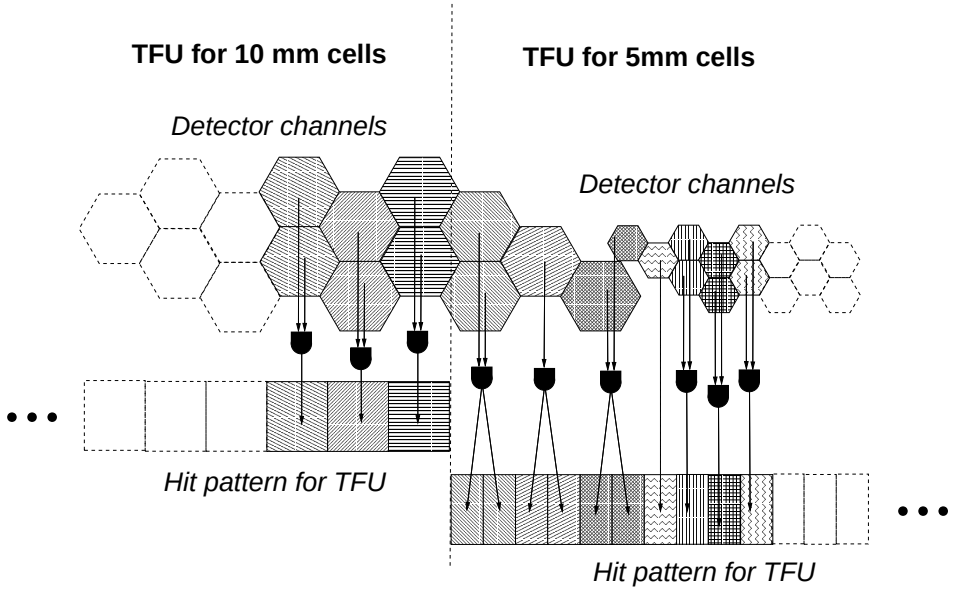

Figure 3.6. Mapping of detector hits to the TFU memory. The dashed line separates the regions covered by two TFUs. The left TFU processes hits coming from 10 mm OTR cells. The right TFU handles both cell sizes. In order to guarantee equal spacing, hits coming from 10 mm cells are split in two in the overlapping region. Hits from the two layers of a double layer along z are always ORed.

Wire memory bits associated to non existing channels in the gap regions between two detector modules are constantly set to one (hard coded 1). In order to increase the efficiency, a logical OR is performed between two adjacent channels in the $+5^\circ$ stereo layer, in the hit pattern prepared for the TFU of figure 3.6. After mapping, data are serialised by AUTOBAHN chips and transmitted to the TFUs in two packages of 32 bits (24 for data and 8 for BX) with 50 m long optical fibers. Since the FLT operates independently from the HERA clock, the bunch crossing number (BX) is attached to the data stream on the TLB. The BX number is also used to check for transmission errors, by comparing the BX values in two consecutive packages. The same type of AUTOBAHN chips receive the signals on the TFU and distribute them to the WMs.

3.3.3 Comparison between FLT and OTR hit patterns

We performed a test of the data transmission between the outer tracker and the first level trigger by comparing the content of the FLT wire memory with the expected hit pattern produced by the outer tracker in the FLT. This procedure allows to identify unplugged cables, hot and dead outer tracker channels and wrongly mapped outer tracker hits in the FLT wire memory.

Since the content of the wire memory cannot be read-out when the FLT is used in trigger mode, a special setup was built to allow the simultaneous access to the FLT memory and the detector hit patterns. Since the FLT is normally asynchronous with the rest of the detector, when it is used as trigger, we had to synchronise it with the outer tracker in order to perform an event by event comparison. This comparison failed due to (non-understood) difficulties in the synchronisation between OTR and FLT. However, the statistical comparison of the WM occupancy with that predicted from OTR hits agrees well. In figure 3.7 we show the comparison for a TFU, which allows to make several observations.

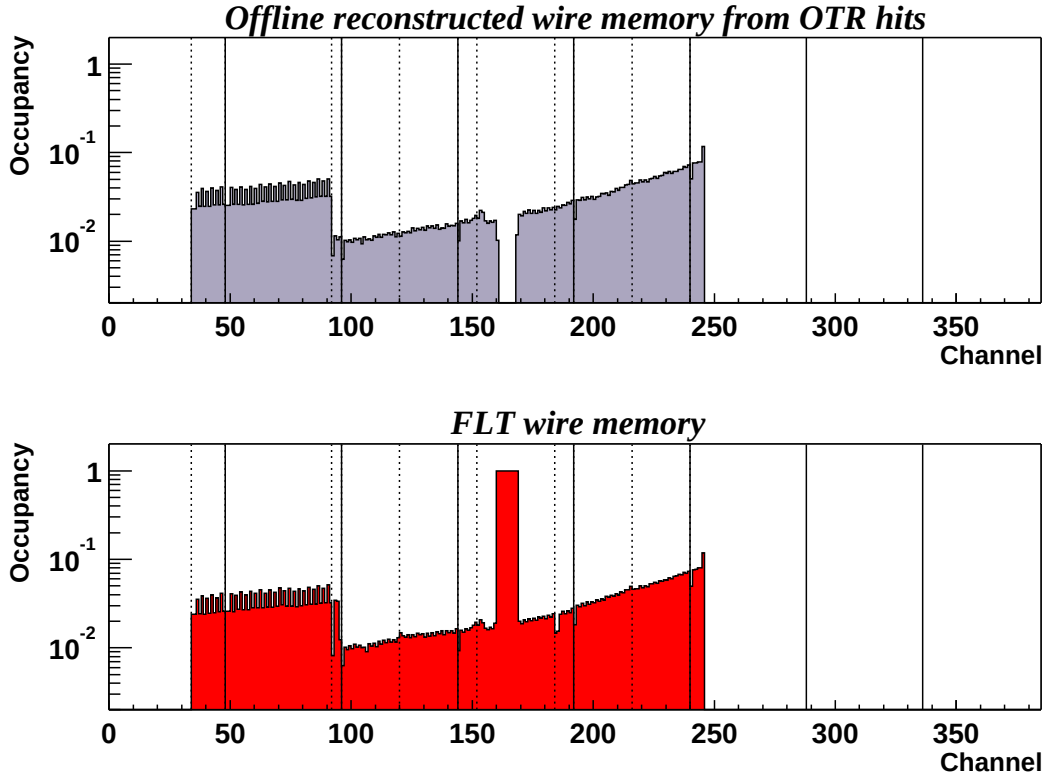

Figure 3.7. Comparison between the hit occupancy in the FLT wire memory recorded on-line (bottom) and the corresponding off-line reconstructed occupancy from OTR hits (top). Full lines delimit the groups of 48 bits associated to one optical link. Dotted lines correspond to individual TDC cables.

We observe that, in most channels, the occupancy in the FLT is correctly reproduced by that expected from the analysis of OTR hits. The occupancy increases with the channel number. This corresponds to the fact that the channel number increases going towards the inner part of the detector, where the track density is higher. A sudden change of occupancy can be noticed around channel 92. The outer tracker is made, in fact, of modules with different sizes. The larger size cells (10 mm) are located in the outer region, where the occupancy is lower. The smaller size cells (5 mm) cover the inner part of the detector, where the occupancy is higher. The transition at channel 92 reflects the relative occupancy in these different cell sizes.

The outer tracker channels between 161 and 169 have zero occupancy. They are dead. In order to avoid a loss of trigger efficiency due the dead channels, we set them to 1 in the FLT. Since this procedure artificially increases the load of the FLT network, it is limited by the constraint that it should not lead to a dead time.

Channels between 33 and 92 exhibit a special feature. Once every two channels, the occupancy is double than the previous channel, giving rise to a "comb" shape. This is due to the combination of two effects. Firstly, in the positive stereo view, each bit is ORed with the previous one in order to increase the FLT track efficiency. Secondly, hits coming from 10 mm cells, in the border region with the 5 mm cells, are split in two and sent to two adjacent bits of the FLT memory. This splitting procedure allows to use a simplified geometry in the FLT algorithm, in which the distance between two adjacent OTR cells is considered constant over the entire detector (figure 3.6).

We observe that the occupancy in the off-line reconstructed wire memory is lower than that recorded in the FLT, between channels 96 and 100. This group of bits is delimited by dashed lines in figure 3.7, which means that they corresponds to an entire TDC cable or optical link. This observation suggests that the hit occupancy in the FLT memory may correspond to a different group of outer tracker hits, wrongly mapped to the FLT memory. These kind of problems are due to cable swapping during the detector installation. The experimental way to identify swapped cables is to look for the occurrence of the same profile of occupancy in a different TFU.

During data taking, in the run initialisation phase, a test of the optical link transmission was performed. The test consisted in a threshold scan of the TFU receiver, checking the counting of the three least significative bits. Bad functioning links were masked and the corresponding bits in the FLT memory were set to 1. Typically, 5% of the links showed problems. The main reason were the AUTOBAHN transmitters located on the TLB, which were used to perform the serialisation of the signals. At the beginning of each run, the FLT memory was read-out and stored in the database. The OTR hit occupancy during the run could be used to make an off-line reconstruction of the FLT hit occupancy. Even though the synchronisation was lost, a statistical comparison of the two hit occupancy distributions could be used as a data quality check to verify, for instance, that the problematic optical links were properly masked.

3.4 Efficiency study

The commissioning phase revealed that the FLT performance was unstable, due to the optical transmission with the outer tracker, and could not be reproduced with a Monte Carlo simulation. A comparison between real and simulated FLT track efficiency showed an overestimate of $10 - 20\%$ in the simulation [114].

Trigger configuration and efficiency

Due to the instable FLT performance, the collaboration decided to implement a trigger configuration for data taking that was only partially based on the first level decision. The FLT was to accept events in case one track was fully reconstructed from a lepton pretrigger seed, and a second lepton pretrigger seed of the same type was found. Such events were passed to the SLT which used the two pretriggers for an independent search of two lepton tracks.

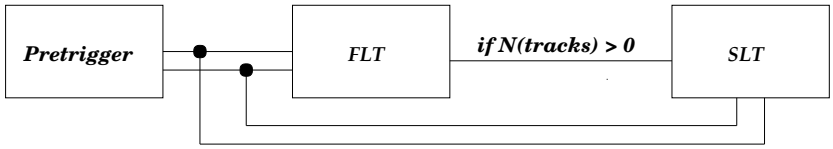

Figure 3.8. Trigger configuration used in data taking.

The trigger efficiency can be factorised as product of the pretrigger and SLT efficiency, which are estimated through Monte Carlo simulations, and the FLT efficiency, which is extracted from data. The FLT efficiency is expressed by an "event weight" ($\mathrm{w}_{\mathrm{FLT}}$), which is the probability that an event triggered by the SLT also fires the FLT, and is related to the track efficiency ($\varepsilon_{\mathrm{FLT}}$) by the formula

$$\mathrm{w}_{\mathrm{FLT}} = 1 - \prod_i (1 - \varepsilon_{\mathrm{FLT},i}), \tag{3.2}$$

where i runs over all simulated SLT tracks. The presence of SLT clone tracks artificially biases the efficiency towards higher values. Therefore, it is avoided by requiring a minimum distance between the projections of the two SLT tracks at the TC2 super layer.

3.4.1 Track efficiency determination

The FLT track efficiency is extracted from data. For the sake of simplicity, we use events with exactly two SLT tracks since they constitute more than 90% of the total sample. The FLT track used to issue the trigger decision must match an SLT track by definition. It is labelled as reference track. The SLT track which is not necessarily found by the FLT can be used for the determination of the FLT efficiency. It is

labelled as probe track. Events without any track in common between FLT and SLT can be observed. Since their origin is obscure, and the trigger efficiency for such events is not easy to calculate, those events are rejected from all physics analysis. Events with at least one SLT track matched to an FLT track are used to determine the FLT efficiency according to the formula

$$< \varepsilon_{\mathrm{FLT}} >= \frac{n_{12} + n_{21}}{n_1 + n_2}, \tag{3.3}$$

where n_{12} (n_{21}) is the number of events in which the first (second) SLT track is a reference track and the probe track matches an FLT track. The number n_1 (n_2) is the total number of events in which the first (second) SLT track is a reference track. This formula treats the two tracks on equal footing, adding up the two scenarios in which the first is the reference and the second is the probe, and vice versa. When the definition of matching criterion for reference and probe tracks are equal, $n_{12} = n_{21}$.

In order to define the matching criterion between FLT and SLT tracks, we investigate the difference between the extrapolated x and y coordinates at the z position of super layers PC1 and TC2 (see figure 3.9).

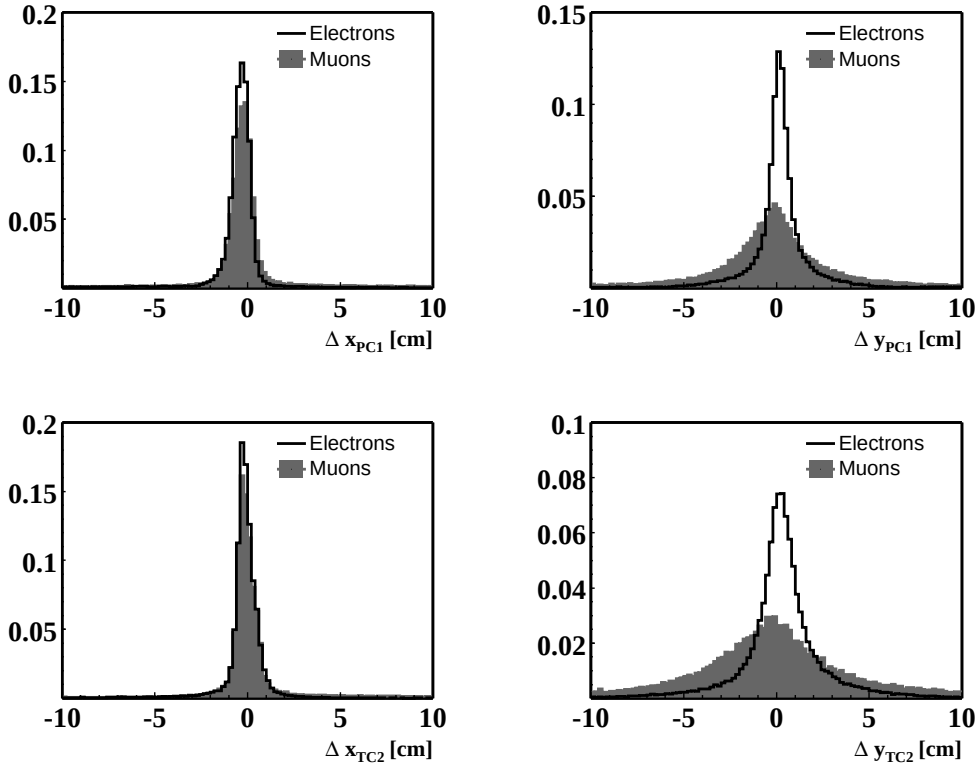

Figure 3.9. Distance between SLT tracks and closest FLT track. The plots refers to the extrapolated x (left) and y (right) coordinates at super layers PC1 (top) and TC2 (bottom). Results for electrons and muons are superimposed.

Even though they start from the same pretrigger seeds, FLT and SLT perform two independent track searches, which can lead to different results. The SLT uses all tracking chambers for the determination of the track parameters, while the FLT processes only hits coming from four tracking chambers. In addition, the SLT updates the track parameters with vertex detector hits. Therefore, the accuracy of the track parameters at the second level trigger is higher. The widths of the distributions are different for electrons and muons. The width is larger for muons. This is due to the fact that the extrapolation of muon track parameters is more affected by multiple scattering, since muons are required to pass through thick absorber walls.

Definition of matching criterion

Given the distributions in figure 3.9, we define the distance dr between two tracks as the average x and y deviation at the z position of PC1 ($z = 704$ cm) and TC2 ($z = 1305$ cm), each divided by the corresponding width,

$$\begin{aligned} dr_e &= \tfrac{1}{4} \cdot \left(\tfrac{|\Delta x_{\mathrm{PC1}}|}{1.0} + \tfrac{|\Delta y_{\mathrm{PC1}}|}{1.5} + \tfrac{|\Delta x_{\mathrm{TC2}}|}{1.0} + \tfrac{|\Delta y_{\mathrm{TC2}}|}{2.0}\right), \\ dr_\mu &= \tfrac{1}{4} \cdot \left(\tfrac{|\Delta x_{\mathrm{PC1}}|}{1.0} + \tfrac{|\Delta y_{\mathrm{PC1}}|}{4.0} + \tfrac{|\Delta x_{\mathrm{TC2}}|}{1.0} + \tfrac{|\Delta y_{\mathrm{TC2}}|}{8.0}\right). \end{aligned} \tag{3.4}$$

The distance between FLT and SLT tracks is plotted in figure 3.10.

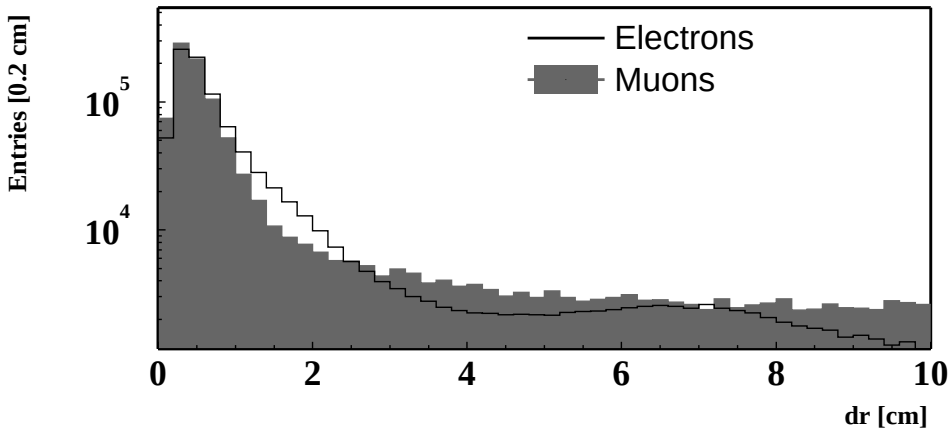

Figure 3.10. Distance between FLT and SLT track for electrons and muons.

We assume that two tracks are identical when the distance dr is less than 2 cm. In this way a certain fraction of real tracks is lost. However, the contribution of fake tracks is suppressed. We estimate the systematic uncertainty due to the definition of matching criterion by moving the limit to 5 and to 10 cm (see table 3.1).

3.4.2 Efficiency for J/ψ events

The main physics program at HERA-B is the study of J/ψ production, which includes the measurement of the x_F and p_T differential distributions. Therefore, we extract the FLT efficiency for a special set of reference tracks, namely electrons and muons produced in J/ψ decays, and discuss the dependence of the efficiency on the parameters which could be related to the x_F and p_T of the J/ψ. For this purpose we use the following selection of reference tracks[1]:

- SLT track matched to an off-line reconstructed track;
- standard clone removal;
- at least 5 hits in the vertex detector;
- at least 15 hits in the outer tracker;
- probability χ^2 of the track fit larger than 0.3%.
- momentum between 5 and $200\ \mathrm{GeV}/c$;
- transverse momentum between 0.7 and $5.0\ \mathrm{GeV}/c$;

For muons, we require at least 9 hits in the MUON chambers and a muon likelihood larger than 0.05. For electrons, we require that the energy over momentum is close to unity ($0.88 < e/p < 1.20$), in order to suppress the large hadronic background. The efficiency as a function of the dilepton mass is shown in figure 3.11.

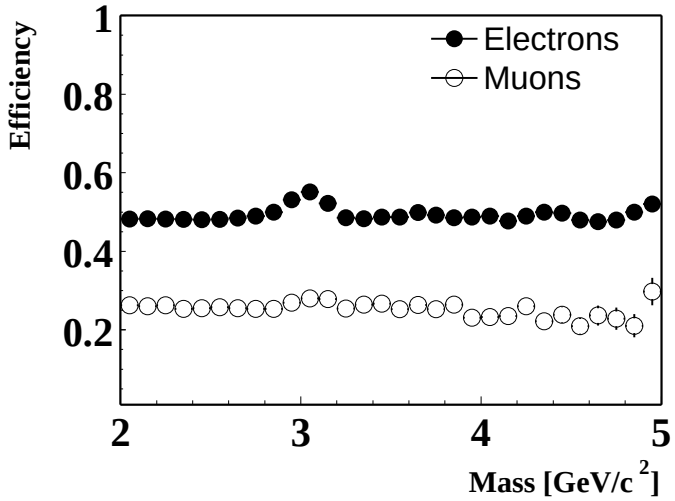

Figure 3.11. FLT track efficiency as a function of the dilepton mass.

The track efficiency for electrons is higher than for muons. One reason is the poor muon chamber performance. The efficiency loss is concentrated at super layer

[1] A detailed explanation of the choice of reference tracks will be given in section 4.4.2.

MU1 [127], where multiple scattering in the iron absorbers affects the trajectory of muons through the MUON chambers. The track finding algorithm, which is based on a linear extrapolation, might fail to find the particle hits.

Furthermore, we notice that the efficiency increases in the J/ψ mass region. This observation suggests that in presence of real leptons the FLT efficiency is higher. For this reason, the total sample of SLT tracks is not adequate to describe the efficiency for leptons produced in J/ψ decays, and one has to restrict the efficiency study to the J/ψ mass region. Since a large fraction of background is still present in that region, specially for electrons, we subtract the contribution of background. This is done with a side-band subtraction technique. We define three mass regions. The J/ψ region, which contains signal and background, and two regions containing only background, which are located at higher and lower masses (side-bands). Subtracting the efficiency distributions of the side-bands from the one in the J/ψ region, properly normalised, we obtain the efficiency for real leptons. The invariant mass of the selected electron and muon tracks is shown in figure 3.12, where we indicate the mass intervals used to identify the J/ψ region and the side-bands.

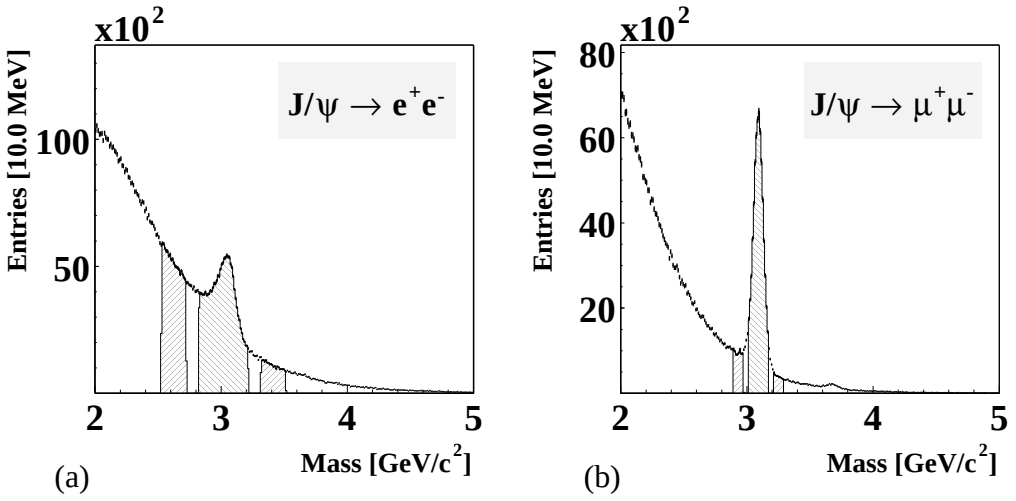

Figure 3.12. J/ψ signal in electron (a) and muon (b) channel in the full data sample. The J/ψ mass region and the side-bands used for background subtraction are also shown.

The normalisation is guaranteed by the fact that the size of the side-bands is tuned until it contains the same amount of background present in the J/ψ mass region. The average FLT track efficiencies for leptons produced in J/ψ decays are

$$\begin{aligned} \varepsilon_e &= 58.74 \pm 0.12_{stat}\ \%, \\ \varepsilon_\mu &= 28.25 \pm 0.12_{stat}\ \%. \end{aligned} \tag{3.5}$$

Effect of matching definition

In order to evaluate the systematic effect due to the definition of a matching criterion, we enlarge the definition to $dr < 2$ cm, $dr < 5$ cm and $dr < 10$ cm, respectively. The systematic uncertainty is evaluated as the maximum variation of the efficiency divided by $\sqrt{12}$. This corresponds, statistically, to assume a 68% confidence level[2]. The results are reported in table 3.1.

Track efficiency [%]	$dr < 2$ cm	$dr < 5$ cm	$dr < 10$ cm
Electrons	58.70 ± 0.12	60.21 ± 0.12	61.54 ± 0.12
Muons	28.25 ± 0.12	29.14 ± 0.12	30.72 ± 0.12

Table 3.1. Average FLT track efficiency for leptons coming from J/ψ, obtained with three definitions of matching with SLT tracks.

The systematic uncertainty is 1.4% for electrons and 2.5% for muons.

Effect of bremsstrahlung tag for electrons

Bremsstrahlung photons emitted by electrons before the magnet travel together with the electron until the magnet. Electrons are deviated by the magnetic field. Photons keep a straight line trajectory. A linear extrapolation of the electron track from the vertex detector to the electromagnetic calorimeter provides the position where possible bremsstrahlung photons are expected to hit the calorimeter (figure 3.13).

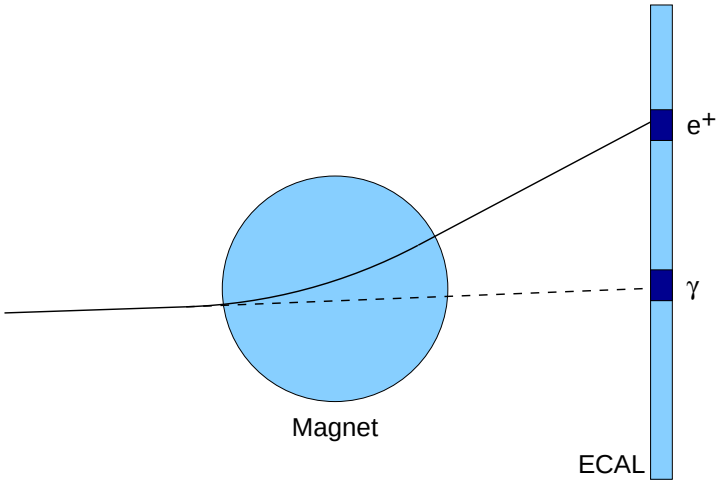

Figure 3.13. Schematic view of the bremsstrahlung tag technique for electron identification.

[2]The width of a flat distribution between x_1 and x_2 is $\sigma = L/\sqrt{12}$, where $L = x_2 - x_1$.

The presence of energetic clusters due to bremsstrahlung photon emission serves as electron tag and allows to suppress a large fraction of background in particle identification. Note that this might lead to a decrease of efficiency. The energy released by the photon in the calorimeter can be used to increase the accuracy in the electron momentum estimate. The J/ψ signal, when at least one of the two electrons has been identified with a bremsstrahlung tag, is reported in figure 3.14(a).

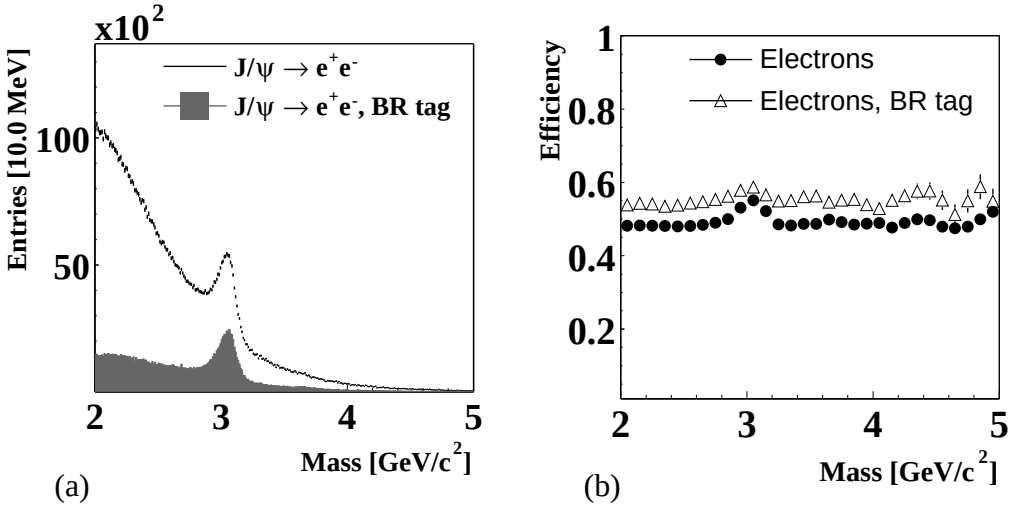

Figure 3.14. J/ψ signal in the electron channel (a) and FLT track efficiency as a function of the dielectron invariant mass (b), with and without bremsstrahlung photon requirement.

The significance of the J/ψ signal increases when the photon tag is required. However, the number of electrons available for the FLT efficiency calculation diminishes. The FLT track efficiency as a function of the dielectron invariant mass, when the photon tag is applied to the electron probe track, is shown in figure 3.14(b). Note that the photon tag is not applied to reference tracks, since they are not used to calculate the efficiency. The efficiency is higher for all masses, even though the relative increase inside the J/ψ mass region is lower. When the photon tag is applied, the dependence of the efficiency with the mass becomes almost flat. This indicates that the background is remarkably reduced.

When electrons are tagged, the relative increase of efficiency in the J/ψ region is 1%, which we consider as a systematic effect in the determination of the average FLT efficiency for electrons. Under the assumption that the systematic uncertainty for the matching definition and bremsstrahlung tag are uncorrelated, we sum them in quadrature and obtain a relative systematic uncertainty of 1.7%. The final estimate of the average FLT track efficiency is

$$\begin{aligned} \varepsilon_e &= 58.74 \pm 0.12_{stat} \pm 1.0_{sys}\ \%, \\ \varepsilon_\mu &= 28.25 \pm 0.12_{stat} \pm 0.7_{sys}\ \%. \end{aligned} \tag{3.6}$$

Efficiency dependence on the position

The efficiency dependence on the spatial position inside the detector is important for the study of the x_{F} distribution of J/ψ mesons. The x_{F} of the J/ψ is related to the decay angle between the lepton tracks in the laboratory frame. To a good approximation, a positive x_{F} is translated in a small angle and a negative x_{F} to a large angle. Any dependence of the efficiency on the position should be taken into account, in order to reproduce the correct experimental x_{F} distribution. The track efficiency as a function of the x and y position at TC2 is shown in figure 3.15.

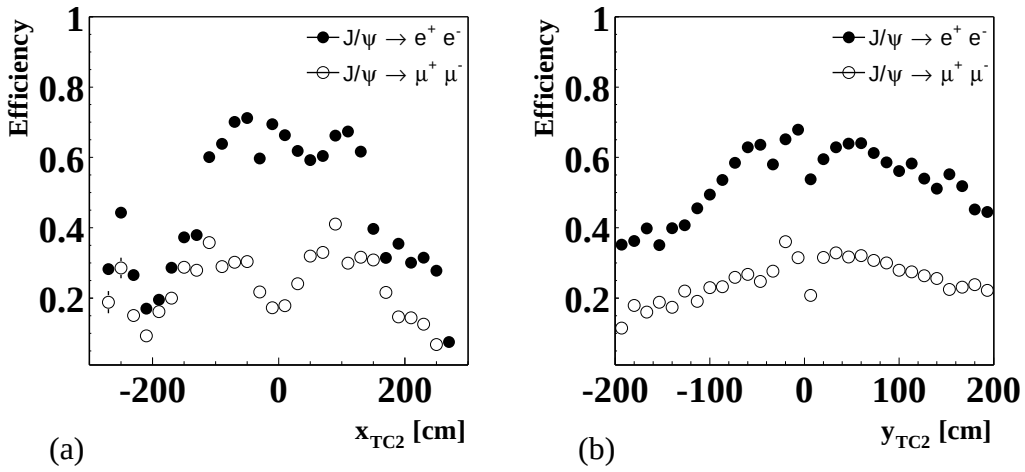

Figure 3.15. FLT track efficiency as a function of the x (a) and y (b) position at TC2.

The variations are due to the fact that the outer tracker is divided in sectors in the FLT logic, and the FLT performance strongly depends on the sector traversed by the particle. The efficiency is larger in the inner part of the detector because most of the efforts during commissioning were devoted to the improvement of the sectors with the highest occupancy.

Efficiency dependence on the momentum

The efficiency depends also on the particle momentum. This effect is due to the correlation observed between the momentum and the trajectory of the particle through the detector. The average momentum as a function of the radial distance from the beam pipe at the super layer TC2 is shown in figure 3.16(a). High momentum particles are bent less than low momentum particles and preferentially traverse the inner part of the spectrometer, where the efficiency is larger. The track efficiency as a function of momentum is presented in figure 3.16(b). When the momentum becomes too large (and the distance from the beam pipe too small), the efficiency decreases, due to the fact that the beam pipe might absorb the particles.

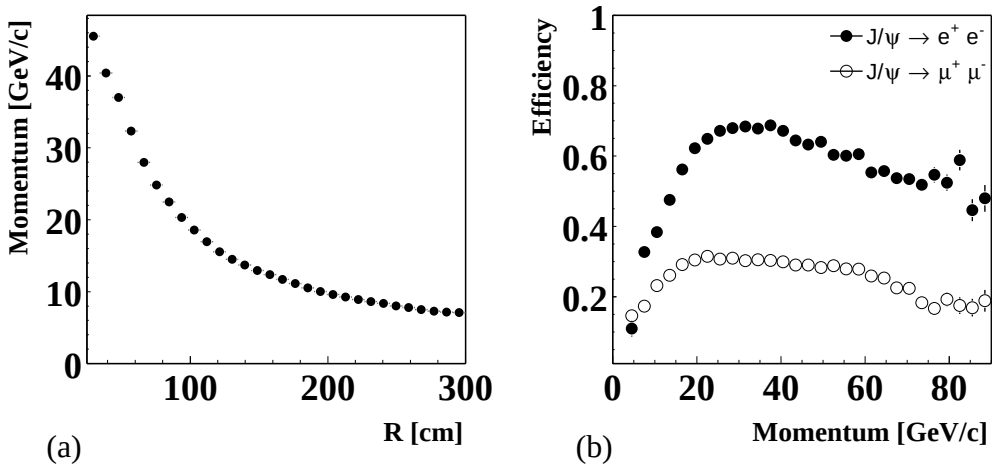

Figure 3.16. Correlation between average momentum and radial distance from the beam pipe at super layer TC2 (a) and track efficiency as a function of the momentum (b).

Efficiency dependence on the OTR hit occupancy

The total number of hits in the outer tracker and the average hit occupancy as a function of the dilepton mass are shown in figure 3.17.

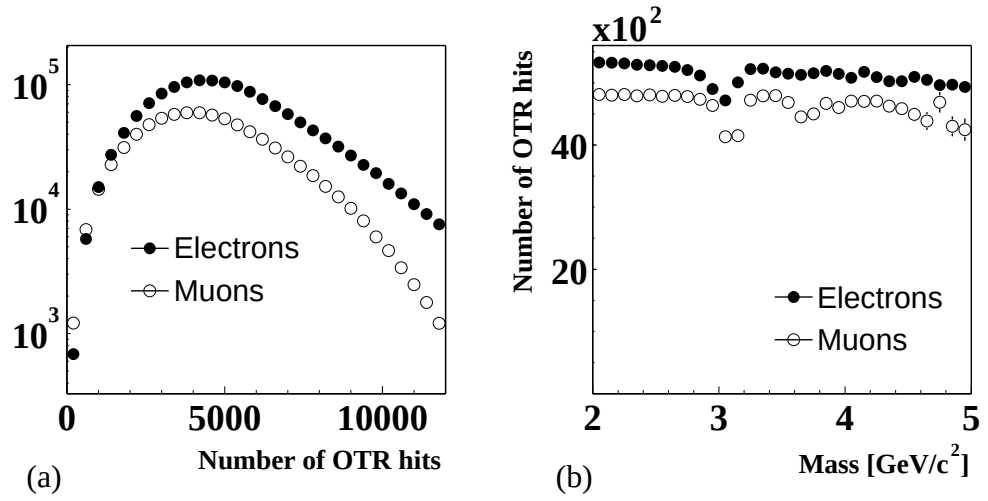

Figure 3.17. Total number of hits in the outer tracker (a) and average hit occupancy as a function of the dilepton mass (b).

Outside the J/ψ mass region, the occupancy does not depend on the mass. The occupancy decreases in the J/ψ mass region. This demonstrates that the FLT preferentially triggers on J/ψ, in real J/ψ events. In events without a J/ψ, the FLT triggers on events with higher occupancy. In effect, the larger the number of hits in

the outer tracker, the higher is the probability that the first level trigger propagates messages and fully reconstructs tracks. The track efficiency as a function of the occupancy is shown in figure 3.18. A linear fit to the data reveals an increase of about 0.01 in efficiency every 1000 hits in both electron and muon channels.

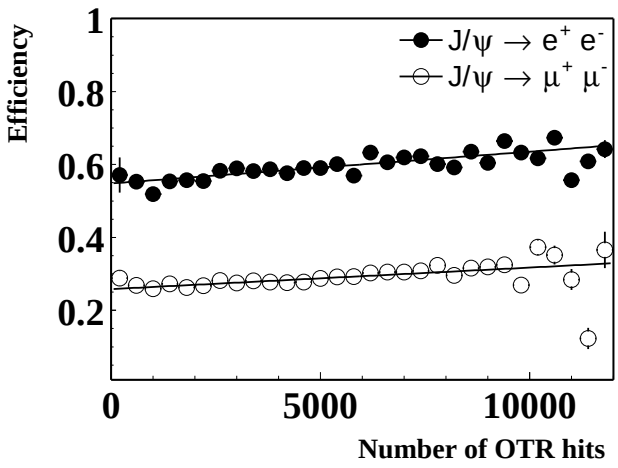

Figure 3.18. FLT track efficiency as a function of the number of hits in the outer tracker.

The dependence of the efficiency on the occupancy might affect the x_{F} and p_T distributions of the J/ψ. The related correlation plots are shown in figure 3.19.

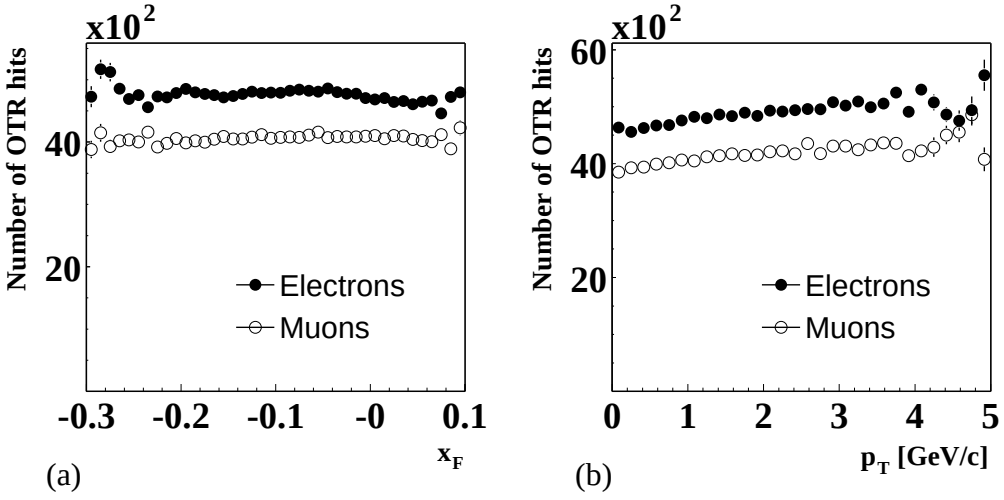

Figure 3.19. Number of outer tracker hits as a function of x_{F} (a) and p_T (b) of the J/ψ.

The occupancy is essentially flat in x_{F}. A slope is observed in the p_T correlation plot. The maximum variation of occupancy in x_{F} and p_T is about 1000 hits, which corresponds to a maximum variation of efficiency of about 1%.

3.4.3 Efficiency map

The observed dependences on position and momentum do not allow to use the average FLT track efficiency to evaluate the event weight in equation (3.2). A specific procedure to assign the correct efficiency to each event is needed. Since we have shown that the dependence on the occupancy leads to a maximum variation in efficiency of 1%, we shall neglect it. The dependences on position and momentum are taken into account by evaluating the efficiency in each elementary cube of a three dimensional space. The three coordinates of this space are the x and y position at TC2 and a linear combination of x at PC1 and x at TC2,

$$0.8654 \times x_{\mathrm{TC2}} - x_{\mathrm{PC1}} \times \frac{z_{\mathrm{TC2}}}{z_{\mathrm{PC1}}}, \tag{3.7}$$

which reflects the track momentum. Such a linear combination is more convenient than the momentum itself since it is directly related to the geometric acceptance of the FLT [128]. The factor 0.8654 guarantees a uniform bin population, since momentum and position are correlated. The granularity of the map in x is determined by the outer tracker area associated to one optical link transmitter, which is 48×0.436 cm. The number of bins in the other two dimensions is chosen to reach a comparable statistics in all bins. The total number of bins is $88 \times 74 \times 10 = 65120$. The information encoded in each efficiency map cube is the particle type (electron or muon), the total number of probe tracks N, and the numbers of efficient entries n_0, n_1 and n_2 for the three matching criterion: $dr < 2$, $dr < 5$ and $dr < 10$. All November 2002 runs have been used to obtain the number of reference tracks per cube shown in figure 3.20.

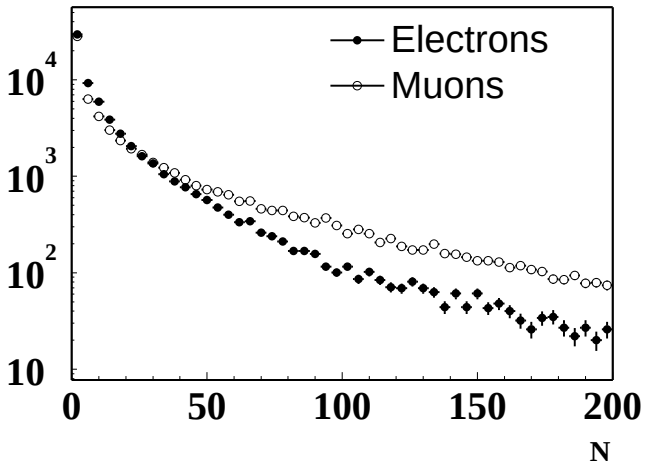

Figure 3.20. Number of reference tracks per cube in the November 2002 efficiency map.

Almost half of the cubes have a number of tracks smaller than 20. In order to increase the accuracy of the efficiency determination, at the expense of a lower

spatial resolution, we adopt a smearing procedure. Bins with $N < 20$ are grouped with adjacent bins until the statistics becomes larger than 20. At this point, the efficiency is calculated and is assigned to each bin used for the calculation. In order to preserve the independence among the bins, each bin is used only once. In figure 3.21, we present the track efficiency in x and y positions at TC2, averaged over the momentum coordinate, over the November 2002 period of data taking.

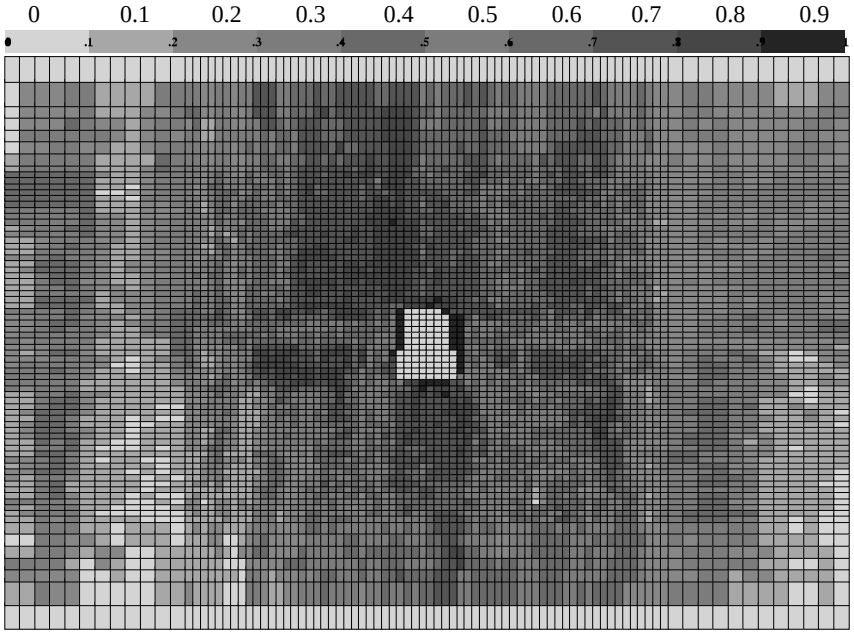

Figure 3.21. Distribution of the FLT track efficiency in x and y positions at TC2 averaged over the momentum.

The old efficiency maps were generated using all SLT tracks as probe tracks. As it was shown in figure 3.11, this procedure leads to underestimate the efficiency for J/ψ mesons, due to the presence of a large fraction of background tracks. The best solution, in principle, would be to produce efficiency maps exclusively selecting leptons generated in J/ψ decays. Since the amount of such leptons is not sufficiently large to guarantee an accurate estimate of the efficiency, we employ a different solution to generate new efficiency maps.

We search for a set of selection criteria which help to identify real leptons, without requiring that the particles originate from J/ψ mesons. In order to reduce the loss of statistics, we apply more stringent cuts only to the probe tracks. We discard SLT tracks which are not matched to an off-line reconstructed track. This helps to reduce the fraction of ghost tracks, which are due to random combinations of hits in the detector. For muons, we require that the muon likelihood is larger than 0.05. For electrons, we require that a bremsstrahlung photon is associated to the track.

Statistics of probe tracks

An efficiency map is generated for each run listed in appendix A, except for the seven March 2003 runs ($\approx$ 2 M events). Under the assumption that within a month the run conditions are stable, the efficiency maps in each month are merged. The main reason for the global change of the run conditions were, in fact, the maintenance activities carried out during the monthly periods of detector shut-down. In table 3.2, we present the total number of probe tracks used to generate efficiency maps in each of the five months of data taking.

	Number of probe electrons	Number of probe muons
October	128,521	359,454
November	1,019,469	2,107,882
December	159,706	514,102
January	1,061,068	1,648,616
February	736,700	1,346,297
Total	3,105,463	5,976,351

Table 3.2. Total number of probe tracks used to generate efficiency maps.

Efficiency dependence on mass, $x_{\rm F}$ and p_T

In figure 3.22(a), we compare the FLT track efficiency obtained with leptons originating from J/ψ (see selection listed in section 3.4.2) and the one extracted from the old and the new maps.

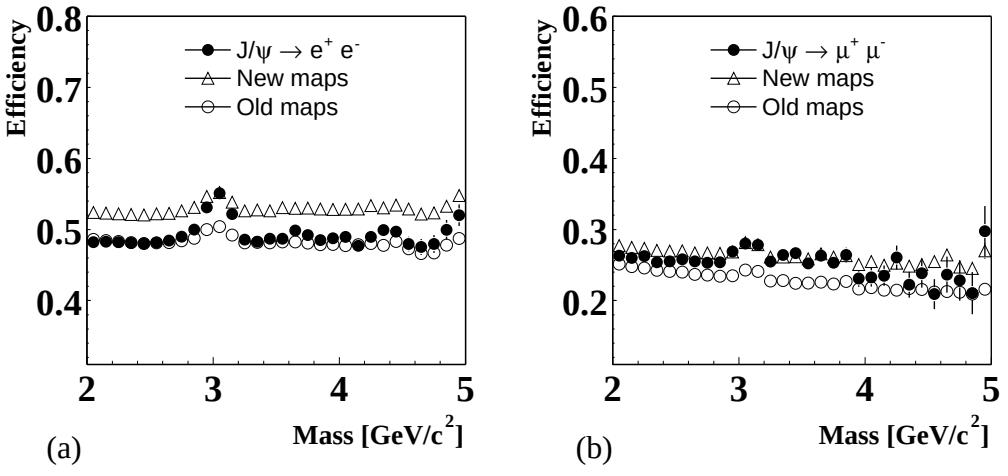

Figure 3.22. FLT track efficiency as a function of the dilepton mass calculated with leptons which pass the J/ψ selection and extracted from the efficiency map.

The efficiency given by the old maps is consistent with the efficiency obtained with leptons outside the J/ψ mass region. This means that the old maps are dominated by background tracks. For both electrons and muons, the efficiency extracted with the new maps is higher, closer to the one obtained in the mass region of the J/ψ, even though the efficiency still exhibits an undesired mass dependence. In figure 3.23 and figure 3.24, we show the FLT efficiency as a function of the $x_{\rm F}$ and p_T of the J/ψ calculated with the maps and with the data.

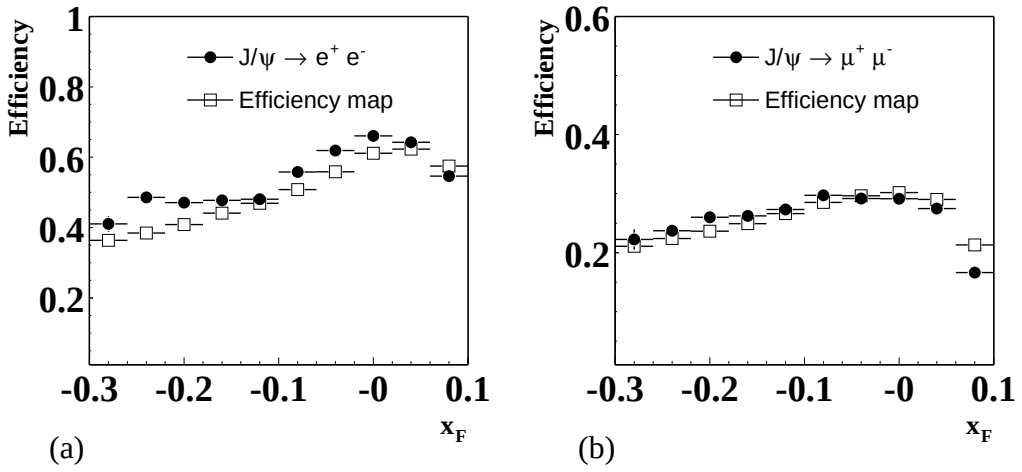

Figure 3.23. FLT track efficiency for electrons (a) and muons (b) as a function of the $x_{\rm F}$ obtained with the J/ψ selection and with the efficiency maps.

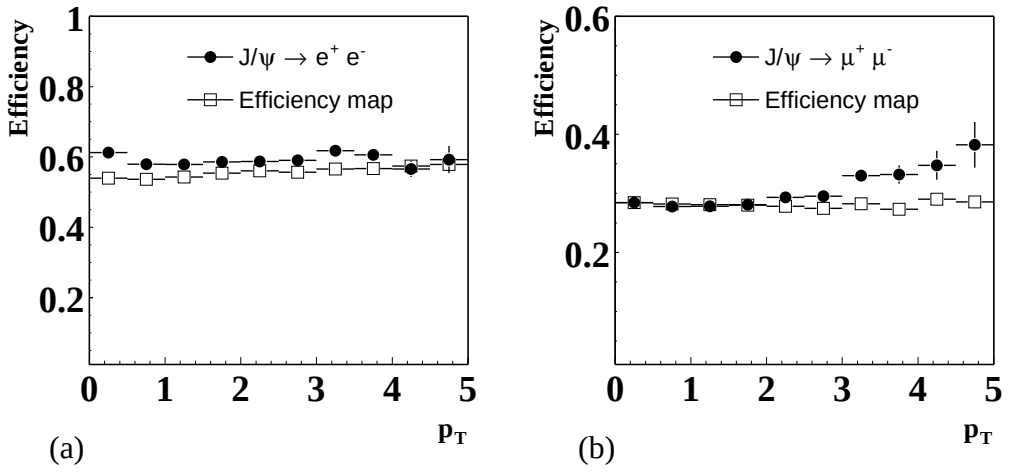

Figure 3.24. FLT track efficiency for electrons (a) and muons (b) as a function of the p_T obtained with the J/ψ selection and with the efficiency maps.

Almost in all x_{F} and p_T bins, the FLT efficiency maps provide a slightly smaller efficiency than the one calculated with the J/ψ selection. A comparison between the FLT trigger weight obtained from J/ψ in data and from efficiency maps in the Monte Carlo simulation, as a function of x_{F} and p_T, reveals that the agreement is satisfactory [114]. This is a hint of the reliability of the FLT efficiency maps.

Efficiency dependence on the run period

The information contained in the efficiency maps can be used to extract the average FLT track efficiency with the formula

$$< \varepsilon >= \frac{\sum_{cubes} n_i}{\sum_{cubes} N_i}, \tag{3.8}$$

where n_i is the number of efficient entries and N_i is the total number of entries in the cube with index i. The average FLT track efficiency as a function of the run number is plotted in figure 3.25.

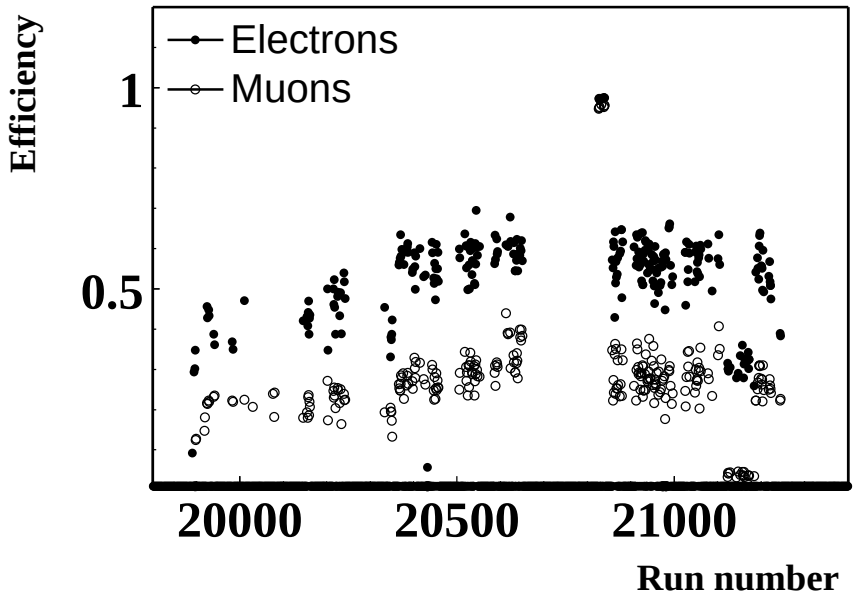

Figure 3.25. Average FLT track efficiency as a function of the run number obtained from the efficiency map.

The FLT efficiency varies with time. The main reason is the instable performance of the optical link transmitters. The latter were tested in the initialisation phase of each run and the problematic ones were masked in order to increase the trigger efficiency of the FLT network. However, experience has shown that these test were not reliable.

The efficiency increases in 2002 due to a constant monitor and repair of faulty links and cabling problems of the FLT. The empty region between runs 20600 and 20800 corresponds to the minimum bias data taking periods. In this configuration the FLT is switched off. Two groups of runs fall outside the general trend. The efficiency for the 17 runs between 21122 and 21183, in both muon and electron channels, is lower than the average. The efficiency for the 7 runs between 20826 and 20839 is close to 100%. This is due to a test trigger configuration, in which the FLT was triggering on events with two fully reconstructed leptons. These tracks were passed to the SLT, which used them as seeds for the refined track search. For this reason, all events present two tracks in common between FLT and SLT.

3.5 Summary

We described the HERA-B first level trigger used in the four months of data taking. In this period, the FLT guaranteed a background reduction factor of approximately 200 and allowed to collect a total sample of $300,000$ J/ψ, at a rate of 1200 per hour, with an average track efficiency $\varepsilon_e = 58.74 \pm 0.12_{stat} \pm 1.0_{sys}$ % for electrons and $\varepsilon_\mu = 28.25 \pm 0.12_{stat} \pm 0.7_{sys}$ % for muons.

We discussed the procedure to generate FLT efficiency maps. We stressed the motivations which led to the production of three dimensional maps, in order to account for the observed dependence of the efficiency on the detector area traversed by the particles and on the particle momentum.

Chapter 4

Beauty Production Cross Section

The elephant man (1980) - D. Lynch

We use two methods to extract the beauty quark production cross section from 150 M dilepton triggered events for 920 GeV pA collisions. The methods are based on the identification of simultaneous muonic decays of $b\bar{b}$ pairs in the muon $x_{\rm F}$ range $[-0.3, 0.1]$. The resulting cross sections are consistent: $\sigma_{b\bar{b}} = 18.6 \pm 5.2_{stat} \pm 3.2_{sys}$ nb/nucleon and $\sigma_{b\bar{b}} = 15.5 \pm 2.4_{stat} \pm 2.3_{sys}$ nb/nucleon.

4.1 Introduction

We present a measurement of the beauty quark production cross section performed with the HERA-B dilepton triggered data. Under our experimental conditions, at first perturbative order, b quarks are mostly produced in pairs with a $\bar{b}$ quark, either via quark-antiquark annihilation or via gluon fusion. The inclusive muonic decays of the b and $\bar{b}$ quarks are used to identify events in which a $b\bar{b}$ pair is produced.

The HERA-B collaboration has already measured the $b\bar{b}$ cross section by using the J/ψ decays originating from b quarks. The analysis presented in this thesis provides an independent confirmation of the previous measurement with a larger sample of signal events. However, the event counting technique strongly relies on Monte Carlo simulations, which potentially implies a larger systematic uncertainty.

In the next section, we discuss the physics processes involved in the analysis, and present the formula used to extract the cross section. Section 4.3 is dedicated to the study of the Monte Carlo simulations of signal and background events. The data analysis is presented in section 4.4. We select the J/ψ sample used for normalisation, and search for inclusive muonic b decays. In section 4.5 we compare our experimental results to those of other experiments and to the results of the available theoretical predictions.

4.2 Measurement method

The beauty cross section is evaluated counting the number of $b\bar{b}$ events relative to that of J/ψ particles. The latter are identified with the weak decay $\mathrm{J}/\psi \to \mu^+\mu^-$ and their number is evaluated with a Gaussian fit to the invariant mass spectrum of unlike-sign muons. The physics processes used to identify $b\bar{b}$ events are "double semi-muonic b decays", which are all possible combinations of primary b and secondary c decays occurring with the emission of a muon. The primary b quark is produced in the proton-nucleus collision. The secondary c quark comes from the decay of the heavier b quark. Muons from double semi-muonic b decays are uncorrelated and do not show up as a peak in the dimuon invariant mass spectrum. Therefore, the number of $b\bar{b}$ events is estimated by subtracting all possible sources of background from the data sample which survives the $b\bar{b}$ selection criteria.

4.2.1 Double semi-muonic b decays

Once a $b\bar{b}$ pair is produced in the proton-nucleus interaction, the b and $\bar{b}$ hadronise according to the probabilities reported in the PDG [2]: $P_{B^+} = (39.7 \pm 1.1)\%$, $P_{B^0} = (39.7 \pm 1.1)\%$, $P_{B_S^0} = (10.7 \pm 1.1)\%$ and $P_{b-baryons} = (9.9 \pm 1.7)\%$. Subsequently, the b-hadrons decay mostly into open charm mesons. For the sake of simplicity, we assume a 100% probability for the b to c decay[1]. Both b and c quarks have a large probability to decay with the emission of a single muon ("semi-muonic decay"). The branching ratios, which we shall denote with "B" and "C" respectively, are taken from the PDG [2] and are reported in table 4.1.

Decay	Branching ratio [%]
$b \to \mu^- X$	$B = 10.95 \pm 0.29$
$c \to \mu^+ X$	$C = 8.8 \pm 0.5$

Table 4.1. Inclusive branching ratios of semi-muonic b and c decays from PDG [2].

Any combination of two simultaneous semi-muonic decays of primary b and secondary c quarks on the b and $\bar{b}$ decay branches produces a dimuon final state, which can be used to identify events in which a $b\bar{b}$ pair is produced. We shall label the four classes of "double semi-muonic b decays" included in this analysis as $bibj$, $bici$, $bicj$ and $cicj$. When both b and $\bar{b}$ quarks undergo a direct muonic decay, we shall label the decay $bibj$. When one b quark decays muonically and the secondary c quark on the same branch undergoes a muonic decay, we define the decay as $bici$. If the secondary c quark on the other branch decays muonically, then we shall call the decay $bicj$. Lastly, $cicj$ decays are the ones in which both secondary c quarks decay muonically. The Feynman diagrams of the simultaneous muonic b and c decays included in this analysis are sketched in figure 4.1.

[1]The b and c decays are used to indicate the corresponding beauty and charm hadrons decays.

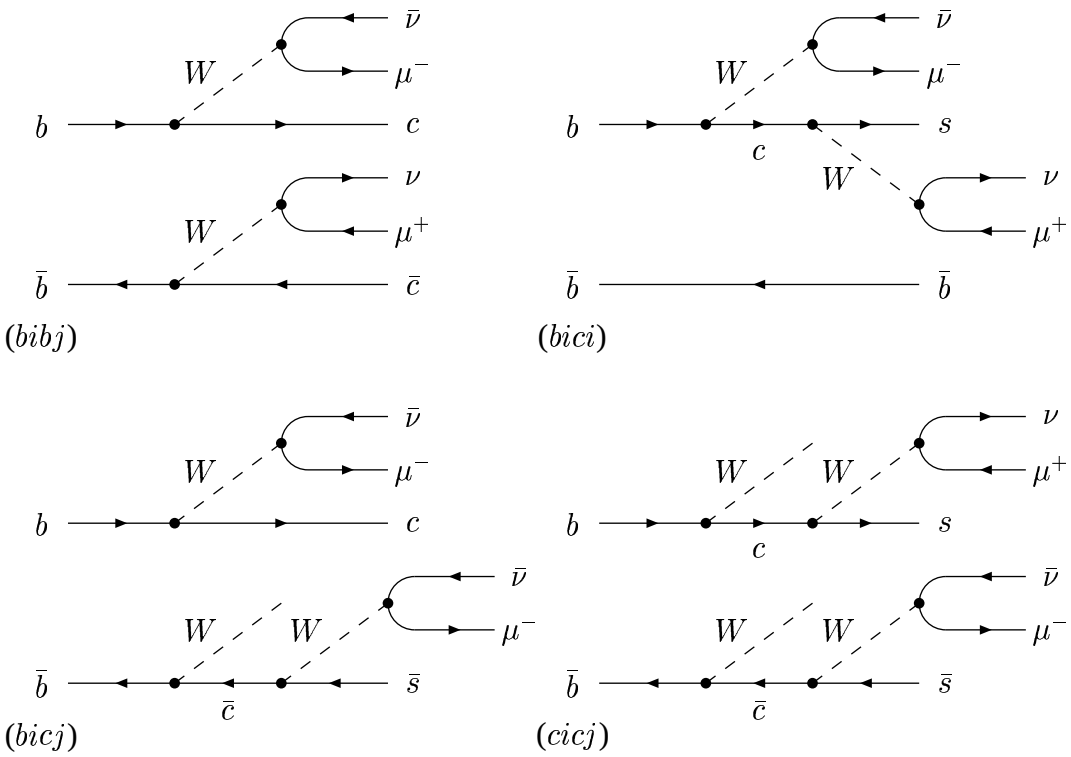

Figure 4.1. Feynman diagrams of the four "double semi-muonic b decays" studied in this analysis. From top-left to bottom-right, the decays labelled $bibj$, $bici$, $bicj$ and $cicj$ are sketched. The letters b and c indicate the flavour of the quarks that undergo muonic decay. The letters i and j indicate the b and $\bar{b}$ decay branch, respectively.

The processes labelled $bibj$, $bici$ and $cicj$ have two oppositely charged muons in the final state, while $bicj$ leads to two muons of the same sign[2]. This statement is only partially correct, since neutral B mesons can oscillate before they decay. Therefore, the charge of the muons depends also on the number of oscillations before the decay. In a first approximation, we calculate the probability of each process shown in figure 4.1 combining the branching ratios of the direct semi-muonic b and c decays reported in table 4.1. The effect of B mixing will be introduced later as a weighting factor to split each signal between the two different muonic final states.

Since the four classes are not mutually exclusive, we must avoid double counting of events falling in more than one category. For instance, events in which both b and c quarks undergo muonic decay simultaneously satisfy the four definitions. Therefore, we assign a priority to the classes (the order is: $bibj$, $bici$, $bicj$ and $cicj$) and introduce the probability that quarks do not decay into muons ($\bar{B} = 1 - B$ and $\bar{C} = 1 - C$). The resulting branching ratios are shown in table 4.2.

[2]The class $bicj$ includes decays with a $\mu^+\mu^+$ final state, which are not shown in figure 4.1. In our notation, the final state $\mu^+\mu^+$ include the conjugate channel $\mu^-\mu^-$.

Decay	$\mu^+\mu^+$ or $\mu^-\mu^-$	$\mu^+\mu^-$	Total BR
$bibj$	0	BB	0.0120
$bici$	0	$2B\bar{B}C$	0.0172
$bicj$	$2B\bar{B}\bar{C}C$	0	0.0157
$cicj$	0	$\bar{B}\bar{B}CC$	0.0061
Total BR	0.0157	0.0353	0.0510

Table 4.2. Branching ratios of the four "double semi-muonic b decays".

A factor 2 is used to include the conjugate final states in $bicj$ and $bici$. The total branching ratio is 5.1%. Since the largest contribution is expected from the unlike-sign muon channel, we shall use decays in this channel to extract the beauty production cross section. However, the study of double semi-muonic b decays in the like-sign channel will be important for a correct background estimate.

Doubly charmed b decays

So far, we assumed that all beauty quarks produced in the main interaction perform a single charm decay. If the virtual W boson, emitted in the b decay, converts in a $\bar{c}s$ pair, then two charm quarks originate from one beauty decay (figure 4.2).

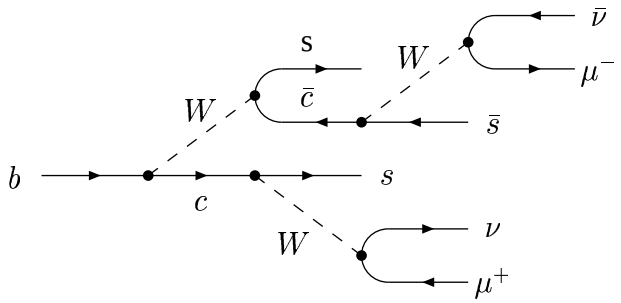

Figure 4.2. Feynman diagram of a $b \to c\bar{c}s$ decay and simultaneous semi-muonic c decays.

This means that the inclusive branching ratio for $b \to \mu^- X$ decays contains a fraction of anticharm muonic decays. Since the branching ratio for doubly charmed b decays is $\text{Br}(b \to c\bar{c}s) = (22 \pm 4)\%$ [2], the fraction of decays via charmed hadrons is $B_C = \text{Br}(b \to c\bar{c}s) \cdot \text{Br}(\bar{c} \to \mu^- X) \approx 2\%$, while the fraction of direct decays is $B_W = B - B_C \approx 9\%$. Therefore, the branching ratios in table 4.2 are recalculated splitting the inclusive branching ratio for muonic b decays in two terms ($B = B_W + B_C$). In this scenario, a new class of decays arises: $cici$. Simultaneous muonic decays of two charm quarks on the same branch are not included in any class defined up to now and have a branching ratio of $2B_C C\bar{B}\bar{C} \approx 0.003$, which is 6% of the total. The corresponding systematic uncertainty, which depends also

on the reconstruction efficiency, is decreased when such decays are assigned to an existing class. We chose the class $bici$ since it also exhibits two oppositely charged muons in the same decay branch. The branching ratios for "double semi-muonic b decays" after corrections for doubly charmed b decays, are reported in table 4.3.

Decay	$\mu^+\mu^+$ or $\mu^-\mu^-$	$\mu^+\mu^-$	Total BR
$bibj$	0	$B_W B_W$	0.0081
$bici$	0	$2B_W\bar{B}C + 2B_C\bar{B}C$	0.0171
$bicj$	$2B_W\bar{B}\bar{C}C$	$2B_W B_C$	0.0164
$cicj$	$2B_C\bar{B}\bar{C}C$	$\bar{B}\bar{B}CC + B_C B_C$	0.0093
Total BR	0.016	0.035	0.0510

Table 4.3. Branching ratios for "double semi-muonic b decays" after applying corrections for doubly charmed b decays.

The effect of doubly charmed b decays is that a fraction of $bibj$ decays is absorbed into the class of $bicj$ decays into oppositely charged muons. Note that the latter class was empty before the corrections were applied. Another fraction of $bibj$ decays is absorbed into the class $cicj$. Finally, part of the $bici$ decays becomes $cicj$ decays into like-sign muons, which was also empty before applying corrections. The branching ratios reported in table 4.3 do not yet include all relevant effects for this analysis. The final branching ratios are obtained by distributing the total branching ratios reported in table 4.3 in the two muonic final states according to the combined effect of doubly charmed decays and B mixing. The size of this effect is determined from Monte Carlo simulations and is discussed in the next section.

Mixing of B^0 and B_s mesons

A large fraction of b quarks hadronises in neutral B mesons [23]. It is known that these mesons may oscillate before the decay (figure 4.3).

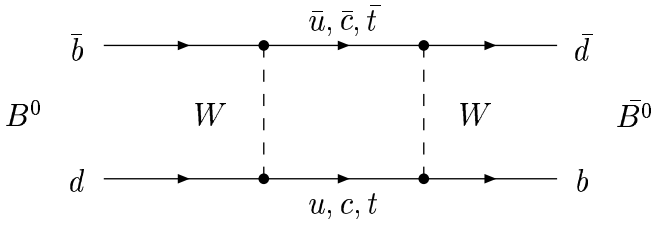

Figure 4.3. Feynman diagram of B^0 mixing. The corresponding diagram for B_s oscillations is obtained replacing the d quark with an s quark.

In order to investigate the effect of B^0 mixing in our Monte Carlo simulations, we report in figure 4.4 the proper time distribution of muons emitted in semi-muonic decays of charged and neutral B mesons.

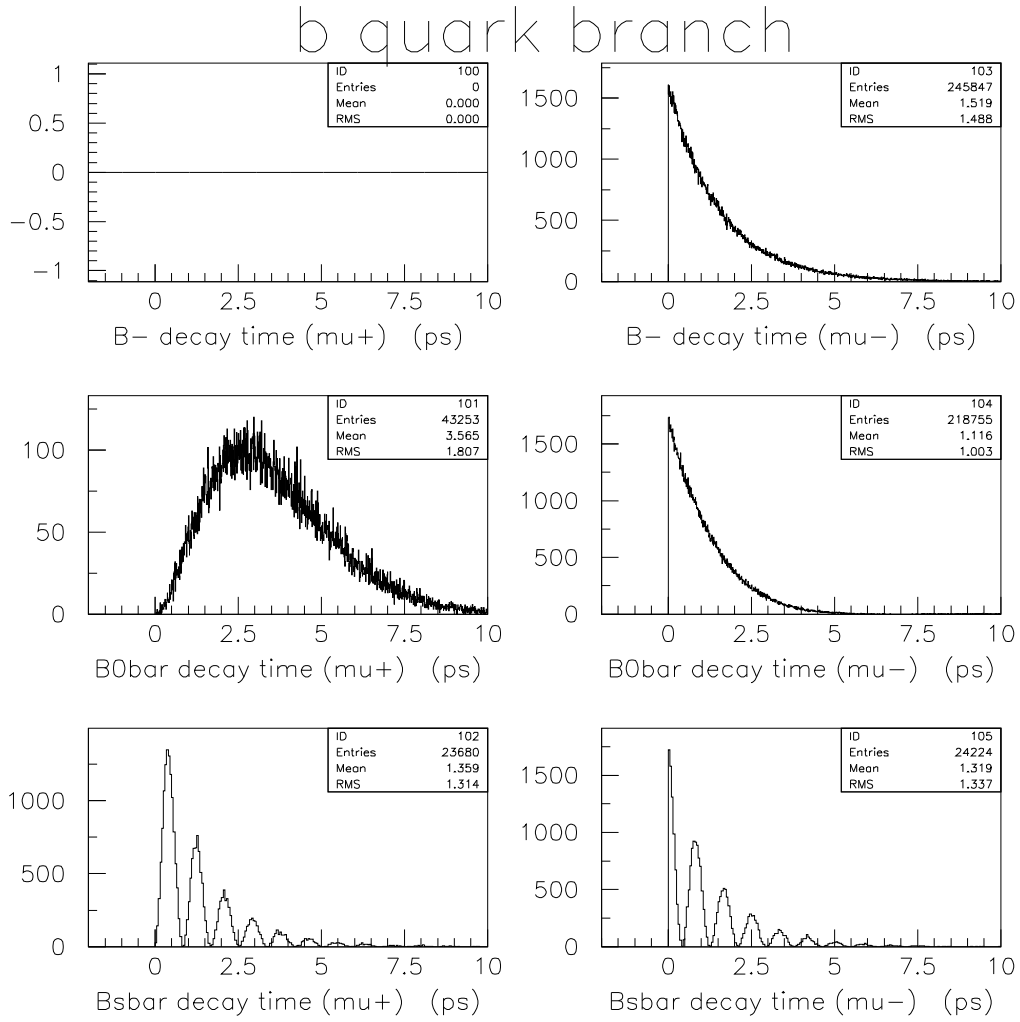

Figure 4.4. Proper time distribution of μ^+(left) and μ^-(right) emitted in semi-muonic decays of B^-(top), $\bar{B}^0$(centre) and $\bar{B}_s$(bottom) mesons.

Without mixing, all histograms on the left side would be empty. At time $t = 0$, when mixing does not yet occur, the right histograms reach the maximum, while those on the left are zero. For times larger than zero, the left $\bar{B}^0$ and $\bar{B}_s$ histograms become populated, due to oscillations before the decay. The distributions exponentially decrease with time, according to the lifetime of the relative meson. The exponential fit to the proper time distribution of B^- yields a lifetime which is in agreement with the PDG value of 1.564 ± 0.014 [ps] [2]. Note that for $\bar{B}_s$ mesons, the oscillations determine the sinusoidal shape of the proper time distribution since, unlike $\bar{B}^0$ mesons, mixing is faster than the decay.

Without B^0 mixing, the charge of the final state muon exclusively depends on the initial quark. It is positive for $\bar{b}$ decays and negative in the case of b decays. Since neutral B mesons oscillate, the charge of the final state muons depends also on the number of oscillations performed before the decay. Therefore, the total branching ratios of table 4.3 are distributed in the two muonic decay channels according to charge weighting factors. These factors are determined by a combination of B mixing and the probability of doubly charmed decays as discussed in the previous section. As a consequence of B mixing, part of the $bibj$ decays have a like-sign muon final state. For $bicj$ and $cicj$ decays, the total effect is a combination of doubly charmed b decays and B mixing, while $bici$ decays are not affected by mixing. The total branching ratio and corresponding charge factors, which are directly extracted from the Monte Carlo simulations, are reported in table 4.4.

Decay	BR $\cdot\theta$ ($\mu^+\mu^+$ or $\mu^-\mu^-$)	BR $\cdot(1-\theta)$ ($\mu^+\mu^-$)	Total BR	θ
$bibj$	0.0015	0.0066	0.0081	0.187
$bici$	0.0000	0.0171	0.0171	0
$bicj$	0.0121	0.0042	0.0164	0.742
$cicj$	0.0029	0.0064	0.0093	0.315
Total BR	0.0166	0.0343	0.0510	

Table 4.4. Branching ratio and charge weighting factors θ for double semi-muonic b decays. The quantity $BR \cdot \theta$ represents the branching ratio for the decay in like-sign muons. The quantity $BR \cdot (1-\theta)$ represents the probability of decay into oppositely charged muons.

4.2.2 Background

Prompt and detached J/ψ counts

In order to make an independent cross section measurement with respect to that reported in reference [22], we exclude the J/ψ mass region ($\pm\ 3.75\sigma$ away from the nominal mass). Still, events in the Gaussian tail of the resonance can be a source of background for this analysis. From Monte Carlo studies, we conclude that the probability to observe J/ψ particles produced on the target (prompt) is negligible. In reference [22], a signal of about $50\ \mathrm{J}/\psi$ produced in b decays is reported. Since the probability to observe events 3σ away from the mean is 0.3%, we should observe $0.2\ \mathrm{J}/\psi$ particles from b decays. Therefore, we shall neglect them.

Combinatorial background

Combinatorial background originates from random combinations of muon tracks reconstructed in our detector. Muons from pions, kaons and low mass resonance decays (ρ, ω and ϕ) contribute to such a background. We estimate the combinatorial background to a large fraction from data and partially with Monte Carlo simulations.

Double semi-muonic c decays

Most c quarks hadronise in long living mesons (at HERA-B D mesons travel in average a few centimeters in the laboratory frame before decaying) having large probabilities to decay into muons. Simultaneous muonic decays of primary $c\bar{c}$ pairs (see figure 4.5) represent an important background, which we evaluate with Monte Carlo simulations. Compared to $b\bar{b}$, the production of $c\bar{c}$ pairs in pA interactions at $\sqrt{s} = 41.6\ \mathrm{GeV}$ is more than three orders of magnitudes larger. Since the lifetime of charmed hadrons is one order of magnitude smaller, a lifetime cut, or any quantity related to it, allows to suppress such background.

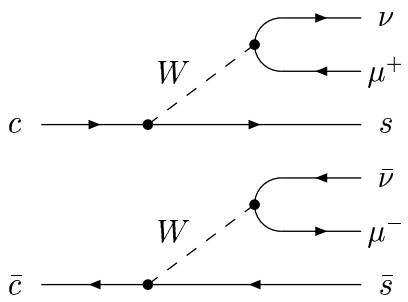

Figure 4.5. Feynman diagram of double semi-muonic $c\bar{c}$ decays.

Drell-Yan

The Drell-Yan process (figure 4.6) is an electromagnetic process in which a lepton pair is produced from quark-antiquark annihilation. Since the reaction is prompt, such leptons are expected to point back to the target. As a consequence, placing a cut on the impact parameter to the target allows to suppress such background. Even before the impact parameter requirement, the Drell-Yan background is expected to be at least 10 times less intense than the combinatorial background, in the region of dimuon invariant mass we are interested in. For this reason, we shall neglect it.

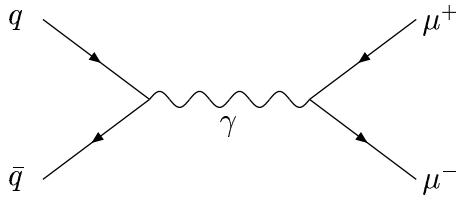

Figure 4.6. Feynman diagram of the Drell-Yan process.

4.2.3 Cross section formula

The formula we use to extract the beauty production cross section is

$$\sigma_{b\bar{b}} = \frac{N_{b\bar{b}}^{+-}}{\mathcal{L} \cdot A \cdot \sum_j \mathrm{Br}_j(b\bar{b} \to \mu\mu) \cdot (1-\theta_j) \cdot \varepsilon_{b\bar{b},j}^{+-}}, \tag{4.1}$$

where $N_{b\bar{b}}^{+-}$ represents the number of $b\bar{b}$ events extracted from unlike-sign muon data, $\mathcal{L}$ is the luminosity and A is the atomic weight of the target. The index j runs over the four double semi-muonic b decays $bibj$, $bici$, $bicj$ and $cicj$, each with its own branching ratio $\mathrm{Br}_j(b\bar{b} \to \mu\mu)$, charge factor θ_j and reconstruction efficiency $\varepsilon_{b\bar{b},j}^{+-}$. We recall that for each class of b decays, the branching ratio $\mathrm{Br}_j(b\bar{b} \to \mu\mu)$ include decays to $\mu^+\mu^-$ and $\mu^+\mu^+$ final states, while the charge weighting factors θ_j account for the probability that the final state is either $\mu^+\mu^-$ or $\mu^+\mu^+$. The branching ratios and charge factors can be found in table 4.4, the reconstruction efficiencies shall be determined from Monte Carlo simulations.

The luminosity is extracted from the yield of prompt J/ψ mesons,

$$\mathcal{L} = \frac{N_{\mathrm{J}/\psi}}{\sigma_{\mathrm{J}/\psi} \cdot A^{\alpha} \cdot \mathrm{Br}(\mathrm{J}/\psi \to \mu^+\mu^-) \cdot \varepsilon_{\mathrm{J}/\psi}}, \tag{4.2}$$

where $N_{\mathrm{J}/\psi}$ is the number of reconstructed J/ψ mesons, $\sigma_{\mathrm{J}/\psi}$ is the J/ψ cross section, α is the nuclear suppression, $\mathrm{Br}(\mathrm{J}/\psi \to \mu^+\mu^-)$ is the branching ratio and $\varepsilon_{\mathrm{J}/\psi}$ is the reconstruction efficiency.

The J/ψ cross section in the HERA-B acceptance ($-0.35 < x_{\mathrm{F}} < 0.15$ and $0 < p_T < 6$ GeV/c) is $\sigma_{\mathrm{J}/\psi} = 417 \pm 37$ nb/nucleon [22]. The nuclear suppression has been measured by the E866 collaboration and results $\alpha = 0.96 \pm 0.01$ [36]. Further details on the reference J/ψ cross section can be found in section 1.8. Note that for open $b\bar{b}$ and $c\bar{c}$ production no nuclear suppression is expected. If we substitute equation (4.2) in (4.1), by taking into account that the reconstruction efficiency depends on the specific target configuration, then we obtain

$$\sigma_{b\bar{b}} = \frac{N_{b\bar{b}}^{+-} \cdot \sigma_{\mathrm{J}/\psi} \cdot \mathrm{Br}(\mathrm{J}/\psi \to \mu^+\mu^-)}{X_{b\bar{b}}^{+-}}. \tag{4.3}$$

The term $X_{b\bar{b}}^{+-}$ is defined as

$$X_{b\bar{b}}^{+-} = \sum_i N_{\mathrm{J}/\psi,i} \cdot A_i^{1-\alpha} \cdot \frac{\sum_j \mathrm{Br}_j(b\bar{b} \to \mu\mu) \cdot (1-\theta_j) \cdot \varepsilon_{b\bar{b},j,i}^{+-}}{\varepsilon_{\mathrm{J}/\psi,i}}, \tag{4.4}$$

where i runs over 14 target configurations. The advantage of this procedure is that the systematic uncertainties due to the detector acceptance and performance, which are in first order identical for the reconstruction of all decays, cancel out to a large extent in the efficiency ratio of equation (4.4).

The number of $b\bar{b}$ events is obtained by subtracting the number $N^{+-}_{c\bar{c}}$ of double semi-muonic c decays and the number N^{+-}_{co} of combinatorial events from the oppositely charged muon pairs $N^{+-}_{\mu\mu}$ which survive the b selection. The combinatorial background is estimated from like-sign muons, as the difference between the number $N^{++}_{\mu\mu}$ of muon pairs in the data and the number of expected double semi-muonic b decays $N^{++}_{b\bar{b}}$ which survive the b selection. Therefore, we can write

$$N^{+-}_{b\bar{b}} = N^{+-}_{\mu\mu} - N^{+-}_{c\bar{c}} - (N^{++}_{\mu\mu} - N^{++}_{b\bar{b}}). \tag{4.5}$$

The charm background is estimated with Monte Carlo simulations. It is normalised to the number of direct J/ψ mesons. We use the formula

$$N^{+-}_{c\bar{c}} = \frac{\sigma_{c\bar{c}} \cdot \mathrm{Br}(c\bar{c} \to \mu^+\mu^-)}{\sigma_{\mathrm{J}/\psi} \cdot \mathrm{Br}(\mathrm{J}/\psi \to \mu^+\mu^-)} \cdot X_{c\bar{c}}, \tag{4.6}$$

where $\sigma_{c\bar{c}}$ is the charm cross section ($30\ \mu$b/nucleon) and $\mathrm{Br}(c\bar{c} \to \mu^+\mu^-)$ is the branching ratio for double semi-muonic c decays. The term $X_{c\bar{c}}$ is defined as

$$X_{c\bar{c}} = \sum_i N_{\mathrm{J}/\psi,i} \cdot A_i^{1-\alpha} \cdot \frac{\varepsilon_{c\bar{c},i}}{\varepsilon_{\mathrm{J}/\psi,i}}, \tag{4.7}$$

where i runs over 14 target configurations and $\varepsilon_{c\bar{c}}$ is the b selection efficiency for double semi-muonic c decays. As for the charm background, $N^{++}_{b\bar{b}}$ is estimated with Monte Carlo simulations and it is normalised to the number of J/ψ mesons,

$$N^{++}_{b\bar{b}} = \frac{\sigma_{b\bar{b}}}{\sigma_{\mathrm{J}/\psi} \cdot \mathrm{Br}(\mathrm{J}/\psi \to \mu^+\mu^-)} \cdot X^{++}_{b\bar{b}}, \tag{4.8}$$

where the term $X^{++}_{b\bar{b}}$ is defined as

$$X^{++}_{b\bar{b}} = \sum_i N_{\mathrm{J}/\psi,i} \cdot A_i^{1-\alpha} \cdot \frac{\sum_j \mathrm{Br}_j(b\bar{b} \to \mu\mu) \cdot \theta_j \cdot \varepsilon^{++}_{b\bar{b},j,i}}{\varepsilon_{\mathrm{J}/\psi,i}}. \tag{4.9}$$

If we assume that the reconstruction efficiencies for double semi-muonic b decays in the two final states are equal, for each decay in each target configuration ($\varepsilon^{++}_{b\bar{b},j,i} = \varepsilon^{+-}_{b\bar{b},j,i} = \varepsilon_{b\bar{b},j,i}$), than the cross section can be written in its final form

$$\sigma_{b\bar{b}} = \frac{\left(N^{+-}_{\mu\mu} - N^{++}_{\mu\mu}\right) \cdot \sigma_{\mathrm{J}/\psi} \cdot \mathrm{Br}(\mathrm{J}/\psi \to \mu^+\mu^-) - \sigma_{c\bar{c}} \cdot \mathrm{Br}(c\bar{c} \to \mu^+\mu^-) \cdot X_{c\bar{c}}}{X_{b\bar{b}}}, \tag{4.10}$$

where the term $X_{b\bar{b}}$ is defined as

$$X_{b\bar{b}} = \sum_i N_{\mathrm{J}/\psi,i} \cdot A_i^{1-\alpha} \cdot \frac{\sum_j \mathrm{Br}_j(b\bar{b} \to \mu\mu) \cdot (1 - 2\theta_j) \cdot \varepsilon_{b\bar{b},j,i}}{\varepsilon_{\mathrm{J}/\psi,i}}. \tag{4.11}$$

4.3 Monte Carlo simulations

We illustrate the Monte Carlo simulations used to evaluate the reconstruction efficiency of beauty and charm decays. The production of heavy quarks in pA collisions is simulated with PYTHIA [129, 130]. After the quark pair is generated, the fragmentation process is simulated with JETSET and the remaining energy is fed into FRITIOF [131, 132] to create secondary soft particles. Eventually, particles are tracked with GEANT 3 [133], which performs a simulation of all but one detector components. As explained in chapter 3, the first level trigger cannot be reproduced by Monte Carlo simulations. Therefore, the FLT efficiency is extracted from data.

4.3.1 Acceptance in $x_{\rm F}$ and p_T

Prompt J/ψ

The simulation of the hard process in the J/ψ production with PYTHIA contains the theoretical uncertainty due to the momentum cut-off imposed in perturbation theory. Correction factors are needed to reproduce the $x_{\rm F}$ and p_T distributions experimentally observed, especially at low transverse momenta. We use the results of the E789 experiment and implement the corrections as weight factors to the Monte Carlo events. Since the acceptance of the E789 experiment is restricted to the positive $x_{\rm F}$ region, while the HERA-B acceptance extends also to negative values, we assume a symmetric distribution around zero. The distributions given by PYTHIA are shown in figure 4.7, with and without the correction factors from E789.

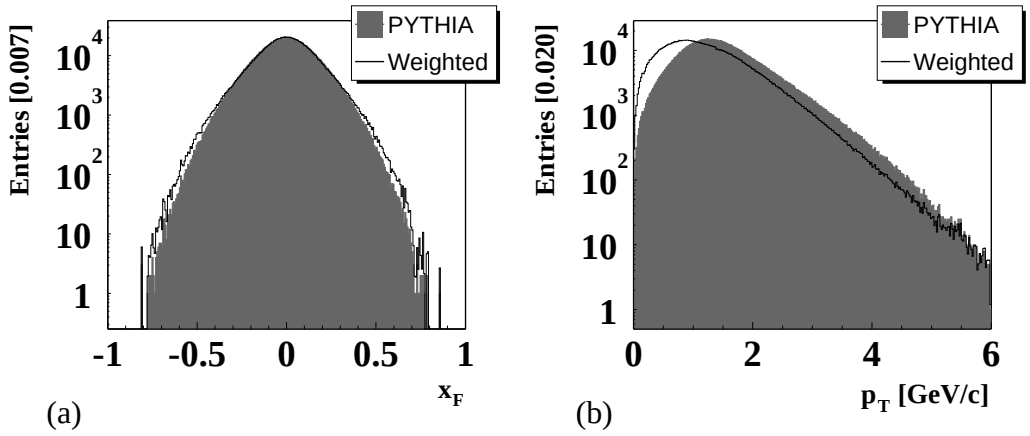

Figure 4.7. Generated and reconstructed $x_{\rm F}$ (a) and p_T (b) distributions of J/ψ mesons.

Note that the corrections are larger at low p_T. Generated and reconstructed $x_{\rm F}$ and p_T spectra (the trigger requirements are also included) are shown in figure 4.8.

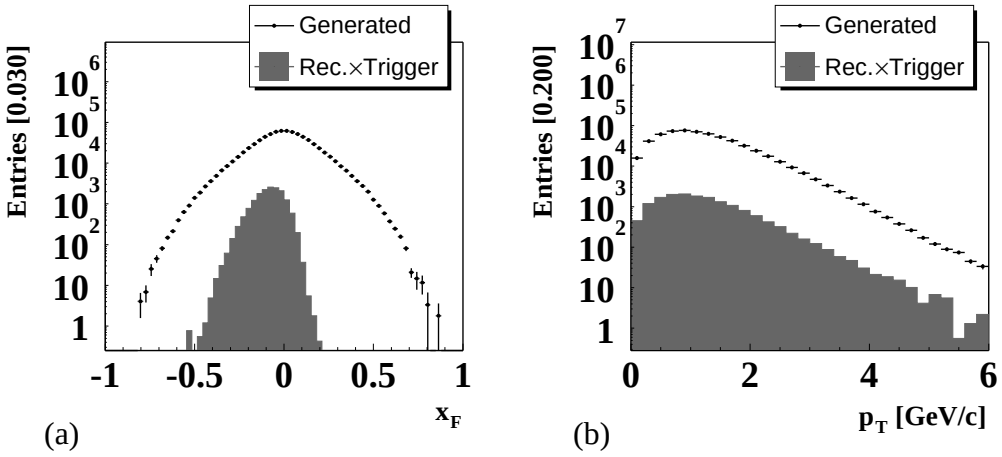

Figure 4.8. Generated and reconstructed x_{F} (a) and p_T (b) distributions of J/ψ mesons.

The x_{F} acceptance is limited in the positive region by the fact that the inner tracker, which is used to detect particles close to the proton beam pipe, was not used in the trigger, since it showed unstable performance during data taking. The x_{F} acceptance is limited in the negative region by the solid angle covered by the spectrometer (200 mrad in x and 160 mrad in y). Due to these limitations, we restrict the x_{F} range to $[-0.35, 0.15]$. The p_T acceptance has no restrictions between 0 and 6 GeV/c and exhibits an almost flat distribution. The x_{F} and p_T acceptance profiles are shown in figure 4.9.

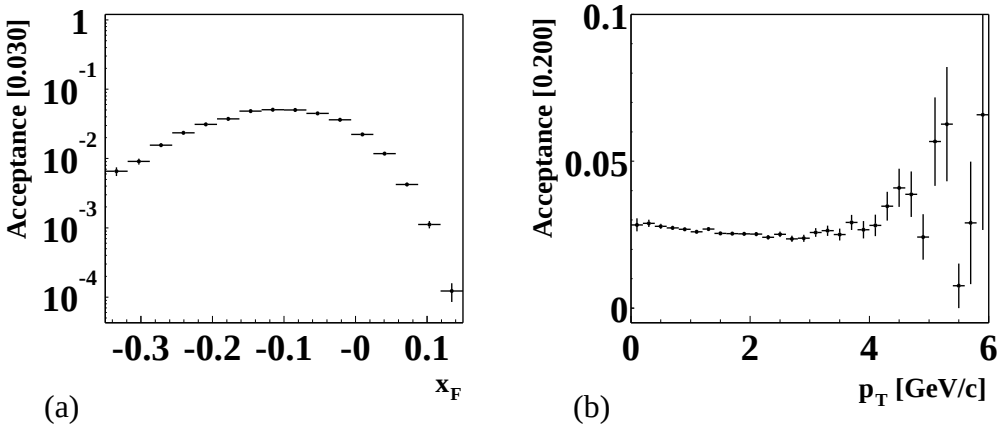

Figure 4.9. Acceptance profiles in x_{F} (a) and p_T (b) of J/ψ mesons.

Double semi-muonic b decays

Contrary to J/ψ decays, we adopt for double semi-muonic b decays the x_{F} and p_T distributions given by PYTHIA without any correction. The generated and reconstructed spectra of the leading muon (the one with the highest p_T) are shown in figure 4.10, while the corresponding acceptance profiles are shown in figure 4.11.

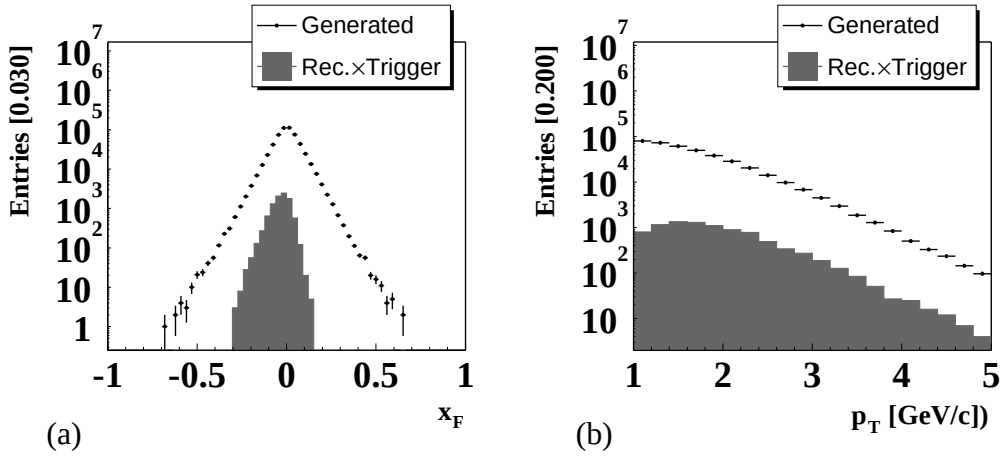

Figure 4.10. Generated and reconstructed x_{F} (a) and p_T (b) distributions of the leading muon in double semi-muonic b decays.

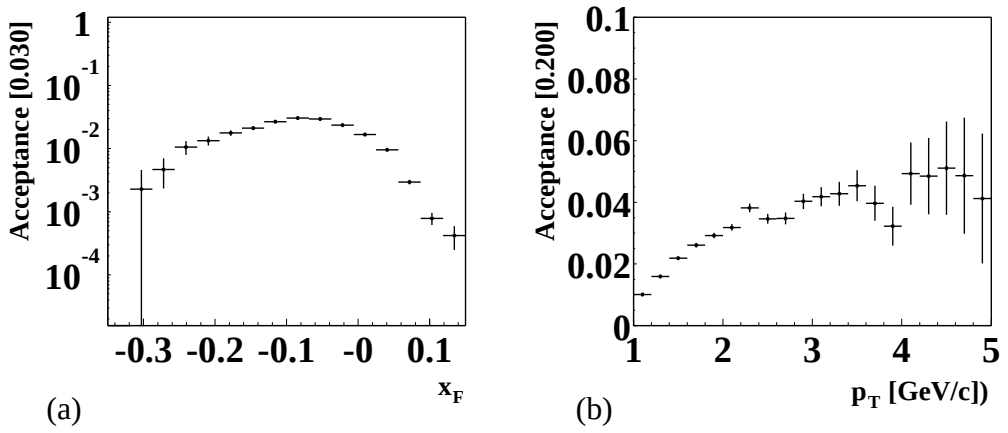

Figure 4.11. Acceptance profiles in x_{F} (a) and p_T (b) of the leading muon in double semi-muonic b decays.

The x_{F} acceptance is limited to the range $[-0.3, 0.1]$. The acceptance in p_T has no restrictions between 1 and $5\ \mathrm{GeV}/c$ (the cut at $1\ \mathrm{GeV}/c$ is the trigger threshold).

Double semi-muonic c decays

Also for double semi-muonic c decays we adopt the x_{F} and p_T distributions given by PYTHIA without any correction. The generated and reconstructed spectra of the leading muon are shown in figure 4.12, while the corresponding acceptance profiles are shown in figure 4.13.

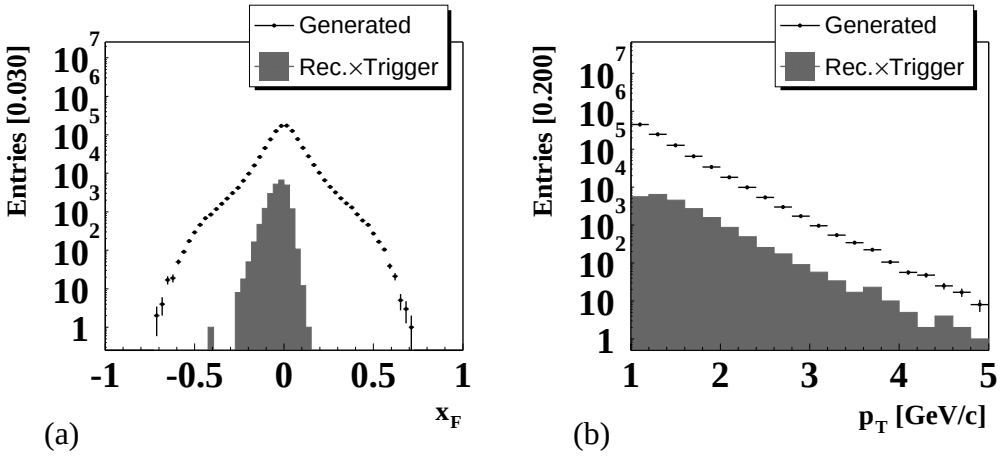

Figure 4.12. Generated and reconstructed x_{F} (a) and p_T (b) distributions of leading muon in double semi-muonic c decays.

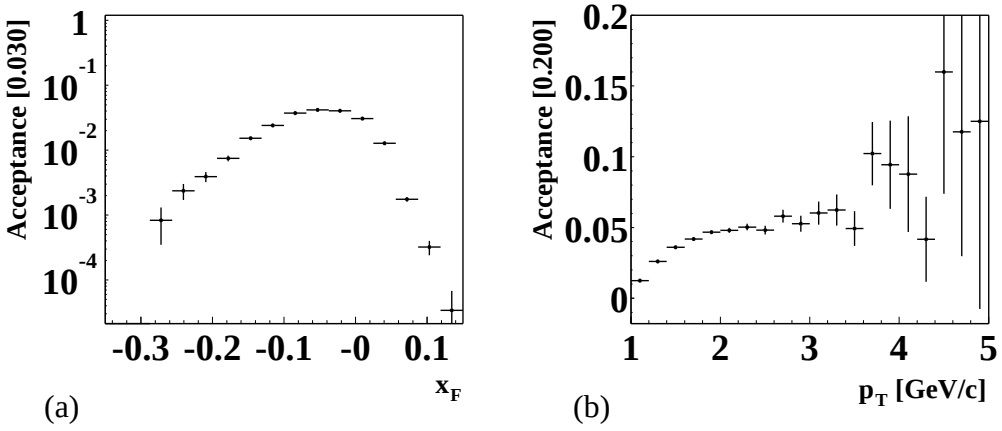

Figure 4.13. Acceptance profiles in x_{F} (a) and p_T (b) of the leading muon in double semi-muonic c decays.

The x_{F} acceptance is limited to the range $[-0.3, 0.1]$. The acceptance in p_T has no restrictions between 1 and $5\ \mathrm{GeV}/c$ (the cut at $1\ \mathrm{GeV}/c$ is the trigger threshold).

4.3.2 Reconstructed samples

Data for physics analysis were taken with 9 target configurations, four with one wire ($i2$, $b1$, $b2$, $o2$) and five with two wires ($i2i1$, $b1i1$, $b1i2$, $b1b2$, $b1o2$). The letter indicates the wire position (i for inner, b for below, o for outer). The number specifies the target station. The target system was described in section 2.4. Since the reconstruction efficiency depends on the specific target configuration, different Monte Carlo simulations are needed. Double wire runs are simulated with two samples, depending on which wire the hard process is located, leading to the 14 Monte Carlo samples listed in table 4.5.

Wire	J/ψ	$bibj$	$bicj$	$cicj$	$bici$	$c\bar{c}$
$i2$	613142	563663	610822	199806	572913	987491
$i2i1$	618874	564492	611961	200463	573719	988485
$i1i2$	601646	520007	567542	184552	529278	596664
$i1b1$	588099	436224	476296	154688	444262	372771
$b1i1$	541388	324323	351693	114700	329267	990205
$b1i2$	596413	325841	353266	115028	330855	990221
$b1b2$	543553	325505	353060	115079	330498	990281
$b1o2$	548226	340166	368822	119602	345678	1003504
$b1$	487318	325468	352833	114893	330469	990187
$i2b1$			Simulated with $i2i1$			
$b2b1$			Simulated with $i1i2$			
$o2b1$			Simulated with $i1i2$			
$b2$			Simulated with $i2$			
$o2$			Simulated with $i1i2$			

Table 4.5. Statistics of Monte Carlo samples used for the present analysis.

For instance, the two samples associated with the $i1i2$ configuration are called $i1i2$ and $i2i1$, where the hard process is generated on the first wire and a minimum bias event takes place on the second wire. The simulation of b and c muonic decays are available only for part of the target configurations listed in table 4.5. As Monte Carlo simulations of the missing target configurations, we use the existing ones with the same material. This means that we use the same Monte Carlo simulation for wires with different orientation, sometimes also located on different stations.

Once every month the experiment was shut down for a few days in order to access the detector area. In this period, all efforts were concentrated to improve the detector performance, leading to a general change of the running conditions. For this reason different Monte Carlo samples are generated on a monthly basis, to provide a better detector simulation.

4.4 Data analysis

For the data analysis we use 150 million dilepton triggered events of proton-nucleus interactions with three wire targets of different materials (carbon, titanium and tungsten). Events are distributed over several runs. The following ones are discarded:

- runs with low statistics;
- runs for efficiency study;
- runs for trigger test;
- runs with anomalous data quality distributions;
- runs with wrong interaction rate;
- runs with broken targets;
- runs with missing detector subsystems.

A list of the runs selected for this analysis can be found in appendix A. The analysis is carried out in the HERA-B analysis framework, called ARTE, with the reprocessing version "rp0005".

4.4.1 Dilepton trigger

The main motivation which lead to the final choice of the HERA-B trigger configuration is the study of charmonium production in pA interactions.

A dilepton trigger configuration increases the probability to select events in which a J/ψ meson is produced, compared to randomly triggered events. Decays like $\mathrm{J}/\psi \to l^+l^-$ are triggered when a pair of leptons is found in a three level trigger chain. At pretrigger level, two seeds are required, either from the muon chambers or from the electromagnetic calorimeter. They are passed to the first level trigger where the full reconstruction of at least one track is required. At the second level trigger, an independent search for a pair of lepton tracks is performed. The event is finally accepted when a common vertex, which lies in a region close to the target position, is found.

This trigger configuration allowed to collect an average of 1200 J/ψ per hour, in both lepton channels, at 5 MHz interaction rate.

4.4.2 Muon selection

The last detector subsystem in the downstream direction (with respect to the target) is used for muon identification. Tube and pad gas chambers are used to reveal the passage of muons through the detector. Thick iron absorbers are placed in front of the chambers in order to filter all particles but muons, allowing for a clean muon identification. Therefore, a set of soft selection criteria suffices to guarantee a proper muon identification.

Specifically, a muon candidate must have:

- an SLT flag;
- standard clone removal;
- at least 5 hits in the vertex detector;
- at least 15 hits in the outer tracker;
- a probability χ^2 of the track fit larger than 0.3%;
- momentum between 5 and 200 GeV/c;
- transverse momentum larger than 0.7 GeV/c;
- at least 9 hits in the muon chambers;
- a muon likelihood larger than 0.05.

All requirements listed above, except for the SLT flag and the muon likelihood, are indicated in the following as "track quality".

The SLT flag is used to label tracks that are found on-line by the SLT and off-line by the track reconstruction algorithm. The SLT flag is mandatory to get a correct estimate of the SLT efficiency from the Monte Carlo simulation. Suppose that a J/ψ decays into two muons and the SLT triggers on muons different from the ones produced in the J/ψ decay. In this case, the SLT efficiency depends on the characteristics of the whole event, which are usually difficult to simulate. In order to remove this dependence, we require the SLT flag both in the data and the Monte Carlo. The main task of the track reconstruction algorithm is to collect the track segments provided by the several detector subsystems and to combine them in a unique set of tracks corresponding to the trajectories of the physical particles through the detector. When the same track segment is used more than once by the reconstruction algorithm, tracks which do not correspond to a physical particle are generated. We shall label such tracks "clones". In order to avoid the occurrence of clone tracks, we use in this analysis the standard routine developed by the HERA-B collaboration (see reference [134]), which reject tracks sharing segments with other tracks. A minimal amount of hits in the tracking system, together with a lower limit set on the probability χ^2 of the track fit, allows to reject ghost tracks. These tracks are typically generated by the occurrence of a few random hits in the tracking system. Since real muons traversing the absorber walls have momentum larger than 4.5 GeV/c, a lower limit on their momentum rejects possible unphysical tracks. In addition, the latter cut suppresses muons that are not produced in the decay of heavy quarks. The upper limit on the momentum rejects unphysical tracks having an energy larger than the one expected in our experiment. Finally, the definition of the likelihood probability is based on the comparison of the parameters of the reconstructed segments in the main tracker to those of the muon system. A lower limit set on the muon likelihood, together with a minimal number of hits in the muon chambers, guarantees a higher probability to select real muon tracks rather than ghost tracks.

4.4.3 Primary vertex reconstruction

For several purposes, it is interesting to know the position where the main interaction takes place. Since HERA-B is a fixed target experiment, the interaction between protons and nuclei takes place on the target, whose position is well known. The targets used in this experiment are either ribbons or wires. Both targets have one dimension dominant with respect to the others. The z coordinate is always well known, while the precision of the other coordinates depends on the orientation of the target. In order to establish with high precision both the x and y coordinate, we combine the tracks reconstructed in the event, in order to determine the position of the primary vertex. Not all tracks can be used for this purpose. For instance, muons produced in the decay of long living particles typically have large impact parameters to the primary vertex. These tracks must be excluded from the primary vertex search because they would artificially shift its position downstream.

A target wire is associated to the primary vertex with the minimisation of the quantity

$$\chi = \sqrt{\left(\frac{\Delta_x}{\sigma_x}\right)^2 + \left(\frac{\Delta_z}{\sigma_z}\right)^2}, \tag{4.12}$$

where Δ_x is the difference between the x coordinate of the target and primary vertex, σ_x is the uncertainty of this difference. Depending on the orientation of the target, the x subscript has a different meaning. When the target is oriented vertically x remains the x coordinate, while when the target is oriented horizontally, x denotes in fact the y coordinate. Note that σ_x is dominated by the uncertainty in the position of the primary vertex.

A target wire is also associated to the dimuon. For single target runs this is trivial, while for double target runs we minimise the quantity

$$\chi = \sqrt{\left(\frac{I_w^{\mu^+}}{\sigma_{I_w^{\mu^+}}}\right)^2 + \left(\frac{I_w^{\mu^-}}{\sigma_{I_w^{\mu^-}}}\right)^2 + \left(\frac{I_w^{\mathrm{J}/\psi}}{\sigma_{I_w^{\mathrm{J}/\psi}}}\right)^2}, \tag{4.13}$$

where $I_w^{\mu^+}$, $I_w^{\mu^-}$ and $I_w^{\mathrm{J}/\psi}$ are the impact parameters to the target of μ^+, μ^- and J/ψ respectively. The impact parameter is defined as the distance between the particle and the target in the plane of the target perpendicular to the beam. In order to take into account errors on the position of the target and on the track parameters, each impact parameter is divided by the corresponding uncertainty.

Following a similar procedure, a primary vertex is also assigned to the dimuon. In case the target wire associated to the primary vertex and the one associated to the dimuon are different, the event is rejected. Sometimes it happens that muons point to a primary vertex that is different from the one assigned to the target. Rejecting these events (less than 1% of the total muon pairs) helps to reduce background in the selection of real decays.

4.4.4 The J/ψ selection

Once the muons are identified with the prescription given in section 4.4.2, a vertex fit is performed with the Grover vertex package [112]. The following requirements allow to complete the selection of J/ψ decays:

- muons with the largest p_T;
- x_F between -0.35 and 0.15;
- probability χ^2 of the dimuon vertex fit larger than 1%.

Less than 10% of the events have more than two muons. In these cases, we select those muons that have the largest p_T, occasionally dubbed as "Best muons", since muons coming from heavy quarks decays preferentially have large transverse momenta. The second requirement removes badly reconstructed tracks falling outside the detector acceptance. The third cut improves the selection of tracks coming from a common vertex over the random combinations of muons.

The dimuon invariant mass after J/ψ selection is shown in figure 4.14.

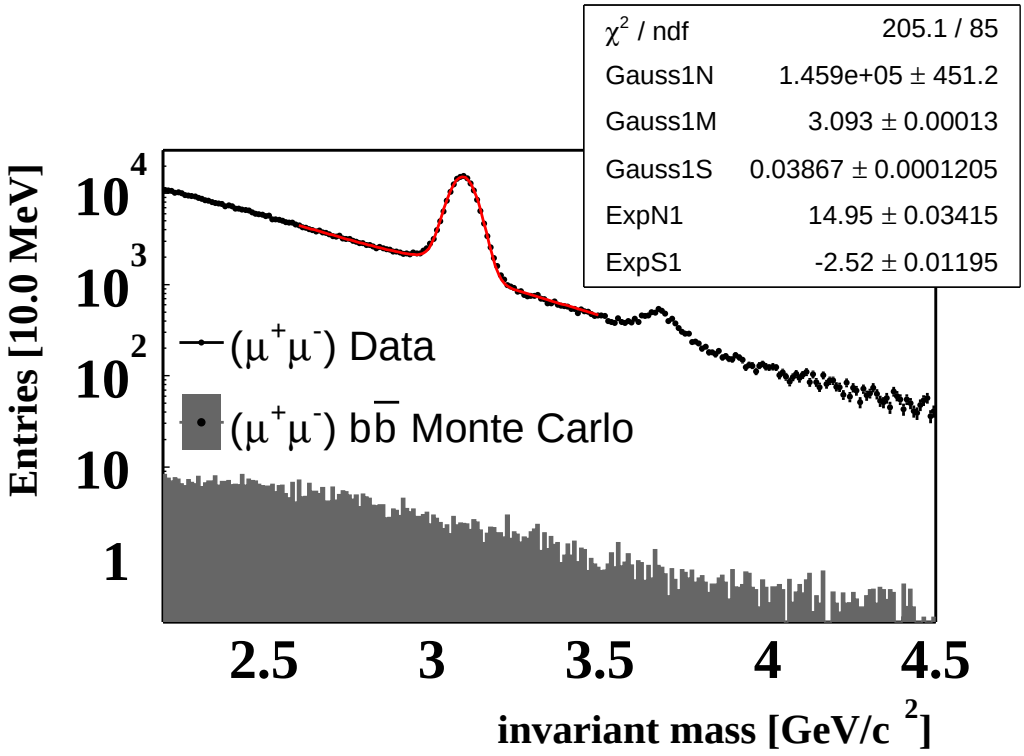

Figure 4.14. Invariant mass of unlike-sign muons in the full data sample after J/ψ selection (dotted histogram). Two peaks emerge above the background (J/ψ and ψ'). The fit to the J/ψ peak is superimposed. The shadowed histogram is the Monte Carlo simulation of double semi-muonic b decays under the assumption that $\sigma_{b\bar{b}} = 15$ nb/nucleon.

The prominent signal around $3.1\ \mathrm{GeV}/c^2$ corresponds to the J/ψ particle, while the less intense peak visible at $3.7\ \mathrm{GeV}/c^2$ is due to the ψ'. The width of the signal is dominated by the experimental mass resolution, which is much larger than the intrinsic width of the J/ψ. The Monte Carlo simulation of semi-muonic b decays is also shown in figure 4.14, under the assumption that the $b\bar{b}$ cross section is $15\ \mathrm{nb}/\mathrm{nucleon}$. The latter value has been extracted by the collaboration in a different analysis [22]. Note that, at this stage of the selection, the fraction of muons originating from b quark decays is negligible. In order to obtain the correct number of reconstructed J/ψ mesons, the spectrum has to be fitted with a function that describes sufficiently well the mass profile around $3.1\ \mathrm{GeV}/c^2$.

The background is fitted with the exponential function

$$N(m) = A \cdot e^{-Bm}. \tag{4.14}$$

A simple Gaussian is not enough to fit the signal, especially at low masses, where the mass distribution is affected by $\mathrm{J}/\psi \to \mu^+\mu^-\gamma$ decays. The emission of photons, in fact, causes a loss of energy and, as a consequence, lower reconstructed muon momenta. This effect translates in a lower dimuon invariant mass and explains the tail visible in the J/ψ mass distribution[3]. The study of a suitable fit function to account for the tail can be found in reference [135], where the function used to fit the J/ψ peak is

$$N(m) = N \cdot \left[(1-\epsilon_{rad}) \cdot G(m|M,\sigma) + \epsilon_{rad} \cdot N(\sigma) \cdot \mathcal{P}(m|M,\sigma)\right], \tag{4.15}$$

where N is the number of J/ψ events and ϵ_{rad} defines the contribution of the tail relative to the total mass spectrum. The function $G(m|M,\sigma)$ is a simple Gaussian distribution,

$$G(m|M,\sigma) = \frac{1}{\sqrt{2\pi}\sigma} e^{-\frac{(m-M)^2}{2\sigma^2}}, \tag{4.16}$$

where M and σ are respectively the mean and the width of the distribution. The function $\mathcal{P}(m|M,\sigma)$ is defined as

$$\mathcal{P}(m|M,\sigma) = \begin{cases} G(m|M,\sigma), m > m_{th} \\ \\ C \cdot G(m|M,\sigma(m)), m < m_{th}. \end{cases} \tag{4.17}$$

Here, m_{th} is the threshold mass for the tail description and C is a constant. The parameters C and m_{th} are determined by imposing the continuity of $\mathcal{P}(m|M,\sigma)$ and its first derivative in m_{th}. For masses larger than m_{th}, $\mathcal{P}(m|M,\sigma)$ is a simple

[3]Since the reconstructed J/ψ particles with a mass lower than the centre value originate from the energy loss due to photon emission, the tail is labelled "radiative".

Gaussian. For masses smaller than m_{th}, it is a Gaussian with a mass dependent width $\sigma(m)$. The mass dependence is parameterised with

$$\sigma(m) = \sum_i a_i^2 (M - m)^i, \tag{4.18}$$

where a_i are constants. The remaining parameters in equation (4.15) are M, σ and a_i. They are determined from the best fit to the experimental mass distribution. The factor $N(\sigma)$ serves as normalisation. It is defined as

$$N(\sigma) = \frac{1}{\int \mathcal{P}(m|\sigma) dm}. \tag{4.19}$$

The result of the mass fit is superimposed to the histogram in figure 4.14. The peak position is 3.0928 ± 0.0001 GeV/c^2. It differs by 4 MeV/c^2 from the PDG value (3.096916 ± 0.000011 GeV/c^2[2]). This effect could be due to a misalignment between vertex detector and main tracker affecting the reconstruction of muon momenta. The effect is visible in the J/ψ peak due to the large statistics, but it can be safely neglected for b events.

Reconstruction efficiency

The muon and J/ψ selection efficiencies are determined with Monte Carlo simulations. The agreement between data and simulated distributions is important to correctly estimate the efficiency. The comparison for the vertex probability and muon likelihood are shown in figure 4.15.

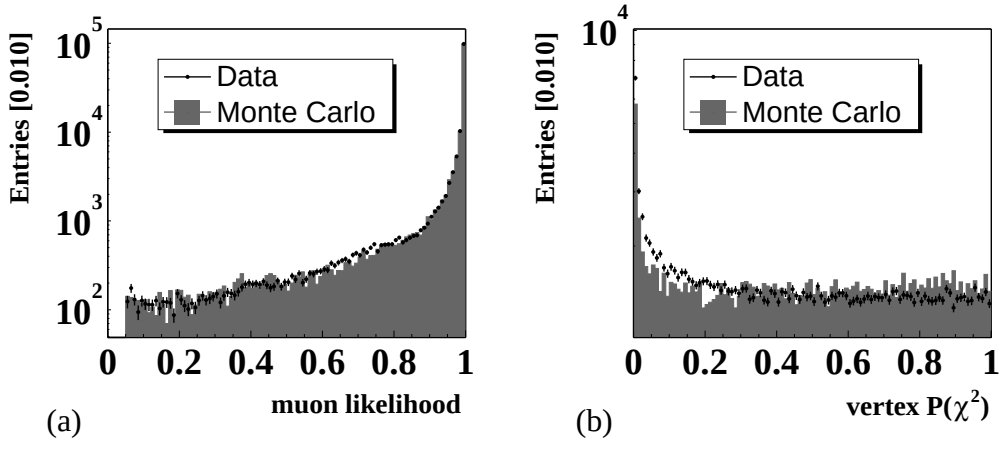

Figure 4.15. Comparison between data and Monte Carlo simulations of the muon likelihood (a) and the J/ψ vertex probability (b).

The muon likelihood is shown only for values larger than the cut applied in the preselection (0.05). The agreement is satisfactory in the entire range displayed. The efficiency of each cut relative to the previous one is reported in table 4.6.

Selection	Efficiency
Reco.$\times$Trig.	0.024
FLT weight	0.511
Target assignment	0.985
SLT flag	0.941
Track quality	0.938
Muon likelihood	0.975
Best muons	0.983
$x_{\rm F}$ $[-0.35, 0.15]$	1.000
Vertex $P(\chi^2)$	0.962
Total	$(0.999 \pm 0.008) \cdot 10^{-2}$

Table 4.6. Efficiency for prompt J/ψ selection in the Monte Carlo simulation of the full data sample. Each efficiency is calculated with respect to the previous one.

In table 4.7 we report rate, mass, width and total selection efficiency for the J/ψ signal in each target configuration.

Target	$N_{\mathrm{J}/\psi}$ $[10^3]$	$m_{\mathrm{J}/\psi}$ [GeV/c^2]	$\sigma_{\mathrm{J}/\psi}$ [MeV/c^2]	efficiency $[10^{-2}]$
$i2$	27.21 ± 0.19	3.0938 ± 0.0003	40.00 ± 0.28	1.0216 ± 0.013
$i2i1$	8.60 ± 0.11	3.0914 ± 0.0005	37.60 ± 0.46	0.9110 ± 0.012
$i1i2$	8.36 ± 0.11	3.0913 ± 0.0006	38.40 ± 0.53	0.8636 ± 0.012
$i1b1$	8.76 ± 0.12	3.0902 ± 0.0006	38.42 ± 0.51	0.6718 ± 0.011
$b1i1$	8.47 ± 0.11	3.0903 ± 0.0005	38.26 ± 0.48	0.7103 ± 0.012
$b1i2$	9.99 ± 0.12	3.0933 ± 0.0005	38.07 ± 0.44	1.6073 ± 0.016
$i2b1$	7.76 ± 0.10	3.0928 ± 0.0005	37.89 ± 0.49	Simulated with $i2i1$
$b1b2$	3.58 ± 0.07	3.0945 ± 0.0008	37.69 ± 0.73	1.3351 ± 0.016
$b2b1$	4.66 ± 0.08	3.0948 ± 0.0008	39.99 ± 0.76	Simulated with $i1b1$
$b1o2$	17.75 ± 0.15	3.0930 ± 0.0004	38.07 ± 0.33	1.4010 ± 0.016
$o2b1$	20.18 ± 0.17	3.0930 ± 0.0004	38.69 ± 0.33	Simulated with $i1b1$
$b1$	9.18 ± 0.11	3.0921 ± 0.0005	37.67 ± 0.46	1.7192 ± 0.019
$b2$	7.92 ± 0.11	3.0953 ± 0.0006	39.91 ± 0.53	Simulated with $i2$
$o2$	3.67 ± 0.07	3.0945 ± 0.0009	39.39 ± 0.84	Simulated with $i1b1$
All	145.94 ± 0.45	3.0928 ± 0.0001	38.67 ± 0.12	0.999 ± 0.008

Table 4.7. Rate, mass and width of the J/ψ signal observed in each target configuration.

We recall that events without tracks in common between the FLT and SLT are discarded. As explained in section 3.4, this is compulsory to obtain a correct trigger efficiency and implies the rejection of about 10% of the data.

4.4.5 Combinatorial background

Before discussing the selection criteria and their optimisation, we give a short explanation of the method we use to estimate one of the most important sources of background for double semi-muonic b decays: the combinatorial background. We demonstrate that like-sign muons can be used to estimate the combinatorial background in the oppositely charged muon channel.

The invariant mass spectra after J/ψ selection are shown in figure 4.16(a).

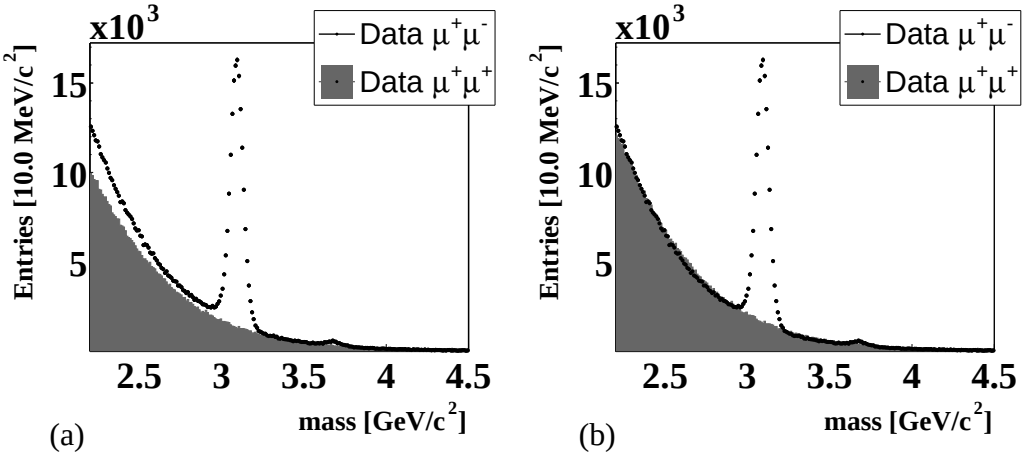

Figure 4.16. Invariant mass of unlike-sign and like-sign muons, before (a) and after (b) normalisation to the upstream detachment spectrum.

The unlike-sign spectrum exhibits the J/ψ peak around $3.1\ \mathrm{GeV}/c^2$. As expected, no resonance is visible in the like-sign channel.

The mass spectra of unlike-sign and like-sign muons, far from the J/ψ and ψ' resonances, are dominated by combinatorial background. Therefore, they are expected to be similar. On the contrary, especially at low masses, the distributions look different. This could be due to the fact that unlike-sign muons are preferentially bent towards opposite halves of the detector by the magnetic field, while like-sign muons go into the same part of the detector. A discrepancy in the behaviour of the two detector halves might produce different mass distributions. The discrepancy disappears when the two mass spectra are normalised to the upstream side, according to the procedure given in the next section. The invariant mass distributions after normalisation are shown in figure 4.16(b).

The agreement between the spectra in the region far from the resonances is improved, even though a discrepancy at low masses can still be observed.

Normalisation procedure

The normalisation is performed by looking at the position of dimuon vertices relative to the target along the beam axis (Δz).

Depending on the experimental spatial resolution, which is typically 500 μm for primary vertices, a vertex is consistent with the target position for short living particles and is downstream for long living particles. Upstream vertices cannot be due to the decay of real particles, but only to random combinations of muons. Contrary to the case of downstream vertices, they are expected to be identical for like-sign and unlike-sign muons. As shown in figure 4.17(a), the Δz distributions in the two channels are different.

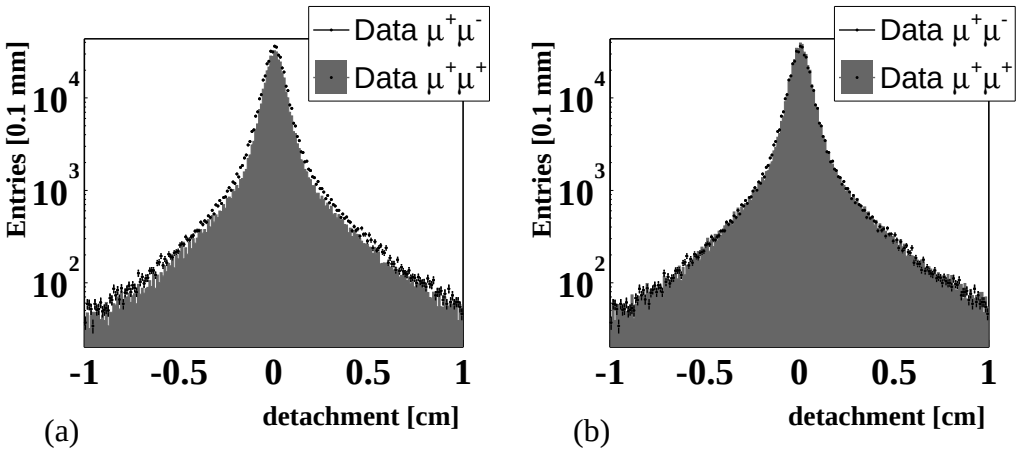

Figure 4.17. Dimuon vertex detachment before (a) and after (b) normalisation to the upstream spectrum.

The plot shows that like-sign muons underestimate the combinatorial background in the unlike-sign channel. For this reason, we normalise the two spectra to the upstream side ($\Delta z < -0.2$ mm), where they are expected to be identical. The result is shown in figure 4.17(b).

We conclude that, apart from small deviations, the normalisation procedure allows to use downstream like-sign muons to estimate the combinatorial background in the unlike-sign channel. We must keep in mind that, with more stringent selection criteria, the downstream like-sign spectrum might be affected by the decay of long living particles. This contribution must be subtracted, in order to get the correct estimate of the combinatorial background (see section 4.2.3).

4.4.6 Double semi-muonic b decays

Our attempt to identify double semi-muonic b decays at HERA-B starts from the prompt J/ψ selection presented in section 4.4.2. However, we remove the requirements on x_F and χ^2 probability of the dimuon vertex. The quality of the dimuon vertex is not necessarily sufficient to justify a selection on a large χ^2 probability. In order to suppress background in favour of double semi-muonic b decays, we investigate further the characteristics of the muon tracks and dimuon vertices. We give the motivations which lead us to the choice of the selection variables and we discuss the algorithm used to optimise them.

Track χ^2 probability

A large contribution to the combinatorial background comes from muonic decays of kaons and pions. Due to the kinematics of the two body decay, the angle between the emitted muon and the mother particle is small. Therefore, the track reconstruction algorithm is not able to distinguish between mother and daughter particles and merge them into a single track. The global effect is a larger χ^2, compared to the average reconstructed tracks, hence a smaller χ^2 probability. A lower limit on the χ^2 probability of the track will help to reduce the combinatorial background.

Kaon likelihood

Another possibility to reduce background from muonic kaon decays is to look at the kaon likelihood of the track. As explained in section 4.4.2, the most important requirement for the muon identification is a signal in the muon chambers. This is the last detector subsystem along the particle direction of motion and it is preceded by the RICH detector, which allows kaon identification. If a kaon decays between the RICH and MUON systems, then the emitted muon, which is reconstructed as a single track with the mother kaon, leaves a signal in both detectors. This results in a class of tracks that are simultaneously identified as muons and kaons. Setting an upper limit on the kaon likelihood of the track will help to suppress this background.

Transverse momentum

In b decays, the large mass of the mother quark causes decay products with large transverse momenta. As a consequence, muons emitted in b decays are expected to have larger transverse momenta, compared to the more abundant muons produced in the decays of lower mass particles. Since c quarks are lighter than b quarks, muons emitted in c decays have smaller transverse momenta, in average, compared to those emitted in b decays. A lower limit on the transverse momentum will help to suppress combinatorial background and double semi-muonic c decays.

Impact parameter

Most muons point back to the position where the primary interaction takes place. In other words, most muons have an impact parameter to the target consistent with zero, within the spatial resolution. Muons from b decays can have a large impact parameter to the target. The impact parameter of the emitted muons, in fact, is correlated with the lifetime of the decaying particle. The longer the lifetime of the decaying particle, the larger is the impact parameter of the emitted muon. As a consequence, a lower limit cut on the impact parameter of the muon will help to discriminate muons produced in b decays from combinatorial background, and also from double semi-muonic c decays, since charmed mesons have a smaller lifetime than B mesons. Note that, to a good approximation, the impact parameter does not depend on the momentum of the emitted particle. The increase in impact parameter due to a large particle momentum is compensated by an increased boost, which determine a smaller decay angle in the laboratory frame and, as a consequence, a smaller impact parameter. In order to use the full information provided by the track reconstruction algorithm, we select on the significance of the impact parameter. The significance is expressed as ratio of the impact parameter over its uncertainty and takes into account uncertainties on the track parameters.

Vertex detachment

In the strongly boosted pA interactions at HERA-B, a combination of tracks coming from two different long living particle decays produce a vertex preferentially located downstream of the target. The quality of this vertex is usually poorer than that of vertices originating from real particle decays. A suitable example is the case of semi-muonic decay of two B mesons. Since the standard algorithm used for vertexing (GROVER) might occasionally fail to find these vertices, we shall not use it for b event selection. We rather use a simple algorithm that associates a vertex to each track pair, neglecting the uncertainty on the track parameters. We define the position of the vertex along the beam axis as the point of minimum distance between the two tracks, in the plane perpendicular to the beam axis. This algorithm allows to investigate the position of the vertices to identify b events, without the unwanted efficiency loss produced by GROVER.

4.4.7 Cut optimisation

The cut optimisation for double semi-muonic b decays is done searching for the cut values that simultaneously maximise the signal efficiency and the background rejection. We apply the prescriptions of the so called “blind analysis”, in the sense that signal and background are estimated with Monte Carlo simulations or, if needed, with the fraction of data that does not contain the signal we are looking for. The “blind analysis” has the advantage of removing the possible bias due to the presence of signal events in the data sample used for optimisation.

The quantity we optimise is the signal significance

$$S = N_{b\bar{b}}^{+-} / \sqrt{N_{b\bar{b}}^{+-} + N_{c\bar{c}}^{+-} + N_{co}^{+-}}, \tag{4.20}$$

where $N_{b\bar{b}}^{+-}$, $N_{c\bar{c}}^{+-}$ and N_{co}^{+-} are respectively the number of $b\bar{b}$, $c\bar{c}$ and combinatorial background events surviving the selection, assuming $\sigma_{b\bar{b}} = 15$ nb/nucleon and $\sigma_{c\bar{c}} = 30$ μb/nucleon. The numbers $N_{b\bar{b}}^{+-}$ and $N_{c\bar{c}}^{+-}$ are extracted from Monte Carlo simulations with equations (4.5) and (4.6). The number N_{co}^{+-} is obtained from data, with the prescription given in section 4.4.5.

The entire data sample is simulated by mixing the Monte Carlo simulations of different target configurations. Each sample is weighted according to the relative luminosity. The latter is calculated as ratio of the number of J/ψ events over the corresponding reconstruction efficiency (table 4.7). The systematic effect due to a possible dependence of the luminosity ratio on the target material is neglected.

The first two selection criteria, which we independently optimise, are the track probability χ^2 and the kaon likelihood of the muon candidates. An independent optimisation is possible only when the two variables are not correlated. Therefore, we show the corresponding correlation plots in figure 4.18.

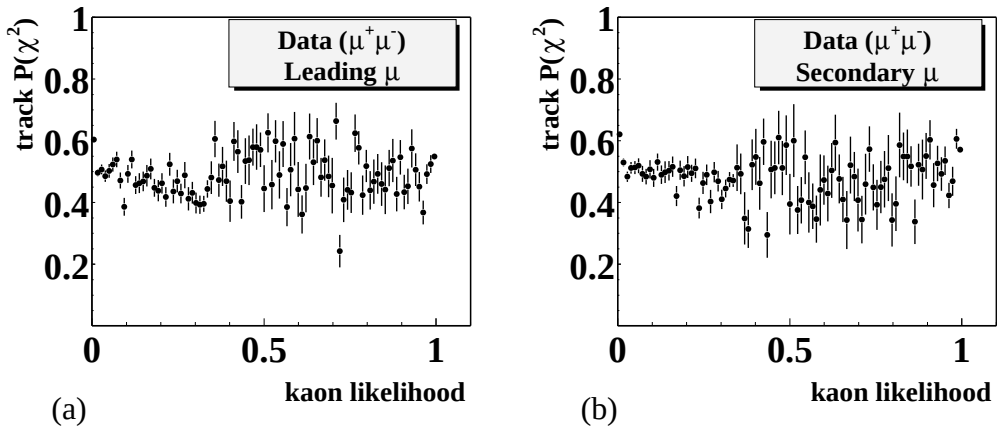

Figure 4.18. Track P(χ^2) as a function of the kaon likelihood for the leading (a) and secondary (b) muon.

The track P(χ^2) is essentially a constant function of the kaon likelihood. This proves that the variables are uncorrelated and can be separately optimised. The significance as a function of the lower limit imposed to the track P(χ^2) is plotted in figure 4.19(a). In the same plot, we show the dependence of the expected rate of semi-muonic $b\bar{b}$ and $c\bar{c}$ decays and the combinatorial background as a function of the probability cut. For this purpose, we use the charm production cross section of 30 μb/nucleon and we assume a beauty production cross section of 15 nb/nucleon. All histograms are normalised to the maximum value obtained in the optimisation

range. The significance is maximum for a probability larger than 0.04. This value is more than one order of magnitude higher than the cut applied in the J/ψ selection (P(χ^2) > 0.003). Keeping the optimised cut on the probability χ^2 of the track, we investigate the effect of an upper limit on the kaon likelihood, since we have shown that the two variables are uncorrelated. The dependence of the significance on the upper limit set to the kaon likelihood is plotted in figure 4.19(b).

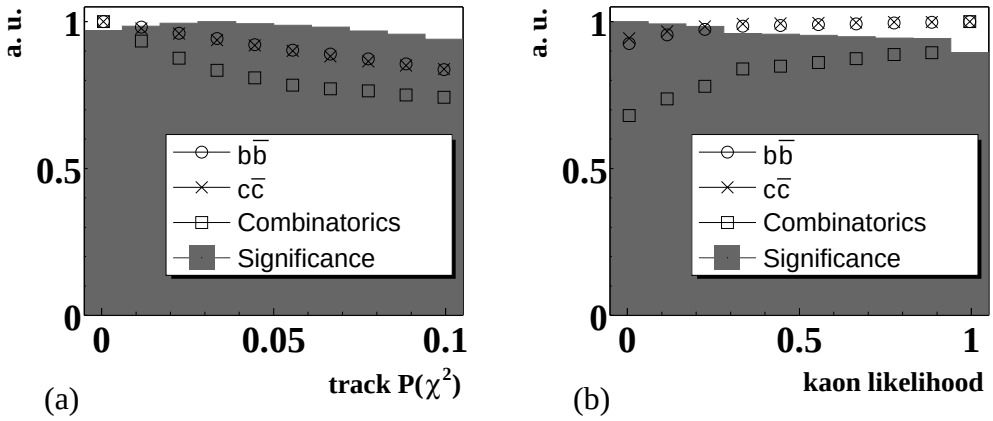

Figure 4.19. Cut optimisation of the track P(χ^2) (a) and kaon likelihood (b).

The maximum is obtained for a kaon likelihood smaller than 0.1 (the lower limit of the range under study). The plot also shows that the difference in significance between a cut at 0.1 and 0.9 is small. The rejection of tracks with a kaon likelihood larger than 0.9 already guarantees a large suppression of the combinatorial background. For this reason, we apply an upper limit on the kaon likelihood of 0.9. Keeping the optimal cuts on kaon likelihood and probability χ^2 of the track, we simultaneously optimise the impact parameter to the target, the transverse momentum and the dimuon vertex detachment. The optimisation procedure is performed in 12^3 steps. The significance is evaluated for 12 lower limits on the impact parameters between 1.5 and 7.0σ, for 12 lower limits on the transverse momenta, between 1.0 and 3.2 GeV/c for the leading muon and between 1.0 and 2.1 GeV/c for the secondary muon, and 12 lower limits on the vertex detachments between -0.2 and 0.9 cm. The reason why we use an asymmetric cut on the transverse momenta is that muons are ordered in p_T. By definition, the leading muon has a larger p_T than the secondary muon. The lower limit on p_T cannot be smaller, because the Monte Carlo simulation of $c\bar{c}$ decays is generated with a preselection cut at 1.0 GeV/c.

The maximum significance is obtained for impact parameters larger than 4.0σ, transverse momenta larger than 1 GeV/c and vertex detachments larger than 0.2 cm. The optimisation point does not change when the kaon likelihood cut is removed. The significance as a function of the cut, when the other two cuts are set at their optimal value, is shown in figure 4.20, for each of the three variables.

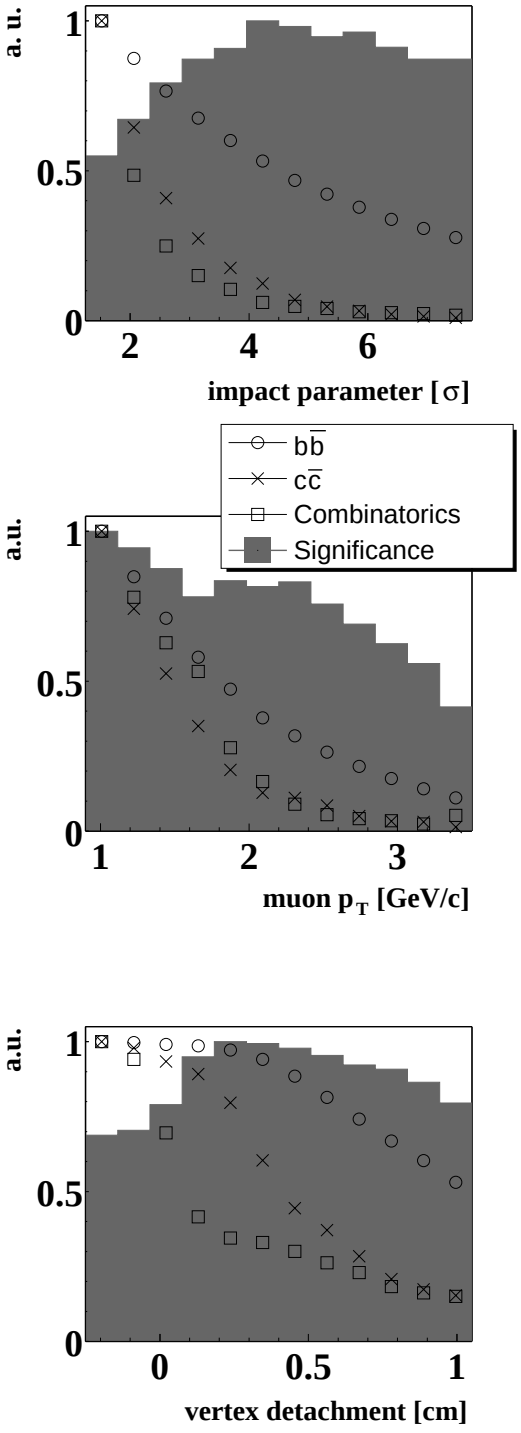

Figure 4.20. Simultaneous cut optimisation of muon impact parameter (top), muon transverse momentum (middle) and dimuon vertex detachment (bottom). The significance is shown for the optimal value of the other two cuts.

4.4.8 Reconstruction efficiency

The selection efficiency for all semi-muonic b and c decays is reported in table 4.8. Each efficiency is determined relatively to the previous one.

	$bibj$	$bicj$	$cicj$	$bici$	$c\bar{c}$
Sample	1560898	1696288	552844	1586860	1789751
Gen. cut	0.6790	0.6790	0.6790	0.6790	0.0018
Reco.×Trig.	0.016	0.011	0.009	0.013	0.019
$\varepsilon_{\mathrm{FLT}}$	0.53	0.53	0.54	0.53	0.52
Target assign.	0.97	0.96	0.95	0.97	0.99
SLT flag	0.83	0.56	0.35	0.66	0.92
Track quality	0.93	0.88	0.85	0.88	0.93
L(μ)	0.97	0.97	0.98	0.97	0.98
Best muons	0.98	0.96	0.94	0.96	0.98
Preselection	0.38	0.28	0.20	0.28	0.14
Mass cut	0.68	0.68	0.80	0.67	0.82
Upper limits	0.97	0.99	0.99	0.97	1.00
$P(\chi^2)$, L(K)	0.93	0.92	0.89	0.92	0.92
Impact	0.41	0.46	0.50	0.57	0.07
Detachment	0.93	0.93	0.99	0.99	0.77
N_{reco}	813 ± 28	336 ± 18	50 ± 7	520 ± 23	76 ± 9
Total efficiency	3.54 ± 0.12 $[10^{-4}]$	1.34 ± 0.07 $[10^{-4}]$	6.18 ± 0.87 $[10^{-5}]$	2.23 ± 0.10 $[10^{-4}]$	7.68 ± 0.88 $[10^{-8}]$

Table 4.8. Cut efficiencies for all Monte Carlo samples.

The first line in the table indicates the number of generated events in which both muons have a transverse momentum larger than $0.6\ \mathrm{GeV}/c$ for semi-muonic b decays, and larger than $1.0\ \mathrm{GeV}/c$ for semi-muonic c decays. This number must be scaled by the generation efficiency (second line in the table) in order to obtain the total number of generated events. Muons with small transverse momenta are rejected at generation, since they will not pass the trigger requirements. This operation saves reprocessing time. Muons with impact parameters smaller than 1.5σ and transverse momenta smaller than $1\ \mathrm{GeV}/c$ are rejected in a preselection phase. We discard muon pairs with an invariant mass larger than $2.95\ \mathrm{GeV}/c^2$ and smaller than $3.25\ \mathrm{GeV}/c^2$ (J/ψ mass region), as well as those pairs having a mass smaller than $2\ \mathrm{GeV}/c^2$ or larger than $8\ \mathrm{GeV}/c^2$. In order to reject unphysical tracks, upper limits are set on the impact parameter (50σ) and the transverse momentum of leading and secondary muons (5 and $3\ \mathrm{GeV}/c$, respectively). The cut on the track probability χ^2, kaon likelihood, impact parameter and vertex detachment were determined with the optimisation procedure discussed in section 4.4.7.

The last entries in the table are the number of selected events (N_{reco}) and the total efficiency. We observe that the efficiency in the $bibj$ channel is about a factor 1.5 larger than that for the $bici$ channel, a factor 3 larger than that for the $bicj$ channel and a factor 6 larger than that for the $cicj$ channel. Most of the difference in efficiency is due to the trigger requirements. The efficiency for each Monte Carlo sample in each target configuration is shown in table 4.9.

Wire	ε_{bibj} $[10^{-4}]$	ε_{bicj} $[10^{-4}]$	ε_{cicj} $[10^{-5}]$	ε_{bici} $[10^{-4}]$	$\varepsilon_{c\bar{c}}$ $[10^{-8}]$
i2	3.45 ± 0.23	1.13 ± 0.13	5.53 ± 1.66	2.56 ± 0.17	8.04 ± 1.21
i2i1	3.03 ± 0.21	1.01 ± 0.12	3.71 ± 1.35	1.87 ± 0.15	7.11 ± 1.14
i1i2	3.66 ± 0.24	1.27 ± 0.14	8.22 ± 2.10	2.27 ± 0.17	12.30 ± 1.93
i1b1	2.87 ± 0.24	0.74 ± 0.12	3.18 ± 1.43	1.72 ± 0.16	11.58 ± 2.37
b1i1	1.64 ± 0.21	0.52 ± 0.12	1.87 ± 1.28	1.16 ± 0.15	0.55 ± 0.32
b1i2	4.03 ± 0.32	1.17 ± 0.18	5.68 ± 2.21	2.98 ± 0.24	1.50 ± 0.52
b1b2	3.48 ± 0.30	0.96 ± 0.16	4.73 ± 2.02	2.74 ± 0.24	0.56 ± 0.32
b1o2	3.84 ± 0.38	1.09 ± 0.20	4.92 ± 2.50	2.42 ± 0.27	7.55 ± 1.98
b1	4.51 ± 0.34	1.53 ± 0.20	6.15 ± 2.31	3.89 ± 0.28	1.11 ± 0.45

Table 4.9. Total selection efficiency for $b\bar{b}$ and $c\bar{c}$ decays in each target configuration.

The statistical uncertainties due to the limited size of the Monte Carlo samples is negligible for J/ψ mesons, while it is of the order of 10% for the $b\bar{b}$ and $c\bar{c}$ decays, except for the $cicj$ decays where it reaches 30%.

4.4.9 Calculation of the $b\bar{b}$ cross section

Applying the optimised b selection criteria to the full data sample, we obtain the detachment spectra of unlike-sign and like-sign muons shown in figure 4.21. For illustrative purposes, we removed the detachment cut. The upstream detachment spectra ($\Delta z < -0.2$ cm) and the peaks around zero are mostly due to background events. The downstream spectra ($\Delta z > 0.2$ cm) present two structures, probably due to b events. The number of downstream unlike-sign muons is

$$N_{\mu\mu}^{+-} = 225 \pm 15. \tag{4.21}$$

This number is only partially due to double semi-muonic b decays. The downstream spectrum contains $c\bar{c}$ and combinatorial background events, which we shall compute and subtract. The upstream like-sign spectrum contains 63 ± 8 events and the upstream unlike-sign spectrum contains 62 ± 8 events. Since these two values are consistent, we do not need to normalise the two spectra. The number of downstream like-sign muons is

$$N_{\mu\mu}^{++} = 117 \pm 11. \tag{4.22}$$

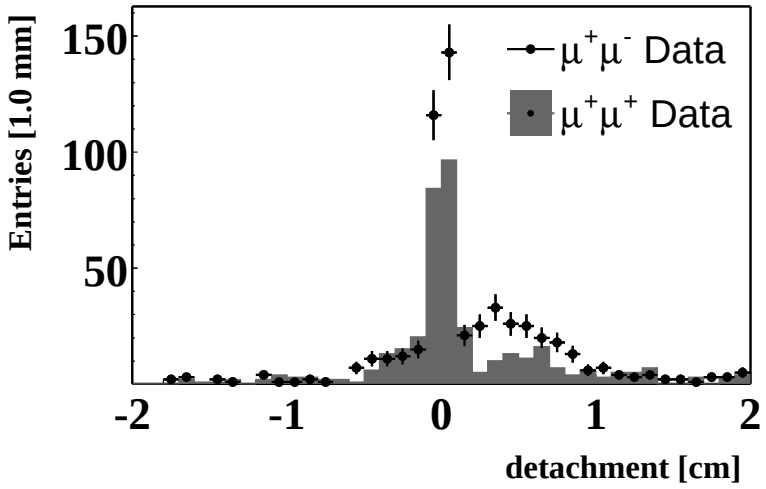

Figure 4.21. Detachment of unlike-sign and like-sign muon pairs after b selection. The detachment cut is removed in order to show both upstream and downstream events.

With equation (4.10) we extract a first value of the $b\bar{b}$ cross section,

$$\sigma_{b\bar{b}} = 28.0 \pm 5.5_{stat} \text{ nb/nucleon}. \tag{4.23}$$

By using this cross section and equation (4.8), we determine the number of double semi-muonic b decays in like-sign muons. The latter is subtracted from the number of downstream like-sign muons obtained in (4.21), in order to estimate the combinatorial background. We compute the number of $c\bar{c}$ decays in unlike-sign muons with equation (4.6). The number of double semi-muonic b decays in unlike-sign muons is obtained with equation (4.5). We subtract $c\bar{c}$ events and combinatorial background from the the number $N^{+-}_{\mu\mu}$ obtained in equation (4.21). All numbers of events are presented in table 4.10.

	$\mu^+\mu^+$	$\mu^+\mu^-$
N_{bb}	43 ± 8	138 ± 27
N_{cc}	0	13.3 ± 0.8
N_{co}	74 ± 14	74 ± 14
Total	117 ± 11	225 ± 15

Table 4.10. Number of signal and background events extracted from the data.

We use the cross section value in equation 4.23 to normalise the Monte Carlo distributions of semi-muonic b decays to the expected number of events in data. The comparison between data and Monte Carlo simulation is shown in figure 4.22.

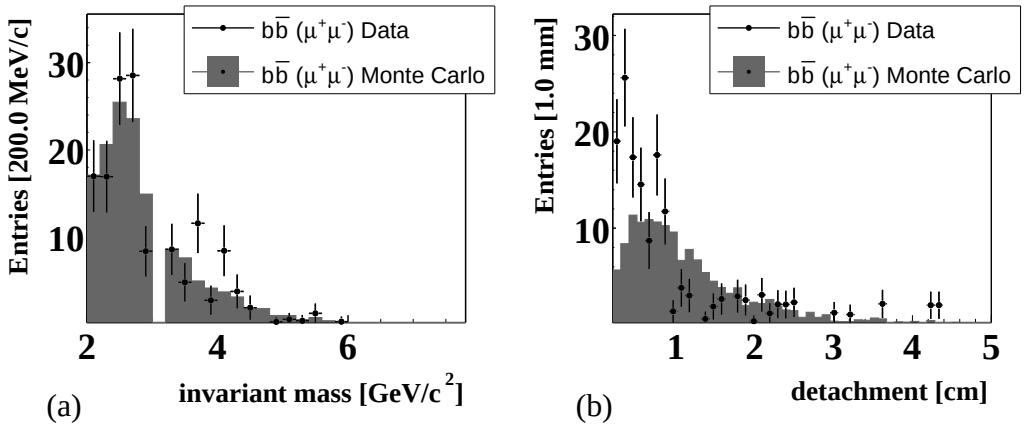

Figure 4.22. Comparison between data and Monte Carlo simulations of invariant mass (a) and detachment (b) distributions of double semi-muonic b decays to oppositely charged muons. Events in the J/ψ mass region ($2.95\ \mathrm{GeV}/c^2 < m < 3.25\ \mathrm{GeV}/c^2$) are removed.

The invariant mass is reproduced by the simulation, within the errors. A discrepancy is observed in the first two detachments bins ($\Delta z < 0.4$ cm). This could be either due to an improper background estimate, or to an improper Monte Carlo simulation. For this reason, we increase the vertex detachment cut to 0.4 cm. The new value of the $b\bar{b}$ cross section is

$$\sigma_{b\bar{b}} = 18.6 \pm 5.2_{stat}\ \mathrm{nb/nucleon}. \tag{4.24}$$

The total statistical uncertainty is 28% and is mostly due to the uncertainty in data event counting (24%). The remaining 4% is due to the limited size of the Monte Carlo samples used to extract the efficiencies. The new estimates of the number of double semi-muonic decays and combinatorial background events extracted from the data are reported in table 4.11.

	$\mu^+\mu^+$	$\mu^+\mu^-$
N_{bb}	25 ± 7	83 ± 23
N_{cc}	0	8.1 ± 0.6
N_{co}	76 ± 12	76 ± 12
Total	100 ± 10	167 ± 13

Table 4.11. Number of signal and background events extracted from the data, when the vertex detachment cut is increased to 0.4 cm.

4.4.10 Likelihood fit

In this section we perform a likelihood fit of the simulated distributions of signal and background events to the selected data. For this purpose, we release the analysis cuts and allow a larger fraction of background events. Compared to the previous approach, the likelihood fit relies more on the Monte Carlo simulations, since they are used to describe the shape of signal and background events in a wider range. In order to perform a likelihood fit, we need to define a likelihood function that depends on the kinematic distributions of signal and background events. We use

$$L(N_s, N_b) = \frac{(N_s + N_b)^N e^{-(N_s+N_b)}}{N!} \cdot \prod_{i=1}^{N} \left(\frac{N_s P_s + N_b P_b}{N_s + N_b} \right), \tag{4.25}$$

where N_s and N_b are the number of signal and background events in the data. These are left as free parameters in the fit. The quantities P_s and P_b are the corresponding probability functions. The exponential factor accounts for the Poissonian fluctuations of signal and background. As signal, we study distributions of $bibj$ and $bici$ decays in unlike-sign muons, which are expected to be dominant over $bicj$ and $cicj$ decays. As background, we study distributions of Monte Carlo simulated $c\bar{c}$ decays and combinatorial background. The latter is obtained by subtracting semi-muonic b decays from the distribution of like-sign muon data, under the assumption that $\sigma_{b\bar{b}} = 15$ nb/nucleon. We report in table 4.12 the relative weight of all signal and background contributions, evaluated as a product of branching ratio and efficiency for several lower limits on the muon impact parameters.

	Signal				Background	
Impact cut [σ]	$bibj$ [%]	$bicj$ [%]	$cicj$ [%]	$bici$ [%]	comb [%]	$c\bar{c}$ [%]
2.00	37.2	8.4	5.6	48.8	88.1	11.9
2.50	35.9	8.3	5.7	50.1	84.1	15.9
3.00	34.9	8.3	5.5	51.3	81.8	18.2
3.50	33.6	8.2	5.6	52.6	83.5	16.5
4.00	32.8	8.0	5.5	53.7	78.7	21.3
4.50	32.4	7.9	5.3	54.3	83.0	17.0
5.00	31.7	7.8	5.1	55.4	87.2	12.8
5.50	31.5	7.5	4.9	56.1	85.5	14.5
6.00	31.5	7.1	4.6	56.9	89.2	10.8

Table 4.12. Relative weight of signal and background contributions for several lower limits set to the muon impact parameters.

4.4.11 Choice of muon kinematic distributions

The kinematic distributions used to define the probability functions are chosen according to three criteria: independence, parameterisability and selectivity.

The choice of independent variables allows to factorise the total probability P in the product of single probabilities. When the variables are correlated, the total probability cannot be factorised and must be defined as a function of all correlated variables. In order to be well defined as probability density functions, the kinematic distributions need to be fitted and normalised to unity in the range in which they are used. In addition, the shape of the fitting functions should differ as much as possible for all signal and background events. This allows to discriminate the different types of events, keeping the uncertainty on the fit parameters low. In order to search for the best kinematic variables, we use the following selection criteria:

- impact parameters larger than 2.0σ;
- transverse momenta larger than $1\ \mathrm{GeV}/c$;
- vertex detachments larger than 0.2 cm.

Correlation study

The impact parameters and the transverse momenta of leading and secondary muons potentially fulfil all requirements for the likelihood fit. The impact parameters are shown in figure 4.23(a). They are independent. The transverse momenta are shown in figure 4.23(b). They are correlated. This is due to the fact that muons are ordered in p_T, the leading muon having larger p_T than the secondary muon, by definition.

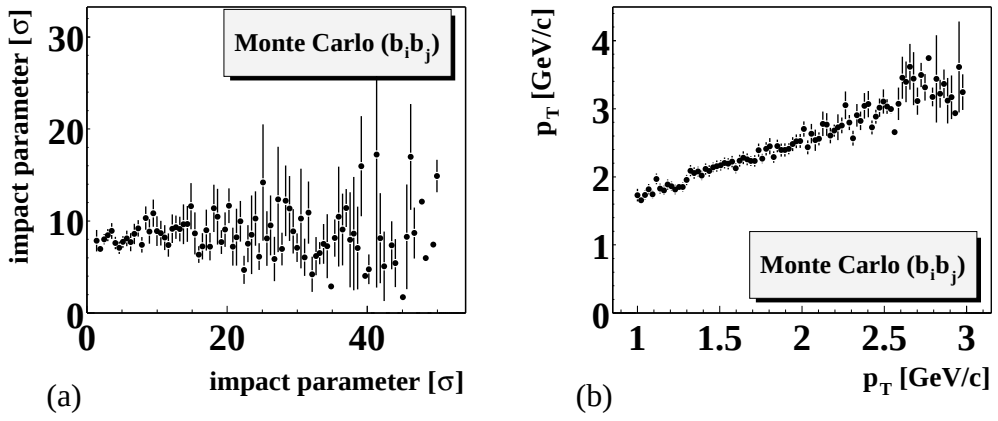

Figure 4.23. Correlation plots between the impact parameter (a) and the p_T (b) of the leading and the secondary muons in $bibj$ Monte Carlo simulation. Similar plots are obtained for other signal and background events.

In order to remove the correlation, we do not normalise the p_T distribution of the leading muon in full range ($[0,\ 5]\ \mathrm{GeV}/c$), but we start from the p_T of the secondary muon. This is a dynamical normalization, in the sense that it changes on an event by event basis. For both muons, we observe that the transverse momentum does not depend on the impact parameter (figure 4.24).

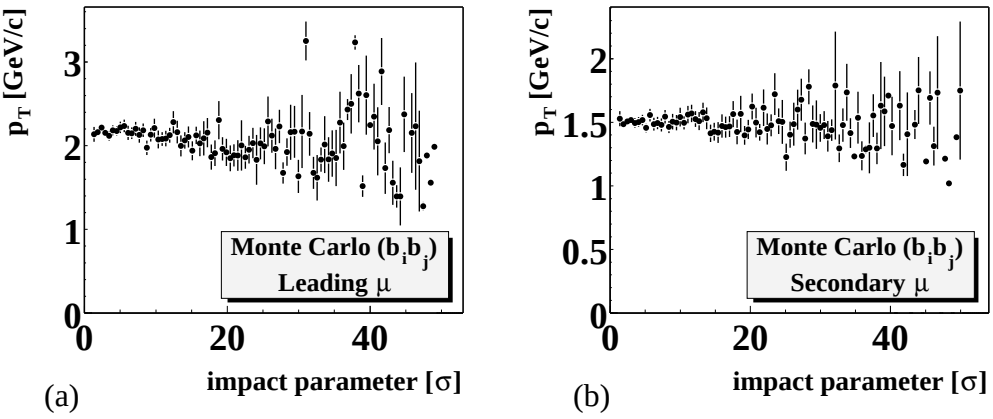

Figure 4.24. Correlation plots between the leading muon p_T and the impact parameter of the leading (a) and the secondary (b) muon in $bibj$ Monte Carlo simulation. Similar plots are obtained for other signal and background events.

Furthermore, we have investigated the possibility to use the dimuon invariant mass and muon longitudinal momentum. The invariant mass is correlated with the transverse momentum, hence cannot be used. It turns out that the longitudinal momentum is correlated with the transverse momentum, probably due to the detector geometry. Fast particles going through the beam pipe are not detected, and the total momentum can be correlated with the minimum transverse momentum the particle needs to evade the beam pipe. Due to the observed correlations, we parameterise only the muon impact parameters and the transverse momenta.

Parameterisation

The impact parameter and the p_T of muons in simulated semi-muonic b decays are shown in figure 4.25. The results of the fits, which will be discussed in details in this section, are shown as an indication of the quality of the parameterisation. In appendix D we show the impact parameter and the p_T distributions in all other samples. The impact parameter is fitted with the exponential function

$$y = Ae^{-\lambda\cdot(x-x_1)}, \tag{4.26}$$

where the parameter A is the value obtained for an impact $x = x_1$ and λ is the exponential slope. The value of x_1 is fixed at 2.0σ.

This parameterisation is not suitable for the transverse momentum. The latter is better fitted with the product of an exponential function, which correctly describes the distribution for large p_T values, and the complementary error function, which provides the smearing at low p_T. The function is

$$y = Ae^{-\lambda\cdot(x-x_{th})} \cdot \frac{1}{2}\mathrm{erfc}\left(\frac{x_{th}-x}{\sqrt{2\sigma_{th}^2}}\right). \tag{4.27}$$

The parameters A and λ describe the exponential part. The parameters x_{th} and σ_{th} are used for the error function. Since the complementary error function is equal to unity in the origin, the parameter A is the value obtained for $x = x_{th}$.

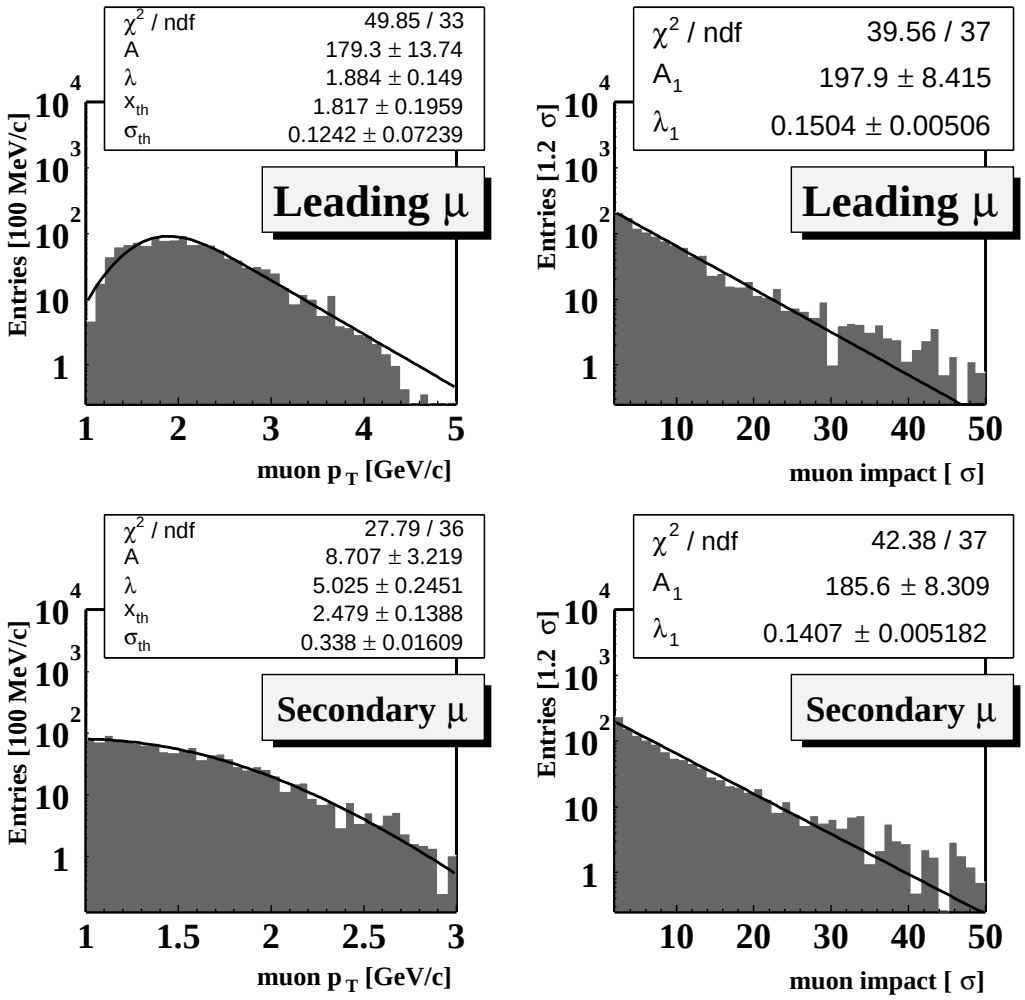

Figure 4.25. Distribution of p_T (left) and impact parameter (right) of leading (top) and secondary (bottom) muons in the Monte Carlo simulation of double semi-muonic $bibj$ decays. The impact parameter is fitted with an exponential function. The momentum is fitted with the product of an exponential and a complementary error function.

From the χ^2 of the fit, we deduce that the quality of the parameterisation is acceptable for b decays. The quality of the other fits is also acceptable, which the exception of the combinatorial background. In this case, two exponential functions better describe the shape of the impact parameter distribution. All plots are reported in appendix D. For the combinatorial background, we use the function

$$y = A_1 e^{-\lambda_1 \cdot (x - x_1)} + A_2 e^{-\lambda_2 \cdot (x - x_2)}. \tag{4.28}$$

The value of x_1 is fixed at 2.0σ. The value of x_2 is left as free parameter in the fit. The resulting fits are shown in figure 4.26.

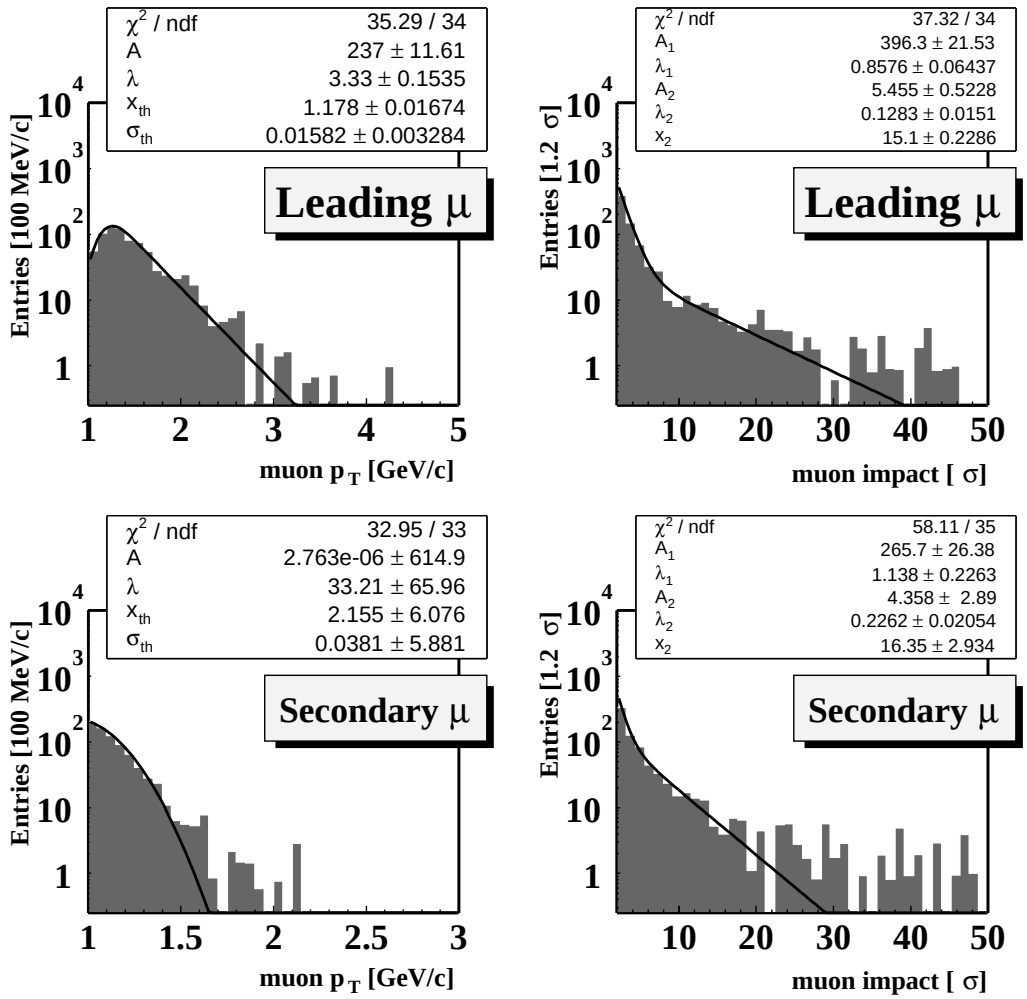

Figure 4.26. Distribution of p_T (left) and impact parameter (right) of leading (top) and secondary (bottom) muons in combinatorial background. The impact parameter is fitted with two exponential functions. The momentum is fitted with the product of an exponential and a complementary error function.

Selectivity

All fitting functions are normalised to unity and depicted together with the corresponding unlike-sign muon data distributions in figure 4.27.

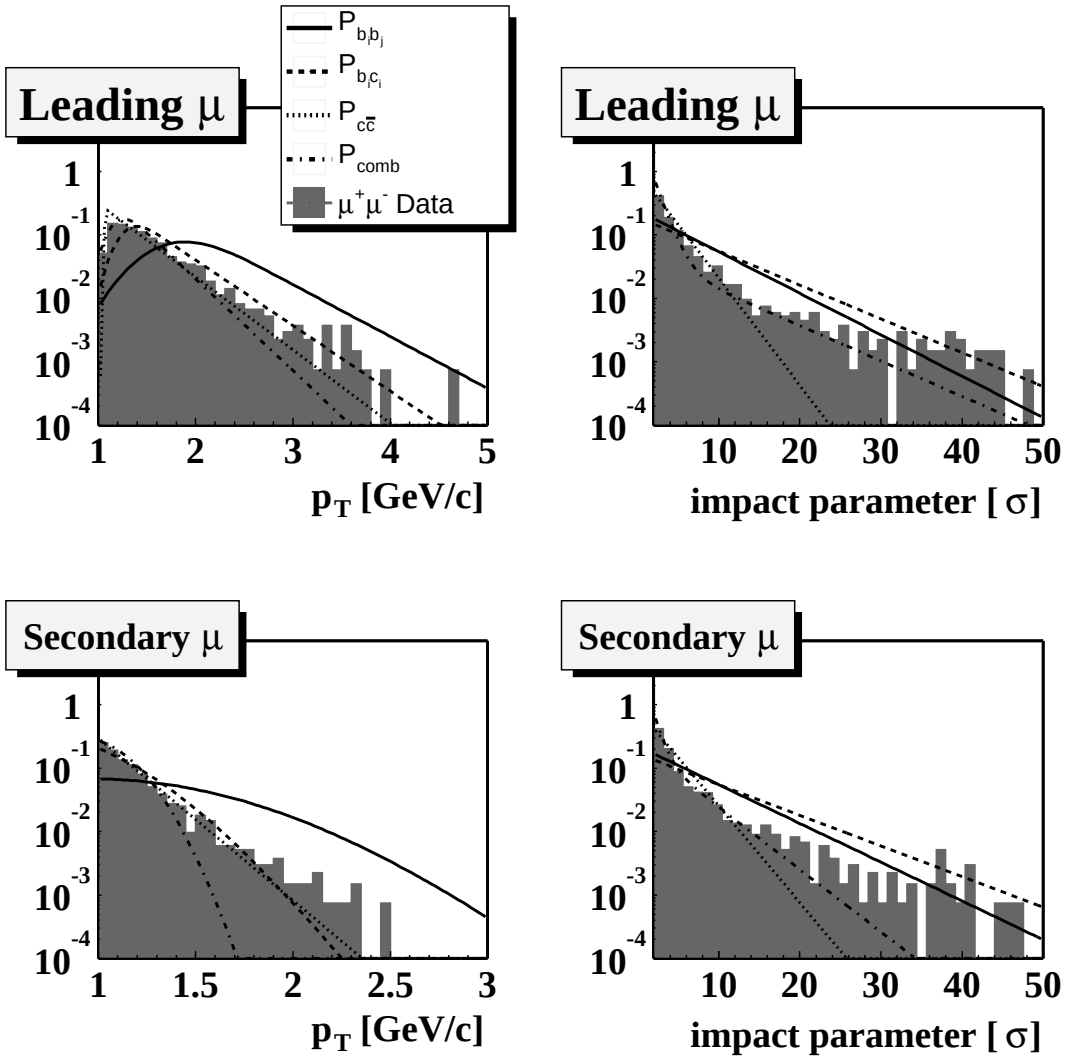

Figure 4.27. Probability functions used to describe double semi-muonic b and c decays and combinatorial background. The p_T (left) and the impact parameter (right) of leading (top) and secondary (bottom) muons are shown. The corresponding distribution in unlike-sign muon data are superimposed.

As expected, the impact parameter of leading and secondary muons in b decays is larger than that of $c\bar{c}$ and combinatorial background events. Furthermore, the momentum distributions allow to distinguish between the $bibj$ and $bici$ classes of b decays. This allows to sufficiently well discriminate between different types of signal and background events.

4.4.12 Likelihood function and fit results

In order to reduce the statistical uncertainty, we only use two free parameters in the likelihood fit: N_s and N_b. The probability functions for signal and background are defined by adding the functions P_{bb}, P_{bc}, P_{cc} and P_{co} according to the expected ratios obtained from Monte Carlo simulations. In particular, we define

$$P_s = C_s \cdot (R_s P_{bb} + P_{bc}) \quad \text{and}$$
$$P_b = C_b \cdot (R_b P_{cc} + P_{co}),$$

where C_s and C_b are normalisation constants, R_s and R_b are the expected ratios of $bibj$ over $bici$ decays and charm over combinatorial background, respectively. From table 4.12, we deduce that the values of R_s and R_b depend on the impact parameter cut. Therefore, we perform a likelihood fit for each of the four hypothesis reported in table 4.13.

	R_s	R_b
Hyp. 1	0.5	0
Hyp. 2	1	0
Hyp. 3	1	0.1
Hyp. 4	1	0.25

Table 4.13. Four hypothesis used for the signal and background composition.

Since impact parameter and p_T are uncorrelated (figure 4.23), all likelihood fits are performed with the p_T probability function obtained with the lowest impact parameter cut. The likelihood function of equation (4.25) is maximised by using the *TMinuit* function in ROOT [136]. The cross section as a function of the impact parameter cut is plotted in figure 4.28 (Method II), where we also report the results obtained with the first approach presented in section 4.4.9 (Method I).

The cross section is stable with an impact parameter cut larger than 4σ. The results obtained with the likelihood fit are more stable than those obtained with Method I. The output of the likelihood fit, for a 4σ impact parameter cut and for each hypothesis on signal and background composition, is reported in table 4.14.

	N_s	N_b
Hyp. 1	86 ± 15	139 ± 10
Hyp. 2	77 ± 15	148 ± 10
Hyp. 3	76 ± 15	149 ± 10
Hyp. 4	76 ± 15	149 ± 10

Table 4.14. Signal and background events extracted from the data with the likelihood fit.

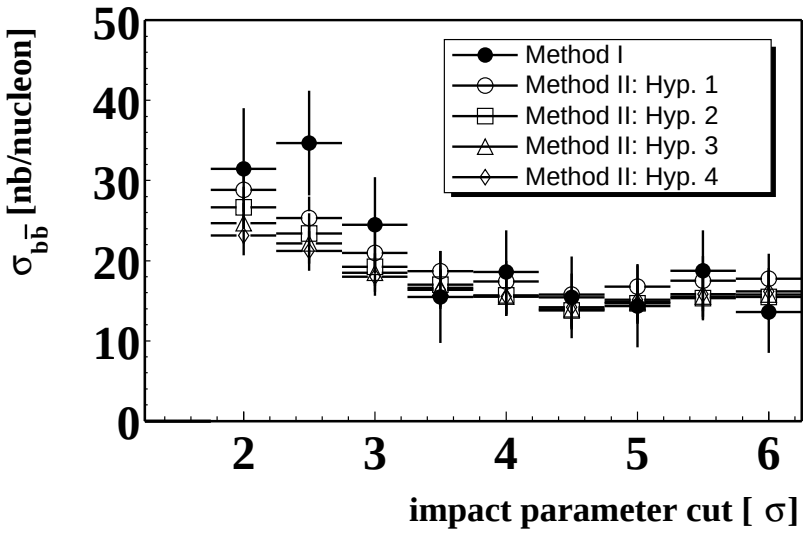

Figure 4.28. Dependence of the $b\bar{b}$ cross section extracted from the data on the muon impact parameter cut, when the four hypothesis on signal and background composition of table 4.13 are used. Method I is the cut-based analysis. Method II is the likelihood fit.

The resulting cross section is

$$\sigma_{b\bar{b}} = 15.5 \pm 2.4_{stat} \text{ nb/nucleon}. \tag{4.29}$$

This result is consistent with that of equation (4.24), even though one has to keep in mind that the statistical errors of the two results are correlated, since they were obtained with the same set of events. In the likelihood fit, the statistical uncertainty is reduced by a factor two.

4.4.13 Study of the systematic uncertainty

Branching ratios

The branching ratios for semi-muonic b and c decays affect the measurement with a systematic uncertainty of 3.5% (3.6%) and 5% (3.1%) in Method I (Method II), respectively. This effect is estimated as the variation of the $b\bar{b}$ cross section obtained when the branching ratios are artificially increased by one standard deviation. The branching ratio for $b \to c\bar{c}s$ decay is not accurately known. We assign a total 6% uncertainty for the two methods, including also the effect of the reassignment of $cici$ decays. The uncertainty on the J/ψ cross section introduces a systematic effect of 10% (9%) in Method I (Method II).

Detector and trigger simulation

Most of the systematic effects due to the detector and trigger simulations cancel out in the efficiency ratio of equations (4.4) and (4.9). We assume a conservative estimate of 5%. This value includes the effect due to a possible shift of the target position assumed by the SLT, which would affect the detection of particles with a large impact parameter.

Monte Carlo simulation of J/ψ mesons

The Monte Carlo simulations of p_T and x_F of J/ψ mesons are weighted, in order to match the experimental distribution observed in the data. This is not done for b events. The corresponding uncertainty is 2.5%.

Beauty production and decay models

Theoretical models are used for the Monte Carlo simulation of beauty quark production and decay. The systematic effect due to the theoretical uncertainty in these models has been estimated to be 5%. This effect is estimated by changing several input parameters of the theoretical predictions. The intrinsic p_T of the incoming parton is changed from 0.125 to 2.0 GeV/c. The parton distribution functions is changed from MRST [14] to CTEQ5 [13]. The b quark mass is changed from 4.5 to 5.0 GeV/c^2. The QCD normalisation scale is changed from $0.5\sqrt{m_b^2+p_T^2}$ to $2\sqrt{m_b^2+p_T^2}$. The Peterson fragmentation function (with parameter ε from 0.0022 to 0.008) is replaced by the Kartvelishvili function (with parameter $\alpha = 13.7$) [23]. The b lifetime is accurately measured (1.564 ± 0.014 [ps]) [2] and contributes with an uncertainty of 1%.

Running conditions

The Monte Carlo simulations are produced with an interaction rate fixed to the nominal value of 5 MHz. Possible rate instabilities might affect the track multiplicity in the data. This effect is not properly simulated and contributes with a systematic uncertainty of 1%. The position, the shape and the beam sharing between different wires contribute with an uncertainty of 0.5%.

Analysis cuts

The systematic uncertainty of the impact parameter cut is estimated as the maximum variation observed in figure 4.28 between 3.5 and 6σ, divided by $\sqrt{12}$. The result is an uncertainty of 7% in Method I and 5% in Method II.

Signal and background composition

This is the systematic uncertainty due to the assumption that the signal is composed by $bibj$ and $bici$ decays in the ratio R_s and the background is composed of $c\bar{c}$ and combinatorial pairs in the ratio R_b. The maximum variation observed in figure 4.28 for a 4σ impact parameter cut, divided by $\sqrt{12}$, results in an uncertainty of 3.8%. This uncertainty affects only Method II.

All systematic uncertainties are reported in table 4.15.

Systematic effect	**Uncertainty**	
Detector and trigger simulation	5%	
J/ψ production models ($x_{\rm F}$ and p_T)	2.5%	
Beauty production and decay models	5%	
Beauty lifetime	1%	
Interaction rate	1%	
Beam position, shape and sharing	0.5%	
	Method I	**Method II**
J/ψ cross section	10%	9%
Branching ratio ($b \to \mu^- X$)	3.5%	3.6%
Branching ratio ($c \to \mu^+ X$)	5%	3.1%
Branching ratio ($b \to c\bar{c}s$)	6%	6%
Analysis cuts	7%	5%
Signal and background composition	–	3.8%
Total	17%	15%

Table 4.15. Systematic uncertainties on the measurement of the $b\bar{b}$ cross section.

Assuming that all uncertainties are independent, we sum them in quadrature and obtain a total uncertainty of 17% for Method I and 15% for Method II.

4.4.14 Final results

From all values presented in the previous sections, we obtain the final $b\bar{b}$ cross section

$$\sigma_{b\bar{b}} = 18.6 \pm 5.2_{stat} \pm 3.2_{sys} \text{ nb/nucleon} \qquad (\text{Method I}),$$
$$\sigma_{b\bar{b}} = 15.5 \pm 2.4_{stat} \pm 2.3_{sys} \text{ nb/nucleon} \qquad (\text{Method II}).$$

4.5 Comparison with theoretical predictions

The first measurement of the beauty production cross section at HERA-B was based on the identification of $b \rightarrow \mathrm{J}/\psi \rightarrow l^+l^-$ decays, with the x_F of the J/ψ limited to the range $[-0.35, 0.15]$. The large lifetime of B hadrons, together with the boost provided in fixed target experiments, allows the identification of b events with the J/ψ mesons detached from the interaction point. The results provided by two independent analysis performed in the muon and electron channels were combined. A J/ψ cross section of $\sigma_{\mathrm{J}/\psi} = 417 \pm 37$ nb/nucleon was used. Further details can be found in reference [22]. The result is

$$\sigma_{b\bar{b}} = 14.9 \pm 2.2_{stat} \pm 2.4_{sys} \text{ nb/nucleon}, \tag{4.30}$$

and is consistent with the value obtained from double semi-muonic b decays, which was presented in this thesis. The $b\bar{b}$ cross section extracted from HERA-B data and the results obtained at Fermilab in similar experimental conditions are reported in table 4.16.

					$\sigma_{b\bar{b}}$ [nb/nucleon]	
Experiment	Year	Target	E[GeV]	Events	@ E[GeV]	@ 920 GeV
E789 [7]	1995	Au	800	19	$5.7 \pm 1.5 \pm 1.3$	$8.1 \pm 2.2 \pm 1.8$
E771 [6]	1999	Si	800	15	$43^{+27}_{-17} \pm 7$	$61^{+38}_{-24} \pm 10$
HERA-B[22]	2002/5	C/Ti/W	920	93	$14.9 \pm 2.2 \pm 2.4$	
HERA-B	2006	C/Ti/W	920	77	$15.5 \pm 2.4 \pm 2.3$	

Table 4.16. Measurements of $\sigma_{b\bar{b}}$ at HERA-B and Fermilab experiments. The results of Fermilab are also extrapolated to the HERA-B proton beam energy of 920 GeV.

The E771 collaboration extracted the $b\bar{b}$ cross section by using simultaneous decays of the b quarks. The E789 collaboration performed the same measurement with the inclusive J/ψ decays. The results of HERA-B and Fermilab experiments cannot be directly compared since the proton beam energy is different and both experiments operate in a near threshold regime. Therefore, all results are extrapolated to the HERA-B energy. The relative increase of the cross section, according to QCD calculations, is $42 \pm 9\%$. The HERA-B results are consistent with the E789 and E771 results, at most within 2σ.

We compare the experimental results reported in table 4.16 with the most recent theoretical predictions of Bonciani *et al.*[19] and Kidonakis *et al.*[21]. Both methods are based on QCD calculations at NLO. They include the large contributions of soft gluon emissions, which are computed with a resummation technique (see section 4.4.9). A comparison between the theoretical predictions and all available experimental results is presented in figure 4.29, where the beauty production cross section is shown as a function of the incoming proton beam energy in fixed target experiments.

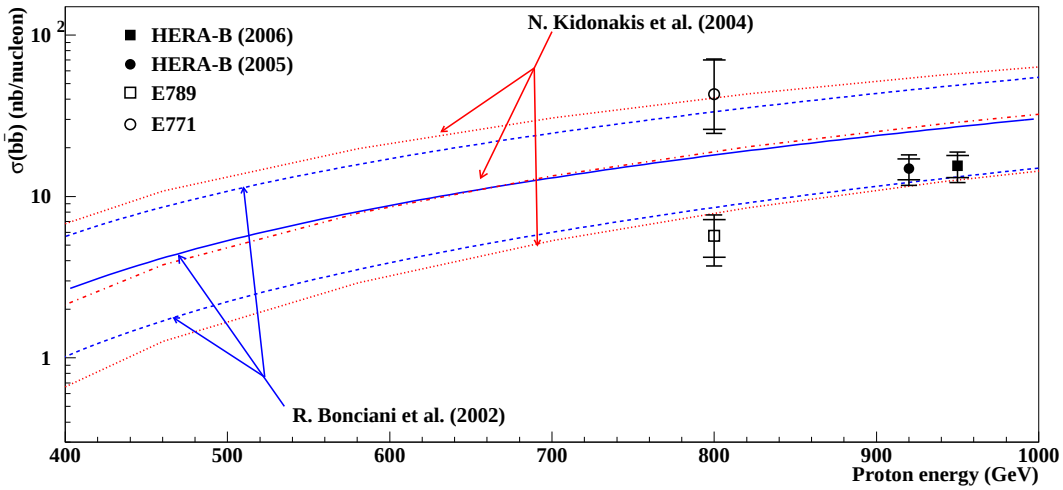

Figure 4.29. Beauty cross section per nucleon as a function of the proton energy in fixed target pA collisions predicted by Bonciani *et al.*[19] and by Kidonakis *et al.*[21]. The predicted curves are accompanied by an upper and a lower curve accounting for the theoretical uncertainty. The HERA-B(2005) result is obtained from $b \to \mathrm{J}/\psi \to l^+l^-$ decays and includes both electron and muon channels. The HERA-B(2006) result has been presented in this thesis and is based on the identification of $b\bar{b} \to \mu\mu$ decays (in the plot it is reported at a higher energy in order to make it visible).

The HERA-B results are the most accurate and are consistent with the theoretical predictions.

4.6 Summary

We searched for $b\bar{b} \to \mu\mu$ decays in 150 M dilepton triggered events collected with the HERA-B detector in 920 GeV pA collisions by using two different methods. Firstly, we isolate events that satisfy a set of optimised selection criteria on impact parameters, transverse momentum and vertex detachment. Secondly, the selection criteria are released and the signal is extracted from a likelihood fit of the simulated distributions to the data. From these events, we extract the $b\bar{b}$ cross section relative to the prompt J/ψ cross section assuming that $\sigma_{\mathrm{J}/\psi} = 417 \pm 37$ nb/nucleon, in the x_{F} range $[-0.35, 0.15]$. The two methods provide consistent results,

$$\sigma_{b\bar{b}} = 18.6 \pm 5.2_{stat} \pm 3.2_{sys} \text{ nb/nucleon} \qquad (\text{Method I}),$$
$$\sigma_{b\bar{b}} = 15.5 \pm 2.4_{stat} \pm 2.3_{sys} \text{ nb/nucleon} \qquad (\text{Method II}),$$

which are in agreement with the value obtained in a third method [22].

Chapter 5

Search for Pentaquarks

The night of the hunter (1955) - C. Laughton

We search the HERA-B minimum bias data for p-K^0_s decays of the exotic baryon $\Theta^+(1540)$ with the pentaquark configuration $uudd\bar{s}$. Since no signal could be established, we extract upper limits on the cross section and rate relative to the conventional $\Lambda(1520)$ hyperon. For $p^{12}\mathrm{C}$ collisions, we obtain $\mathrm{BR}\cdot\frac{d\sigma_{\Theta^+}}{dy} < 1.4$ μb/nucleon and $\frac{d\sigma_{\Theta^+}}{d\sigma_\Lambda} < 0.059$ in the rapidity range $-0.3 < y < 0.3$.

5.1 Introduction

In this chapter, we present the results of a search for the $\Theta^+(1540)$ pentaquark. The search for $\Theta^+ \to pK^0_s$ decays at HERA-B benefits from a clean proton identification and the clear signature of the detached $K^0_s \to \pi^+\pi^-$ decays. Since it is allowed by the conservation of energy, we assume that the $\Theta^+(1540)$ decays always in a nucleon-kaon pair. Assuming that the nucleon has 50% probability to be a proton and that the K^0 has 50% probability to be a K^0_s, we obtain a branching ratio $\mathrm{Br}(\Theta^+ \to pK^0_s \to p\pi^+\pi^-) = 25\% \times 69\% \approx 17\%$, which is a quite large number.

In section 5.2 we illustrate the Monte Carlo simulation of $\Theta^+ \to pK^0_s$ decays. In section 5.3 we perform a search for inclusive Θ^+ decays into proton and K^0_s by reconstructing the invariant mass of all possible combinations of protons and K^0_s. We identify them with a minimal amount of selection criteria and focus in the mass region between 1.5 and 1.6 GeV/c^2. Since the mass of the hypothetical pentaquark is close to the mass of the established $\Lambda(1520)$ hyperon, which also exhibits a similar decay (p-K^-), we compare production rates of the two particles assuming a similar production mechanism. In section 5.4, we attempt to isolate evidence for pentaquarks by applying more stringent selection criteria to the kinematics of the final state particles and to the event topology.

5.2 Monte Carlo simulations

In order to evaluate the reconstruction efficiency for pentaquark decays into p-K^0_s, we use Monte Carlo simulations. The HERA-B event simulation is based on the software packages PYTHIA [129, 130], FRITIOF [131, 132] and GEANT 3 [133]. PYTHIA is used to simulate the hard scattering processes and is not relevant for this analysis. FRITIOF generates inelastic pA collisions and GEANT 3 performs a simulation of the detector.

For the study of the Θ^+, we analyse 320 k events in which a p-K^0_s pair is produced. Since there is no physical model for the production mechanism, we assume the standard cross section dependency on the kinematic variables $x_{\rm F}$ and p_T,

$$\frac{d^2\sigma}{dp_T^2 dx_{\rm F}} = C \cdot (1 - |x_{\rm F}|)^n \cdot e^{-B \cdot p_T^2}, \tag{5.1}$$

with $n = 0$ within $-0.3 \leq\ x_{\rm F} \leq 0.3$ and $B = 2.1$, the typical value for a particle with mass around $1.5\ \mathrm{GeV}/c^2$. The $x_{\rm F}$ and p_T^2 spectra generated by FRITIOF are shown in figure 5.1(a,b).

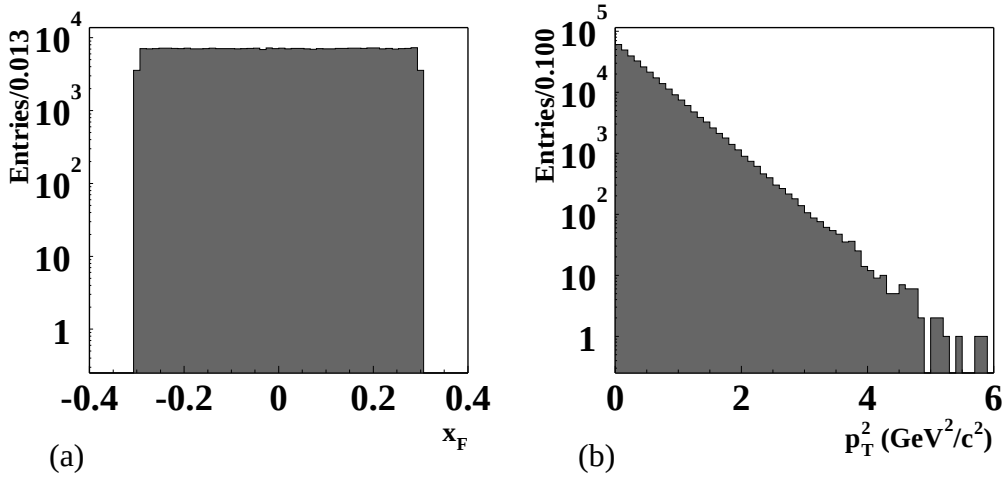

Figure 5.1. Distribution of $x_{\rm F}$ (a) and p_T^2 (b) of p-K^0_s pairs as generated by FRITIOF.

After the generation of the p-K^0_s pair, the remaining momentum is assigned to a π^+, which is fed as a beam particle into FRITIOF to simulate further interactions inside the nucleus. This means that, apart from the kinematics, there is no further requirement on the decay products, such as the production of associated particles with compensating strangeness content. Since the $\Theta^+(1540)$ resonance is claimed to be narrow, we generate p-K^0_s pairs with an intrinsic width of $50\ \mathrm{keV}/c^2$, which is smaller than the spectrometer mass resolution.

5.2.1 Mass resolution

The $\Theta^+(1540)$ decays are searched among all combinations of p and K^0_s pairs. At this step of the analysis, we apply a soft selection, which is sufficient to identify the peak over the background. Specifically, we require for each reconstructed track:

- a charged track;
- standard clone removal;
- at least 5 hits in the vertex detector;
- at least 10 hits in the outer tracker.

A minimum number of hits in the vertex detector and in the tracking system allows to reject ghost tracks, which are typically generated by coincidences of a few random hits. As proton candidates, we consider any positively charged track. For the $K^0_s \to \pi^+\pi^-$ decays, we require:

- two oppositely charged tracks;
- a distance of closest approach between tracks smaller than 700 μm;
- a vertex detachment from the target larger than 2 cm;
- an invariant mass within 50 MeV/c^2 the PDG position.

The loose requirement on the vertex quality removes accidental track combinations that do not originate from a common vertex. The detachment cut suppresses the background made of particles located in the proximity of the target. The Monte Carlo simulation of the reconstructed p-K^0_s invariant mass is shown in figure 5.2.

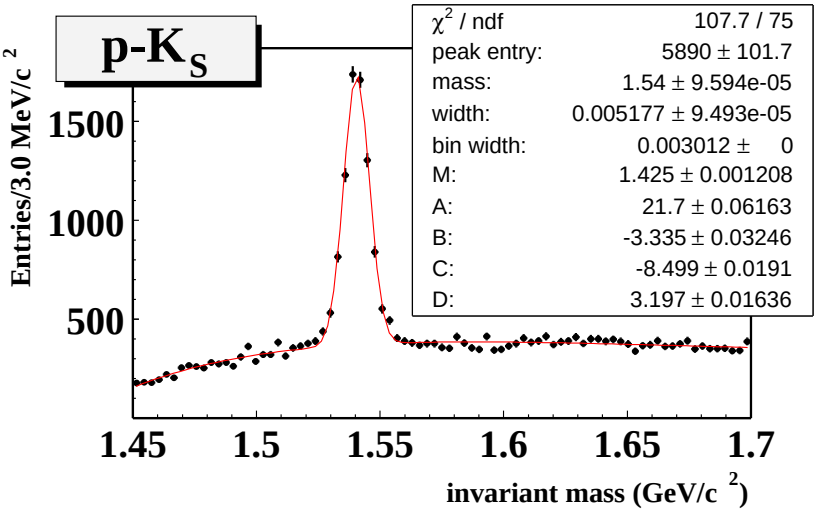

Figure 5.2. Monte Carlo simulation of the reconstructed p-K^0_s invariant mass.

The invariant mass spectrum does not contain $\overline{p}$-K^0_s pairs. The mass fit is performed with a Gaussian for the signal and a five parameter exponential for the background. The functional form used for the background will be introduced in equation (5.7). The width of the signal is 5.2 ± 0.1 MeV/c^2 and is due to the experimental mass resolution, which is two order of magnitude larger than the generated width (50 keV/c^2).

Keeping the general requirement on the track quality, we use different selection criteria to identify $\Lambda(1520)$ decays into protons and kaons. Specifically, we combine oppositely charged tracks with:

- a distance of closest approach smaller than 700 μm;
- a proton RICH likelihood larger than 0.35;
- a kaon RICH likelihood larger than 0.35.

The Monte Carlo simulation of the reconstructed p-K^- invariant mass is shown in figure 5.3.

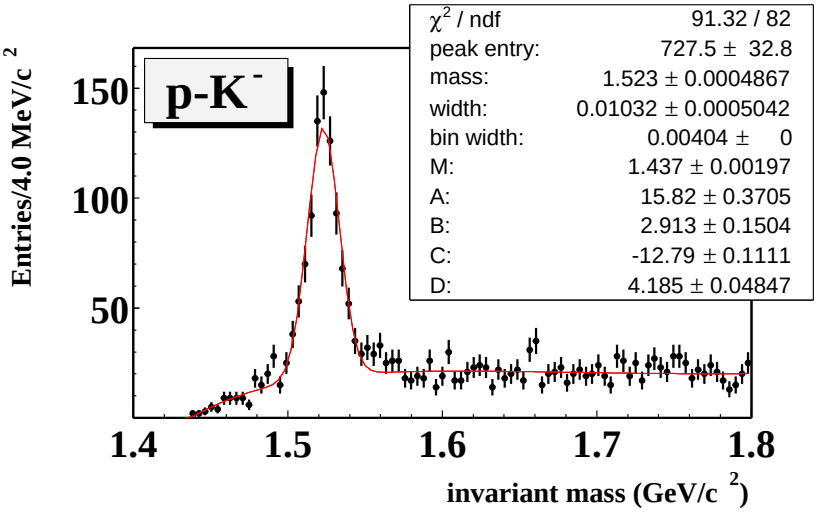

Figure 5.3. Reconstructed p-K^- invariant mass spectrum in Monte Carlo.

The invariant mass spectrum is fitted with a Gaussian for the signal and a five parameters exponential for the background. Again, the functional form used for the background will be introduced in equation (5.7). From the χ^2 of the fit, we conclude that the description of the mass spectrum is satisfactory in the full mass range. The Gaussian fit returns a width of 10.3 ± 0.5 MeV/c^2, which is close to the intrinsic width reported by the PDG ($\Gamma = 15.6 \pm 1.0$ MeV/c^2). The value of the mass is 1523 ± 0.5 MeV/c^2, which is slightly larger than the PDG value. As we shall see later, the statistics is not sufficient to obtain an accurate determination of the reconstruction efficiency.

5.2.2 Acceptance in rapidity and p_T

We describe the detector acceptance for the $\Theta^+(1540)$ in terms of rapidity and transverse momentum. The term acceptance usually indicates the fraction of generated Monte Carlo events that leave a minimum amount of hits in the detector. Here, it includes the requirements that are necessary to identify the peak in the mass spectrum (section 5.2.1). The rapidity and p_T distributions are shown in figure 5.4.

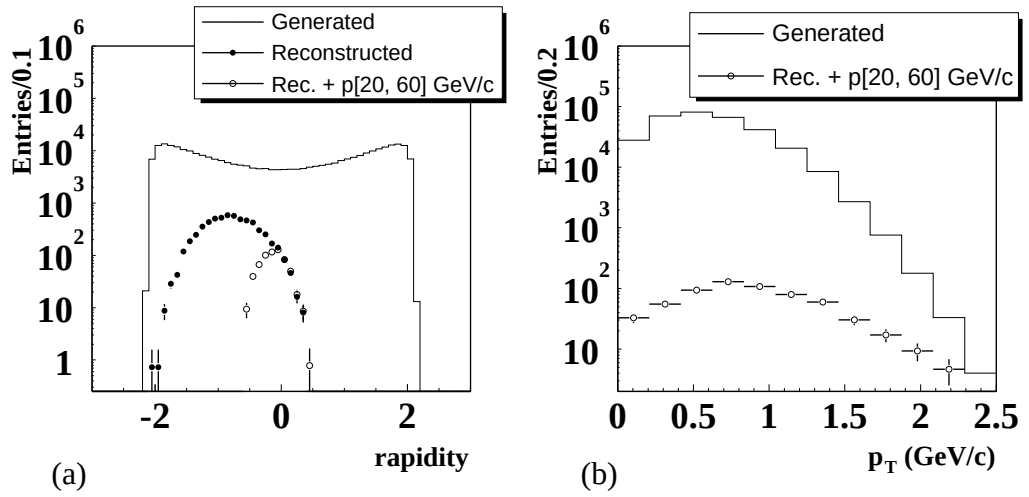

Figure 5.4. Distribution of p-K^0_s rapidity (a) and p_T (b) in generated and reconstructed Monte Carlo events. The rapidity with a cut on the proton momentum is also shown.

The generated spectra divided by the reconstructed ones are shown in figure 5.5.

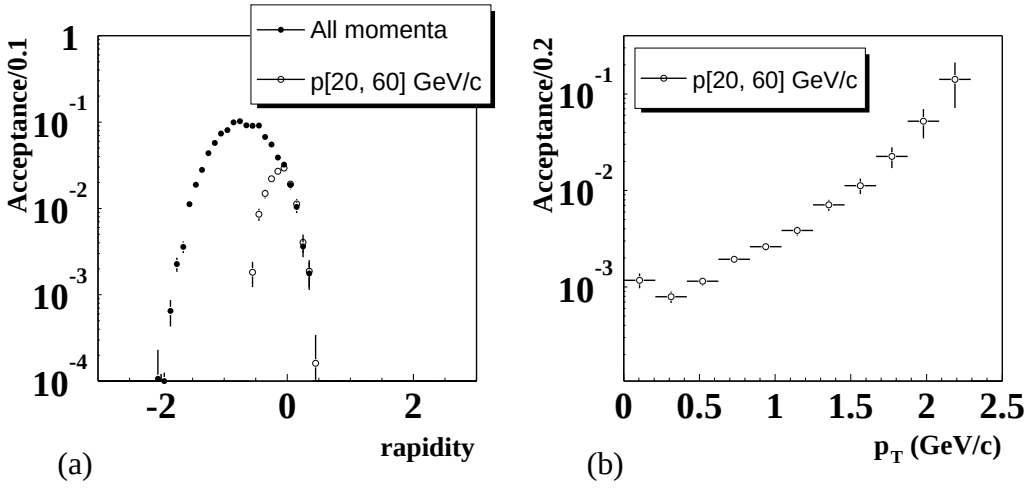

Figure 5.5. Acceptance of p-K^0_s as a function of rapidity (a) and p_T (b). The acceptance in rapidity is shown for two different requirements on the proton momentum.

The reconstruction of protons and kaons leads to a reduction of the $\Theta^+(1540)$ rapidity range. In particular, the rapidity acceptance is limited by the finite angle covered by the detector and by the limitation on the proton momenta. The proton is identified with the RICH detector, which limits the accepted momenta to values larger than $20\ \mathrm{GeV}/c$ (figure 5.8). Without any requirement on the proton momentum, the average acceptance is 1.87%, in the full rapidity range. With the proton momentum cut, the average acceptance decreases to 1.36%, in the rapidity range $[-0.5, 0.5]$. The acceptance increases to 1.83% in the range $[-0.3, 0.3]$. Since the acceptance is significant in a small range around zero, HERA-B is called a mid-rapidity experiment. The acceptance in p_T increases with the value of p_T. With the same procedure used for pentaquarks, we obtain the rapidity and p_T acceptance profiles for the $\Lambda(1520)$ decay into protons and kaons shown in figure 5.6.

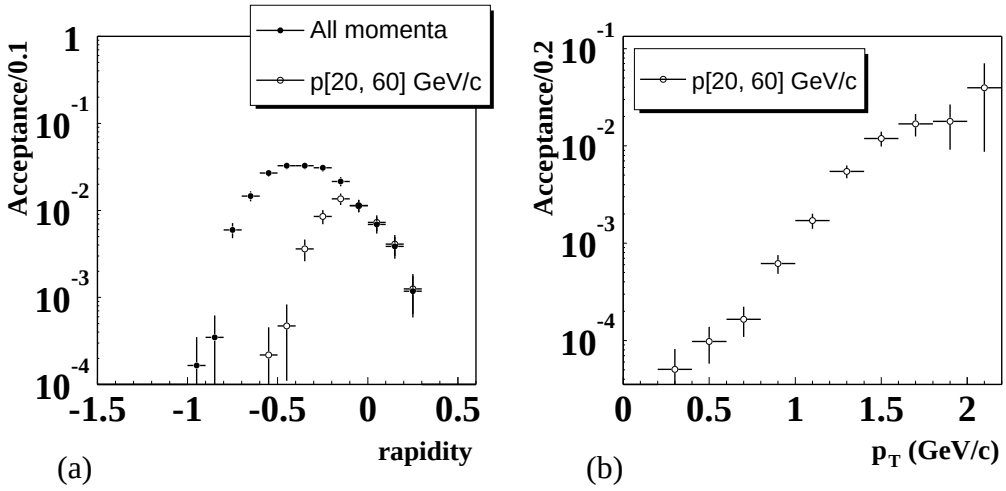

Figure 5.6. Acceptance for $\Lambda(1520)$ as a function of rapidity (a) and p_T (b). The acceptance in rapidity is shown for two different requirements on the proton momentum.

The rapidity acceptance range for p-K^- is narrower compared to p-K^0_s. The average value is smaller. A relevant reduction is due to the RICH likelihood cut, which rejects protons and kaons with low momenta. With the proton momentum cut, the average acceptance is 0.49% in the rapidity range $[-0.5, 0.5]$ and 0.73% in $[-0.3, 0.3]$. Note that the acceptance profiles for $\Theta^+(1540)$ and $\Lambda(1520)$ are not directly comparable. This is due to the fact that the selection criteria used to make the peaks visible in the Monte Carlo simulation are different. The p_T acceptance profiles are similar above $1\ \mathrm{GeV}/c$, where they both increase as a function of p_T, and they are different below $1\ \mathrm{GeV}/c$, where the acceptance for p-K^- drops to zero. We remind the reader that the acceptance for pentaquarks is obtained under the assumption of a standard production mechanism, whereas an exotic mechanism could lead to substantially different acceptances.

5.3 Inclusive Θ^+ decays in data

We search the HERA-B minimum bias data for inclusive decays of pentaquarks in the p-K^0_s channel. The data set consists of 130 million minimum bias events taken with three wire targets (carbon, titanium and tungsten). The list of runs used in this analysis can be found in appendix A. The statistics collected in each wire configuration and the corresponding luminosity are reported in table 5.1.

Target	Statistics	$\mathcal{L}$ [μb^{-1}]
^{12}C	$57,549,704$	252.2 ± 8.8
^{48}Ti	$20,835,047$	33.7 ± 1.2
^{184}W	$52,725,069$	32.1 ± 1.1
All	$131,109,820$	318.1 ± 8.9

Table 5.1. Statistics and luminosity of the data samples used to search for pentaquarks.

The analysis is carried out in BEE, an object oriented analysis framework based on ROOT [136]. Before the analysis, the hit information produced by all detector subsystems, which is stored on tapes in the form of "raw" data, is used to produce track candidates. In this intermediate step, also called reprocessing, clones and badly reconstructed tracks are rejected. We use the reprocessing version 'rp0005', in which the inner tracker, due to its unstable performance, is excluded.

5.3.1 Proton and charged kaon selection

The identification of protons and kaons is done with the RICH, which associates to each track the probability to fulfil different mass hypothesis. The typical distributions of proton and kaon likelihood are depicted in figure 5.7.

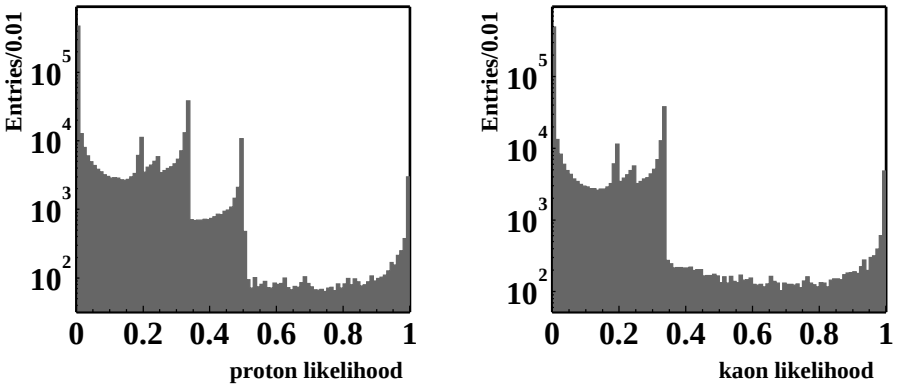

Figure 5.7. Typical distributions of proton (left) and kaon (right) likelihood.

With medium selection criteria, the kaon identification efficiency, when the momentum is between 10 and 60 GeV/c, is between 60% and 95% (see figure 2.9). The corresponding misidentification probability is 5%. For protons with momenta between 20 and 60 GeV/c, the efficiency is between 60% and 80%, with less than 5% misidentification probability (see reference [94]).

We exploit the performance of the proton identification by using $\Lambda \to p\pi^-$ decays. The selection criteria used for this purpose will be discussed in the next section. The efficiency is calculated counting the number of reconstructed Λ decays in the data, with and without requirement on the proton RICH likelihood. This procedure allows to evaluate the proton selection efficiency by using the data rather than the Monte Carlo simulations. The efficiency as a function of the proton momentum, when four conditions are imposed on the likelihood, is displayed in figure 5.8.

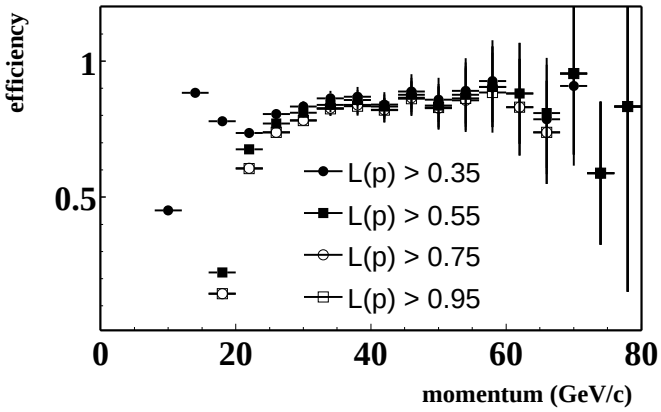

Figure 5.8. Efficiency of the proton identification with the RICH detector, when four conditions are imposed on the proton likelihood L(p).

When the likelihood of the proton is larger than 55%, protons with momenta smaller than 18 GeV/c are lost. Within the accepted range, the efficiency increases with the momentum. The efficiency is larger than 50%, for momenta larger than 20 GeV/c. Since the proton identification is more reliable and efficient for momenta larger than 20 GeV/c, we present our results in the range $[20, 60]$ GeV/c. For smaller momenta, the kaon contamination may play an important role and lead to an increased background. The average efficiency in the selected momentum range is reported in table 5.2, when four requirements on the proton likelihood are applied.

L(p)	0.35	0.55	0.75	0.95
$\varepsilon_{RICH}(p)$ [%]	78.0 ± 0.2	74.4 ± 0.2	70.0 ± 0.2	60.5 ± 0.3

Table 5.2. Average proton identification efficiency in the momentum range $[20, 60]$ GeV/c, when four lower limits are set to the proton RICH likelihood in $\Lambda \to p\pi^-$ decays.

5.3.2 Selection of V^0 particles

The historic name V^0 is used to indicate neutral strange mesons and baryons, such as $K^0_s \to \pi^+\pi^-$, $\Lambda \to p\pi^-$ and $\bar{\Lambda} \to \overline{p}\pi^+$. Their detection is relatively easy at HERA-B because in average they travel a few tens of cm within the detector and they decay in a region where the combinatorial background is low. The selection criteria listed in section 5.2.1, used for data preselection, are already enough to identify clear peaks in the invariant mass spectra (figure 5.9).

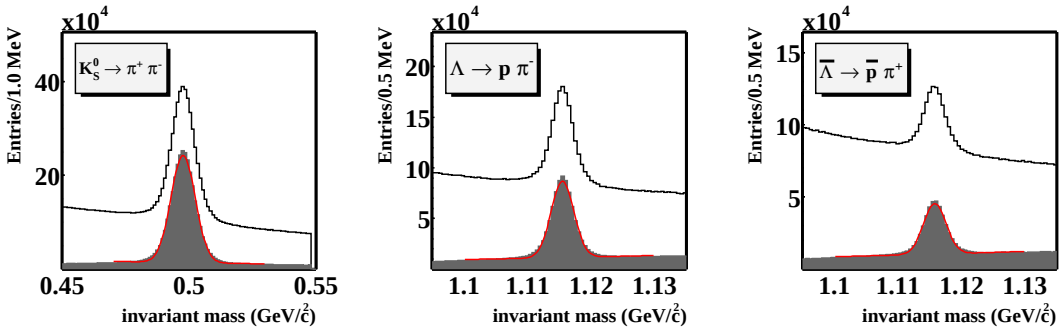

Figure 5.9. Invariant mass spectra of $\pi^+\pi^-$(left), $p\pi^-$(centre) and $\overline{p}\pi^-$(right) pairs before (histogram line) and after (filled histogram) background suppression in the full data sample.

Since a significant amount of background is still present under the peaks, we apply stronger selection criteria. The reconstructed V^0 must have:

- a impact parameter to the target smaller than 1 mm;
- a $p_T \cdot c\tau$ value larger than 0.05 GeV/$c \cdot$ cm.

The first criterion originates from the fact that particles produced in the primary interaction should point back to the target. In other words, the impact parameter to the target of the reconstructed V^0 particles should be small. We apply an upper limit cut of 1 mm, which is a soft requirement and essentially removes badly reconstructed vertices. The second criterion selects particles with a long lifetime, or particles with a short lifetime and large transverse momentum. It turns out that such a combination of cuts has a better performance than the single cuts. Here, p_T is the transverse momentum of the track pair, c is the velocity of light and τ is the proper time of flight. Note that the RICH particle identification is not used. The further suppression of background is illustrated in figure 5.9. The stronger selection criteria allow to substantially reduce the background under the peaks (and to bring it almost to zero in the case of K^0_s).

The mass spectra are fitted with a Gaussian for the peak and a simple exponential function for the background. The signal widths ($\sigma_{K^0_s} = 4.742 \pm 0.005$ MeV/c^2, $\sigma_\Lambda = 1.770 \pm 0.005$ MeV/c^2 and $\sigma_{\bar{\Lambda}} = 1.756 \pm 0.008$ MeV/c^2) are dominated by the experimental mass resolution. The number of reconstructed particles and the

extracted values of mass and width are reported in table B.1 and table B.2, for two rapidity ranges. The K^0_s candidates are accepted for the pentaquark search when the mass is within 3σ of the PDG value ($0.483\ \mathrm{GeV}/c^2 < m < 0.513\ \mathrm{GeV}/c^2$).

5.3.3 Background from Λ-K^0_s ambiguity

We have shown, in section 5.3.2, that the background under the K^0_s peak is small. Nevertheless, such a background could still produce fake structures in the p-K^0_s mass spectrum. This is due to the contamination from Λ and $\bar{\Lambda}$ decays [57]. The usual way to visualize V^0 decays is the Armenteros-Podolanski plot of figure 5.10(a). The transverse momentum of the decay products along the direction of flight of the mother particle is displayed as a function of the longitudinal momentum asymmetry.

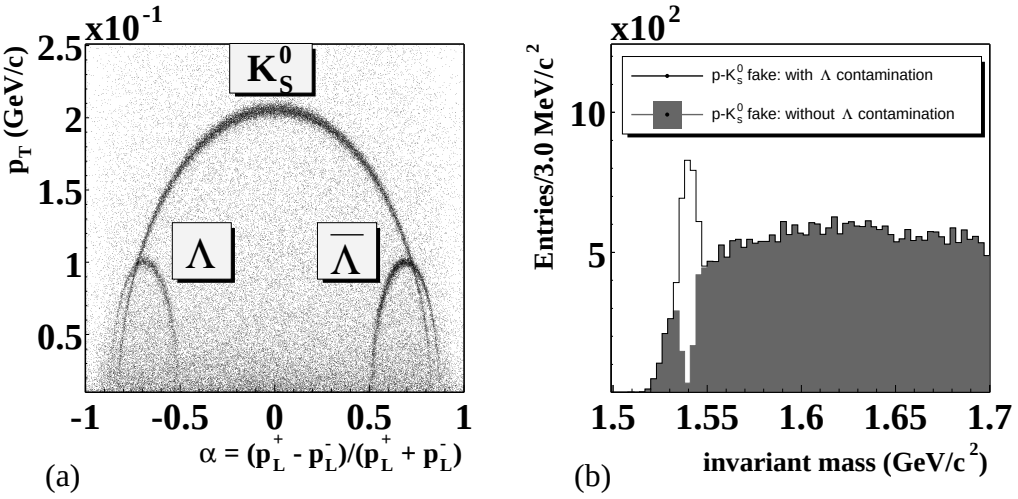

Figure 5.10. Armenteros-Podolanski plot of V^0 decays (a) and p-K^0_s invariant mass (b). In the invariant mass calculation, the proton is a clone of the π^+ originating from the K^0_s decay.

Three signal regions can be identified, one for each V^0 particle. In the region, the concentration of black dots is larger than the uniform background. There are two overlapping areas where the K^0_s cannot be distinguished from Λ and $\bar{\Lambda}$. In this kinematic region, the presence of clones produces narrow structures in the p-K^0_s mass spectrum. Specifically, the K^0_s are identified in the invariant mass spectrum of $\pi^+\pi^-$ combinations. When a clone track of the π^+ is combined with the K^0_s, the $\pi^+K^0_s$ mass spectrum presents a fake peak exactly at the position where the pentaquark signal has been claimed. This scenario is reproduced in figure 5.10(b), where the p-K^0_s invariant mass is plotted with and without K^0_s-Λ ambiguity, when the proton is a clone of the π^+. This background is suppressed with a 3σ cut around the recalculated Λ mass ($1.110\ \mathrm{GeV}/c^2 < m < 1.120\ \mathrm{GeV}/c^2$) in the K^0_s selection.

5.3.4 Selection of $\Lambda(1520)$

A different approach is used for the reconstruction of the excited Λ. The strong decay to p-K^- pairs takes place in the proximity of the target, where the track multiplicity and, as a consequence, the combinatorial background is high. The selection criteria used for data preselection, listed in section 5.2.1, are not enough to identify the $\Lambda(1520)$ signal in the p-K^- invariant mass spectrum. Therefore, we tighten the selection criteria and require:

- a proton RICH likelihood larger than 0.95;
- proton momenta between 20 GeV/c and 60 GeV/c;
- a kaon RICH likelihood larger than 0.95.

The proton momentum cut is necessary, since the proton RICH identification is not reliable outside that momentum range. The resulting invariant mass spectra of p-K^- and $\overline{p}$-K^+ combinations in the full data sample are shown in figure 5.11.

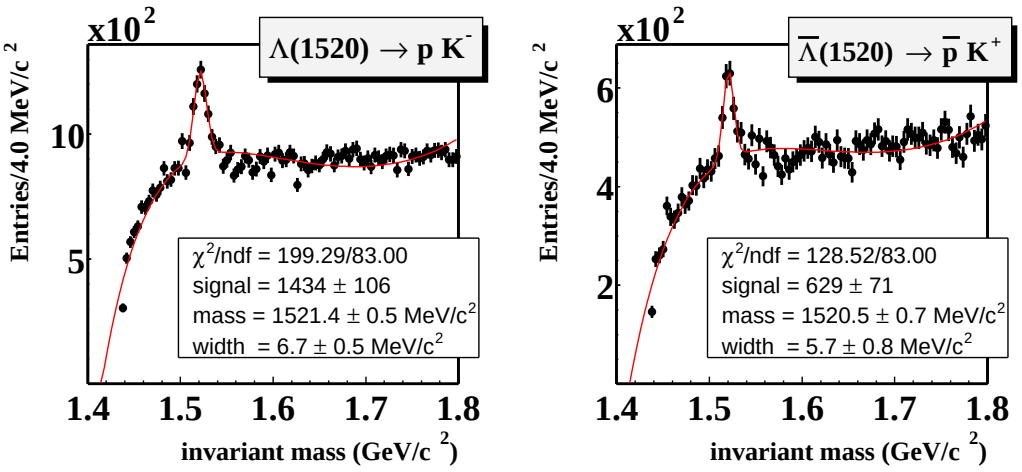

Figure 5.11. Invariant mass of p-K^- (left) and $\overline{p}$-K^+ (right) combinations.

The $\Lambda(1520)$ and $\bar{\Lambda}(1520)$ peaks are visible above a large combinatorial background, demonstrating the reliability of the proton and kaon identification. The invariant mass spectra are fitted with a Gaussian for the signal and an exponential function for the background in the range $[1.4,\ 1.8]$ GeV/c^2. The functional form used to describe the background will be introduced in equation (5.7).

The reconstructed masses, which are $m_{\Lambda(1520)} = 1521.4 \pm 0.5$ MeV/c^2 and $m_{\bar{\Lambda}(1520)} = 1520.5 \pm 0.7$ MeV/c^2, agree with the PDG value (1519.5 ± 1.0 MeV/c^2). The Gaussian width of the $\Lambda(1520)$ signal is 6.7 ± 0.5 MeV/c^2, while the $\bar{\Lambda}(1520)$ width is 5.7 ± 0.8 MeV/c^2. The width reported in the PDG is $\Gamma = 15.6 \pm 0.1$ MeV/c^2. The number of reconstructed particles (1430 ± 100) is more than two times larger than the number of antiparticles (630 ± 70). This reflects the asymmetry in the

production of matter and antimatter in proton-nucleus interactions, which can be understood in terms of quark configuration. The colliding nucleons are made of three valence quarks, in a sea of quark-antiquark pairs. $\Lambda(1520)$ is made of three valence quarks. $\bar{\Lambda}(1520)$ is made of three valence antiquarks. The probability to create a $\bar{\Lambda}(1520)$ is suppressed, since antiquarks are only present in the sea of the colliding nucleons. The number of reconstructed particles, and the experimental values of mass and width, are reported in table B.1 and table B.2, for two choices of the rapidity range.

5.3.5 Experimental p-K^0_s invariant mass

Once a proton and a K^0_s are identified, a common vertex is formed and the invariant mass is calculated. At this point of the analysis, we present the p-K^0_s mass spectra in the rapidity range $[-0.3, 0.3]$, which we shall label as mid-rapidity range. In the next section, we will check the validity of this choice. The invariant mass spectra of p-K^0_s combinations at mid-rapidity in the carbon, titanium and tungsten samples, as well as in the full sample, are shown in figure 5.12.

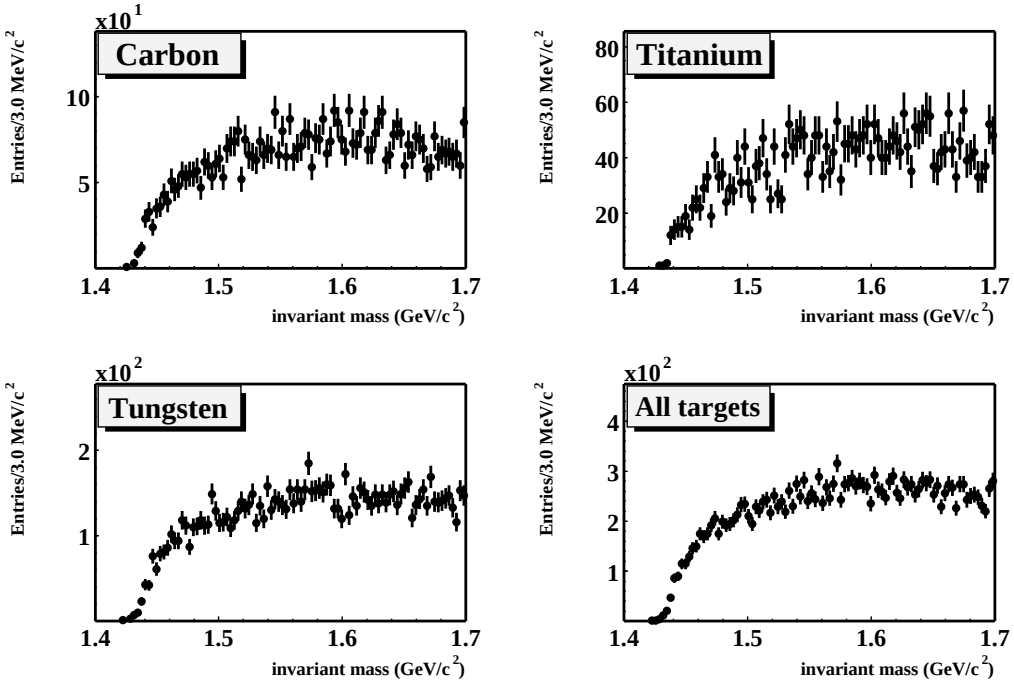

Figure 5.12. Invariant mass of p-K^0_s combinations for carbon (top-left), titanium (top-right), tungsten (bottom-left) and the full sample (bottom-right) at mid-rapidity.

Apart from statistical fluctuations, no structure is visible at the position of the claimed pentaquark, as well as at any other mass, in the presented mass spectra. Therefore, we proceed to extract the cross section upper limits.

5.3.6 Choice of rapidity range

In the previous section, we presented the invariant mass spectra in the rapidity range $[-0.3, 0.3]$. We check the consequences of enlarging the range to $[-0.5, 0.5]$. We estimate the quality of the rapidity range on the basis of the signal significance η, which we defined as

$$\eta = \frac{\varepsilon_{MC}}{N_{data}}, \tag{5.2}$$

where ε_{MC} is the pentaquark signal efficiency and is obtained with Monte Carlo simulations. The quantity N_{data} is the number of entries in the experimental mass spectrum within 3σ of the pentaquark mass (between $1.51\ \mathrm{GeV}/c^2$ and $1.57\ \mathrm{GeV}/c^2$). We take N_{data} as an estimate of the background in the pentaquark mass region. The signal significance in the two rapidity ranges is

$$\eta = (1.03 \pm 0.06)\% \times 10^{-3}, \qquad -0.3 < y < 0.3, \tag{5.3}$$

$$\eta = (0.63 \pm 0.03)\% \times 10^{-3}, \qquad -0.5 < y < 0.5. \tag{5.4}$$

Since the significance decreases when enlarging the rapidity range, we keep the mid-rapidity range $[-0.3, 0.3]$. At mid-rapidity, the total pentaquark selection efficiency, except for the proton likelihood efficiency, is

$$\varepsilon_{\Theta^+} = (0.0148 \pm 0.0007)\%, \qquad P(p) \in [20, 60]\ \mathrm{GeV}/c \tag{5.5}$$

$$\varepsilon_{\Theta^+} = (0.0218 \pm 0.0009)\%, \qquad P(p) \in [0, +\infty]\ \mathrm{GeV}/c \tag{5.6}$$

for two requirements on the proton momenta. The reduction of the proton momentum range implies an efficiency loss of about 30%. We remind the reader that the proton likelihood efficiency is evaluated from data (see section 5.3.1).

5.3.7 Event mixing

In order to quantify the statistical fluctuations visible in the experimental mass spectra, we need a functional model to parameterise the shape of the background.

Since we assume that the background is mostly composed of random combinations of protons and kaons, we use an "event mixing" technique to estimate the background. The idea is to simulate random combinations of tracks by mixing tracks of different events in the data. For this purpose, the K^0_s of each event is combined with protons of the next three events that pass the pentaquark selection. Since the shape of the combinatorial background could be affected by the number of reconstructed tracks per events, we mix events with the same track multiplicity. The invariant mass distribution of p-K^0_s combinations, after event mixing, in the carbon, titanium and tungsten samples, as well as in the full sample, are shown in figure 5.13.

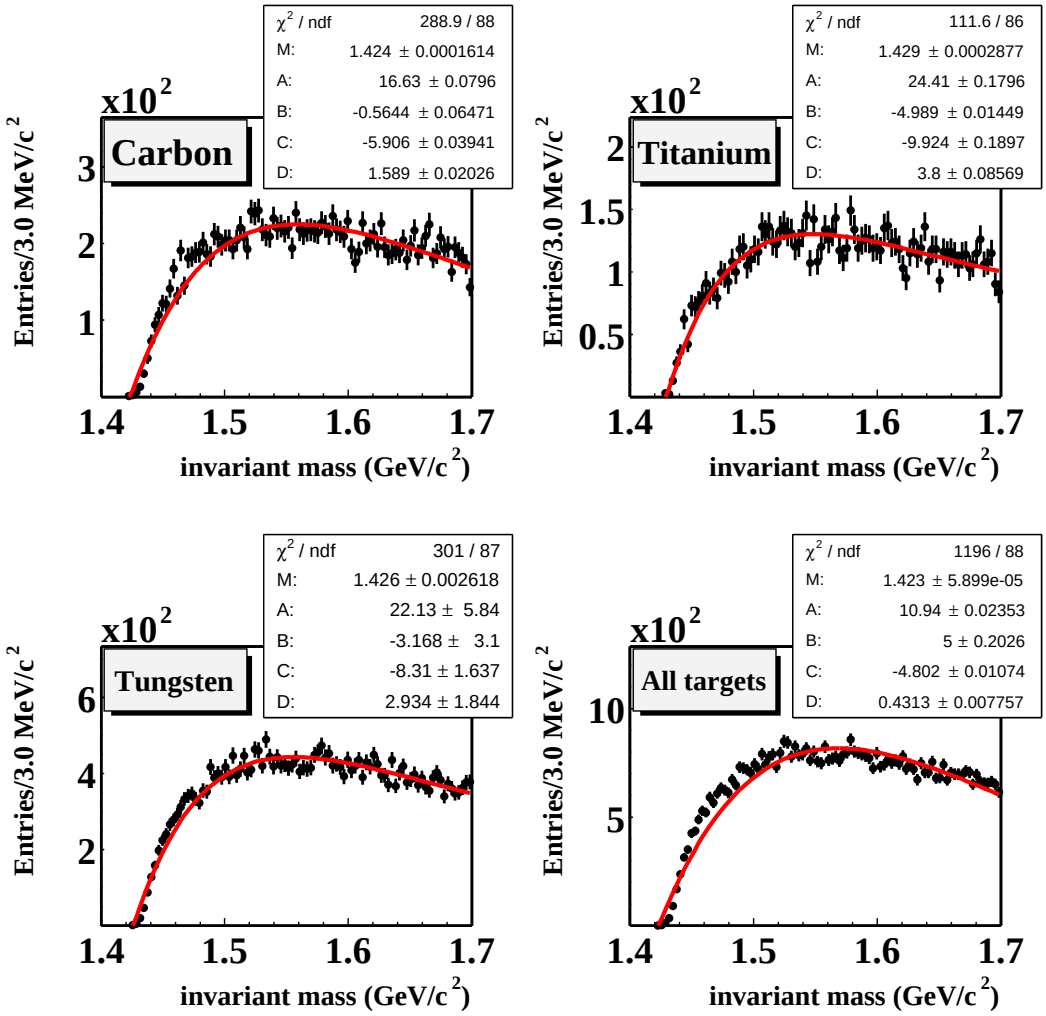

Figure 5.13. Invariant mass of p-K^0_s combinations for carbon (top-left), titanium (top-right), tungsten (bottom-left) and the full data sample (bottom-right), after event mixing. A five parameter exponential fit to the background shape is superimposed to each histogram.

The shape of the background is parameterised by the five parameter exponential function

$$f(m) = (m - M) \cdot e^{A+B\cdot m+C\cdot m^2+D\cdot m^3}. \tag{5.7}$$

The results of the fits are superimposed to the histograms in figure 5.13. We conclude that the quality of the parameterisation is satisfactory, in the mass region of the Θ^+. Since the number of entries in the mixed mass spectra are larger than those in the experimental spectra, a normalisation procedure is needed. Note that by using only data, the mixing procedure has the advantage of being independent of the quality of the Monte Carlo simulations.

5.3.8 Calculation of the cross section upper limit

The invariant mass spectra are fitted with a combination of a Gaussian signal and the background function of equation (5.7).

The Gaussian mean is fixed to $1540\ \mathrm{MeV}/c^2$. The Gaussian width is fixed to the experimental mass resolution ($5.2\ \mathrm{MeV}/c^2$). The parameters of the exponential function are obtained from a fit to the mixed mass spectra. They are fixed, with the only exception of a normalisation factor (related to the parameter A). The results of the fits are presented in figure 5.14.

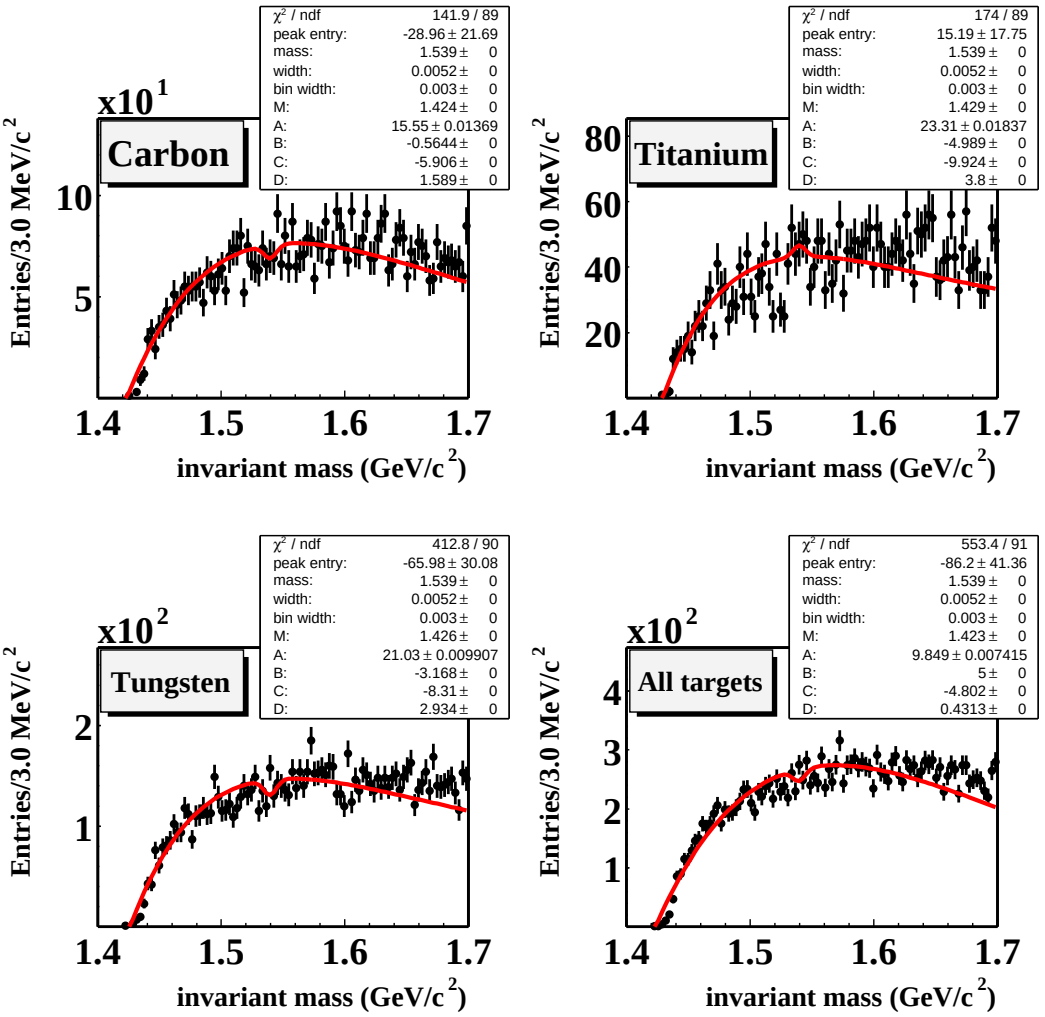

Figure 5.14. Invariant mass of p-K^0_s combinations for carbon (top-left), titanium (top-right), tungsten (bottom-left) and the full sample (bottom-right). The signal is fitted with a Gaussian having the mean fixed to $1540\ \mathrm{MeV}/c^2$ and the width fixed to the experimental mass resolution ($5.2\ \mathrm{MeV}/c^2$). The shape of the background is fixed, while a normalisation constant is left as a free parameter.

We calculate the the significance of the signal as number of entries in the peak over the uncertainty. With the tables of G.J. Feldman and R.D. Cousins [137] (see appendix C), the significance is translated into an upper limit at 95% confidence level. The upper limit on the number of counts N_{Θ^+} is then obtained as a product of the upper limit on the significance and the uncertainty of the signal. Note that this method allows to perform calculations also in case of negative signals. The formula we use to extract the cross section upper limits at mid-rapidity is

$$\mathrm{Br}(\Theta^+ \to pK^0_s) \cdot \frac{d\sigma_{\Theta^+}}{dy} < \frac{N_{\Theta^+}}{\varepsilon_{\Theta^+} \cdot \varepsilon_{RICH} \cdot \mathcal{L} \cdot A^\alpha}, \tag{5.8}$$

where $\mathcal{L}$ is the luminosity (see table 5.1), ε_{Θ^+} is the reconstruction efficiency obtained from the Monte Carlo simulations (see equation 5.5), ε_{RICH} is the proton likelihood efficiency evaluated from data, A is the atomic weight of the target and α is the nuclear suppression. We assume that the nuclear suppression is given by the geometric factor $\alpha = 2/3$.

As we have shown in figure 5.8, the proton RICH efficiency depends on the momentum. Since the momentum of protons from $\Theta^+(1540)$ and $\Lambda(1520)$ decays could be different, the correct procedure to calculate the efficiency is to convolute efficiency, as a function of the momentum, with the proton momentum distribution. The momentum distribution of protons from $\Theta^+(1540)$ and $\Lambda(1520)$ decays, when the proton likelihood is larger than 95%, is shown in figure 5.15. For $\Theta^+(1540)$, we plot the proton momentum when the p-K^0_s invariant mass is within 3σ the nominal mass position, since there is no signal in data.

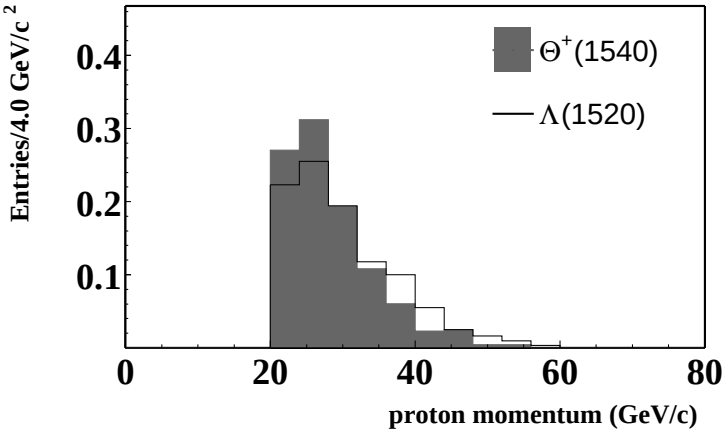

Figure 5.15. Momentum distribution of protons from $\Theta^+(1540)$ and $\Lambda(1520)$ decays, when the likelihood is larger than 95% and the invariant mass is within 3σ of the nominal position.

The distributions are normalised to the total number of entries. Protons from $\Lambda(1520)$ decays have larger momenta, as one would naively expect comparing protons produced in real particle decays with combinatorial background. The efficien-

cies of four conditions on the proton RICH likelihood, obtained as a convolution of the efficiency with the proton momentum, are shown in table 5.3.

L(p)	0.35	0.55	0.75	0.95
$\varepsilon_{RICH}(p)$ [%]	80.5 ± 0.19	77.0 ± 0.19	73.3 ± 0.19	73.1 ± 0.19

Table 5.3. Efficiency convoluted with the proton momentum, in the range $[20, 60]$ GeV/c, of four lower limits set on the RICH likelihood of the proton in p-K^0_s combinations.

The comparison with the average efficiencies presented in table 5.2 shows that the new efficiencies are larger. The upper limits on the signal counts and corresponding production cross sections, when a 95% lower limit is applied to the proton likelihood, are shown in table 5.4, for each target material. Since the Monte Carlo simulation of the carbon sample is the only available for this analysis, we assume equal efficiencies for all target configurations.

Target	Mass [GeV/c^2]	N_{Θ^+}	BR $\cdot \frac{d\sigma_{\Theta^+}}{dy}$ [μb]	BR $\cdot \frac{d\sigma_{\Theta^+}}{dy}$ [μb/nucl.]
^{12}C	1.540	19.734	7.230	1.379
^{48}Ti	1.540	50.774	139.261	10.544
^{184}W	1.540	17.749	51.108	1.580

Table 5.4. Upper limits on $\Theta^+(1540)$ production cross section at mid-rapidity.

The carbon target is the most suitable for the pentaquark search because it has the smallest atomic weight and, as a consequence, the smallest track multiplicity and combinatorial background. From this sample, we extract the upper limit on the cross section per nucleon at mid-rapidity as

$$\text{BR} \cdot \frac{d\sigma_{\Theta^+}}{dy} < 1.4 \ \mu\text{b/nucleon}. \tag{5.9}$$

In order to extract upper limits for the production of pentaquarks with other hypothetical masses between 1.5 and 1.6 GeV/c^2, we perform several mass fits. We change the mean value of the Gaussian and keep the width fixed to the experimental mass resolution. This is a dangerous procedure because the mass resolution, which affect the fit results, might depend on the mass. However, the HERA-B collaboration found that the dependence of the cross section upper limit on the mass resolution is minimal. The signal significance as a function of the mass is depicted in figure 5.16(a). The statistical fluctuations do not exceed 2σ, in the whole mass range. The upper limits on the signal counts are transformed into cross section upper limits with the same procedure illustrated for the $\Theta^+(1540)$. For this purpose, we keep the same set of reconstruction efficiencies. The dependence of the cross section upper limits on the mass are presented in figure 5.16(b). The oscillations reach a maximum of 6 μb/nucleon, for larger masses.

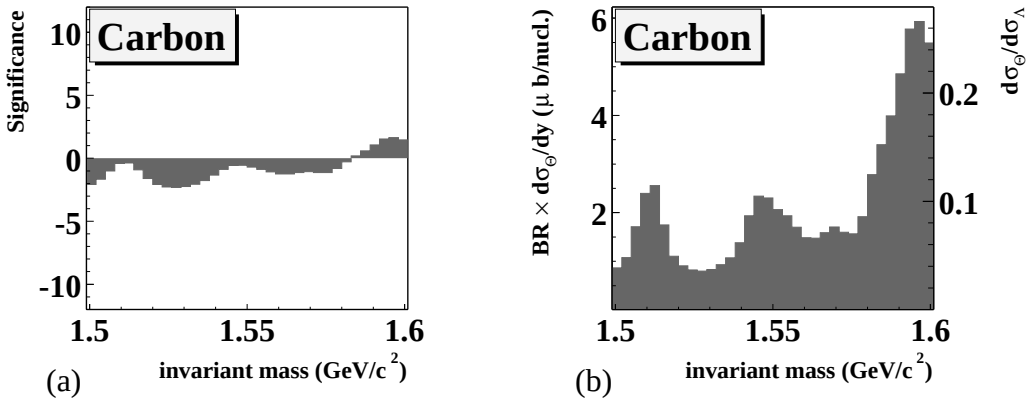

Figure 5.16. Significance of a Gaussian signal (a) and corresponding cross section upper limit (b) as a function of the p-K^0_s invariant mass. The results are extracted from the carbon sample.

Upper limit on cross section ratio

Since a clear $\Lambda(1520)$ signal could be observed, we also extract upper limits on the rate of $\Theta^+(1540)$ relative to $\Lambda(1520)$. The comparison is interesting because these resonances are close in mass and exhibit similar decay channels. However, the production mechanism for pentaquarks might be different from that of the conventional resonances, leading to different acceptances. Assuming the same nuclear dependence for both cross sections, the formula we use to extract the upper limit on the production cross section ratio at mid-rapidity is

$$\frac{d\sigma_{\Theta^+}}{d\sigma_\Lambda} < \frac{N_{\Theta^+}}{N_\Lambda} \cdot \frac{\varepsilon_\Lambda}{\varepsilon_{\Theta^+}} \cdot \frac{\mathrm{Br}(\Lambda \to pK^-)}{\mathrm{Br}(\Theta^+ \to pK^0_s) \times \mathrm{Br}(K^0_s \to \pi^+\pi^-)}, \tag{5.10}$$

where N_{Θ^+} is the upper limit on the number of pentaquarks, N_Λ is the number of reconstructed $\Lambda(1520)$ decays, ε_Λ and ε_{Θ^+} are the total reconstruction efficiencies, except for the proton likelihood cut (ε_{RICH}). The efficiency ε_{Θ^+} can be found in equation (5.5). The efficiency ε_Λ, when two conditions are imposed to the proton momentum, is

$$\begin{aligned} \varepsilon_\Lambda &= (0.0063 \pm 0.0006)\%, & P(p) &\in [20, 60]\ \mathrm{GeV}/c \\ \varepsilon_\Lambda &= (0.0102 \pm 0.0007)\%, & P(p) &\in [0, +\infty]\ \mathrm{GeV}/c. \end{aligned}$$

The momentum restriction implies an efficiency loss of 40%, which is slightly larger than the corresponding loss for Θ^+. The branching ratio for $\Lambda \to pK^-$ decays is $45 \pm 1\%$ [2]. For pentaquarks we use a branching ratio of $25\% \times 69\% \approx 17\%$ (see section 5.1). Since the requirement on the proton likelihood is the same for the two decays, the corresponding efficiency (ε_{RICH}) should cancel out in the ratio.

Actually, we have seen in figure 5.15 that the proton momentum distributions for $\Theta^+(1540)$ and $\Lambda(1520)$ decays are slightly different. As an effect of the convolution between efficiency and momentum, the efficiency ratio could differ from unity. The upper limits for each target material, when the proton and kaon RICH likelihood are larger than 95% and the proton momentum is limited to the range $[20, 60]$ GeV/c, are shown in table 5.5.

Target	Mass [GeV/c^2]	N_{Θ^+}	N_Λ	$\frac{d\sigma_{\Theta^+}}{d\sigma_\Lambda}$
^{12}C	1.540	19.734	371	0.059
^{48}Ti	1.540	50.774	272	0.207
^{184}W	1.540	17.749	609	0.032

Table 5.5. Upper limits on $\Theta^+(1540)$ cross section relative to that of the $\Lambda(1520)$.

For the carbon sample, at mid-rapidity, we extract an upper limit of

$$\frac{d\sigma_{\Theta^+}}{d\sigma_\Lambda} < 0.059. \tag{5.11}$$

We evaluate upper limits on the cross section ratio of pentaquarks with other hypothetical masses between 1.5 and 1.6 GeV/c^2. The results, as a function of the mass, are displayed in figure 5.16(b), on the right vertical axis. In the same picture, on the left axis, we report the cross section upper limits, since they only differ by a constant factor, which is the Λ reconstruction efficiency. The upper limits oscillate around 0.05, for masses between 1.50 and 1.58 GeV/c^2, and reach values as large as 0.2, for larger masses.

5.3.9 Systematic uncertainties

We discuss the systematic uncertainties due to luminosity, branching ratios and reconstruction efficiencies. These quantities appear in equations (5.8) and (5.10).

Luminosity

The uncertainty on the measurement of luminosity affects the absolute Θ^+ cross section upper limit. The main contribution comes from the presence of a possible coasting beam [118] which is a continuous proton current under the proton bunch crossing. The systematic uncertainty has been estimated to be between 2.5% and 4.2% [118].

Branching ratios

The uncertainties on the branching ratios for $\Lambda \to pK^-$ and $\Theta^+ \to pK^0_s$ decays affect the estimate of the cross section ratio. Assuming the same uncertainty on both branching ratios, the total systematic uncertainty is 3%.

RICH likelihood

In order to study the dependence of the upper limit on the cut applied to the RICH likelihood of protons and kaons, we decrease the lower limits set to the likelihood, from 0.95 to 0.35. We keep the proton momentum within the range $[20, 60]$ GeV/c. The results for the carbon target and all efficiencies and particle yields involved in the calculations, are presented in table 5.6.

L(p)	L(k)	N_{Θ^+}	ε_{Θ^+}	ε_{RICH}	BR$\frac{d\sigma_{\Theta^+}}{dy}$ [μb/nucl.]	N_Λ	ε_Λ	$\frac{d\sigma_{\Theta^+}}{d\sigma_\Lambda}$
0.95	0.95	19.734	0.0148	0.731	1.379	371	0.0063	0.059
0.35	0.95	18.781	0.0148	0.805	1.192	406	0.0063	0.051
0.55	0.95	16.728	0.0148	0.770	1.110	392	0.0063	0.047
0.75	0.95	16.763	0.0148	0.733	1.168	362	0.0063	0.051
0.95	0.35	19.734	0.0148	0.731	1.379	410	0.0073	0.062
0.95	0.55	19.734	0.0148	0.731	1.379	393	0.0067	0.059
0.95	0.75	19.734	0.0148	0.731	1.379	354	0.0066	0.065

Table 5.6. Upper limits on the $\Theta^+(1540)$ cross section for different lower limits set on the RICH likelihood (L) of proton and kaon, selection efficiencies and particles yields.

The systematic uncertainty is evaluated as maximum efficiency variation, divided by $\sqrt{12}$. This corresponds, statistically, to assume a 68% confidence level (see footnote in section 3.4.2). Within the selected proton momentum range, the systematic uncertainty due to the RICH likelihood cut on the proton is 6%, for both measurements. The RICH likelihood cut on the kaon affects the relative yield with an uncertainty of 3%. All systematic uncertainties are reported in table 5.7.

Systematic effect	**Uncertainty on σ_{Θ^+}**	**Uncertainty on $\frac{d\sigma_{\Theta^+}}{d\sigma_\Lambda}$**
ε_{Θ^+}	5%	5%
$\varepsilon_{RICH}(p)$	6%	6%
$\varepsilon_{RICH}(K)$	-	3%
ε_Λ	-	9%
Luminosity	4.2%	-
Branching ratio	-	3%
Total	9%	13%

Table 5.7. Summary of the systematic effects on the measurement of σ_{Θ^+} and $\frac{d\sigma_{\Theta^+}}{d\sigma_\Lambda}$.

Assuming that all systematic uncertainties are independent, we sum them in quadrature. The total systematic uncertainty is 9%, for the upper limit on Θ^+ cross section. It is 13%, for the yield relative to $\Lambda(1520)$.

5.4 Exclusive Θ^+ decays in data

The large number of tracks causes a significant combinatorial background for the pentaquark search in the p-K^0_s channel. In order to eliminate the possibility that any weak signal for an exotic state is buried underneath this background, we apply more stringent cuts and we study the effect, on the invariant mass spectrum, of several parameters that could possibly lead to the evidence of a physical signal.

The starting point is the proton and K^0_s selection presented in the previous section. In that case, the largest background suppression is caused by the restriction of proton momenta to values larger than $20\ \mathrm{GeV}/c$ and by the RICH likelihood cut. Still the background, which is essentially combinatorial, is at a level of 50 to 100 counts per $3\ \mathrm{MeV}/c^2$. All invariant mass spectra, which we shall discuss in this section, are collected in appendix D. In the appendix, as we do for most of the results shown in this section, we present results for p-K^0_s and $\overline{p}$-K^0_s channels.

5.4.1 Event topology

In order to reduce the combinatorial background, we limit the event topology by looking at events with a low track multiplicity. The fact that we restrict the search to low track multiplicity events can be interpreted as an attempt to reconstruct exclusive Θ^+ decays. This search was triggered by a similar analysis performed at HERA-B (see reference [138]). Furthermore, we apply an event tagging technique. We look at strange particles that might be simultaneously produced with the hypothetical exotic baryon ("strangeness tag").

Track Multiplicity

We use two definitions of track multiplicity, depending on the region of the detector that is crossed by the particles. We define "*long-tracks*" all reconstructed tracks that fulfil the following selection criteria,

- charged track;
- standard clone removal;
- at least 5 hits in the vertex detector;
- at least 10 hits in the outer tracker.

These tracks are labelled as "*long-tracks*" because they cross the entire detector, leaving signals in the tracking systems, before and after the magnet. We define "*short-tracks*" all tracks that have at least a track segment in the vertex detector. This definition includes particles that decay before the magnet. Vertex segments are usually discarded from the analysis because their momentum cannot be estimated. However, they provide useful information to improve the quality of the

reconstructed primary vertex position. Note that *long-tracks* are also used to reconstruct primary vertices. The typical distribution of track multiplicity in events selected for the pentaquark search are shown in figure 5.17.

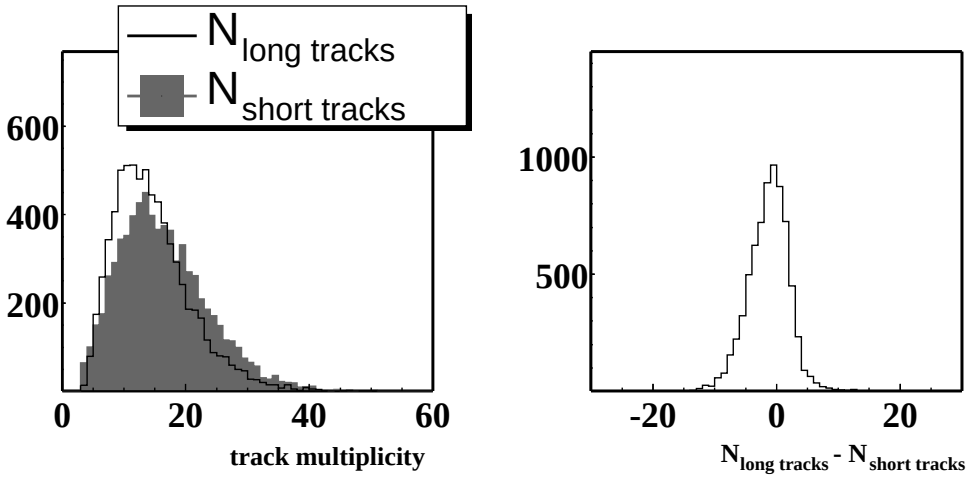

Figure 5.17. Typical *long-track* and *short-track* multiplicity distributions.

The difference between the two types of multiplicities can reach the value of 15. Therefore, we separately study the effects of several limits imposed to the number of *long-tracks* and *short-tracks*. The p-K^0_s invariant mass spectra for different values of the track multiplicity are shown in appendix D (figure D.1 and figure D.2). No structure can be seen in the proximity of $1.54\ \mathrm{GeV}/c^2$.

Strangeness tag

In this section, we release the requirement on the proton RICH likelihood (from 0.95 to 0.35) of the proton candidates. We try to compensate the increase of background by looking at other strange particles simultaneously produced with the hypothetical exotic baryon ("strangeness tag").

Since it has a strangeness $S = +1$, the Θ^+ particle must be produced together with a particle of strangeness $S = -1$ (most probably a K^- or a Λ), in order to balance the initial non-strange configuration of the proton-nucleus collision. A similar argument holds for the conjugate particle. The production of a $\bar{\Theta}^-$ is expected to be accompanied by a K^+ or a $\bar{\Lambda}$. In order to investigate the effect of a tagging technique, we present results for "correct" and "wrong" tag combinations. The term "correct" indicates that an associated particle with the expected strangeness content is found together with the Θ^+ (*i.e.* $S = -1$). The term "wrong" means the contrary, of course. The kaons used to tag the events are defined as charged tracks with a kaon likelihood larger than 0.95. One has to keep in mind that such requirement suffers from a certain amount of misidentification (see reference [94]) and sets a limit on the kaon momenta ($p > 10\ \mathrm{GeV}/c$). The Λ identification is clean (see section 5.3.2),

but a price is paid by a relevant decrease in abundance. In figure 5.18, we show the invariant mass spectra with the conditions that a Λ (or a charged kaon) is produced in coincidence with a pentaquark, for several lower limits set on the proton RICH likelihood of the protons.

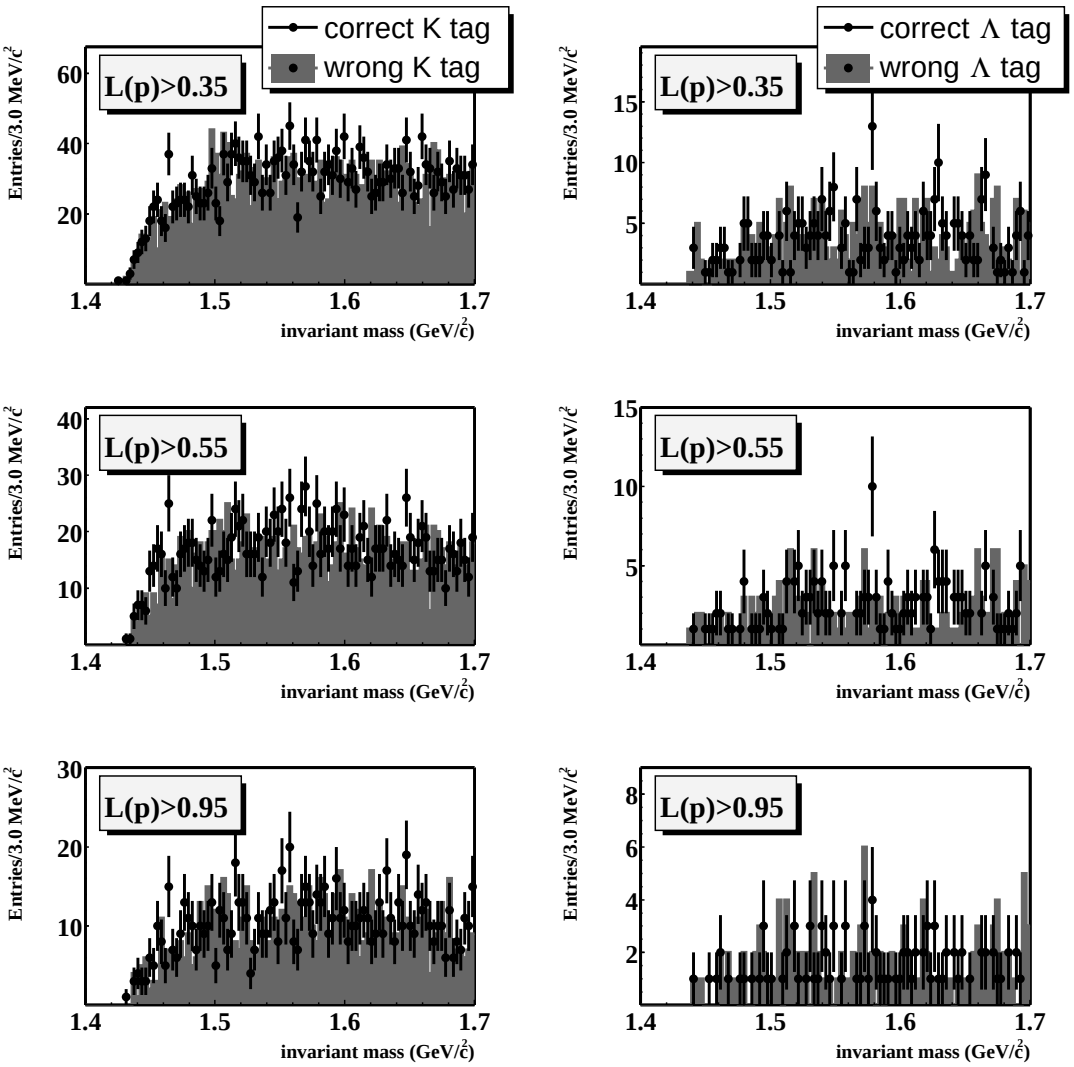

Figure 5.18. Invariant mass spectra of p-K^0_s combinations for different tagging configurations and different conditions on the RICH likelihood of the proton L(p). Dotted histograms indicate a correct tag. Grey filled histograms indicate a wrong tag.

Apart from single channel fluctuations, no structure is visible. We observe that the mass spectra obtained with correct and wrong tag are consistent with each other. Due to the fact that K^0_s and $\bar{K}^0_s$ are indistinguishable in their decay, the tagging procedure applied to K^0_s results in a random selection criterion.

5.4.2 Kinematics

In this section, we investigate the effect of the selection criteria applied to the kinematics of the p-K^0_s vertices. We study the effect of the cuts related to the quality of the secondary vertices and the lifetime of the pentaquark candidates. In addition, we restrict the momentum range of the hypothetical exotic baryons, in order to check if a signal could arise in a specific region of momenta. This effect could be due, for instance, to the existence of a specific production mechanism. Since the momentum is correlated with the invariant mass, this procedure is dangerous and could lead to fake structures in the p-K^0_s mass spectra.

Vertex quality and position

Once proton and K^0_s are combined in a common vertex, the GROVER algorithm, which is used to fit vertices, calculates the distance of closest approach between the two tracks (figure 5.19).

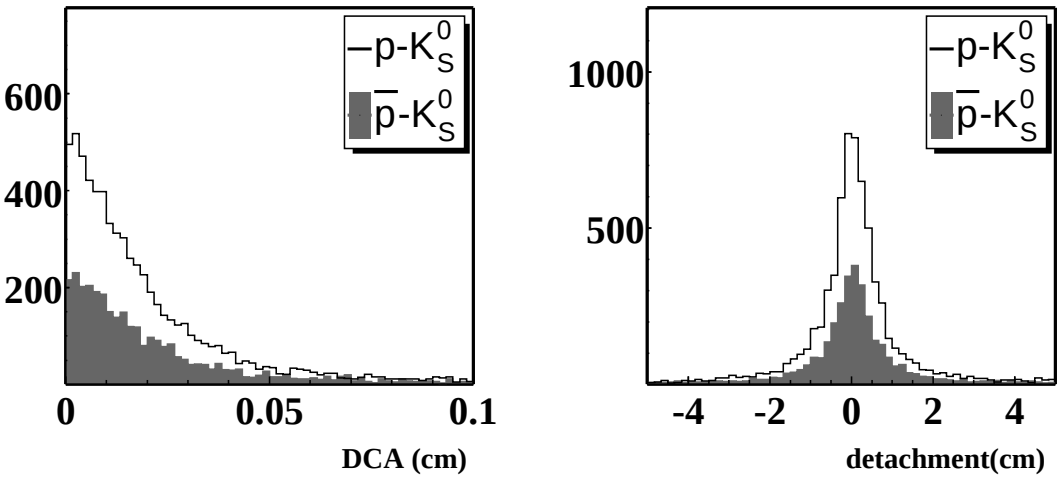

Figure 5.19. Distance of closest approach (left) and detachment (right) of p-K^0_s vertices.

Secondary particles, which are decay products of unstable particles, are expected to be close in space. Therefore, selecting small distances should enhance the signal over random combinations of tracks, which typically have larger distances. The invariant mass spectra, for several upper limits set on the distance of closest approach between proton and K^0_s, are shown in appendix D (see figure D.3).

Furthermore, we investigate the position of the reconstructed p-K^0_s vertex. Particularly interesting is the difference between the vertex and the target positions along the beam axis, which we shall call vertex detachment. The corresponding distribution for all pentaquark candidates is presented in figure 5.19. Firstly, we require that the secondary vertex is right on the target, with varying precision. The

plots are reported in appendix D (see figure D.4). This corresponds to a scenario in which pentaquarks preferentially decay in a prompt process. In addition, we investigate the possibility that there is a displacement between the secondary vertex and the target. The plots are reported in appendix D (see figure D.5). This corresponds to a scenario in which pentaquarks are stable particles. Still, one cannot recognize any suspicious structure in the vicinity of $1.54\ \mathrm{GeV}/c^2$, in any of the presented invariant mass spectra.

Vertex momentum

The effect of several conditions imposed on the transverse and total momentum of p-K^0_s candidates is shown in appendix D (see figures D.6 and D.7). Again, we cannot see no structure around $1.54\ \mathrm{GeV}/c^2$. The momenta distributions are reported in figure 5.20.

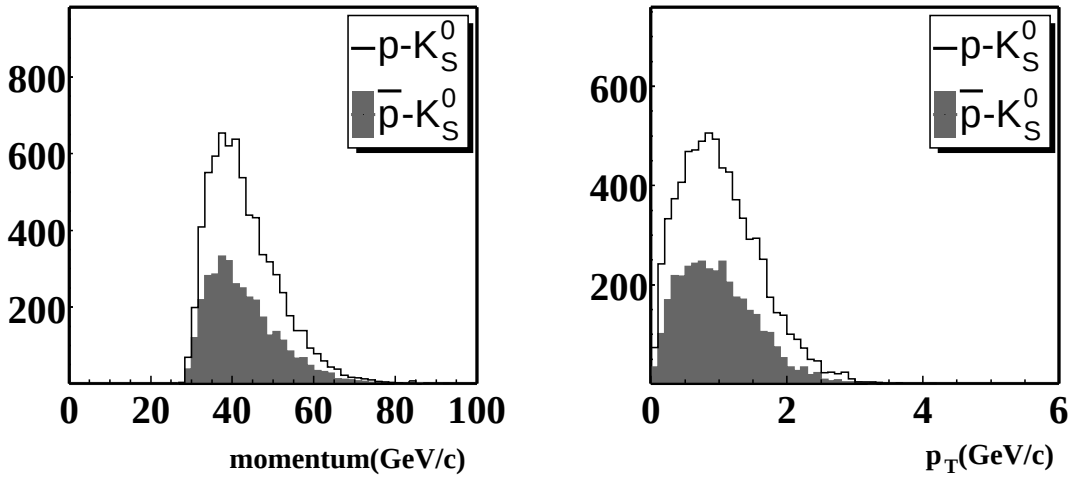

Figure 5.20. Total (left) and transverse (right) momentum of p-K^0_s vertices.

The total momentum of the p-K^0_s vertex is larger than $30\ \mathrm{GeV}/c$ for two reasons. The lower limit set on the the proton momentum ($p > 20\ \mathrm{GeV}/c$) and the detachment cut applied to the K^0_s ($p_T \cdot c\tau > 0.05\ \mathrm{GeV}/c \cdot \mathrm{cm}$).

5.4.3 Effect of $K^*(892)^+$ reflections

Two body decays can be misinterpreted as Θ^+ decays due to an incorrect particle identification. This effect is called reflection and might produce fake structures in the Θ^+ mass spectrum. One such case is the $K^{*+} \to \pi^+ K^0_s$ decay, which can be misinterpreted as a $\Theta^+ \to pK^0_s$ decay, when the pion is misidentified as a proton. In order to investigate the background due to reflections, we recalculate the p-K^0_s

invariant mass replacing the proton mass by the pion mass. The π^+-K^0_s invariant mass, without any particle identification on the pion track, is shown in figure 5.21.

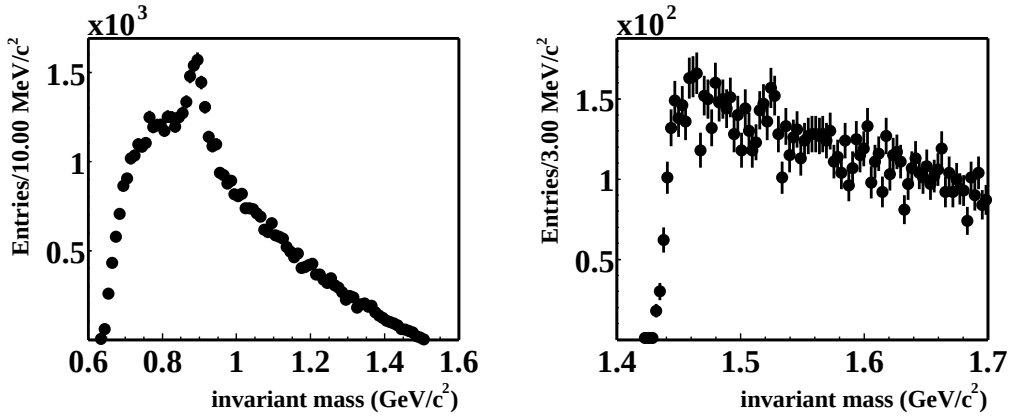

Figure 5.21. The left plot is the invariant mass distribution of π^+-K^0_s combinations, without any requirement on the RICH likelihood of the pion. The right plot is obtained for events close to the $K^*(892)^+$ mass (within 50 MeV/c^2), when the pion mass is replaced by the proton mass.

A clear signal is visible. In the same figure, we show the p-K^0_s invariant mass spectrum, when events close to the $K^*(892)^+$ mass (within 50 MeV/c^2) are selected and the pion mass is replaced by the proton mass. No clear peak is visible. This demonstrates that $K^*(892)^+$ reflections do not significantly affect the p-K^0_s invariant mass spectrum. However, a cut on the $K^*(892)^+$ mass region can introduce structures in the Θ^+ spectrum, and should be avoided. Note that the proton RICH identification helps to diminish the pion contamination in the proton candidates and thus possible mass reflections.

5.5 Summary

We searched the HERA-B minimum bias data for possible pentaquark signals. An inclusive analysis was performed to extract upper limits on the production cross section at mid-rapidity. In an exclusive analysis, we tried to isolate a signal by suppressing background, through cuts on impact parameters, distance of closest approach between tracks, and number of reconstructed tracks in the event. No signal could be established. The HERA-B collaboration was the first one to publish an upper limit for the production of pentaquarks in fixed target pA collisions [123].

"*The risk persists that pentaquarks are ephemeral events escaping the strict laws of physics*" [139].

Appendix A

List of useful runs

Minimum Bias Data

wire	run	IA [MHz]	events	$\mathcal{L}$ [mb^{-1}]	wire	run	IA [MHz]	events	$\mathcal{L}$ [mb^{-1}]
C	20653	1.36	1732592	7971.2	C	20734	0.78	7433569	32527.7
C	20663	0.55	4003997	17065.4	W	20735	0.80	1043289	604.0
C	20668	0.56	2288926	9695.1	W	20738	1.27	2080780	1280.5
C	20669	0.57	418950	1788.7	W	20739	1.20	7003330	4271.8
C	20670	0.68	2580816	11264.2	C	20740	0.74	3786598	16460.5
W	20671	0.93	2625666	1577.1	C	20742	0.73	2714468	11797.8
W	20675	1.28	7730931	4763.0	C	20743	0.75	2641525	15852.9
C	20676	0.82	675437	2973.9	W	20744	1.18	362345	218.3
C	20677	0.90	4568646	20366.5	W	20746	1.23	5002784	3054.1
C	20678	0.88	5120506	22801.7	W	20747	1.26	6219769	3834.0
W	20679	1.27	8675028	5358.3	W	20749	1.24	3897458	2391.0
W	20680	1.32	1374786	847.7	W	20764	0.86	6199374	2460.3
Ti	20682	0.96	5497520	8926.2	W	20766	0.98	4183931	1393.0
Ti	20693	0.98	573379	905.8	W	20767	1.16	2309124	81.4
Ti	20695	0.99	4722483	7566.3	C	20768	0.89	136246	10663.7
C	20705	0.79	1213497	5741.4	C	20769	0.89	2435408	1039.1
C	20723	0.92	2845949	12655.6	C	20770	0.89	7865311	34472.1
C	20724	0.96	247948	1223.3	Ti	20771	1.09	2707408	4417.8
C	20725	0.96	3147911	13742.4	Ti	20772	1.09	1677012	2718.4
C	20728	0.78	451704	1885.5	Ti	20773	1.10	5654007	9201.0

Dilepton Triggered Data

run	wire	IA [MHz]	events	run	wire	IA [MHz]	events
19890	C	2.93	12424	20346	C-W	2.92	30964
19894	C	2.90	175287	20347	C-W	3.68	65501
19896	C	4.62	250603	20348	C-W	4.87	252214
19897	C	6.94	499705	20349	C-W	4.80	246408
19898	C	4.76	51036	20350	C-W	4.77	6584
19899	C	4.79	50450	20366	C-W	2.93	116457
19918	C	4.99	142514	20367	C-W	4.91	130594
19919	C	4.94	203927	20369	C-W	4.90	126883
19924	C	4.93	165818	20370	C-W	4.83	2090779
19925	C	4.94	777164	20371	C-W	4.91	256088
19928	C	4.92	292497	20372	C-W	4.86	525306
19929	C	4.92	756484	20375	C-W	4.38	44461
19939	C	4.78	535628	20377	C-W	4.79	144517
19941	C	6.90	273991	20383	C-W	5.61	565815
19978	C	4.95	566653	20385	C-W	5.78	1286396
19982	C	4.95	90525	20386	C-W	5.43	132463
19984	C	4.94	616865	20387	C-W	4.75	415289
20010	Ti	4.99	404977	20397	C-W	5.15	918124
20029	C	4.95	301442	20398	C-W	4.47	845268
20076	C-W	4.41	150162	20401	C-W	2.96	185469
20079	C-W	4.39	126318	20402	C	2.98	100164
20080	C	4.95	34545	20403	C	4.94	233953
20124	C	3.53	31525	20404	C-W	4.52	228281
20145	C	4.96	428558	20414	C-W	2.32	696179
20154	C	4.96	135091	20423	C-W	4.30	331538
20156	C	4.91	132172	20427	C-W	4.07	146464
20157	C	4.96	102286	20431	C-W	4.67	106999
20158	C	2.93	375471	20442	C-W	4.59	204738
20159	C	2.93	133766	20443	C-W	4.54	249845
20160	C-W	2.68	125818	20446	C-W	4.31	465900
20161	C-W	2.76	39425	20447	C-W	4.39	468890
20201	C	2.96	8666	20448	C-W	4.41	223774
20202	C	2.96	71902	20450	C-W	4.53	580156
20215	C-W	2.85	8988	20451	C-W	4.49	353972
20216	C-W	2.84	245329	20452	C-W	4.45	1152089
20217	C-W	2.36	1434292	20453	C-W	4.54	261889
20218	C-W	2.03	472424	20455	C-W	5.25	821336
20220	C-W	1.97	1590736	20456	C-W	5.85	691994
20225	C-W	2.62	730444	20457	C-W	5.80	437029
20226	C-W	2.47	2619685	20505	C-W	4.21	1266145
20229	C-W	3.56	3811826	20506	C-W	2.37	1127673
20231	C-W	4.20	1660757	20517	C	4.94	137396
20233	C-W	4.10	149987	20520	C	4.95	712562
20239	C-W	3.85	1344443	20521	C	4.95	86899
20240	C-W	4.43	232545	20522	C	4.89	2064333
20242	C-W	4.20	510012	20524	C	4.68	71073
20333	C-W	4.76	974713	20526	C	5.54	202740

Dilepton Triggered Data

run	wire	IA [MHz]	events	run	wire	IA [MHz]	events
20527	C	5.50	1351924	20860	C	3.55	78526
20528	C	2.93	74505	20861	C	2.77	70560
20530	C	4.72	1091067	20862	C	2.73	9512
20531	C	4.74	107517	20863	C	2.78	49753
20534	C	4.94	1102724	20864	C	3.10	70246
20535	C	5.90	146591	20865	C	4.33	60447
20539	C	5.80	755517	20866	C	4.88	28266
20540	C	5.70	702183	20868	C	4.18	48344
20541	C	5.72	2195326	20869	C	3.66	76834
20542	C	5.74	166350	20870	C-W	4.49	89717
20543	C	5.78	30068	20874	C	2.29	99879
20544	C	5.76	5460	20876	C	2.87	123339
20545	C	5.81	1109702	20878	C	3.72	263352
20546	C	5.78	117656	20879	C	3.97	427215
20551	C	5.65	184227	20881	C-W	2.88	1535081
20586	Ti	5.02	2336371	20907	C	4.82	496345
20587	Ti	5.11	270257	20912	C-W	3.92	681443
20588	Ti	4.94	539779	20913	C-W	3.71	762931
20591	Ti	4.54	260364	20914	C-W	3.58	674334
20592	Ti	4.16	166915	20915	C-W	3.56	610099
20593	Ti	3.97	1375178	20917	C-W	3.14	571304
20612	C-W	3.34	14670	20918	C-W	3.38	562305
20616	C-W	1.62	89990	20919	C-W	3.23	83607
20617	C-W	1.45	69403	20921	C-W	3.62	577159
20622	C	0.50	34346	20922	C-W	3.77	542380
20623	C-W	3.59	321137	20923	C-W	3.97	219798
20630	C-W	1.87	31593	20924	C-W	3.84	389812
20631	C-W	1.87	20749	20926	C-W	3.67	1134765
20633	C-W	1.98	239720	20927	C-W	3.75	1039072
20636	C-W	1.89	233551	20928	C-W	3.82	273370
20637	C-W	1.88	507660	20929	C-W	3.87	596485
20638	C-W	4.67	1027138	20932	C-W	3.74	317989
20639	C-W	4.62	962596	20933	C-W	3.68	1005252
20644	C-W	2.19	28921	20934	C-W	3.48	411988
20645	C-W	1.86	711450	20938	C-W	4.44	350861
20647	C	1.83	53134	20939	C-W	4.35	361081
20648	C	2.01	30731	20940	C-W	4.19	1517754
20650	C-W	1.83	21051	20941	C-W	4.19	484234
20826	C	3.01	175399	20942	C-W	4.18	158383
20827	C	3.47	448764	20944	C-W	4.20	601964
20828	C	2.43	49573	20945	C-W	4.12	63509
20832	C	3.75	147864	20948	C-W	4.07	136750
20837	C	3.98	198547	20950	C-W	3.75	261746
20838	C	2.98	663624	20951	C-W	3.95	360011
20839	C	2.66	820953	20952	C-W	4.61	451534
20857	C-W	2.34	536951	20953	C-W	4.46	188955
20859	C	4.47	86530	20954	C-W	4.27	228704

Dilepton Triggered Data

run	wire	IA [MHz]	events	run	wire	IA [MHz]	events
20955	C-W	4.11	746153	21102	C-C	4.86	1238707
20956	C-W	4.31	189391	21104	C-C	4.80	93240
20957	C-W	4.42	332351	21122	C-W	4.74	53646
20959	C-W	2.56	15860	21123	C-W	4.45	262771
20963	C-W	4.62	144860	21124	C	4.92	823630
20964	C-W	4.12	783430	21128	C-W	4.77	60714
20967	C-W	4.05	593821	21143	Ti	5.75	276078
20969	C-W	4.09	781267	21147	C	4.85	1104289
20970	C-W	4.15	2281066	21151	Ti	2.84	269208
20972	C-W	3.15	489105	21156	C	4.56	409720
20973	C-W	3.81	158941	21157	C-W	4.76	253981
20974	C-W	3.61	107765	21159	C-W	4.74	54832
20975	C-W	4.13	830895	21160	C-W	4.58	402277
20977	C-W	3.85	220260	21161	C-W	4.24	223152
20978	C-W	4.11	2256352	21167	C	4.67	128803
20979	C-W	4.18	1675992	21170	C-W	4.61	1799738
20980	C-W	4.12	134529	21171	C-W	4.75	274006
20987	C-W	5.56	51285	21172	C-W	4.92	696274
20988	C-W	4.76	4284053	21183	C-W	4.82	250674
20989	C-W	4.57	2176392	21187	C-W	4.82	652544
20991	C	4.85	349655	21191	C-W	4.83	656000
20994	C	4.82	185987	21192	C-W	4.33	646322
20996	C	4.74	371551	21194	C-W	3.95	105550
21025	C	4.89	150395	21195	C-W	3.87	1441025
21026	C	4.87	98504	21196	C-W	3.83	316874
21028	C	4.70	170440	21197	C-W	4.88	503053
21031	C	4.78	34356	21200	C-W	4.84	410371
21032	C	4.80	163130	21201	C-W	4.86	335464
21034	C	4.79	134039	21202	C-W	4.85	203242
21035	C	4.80	917725	21203	C-W	4.65	166726
21047	C-C	4.77	1146956	21204	C-W	4.92	782594
21049	C-C	4.76	492299	21206	C-W	4.87	961613
21050	C-C	4.09	314238	21217	W	4.92	643034
21051	C-C	4.71	510377	21219	W	4.95	78415
21052	C-C	4.66	200804	21220	W	4.92	644159
21053	C-C	4.76	1310713	21221	W	4.94	2362912
21054	C-C	4.75	1288926	21222	W	4.82	2530565
21056	C-C	4.82	126945	21243	C-W	4.29	799076
21057	C-C	4.84	1013508	21244	C-W	4.64	273950
21058	C-C	4.69	1040989	21297	C-W	5.44	155645
21060	C	2.76	300951	21298	C-W	5.45	40520
21061	C	3.82	295913	21300	C-W	1.85	275988
21077	C-C	4.77	140384	21301	C-W	1.87	289224
21079	C-C	4.68	482971	21302	C-W	1.90	250898
21087	C-C	4.62	43892	21303	C-W	4.08	693443
21100	C-C	4.90	614173	21304	C-W	4.20	1260359

Appendix B

Particles statistics

$-\infty$ < rapidity < ∞			
	Statistics	Mass [MeV/c^2]	Resolution [MeV/c^2]
		K^0_s	
C	960600 ± 1100	497.675 ± 0.005	4.742 ± 0.005
Ti	452900 ± 800	497.639 ± 0.008	4.751 ± 0.008
W	1318600 ± 1200	497.713 ± 0.005	4.783 ± 0.005
All	2731700 ± 1200	497.687 ± 0.003	4.762 ± 0.003
		Λ	
C	208400 ± 500	1115.482 ± 0.005	1.770 ± 0.005
Ti	107200 ± 400	1115.461 ± 0.007	1.763 ± 0.007
W	348900 ± 700	1115.509 ± 0.004	1.792 ± 0.004
All	664600 ± 1000	1115.493 ± 0.003	1.780 ± 0.003
		$\bar{\Lambda}$	
C	102600 ± 400	1115.791 ± 0.008	1.756 ± 0.008
Ti	48100 ± 300	1115.755 ± 0.012	1.748 ± 0.013
W	154700 ± 600	1115.794 ± 0.007	1.759 ± 0.007
All	305400 ± 800	1115.792 ± 0.005	1.756 ± 0.005
		$\Lambda(1520)$	
C	440 ± 50	1520.9 ± 0.8	6.2 ± 0.7
Ti	300 ± 40	1523.4 ± 1.1	7.4 ± 1.2
W	750 ± 90	1521.0 ± 0.9	7.2 ± 1.0
All	1430 ± 100	1521.4 ± 0.5	6.7 ± 0.5
		$\bar{\Lambda}(1520)$	
C	220 ± 40	1525.6 ± 1.0	8.0 ± 1.0
Ti	110 ± 30	1520.2 ± 1.8	6.6 ± 1.6
W	350 ± 50	1519.0 ± 0.9	5.3 ± 0.8
All	630 ± 70	1520.5 ± 0.7	5.7 ± 0.8

Table B.1. Reconstructed hadron signals in the full rapidity range for each wire.

-0.3 < rapidity < 0.3			
	Statistics	Mass [MeV/c^2]	Resolution [MeV/c^2]
		K^0_s	
C	345600 ± 600	497.273 ± 0.009	4.733 ± 0.008
Ti	157600 ± 400	497.261 ± 0.014	4.787 ± 0.013
W	464800 ± 700	497.291 ± 0.008	4.743 ± 0.008
All	968000 ± 1100	497.280 ± 0.005	4.746 ± 0.005
		Λ	
C	36300 ± 200	1115.583 ± 0.011	1.762 ± 0.011
Ti	18110 ± 150	1115.580 ± 0.015	1.752 ± 0.015
W	61700 ± 300	1115.595 ± 0.008	1.800 ± 0.008
All	116100 ± 400	1115.592 ± 0.006	1.779 ± 0.006
		$\bar{\Lambda}$	
C	18580 ± 160	1115.678 ± 0.016	1.768 ± 0.016
Ti	8980 ± 110	1115.691 ± 0.024	1.810 ± 0.024
W	28900 ± 200	1115.660 ± 0.013	1.789 ± 0.013
All	56500 ± 300	1115.673 ± 0.009	1.786 ± 0.009
		$\Lambda(1520)$	
C	370 ± 50	1521.1 ± 0.9	6.3 ± 0.8
Ti	270 ± 40	1523.5 ± 1.4	8.1 ± 1.2
W	610 ± 80	1520.8 ± 0.9	7.0 ± 1.1
All	1250 ± 100	1521.3 ± 0.6	7.1 ± 0.6
		$\bar{\Lambda}(1520)$	
C	210 ± 50	1525.5 ± 2.3	8.1 ± 2.2
Ti	100 ± 30	1519.8 ± 1.9	6.3 ± 1.8
W	300 ± 50	1519.4 ± 0.9	5.4 ± 0.9
All	550 ± 60	1520.7 ± 0.7	5.6 ± 0.7

Table B.2. Reconstructed hadron signals in the rapidity range $[-0.3, 0.3]$ for each wire.

Appendix C

Feldman Cousins table

Table C.1. Confidence intervals for the mean of a Gaussian, constrained to be non-negative, as a function of the mean x_0 (in units of σ), for commonly used confidence levels [137].

x_0	68.27% C.L.	90% C.L.	95% C.L.	99% C.L.
-3.0	0.00, 0.04	0.00, 0.26	0.00, 0.42	0.00, 0.80
-2.9	0.00, 0.04	0.00, 0.27	0.00, 0.44	0.00, 0.82
-2.8	0.00, 0.04	0.00, 0.28	0.00, 0.45	0.00, 0.84
-2.7	0.00, 0.04	0.00, 0.29	0.00, 0.47	0.00, 0.87
-2.6	0.00, 0.05	0.00, 0.30	0.00, 0.48	0.00, 0.89
-2.5	0.00, 0.05	0.00, 0.32	0.00, 0.50	0.00, 0.92
-2.4	0.00, 0.05	0.00, 0.33	0.00, 0.52	0.00, 0.95
-2.3	0.00, 0.05	0.00, 0.34	0.00, 0.54	0.00, 0.99
-2.2	0.00, 0.06	0.00, 0.36	0.00, 0.56	0.00, 1.02
-2.1	0.00, 0.06	0.00, 0.38	0.00, 0.59	0.00, 1.06
-2.0	0.00, 0.07	0.00, 0.40	0.00, 0.62	0.00, 1.10
-1.9	0.00, 0.08	0.00, 0.43	0.00, 0.65	0.00, 1.14
-1.8	0.00, 0.09	0.00, 0.45	0.00, 0.68	0.00, 1.19
-1.7	0.00, 0.10	0.00, 0.48	0.00, 0.72	0.00, 1.24
-1.6	0.00, 0.11	0.00, 0.52	0.00, 0.76	0.00, 1.29
-1.5	0.00, 0.13	0.00, 0.56	0.00, 0.81	0.00, 1.35
-1.4	0.00, 0.15	0.00, 0.60	0.00, 0.86	0.00, 1.41
-1.3	0.00, 0.17	0.00, 0.64	0.00, 0.91	0.00, 1.47
-1.2	0.00, 0.20	0.00, 0.70	0.00, 0.97	0.00, 1.54
-1.1	0.00, 0.23	0.00, 0.75	0.00, 1.04	0.00, 1.61
-1.0	0.00, 0.27	0.00, 0.81	0.00, 1.10	0.00, 1.68
-0.9	0.00, 0.32	0.00, 0.88	0.00, 1.17	0.00, 1.76
-0.8	0.00, 0.37	0.00, 0.95	0.00, 1.25	0.00, 1.84
-0.7	0.00, 0.43	0.00, 1.02	0.00, 1.33	0.00, 1.93

Table C.2. Confidence intervals for the mean of a Gaussian, constrained to be non-negative, as a function of the mean x_0 (in units of σ), for commonly used confidence levels. [137].

x_0	68.27% C.L.	90% C.L.	95% C.L.	99% C.L.
-0.6	0.00, 0.49	0.00, 1.10	0.00, 1.41	0.00, 2.01
-0.5	0.00, 0.56	0.00, 1.18	0.00, 1.49	0.00, 2.10
-0.4	0.00, 0.64	0.00, 1.27	0.00, 1.58	0.00, 2.19
-0.3	0.00, 0.72	0.00, 1.36	0.00, 1.67	0.00, 2.28
-0.2	0.00, 0.81	0.00, 1.45	0.00, 1.77	0.00, 2.38
-0.1	0.00, 0.90	0.00, 1.55	0.00, 1.86	0.00, 2.48
0.0	0.00, 1.00	0.00, 1.64	0.00, 1.96	0.00, 2.58
0.1	0.00, 1.10	0.00, 1.74	0.00, 2.06	0.00, 2.68
0.2	0.00, 1.20	0.00, 1.84	0.00, 2.16	0.00, 2.78
0.3	0.00, 1.30	0.00, 1.94	0.00, 2.26	0.00, 2.88
0.4	0.00, 1.40	0.00, 2.04	0.00, 2.36	0.00, 2.98
0.5	0.02, 1.50	0.00, 2.14	0.00, 2.46	0.00, 3.08
0.6	0.07, 1.60	0.00, 2.24	0.00, 2.56	0.00, 3.18
0.7	0.11, 1.70	0.00, 2.34	0.00, 2.66	0.00, 3.28
0.8	0.15, 1.80	0.00, 2.44	0.00, 2.76	0.00, 3.38
0.9	0.19, 1.90	0.00, 2.54	0.00, 2.86	0.00, 3.48
1.0	0.24, 2.00	0.00, 2.64	0.00, 2.96	0.00, 3.58
1.1	0.30, 2.10	0.00, 2.74	0.00, 3.06	0.00, 3.68
1.2	0.35, 2.20	0.00, 2.84	0.00, 3.16	0.00, 3.78
1.3	0.42, 2.30	0.02, 2.94	0.00, 3.26	0.00, 3.88
1.4	0.49, 2.40	0.12, 3.04	0.00, 3.36	0.00, 3.98
1.5	0.56, 2.50	0.22, 3.14	0.00, 3.46	0.00, 4.08
1.6	0.64, 2.60	0.31, 3.24	0.00, 3.56	0.00, 4.18
1.7	0.72, 2.70	0.38, 3.34	0.06, 3.66	0.00, 4.28
1.8	0.81, 2.80	0.45, 3.44	0.16, 3.76	0.00, 4.38
1.9	0.90, 2.90	0.51, 3.54	0.26, 3.86	0.00, 4.48
2.0	1.00, 3.00	0.58, 3.64	0.35, 3.96	0.00, 4.58
2.1	1.10, 3.10	0.65, 3.74	0.45, 4.06	0.00, 4.68
2.2	1.20, 3.20	0.72, 3.84	0.53, 4.16	0.00, 4.78
2.3	1.30, 3.30	0.79, 3.94	0.61, 4.26	0.00, 4.88
2.4	1.40, 3.40	0.87, 4.04	0.69, 4.36	0.07, 4.98
2.5	1.50, 3.50	0.95, 4.14	0.76, 4.46	0.17, 5.08
2.6	1.60, 3.60	1.02, 4.24	0.84, 4.56	0.27, 5.18
2.7	1.70, 3.70	1.11, 4.34	0.91, 4.66	0.37, 5.28
2.8	1.80, 3.80	1.19, 4.44	0.99, 4.76	0.47, 5.38
2.9	1.90, 3.90	1.28, 4.54	1.06, 4.86	0.57, 5.48
3.0	2.00, 4.00	1.37, 4.64	1.14, 4.96	0.67, 5.58
3.1	2.10, 4.10	1.46, 4.74	1.22, 5.06	0.77, 5.68

Appendix D

List of plots

We report the invariant mass sectra of p-K^0_s and $\overline{p}$-K^0_s combinations for several cuts imposed on kinematical and topological quantities showing the absence of any structures around the mass of the claimed $\Theta^+(1540)$ pentaquark (D.1, D.2, D.3, D.4, D.5, D.6, D.7). The last four plots (D.8, D.9, D.10, D.11) shows the muon distributions used to extract the number of double semi-muonic b decays, and from that the beauty cross section, in the HERA-B dimuon trigger data.

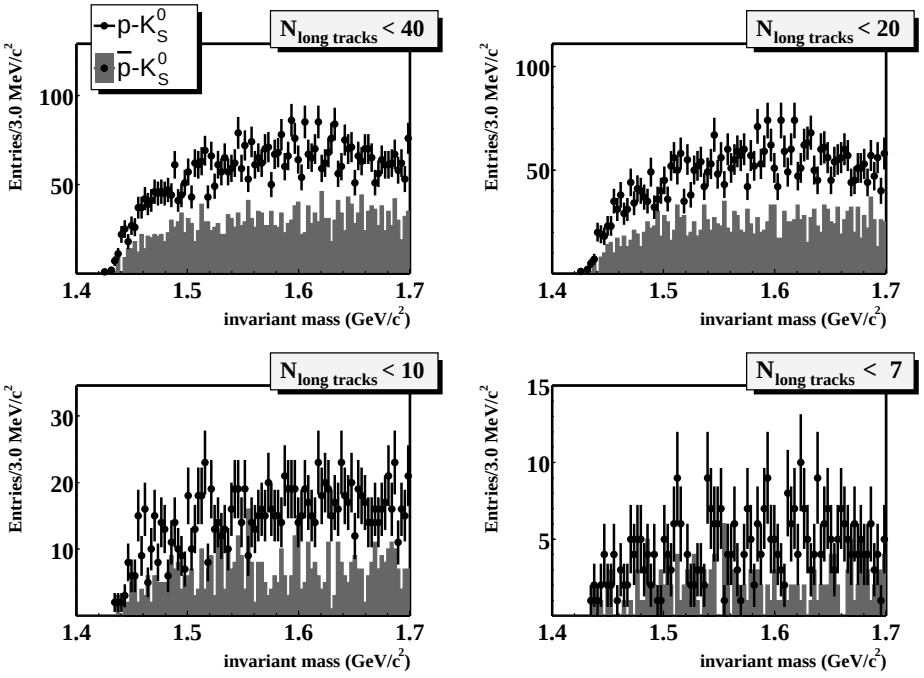

Figure D.1. Invariant mass of p-K^0_s combinations for different values of the *long-track* multiplicity.

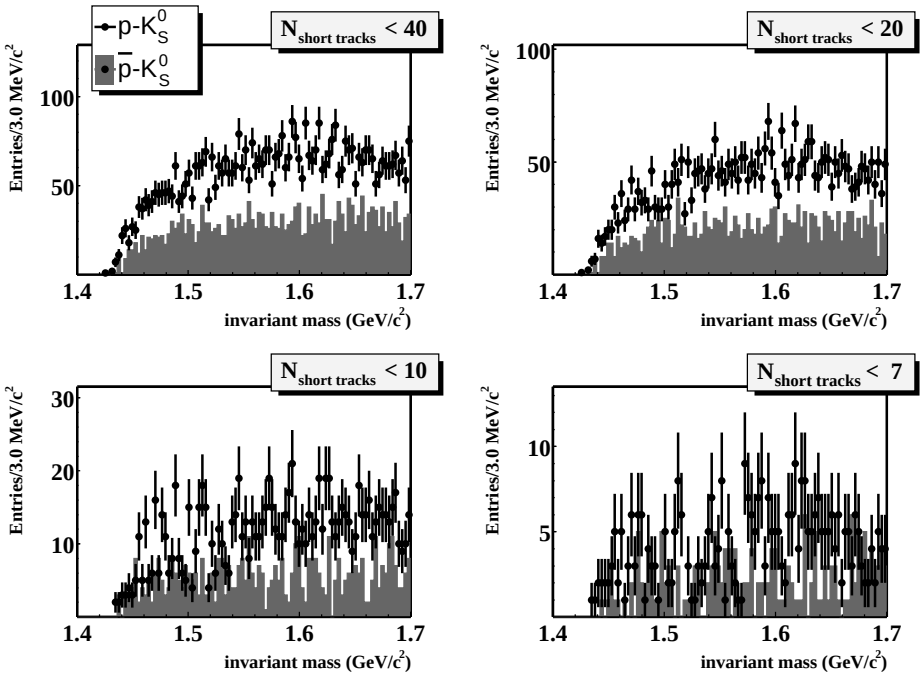

Figure D.2. Invariant mass of p-K_s^0 combinations for different values of the *short-track* multiplicity.

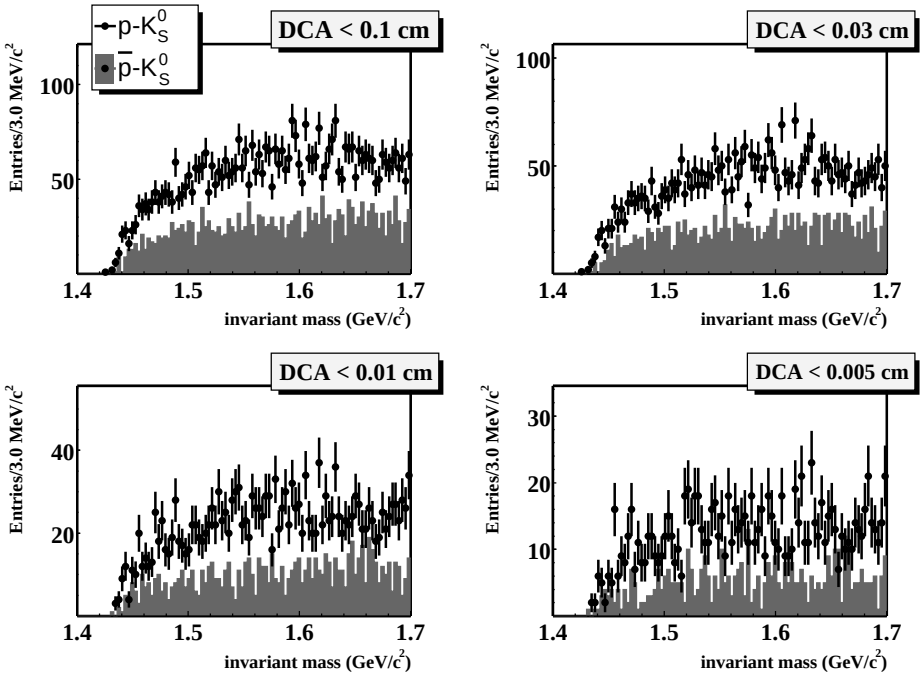

Figure D.3. Invariant mass of p-K_s^0 combinations for different cuts applied to the distance of closest approach between proton and K_s^0.

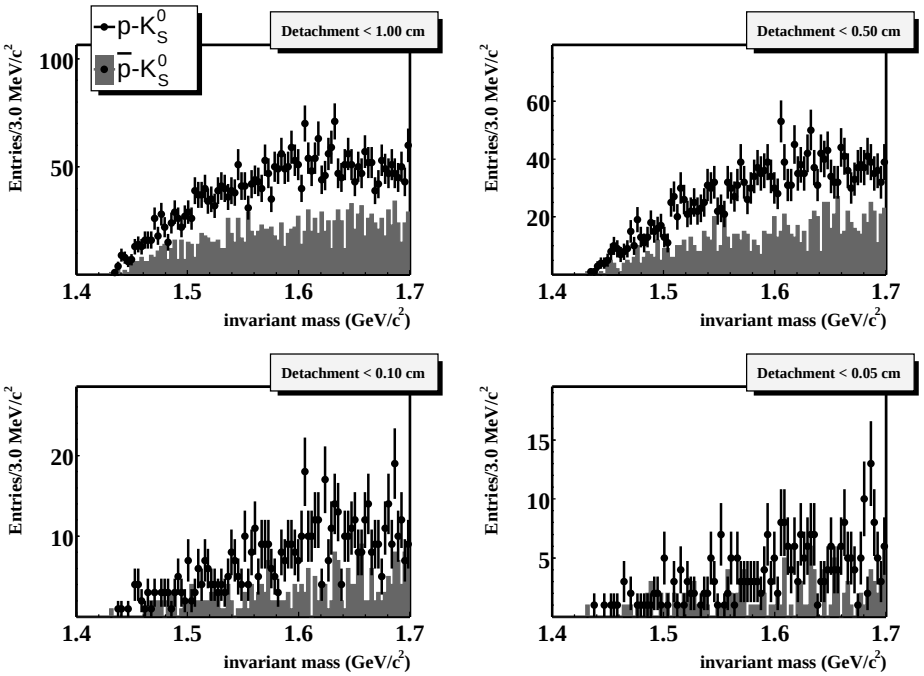

Figure D.4. Invariant mass of p-K_s^0 combinations for different upper limits set to the vertex detachment from the target.

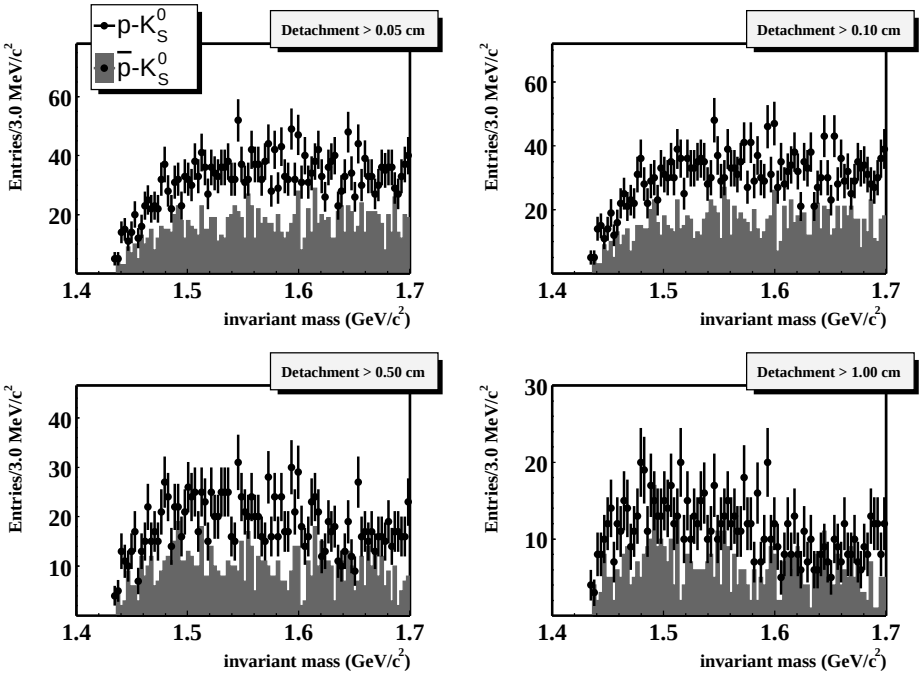

Figure D.5. Invariant mass of p-K_s^0 combinations for different lower limits set to the vertex detachment from the target.

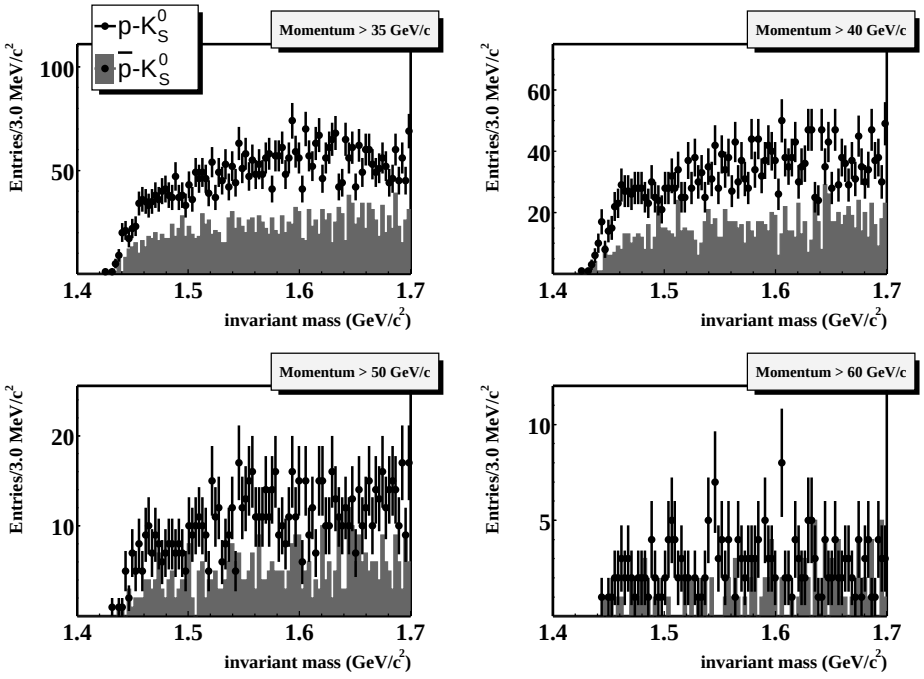

Figure D.6. Invariant mass of p-K^0_s combinations for different lower limits set to the total momentum.

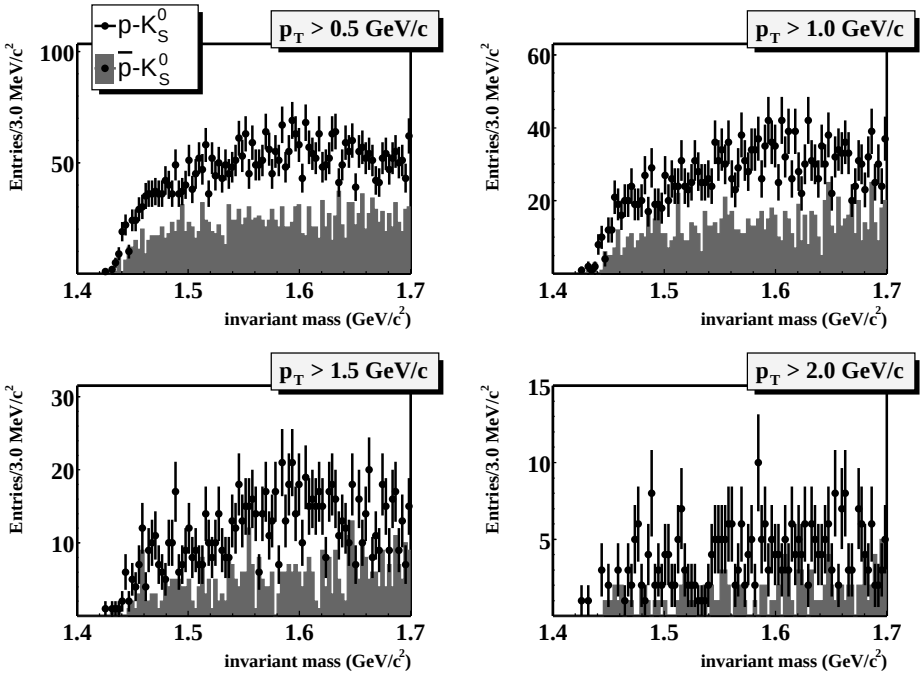

Figure D.7. Invariant mass of p-K^0_s combinations for different lower limits set to the transverse momentum.

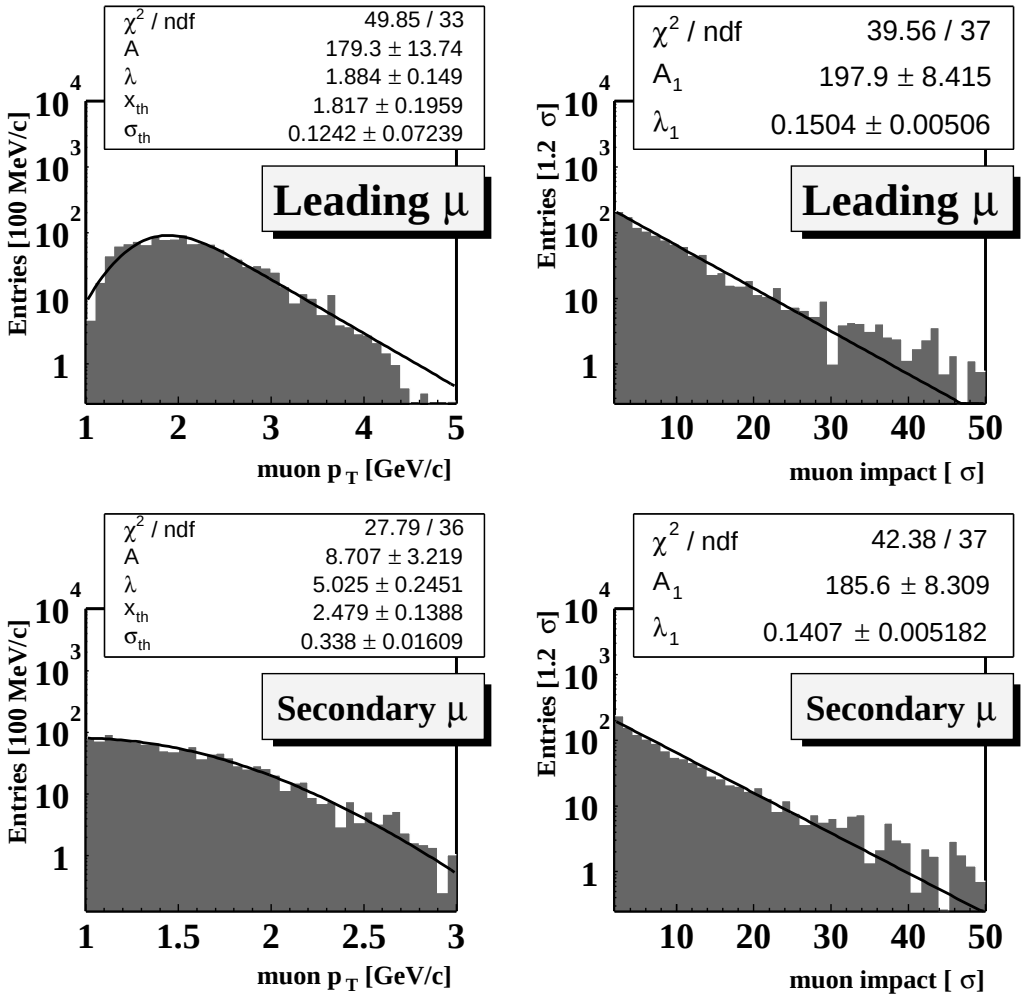

Figure D.8. Distributions of p_T (left) and impact parameter (right) of leading (top) and secondary (bottom) muons in the Monte Carlo simulation of double semi-muonic $bibj$ decays. The impact parameter is fitted with an exponential function. The momentum is fitted with the product of an exponential and a complementary error funtion.

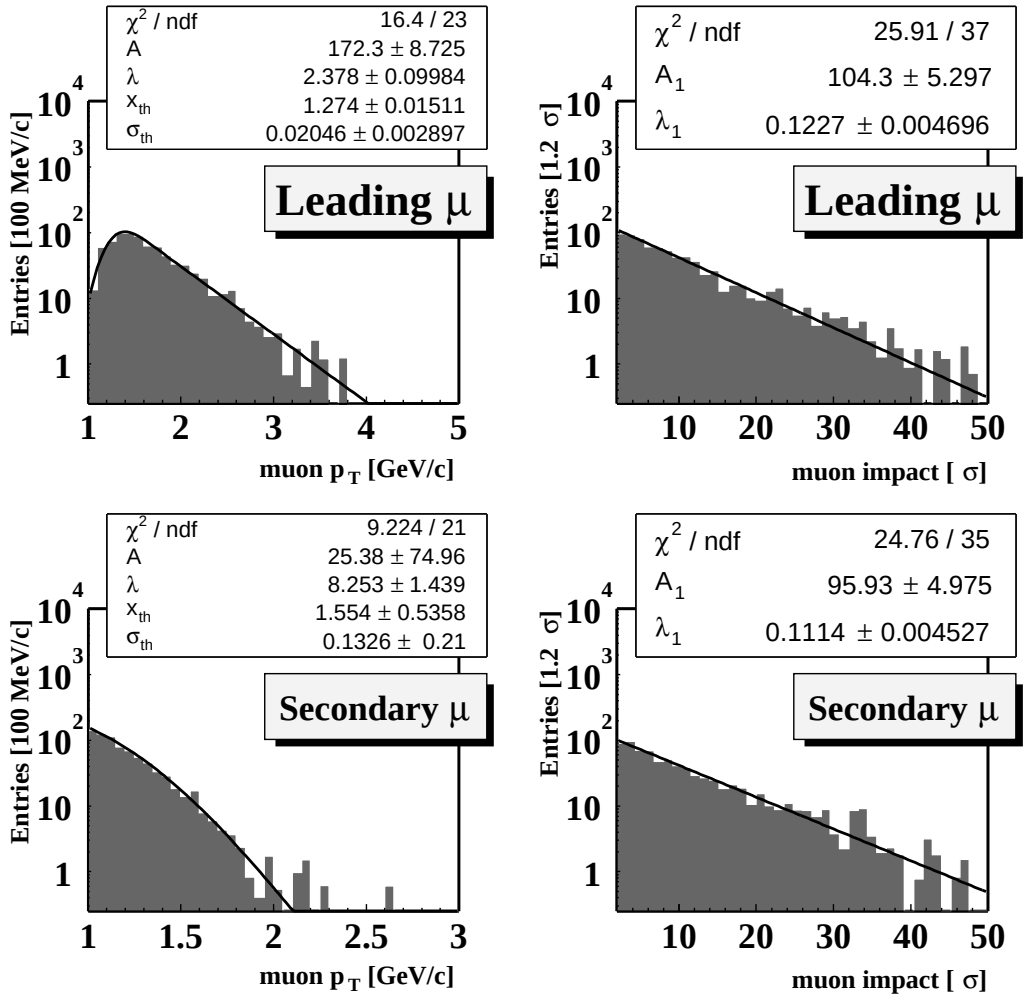

Figure D.9. Distributions of p_T (left) and impact parameter (right) of leading (top) and secondary (bottom) muons in the Monte Carlo simulation of double semi-muonic $bici$ decays. The impact parameter is fitted with an exponential function. The momentum is fitted with the product of an exponential and a complementary error funtion.

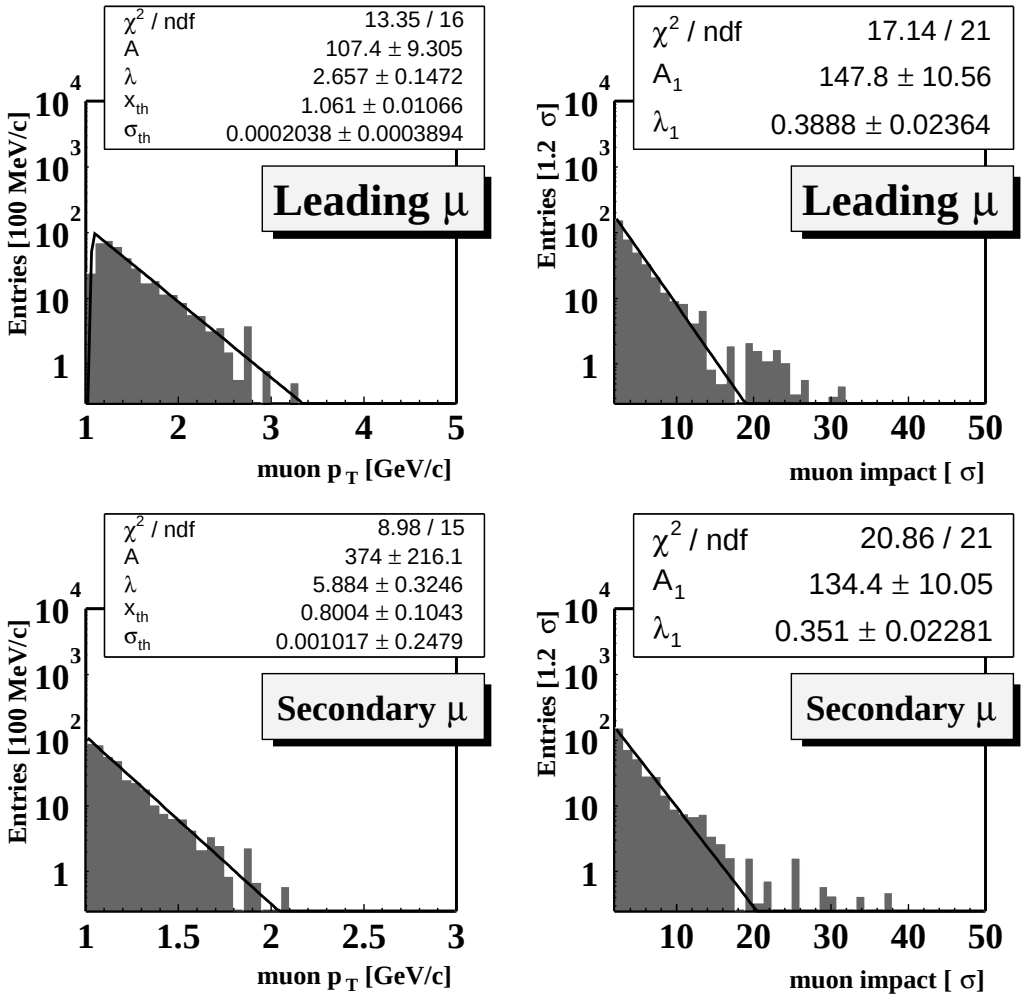

Figure D.10. Distributions of p_T (left) and impact parameter (right) of leading (top) and secondary (bottom) muons in the Monte Carlo simulation of double semi-muonic $c\bar{c}$ decays. The impact parameter is fitted with an exponential function. The momentum is fitted with the product of an exponential and a complementary error funtion.

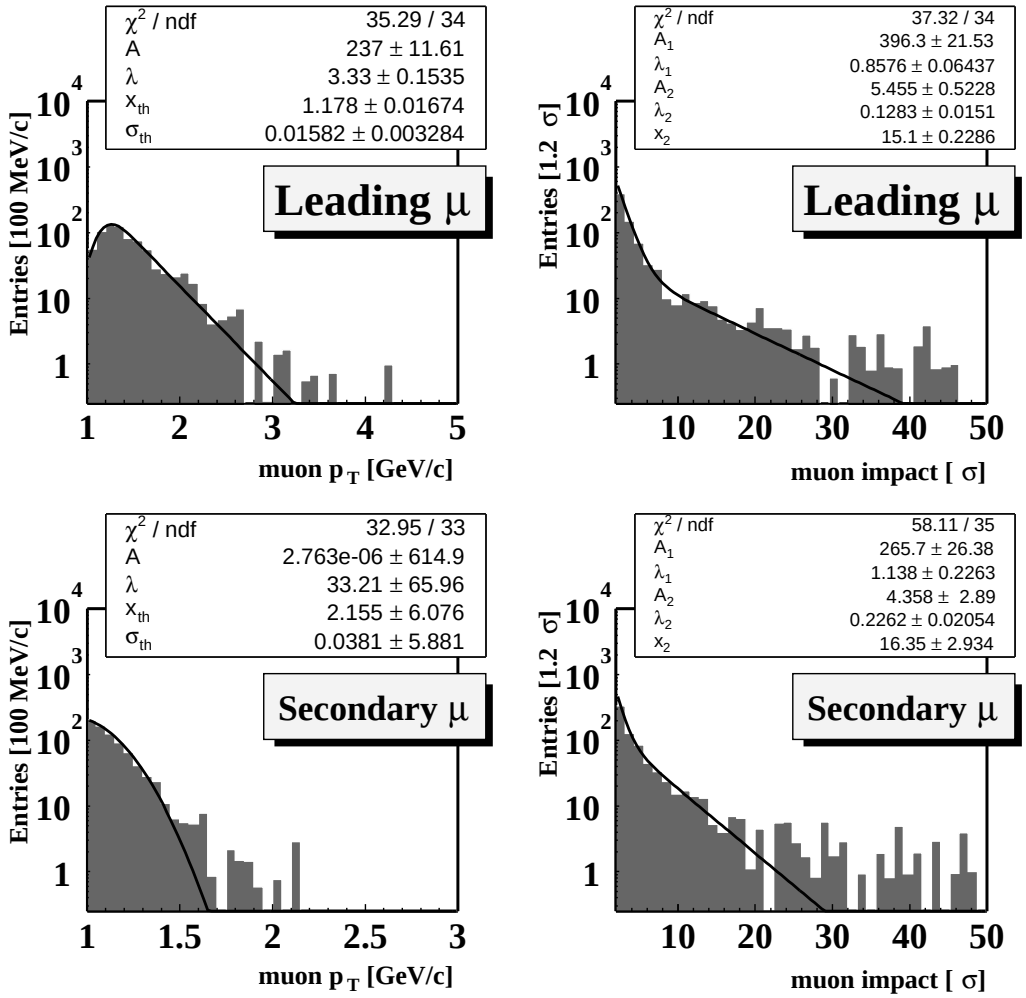

Figure D.11. Distributions of p_T (left) and impact parameter (right) of leading (top) and secondary (bottom) muons in combinatorial background. The impact parameter is fitted with two exponential functions. The momentum is fitted with the product of an exponential and a complementary error funtion.

Bibliography

[1] L. Rosenfeld, *Nuclear forces*, Interscience Publishers, New York, 1948.

[2] S. Eidelman *et al.*, *Review of particle physics*, Phys. Lett. **B592** (2004) 1.

[3] D. Griffiths, *Introduction to elementary particles*, Wiley, New York, 1987.

[4] www.phys.psu.edu/ cteq/handbook.

[5] H. Satz and X. N. Wang, *Hard processes in hadronic interactions*, Int. J. Mod. Phys. **A10** (1995) 2881.

[6] T. Alexopoulos *et al.*, *A measurement of the $b\bar{b}$ cross section in 800 GeV/c p-Si interactions*, Phys. Rev. Lett. **82** (1999) 41.

[7] D. M. Jansen *et al.*, *Measurement of the bottom quark production cross section in 800 GeV/c p-Au collisions*, Phys. Rev. Lett. **74** (1995) 3118.

[8] A. Faessler *et al.*, *Dibaryons in nuclear matter*, J. Phys. **G24** (1998) 791.

[9] www.particleadventure.org.

[10] R. K. Ellis *et al.*, *Factorization and the parton model in QCD*, Phys. Lett. **B78** (1978) 281.

[11] S. Frixione, *Heavy flavors in perturbative QCD*, Eur. Phys. J. **C43** (2005) 103.

[12] G. Altarelli and G. Parisi, *Asymptotic freedom in parton language*, Nucl. Phys. **B126** (1977) 298.

[13] H. L. Lai *et al.*, *Global QCD analysis of parton structure of the nucleon: CTEQ5 parton distributions*, Eur. Phys. J. **C12** (2000) 375.

[14] A. D. Martin, R. G. Roberts, W. J. Stirling, and R. S. Thorne, *NNLO global parton analysis*, Phys. Lett. **B531** (2002) 216.

[15] M. Gluck, E. Reya, and A. Vogt, *Dynamical parton distributions revisited*, Eur. Phys. J. **C5** (1998) 461.

[16] N. Kidonakis *et al.*, *Sudakov resummation and finite order expansions of heavy quark hadroproduction cross sections*, Phys. Rev. **D64** (2001) 114001.

[17] M. L. Mangano, P. Nason, and G. Ridolfi, *Heavy quark correlations in hadron collisions at next-to-leading order*, Nucl. Phys. **B373** (1992) 295.

[18] S. Frixione *et al.*, *Charm and bottom production: theoretical results versus experimental data*, Nucl. Phys. **B431** (1994) 453.

[19] R. Bonciani *et al.*, *NLL resummation of the heavy quark hadroproduction cross section*, Nucl. Phys. **B529** (1998) 424.

[20] E. Laenen, *Resummation for observables at TeV colliders*, Pramana **63** (2004) 1225.

[21] N. Kidonakis *et al.*, *Threshold corrections in bottom and charm quark hadro-production at next-to-next-to-leading order*, Eur. Phys. J. **C36** (2004) 201.

[22] I. Abt, *Improved measurement of the $b\bar{b}$ production cross section in 920 GeV/c fixed-target proton-nucleus collisions*, Phys. Rev. **D73** (2006) 052005.

[23] A. Heister *et al.*, *Study of the fragmentation of b quarks into B mesons at the Z peak*, Phys. Lett. **B512** (2001) 30.

[24] H. Fritzsch, *Producing heavy quark flavours in hadronic collisions: a test of quantum chromodynamics*, Phys. Lett. **B67** (1977) 217.

[25] J. F. Amundson *et al.*, *Quantitative tests of color evaporation: charmonium production*, Phys. Lett. **B390** (1997) 323.

[26] N. Brambilla *et al.*, *Heavy quarkonium physics*, hep-ph/0412158, 2004.

[27] E. L. Berger and D. L. Jones, *Inelastic photoproduction of J/ψ and Υ by gluons*, Phys. Rev. **D23** (1981) 1521.

[28] R. Baier and R. Ruckl, *Hadronic production of J/ψ and Υ: transverse momentum distributions*, Phys. Lett. **B102** (1981) 364.

[29] G. A. Schuler, *Quarkonium production and decays*, hep-ph/9403387.

[30] W. E. Caswell and G. P. Lepage, *Effective lagrangians for bound state problems in QED, QCD and other fields theories*, Phys. Lett. **B167** (1986) 437.

[31] G. C. Nayak *et al.*, *Fragmentation, NRQCD and NNLO factorization analysis in heavy quarkonium production*, Phys. Rev. **D72** (2005) 114012.

[32] G. P. Lepage *et al.*, *Improved nonrelativistic QCD for heavy quark physics*, Phys. Rev. **D46** (1992) 4052.

[33] M. Kramer, *Quarkonium production at high-energy colliders*, Prog. Part. Nucl. Phys. **47** (2001) 141.

[34] G. T. Bodwin *et al.*, *Rigorous QCD analysis of inclusive annihilation and production of heavy quarkonium*, Phys. Rev. **D51** (1995) 1125.

[35] E. Braaten, B. A. Kniehl, and J. Lee, *Polarization of prompt J/ψ at the Tevatron*, Phys. Rev. **D62** (2000) 094005.

[36] M. J. Leitch *et al.*, *Measurement of J/ψ and ψ' suppression in pA collisions at 800 GeV/c*, Phys. Rev. Lett. **84** (2000) 3256.

[37] U. Husemann, *Measurement of nuclear effects in the production of J/ψ mesons with the HERA-B detector*, DESY-THESIS-2005-005.

[38] M. Bruinsma, *J/ψ in pA*, Ph.D. thesis, NIKHEF, 2002.

[39] F. Abe *et al.*, *J/ψ and ψ(2S) production in $p\bar{p}$ collisions at $\sqrt{s} = 1.8$ TeV*, Phys. Rev. Lett. **79** (1997) 572.

[40] W. Buchmuller and S. H. H. Tye, *Quarkonia and quantum chromodynamics*, Phys. Rev. **D24** (1981) 132.

[41] E. J. Eichten and C. Quigg, *Quarkonium wave functions at the origin*, Phys. Rev. **D52** (1995) 1726.

[42] M. Bargiotti *et al.*, *J/ψ production cross section at $\sqrt{s} = 41.6$ GeV by means of NRQCD calculations*, HERA-B Internal Note 05-015.

[43] W. J. Stirling R. K. Ellis and B. R. Webber, *QCD and collider physics*, Cambridge University Press, 1996.

[44] T. Nakano *et al.*, *Observation of S = +1 baryon resonance in photoproduction from neutron*, Phys. Rev. Lett. **91** (2003) 012002.

[45] M. Ripani, *Pentaquarks: the experimental situation*, Prepared for 16th Conference on High Energy Physics (IFAE 2004), Turin, Italy .

[46] N. Mathur *et al.*, *A study of pentaquarks on the lattice with overlap fermions*, Phys. Rev. **D70** (2004) 074508.

[47] D. Diakonov, V. Petrov, and M. V. Polyakov, *Exotic anti-decuplet of baryons: prediction from chiral solitons*, Z. Phys. **A359** (1997) 305.

[48] R. L. Jaffe, *Comment on 'Exotic anti-decuplet of baryons: Predictions from chiral solitons' by D. Diakonov et al.*, Eur. Phys. J. **C35** (2004) 221.

[49] T. H. R. Skyrme, *A unified theory of mesons and baryons*, Nucl. Phys. **31** (1962) 556.

[50] G. S. Adkins, C. R. Nappi, and E. Witten, *Static properties of nucleons in the Skyrme model*, Nucl. Phys. **B228** (1983) 552.

[51] E. Witten, *Current algebra, baryons, and quark confinment*, Nucl. Phys. **B223** (1983) 433.

[52] E. Guadagnini, *Baryons as solitons and mass fomulae*, Nucl. Phys. **B236** (1984) 35.

[53] T. D. Cohen, *Chiral soliton models, large N(c) consistency and the $\Theta^+(1540)$ exotic baryon*, Phys. Lett. **B581** (2004) 175.

[54] R. L. Jaffe and F. Wilczek, *Diquarks and exotic spectroscopy*, Phys. Rev. Lett. **91** (2003) 232003.

[55] V. Kubarovsky *et al.*, *Observation of an exotic baryon with S = +1 in photoproduction from the proton*, Phys. Rev. Lett. **92** (2004) 032001.

[56] A. R. Dzierba *et al.*, *The evidence for a pentaquark signal and kinematic reflections*, Phys. Rev. **D69** (2004) 051901.

[57] M. Zavertyaev, *The invariant mass spectra profile close to pentaquark mass region at 1.54 GeV/c^2*, hep-ph/0311250, 2003.

[58] R. A. Arndt, I. I. Strakovsky, and R. L. Workman, *K^+ nucleon scattering and exotic S = +1 baryons*, Phys. Rev. **C68** (2003) 042201.

[59] J. Barth *et al.*, *Observation of the positive strangeness pentaquark Θ^+ in photo-production with the SAPHIR detector*, Phys. Lett. **B572** (2003) 127.

[60] A. E. Asratyan *et al.*, *Evidence of a narrow p-K^0_s resonance with mass near 1533 MeV in neutrino interactions*, Phys. Atom. Nucl. **67** (2004) 682.

[61] A. Airapetian *et al.*, *Evidence for a narrow |S| = 1 baryon state at a mass of 1528* MeV/c^2 *in quasi-real photoproduction*, Phys. Lett. **B585** (2004) 213.

[62] V. Barmin *et al.*, *Observation of a baryon resonance with positive*

strangeness in K^+ collisions with Xe nuclei, Phys. Atom. Nucl. **66** (2003) 1715.

[63] S. Chekanov *et al.*, *Evidence for a narrow baryonic state decaying to p-K^0_s and $\bar{p}$-K^0_s in deep inelastic scattering at HERA*, Phys. Lett. **B591** (2004) 7.

[64] A. Aleev *et al.*, *Observation of a narrow baryon resonance decaying into p-K^0_s in pA interactions at 70 GeV/c with SVD-2 setup*, hep-ex/0401024.

[65] M. Abdel-Bary *et al.*, *Evidence for a narrow resonance at 1530 MeV/c^2 in the p-K^0_s system of the reaction pp –> $\Sigma^+ p K^0_s$ from the COSY-TOF experiment*, Phys. Lett. **B595** (2004) 127.

[66] C. Alt *et al.*, *Observation of an exotic S = -2, Q = -2 baryon resonance in pp collisions at the CERN SPS*, Phys. Rev. Lett. **92** (2004) 042003.

[67] H. G. Fischer and S. Wenig, *Are there S = -2 pentaquarks?*, Eur. Phys. J. **C37** (2004) 133.

[68] M. I. Adamovich *et al.*, *Search for the exotic $\Xi^{--}(1860)$ resonance in 340 GeV/c Σ^--nucleus interactions*, Phys. Rev. **C70** (2004) 022201.

[69] A. Aktas *et al.*, *Evidence for a narrow anti-charmed baryon state*, Phys. Lett. **B588** (2004) 17.

[70] S. Schael *et al.*, *Search for pentaquark states in Z decays*, Phys. Lett. **B599** (2004) 1.

[71] D. C. Christian *et al.*, *Search for exotic baryons in 800 GeV/c pp –> p $\overline{\Xi}^+ \pi^+ X$*, Phys. Rev. Lett. **95** (2005) 152001.

[72] M. Wang, *Pentaquark results from CDF*, FERMILAB-CONF-04-446-E.

[73] M. J. Longo *et al.*, *High statistics search for the $\Theta^+(1540)$ pentaquark*, Phys. Rev. **D70** (2004) 111101.

[74] B. Aubert *et al.*, *Search for strange pentaquark production in $e^- e^+$ annihilations at $\sqrt{s} = 10.58$ GeV and in $\Upsilon(4S)$ decays*, hep-ex/0408064, 2004.

[75] M. Battaglieri *et al.*, *Search for Θ^+ pentaquark in high statistics measurement of $\gamma\, p \to \bar{K}^0 K^+ n$ at CLAS*, hep-ex/0510061, 2005.

[76] T. Lohse *et al.*, *HERA-B proposal*, DESY-PRC 94/02.

[77] E. Hartouni *et al.*, *HERA-B technical design report*, DESY-PRC 95/01.

[78] B. Schwingenheuer, *Electronics commissioning experience at HERA-B*, HERA-B Internal Note 01-114.

[79] A. Abashian *et al.*, *The Belle detector*, Nucl. Instrum. Meth. **A479** (2002) 117.

[80] B. Aubert *et al.*, *The BaBar detector*, Nucl. Instrum. Meth. **A479** (2002) 1.

[81] HERA-B collaboration, *HERA-B physics in 2001/2002*, December 2002, Letter to the DESY directorate.

[82] HERA-B collaboration, *Update of status and plans for 2001/2002*, HERA-B Internal Note 01-064.

[83] U. Holm *et al.*, *The ZEUS detector: status report 1993*, http://www-zeus.desy.de/bluebook/bluebook.html.

[84] I. Abt *et al.*, *The H1 detector at HERA*, Nucl. Instrum. Meth. **A386** (1997) 310.

[85] K. Ackerstaff *et al.*, *HERMES spectrometer*, Nucl. Instrum. Meth. **A417** (1998) 230.

[86] K. Ehret *et al.*, *Observation of coasting beam at the HERA proton ring*, Nucl. Instrum. Meth. **A456** (2001) 206.

[87] www-hera-b.desy.de/subgroup/detector/target.

[88] C. Bauer *et al.*, *Performance of the HERA-B vertex detector system*, Nucl. Instrum. Meth. **A501** (2003) 39.

[89] I. Abt *et al.*, *Update on the performance of the HERA-B vertex detector system*, Nucl. Instrum. Meth. **A511** (2003) 24.

[90] Y. Bagaturia *et al.*, *Studies of aging and HV break down problems during development and operation of MSGC and GEM detectors for the inner tracking system of HERA-B*, ICFA Instrum. Bull. **24** (2002) 54.

[91] H. Albrecht *et al.*, *The outer tracker detector of the HERA-B experiment. Part II: front-end electronics*, Nucl. Instrum. Meth. **A541** (2005) 610.

[92] W. D. Hulsbergen, *A study of track reconstruction and massive dielectron production in HERA-B*, Ph.D. thesis, NIKHEF, 2002.

[93] H. Albrecht *et al.*, *Aging studies for the large honeycomb drift tube system of the outer tracker of HERA-B*, Nucl. Instrum. Meth. **A515** (2003) 155.

[94] I. Arino *et al.*, *The HERA-B ring imaging Čerenkov counter*, Nucl. Instrum. Meth. **A516** (2004) 445.

[95] A. Zoccoli, *The electromagnetic calorimeter of the HERA-B experiment*, Nucl. Instrum. Meth. **A446** (2000) 246.

[96] V. Eiges *et al.*, *The muon detector at the HERA-B experiment*, Nucl. Instrum. Meth. **A461** (2001) 104.

[97] M. Titov *et al.*, *Aging studies for the muon detector of HERA-B*, Nucl. Instrum. Meth. **A515** (2003) 202.

[98] A. Belkov, *Study of muon misidentification in the HERA-B experiment*, HERA-B Internal Note 02-036.

[99] M. Dam *et al.*, *HERA-B data acquisition system*, Nucl. Instrum. Meth. **A525** (2004) 566.

[100] J. Hernandez *et al.*, *HERA-B framework for online calibration and alignment*, Nucl. Instrum. Meth. **A546** (2005) 574.

[101] www-hera-b.desy.de/subgroup/software/arte.

[102] I. Abt *et al.*, *CATS: a cellular automaton for tracking in silicon for the HERA-B vertex detector*, Nucl. Instrum. Meth. **A489** (2002) 389.

[103] I. Abt *et al.*, *Cellular automaton and Kalman filter based track search in the HERA-B pattern tracker*, Nucl. Instrum. Meth. **A490** (2002) 546.

[104] R. Mankel *et al.*, *The concurrent track evolution algorithm: extension for track finding in the inhomogeneous magnetic field of the HERA-B spectrometer*, Nucl. Instrum. Meth. **A426** (1999) 268.

[105] R. Mankel, *A concurrent track evolution algorithm for pattern recognition in the HERA-B main tracking system*, Nucl. Instrum. Meth. **A395** (1997) 169.

[106] O. Igonkina, *MARPLE - version 1.03*, HERA-B Internal Note 98-129.

[107] V. Alberico *et al.*, *The reconstruction for the electromagnetic calorimeter of the HERA-B experiment*, ICCHEP 97 conference, Tucson, AZ, Nov 1997.

[108] M. Staric and P. Krizan, *An iterative method for the analysis of Čerenkov rings in the HERA-B RICH*, Nucl. Instrum. Meth. **A433** (1999) 279.

[109] www-hera-b.desy.de/subgroup/detector/rich.

[110] R. Pestotnik, *Identification of pions, kaons and protons in the HERA-B spectrometer*, Ph.D. thesis, Univ. Lljubljana, 2001.

[111] B. Fominykh, *MUREC-A reconstruction program for HERA-B muon detector operating in stand-alone mode*, HERA-B Internal Note 97-167.

[112] www-hera-b.desy.de/subgroup/software/arte/grover.

[113] M. C. Abreu *et al.*, *Evidence for deconfinement of quarks and gluons from the J/ψ suppression pattern measured in Pb-Pb collisions at the CERN-SPS*, Phys. Lett. **B477** (2000) 28.

[114] H. Wahlberg, *Bottom production at $\sqrt{s} = 41.6$ GeV*, Ph.D. thesis, NIKHEF, 2005.

[115] S. Frixione, M. L. Mangano, P. Nason, and G. Ridolfi, *Heavy quark production*, Adv. Ser. Direct. High Energy Phys. **15** (1998) 609.

[116] H. Kolanoski, *HERA-B results on heavy flavour production in 920 GeV/c proton-nucleus interactions*, J. Phys. **G31** (2005) S799.

[117] I. Gorbounov, *Pattern recognition in the inner tracking system of HERA-B and measurement of the V0 production cross section in pN collisions*, Ph.D. thesis, 2004.

[118] C. van Eldik, *K*(892) production in proton-nucleus collisions*, DESY-THESIS-2004-019.

[119] E. Klinkby, *$\Lambda/\bar{\Lambda}$ polarisation studies in proton-nucleus collisions at 920 GeV/c proton beam energy*, Ph.D. thesis, 2004.

[120] J. Soffer, *Is the riddle of the hyperon polarizations solved?*, hep-ph/9911373.

[121] L. Apanasevich *et al.*, *Measurement of direct photon production at Tevatron fixed target energies*, Phys. Rev. **D70** (2004) 092009.

[122] I. Abt *et al.*, *Search for the flavor-changing neutral current decay $D^0 \to \mu^+\mu^-$ with the HERA-B detector*, Phys. Lett. **B596** (2004) 173.

[123] I. Abt *et al.*, *Limits for the central production of Θ^+ and Ξ^{--} pentaquarks in 920 GeV/c pA collisions*, Phys. Rev. Lett. **93** (2004) 212003.

[124] V. Balagura *et al.*, *The first-level trigger of the HERA-B experiment: performance and expectations*, Nucl. Instrum. Meth. **A494** (2002) 526.

[125] H. Fleckenstein, *Performance of the TFU network of the first level trigger of HERA-B and determination of efficiencies for $J/\psi \to \mu^+\mu^-$*, DESY-THESIS-2002-011.

[126] H. Albrecht, *The outer tracker detector of the HERA-B experiment. Part I: detector*, physics/0507048, 2005.

[127] V. Balagura, *MU1 efficiency at FLT*, HERA-B Internal Note 02-035.

[128] V. Balagura, *FLT efficiency maps*, HERA-B Internal Note 03-024.

[129] J. Ivarsson *et al.*, *PYTHIA and FROTIOF: event generators for HERA-B*, HERA-B Internal Note 99-067.

[130] T. Sjostrand, *High-energy physics event generation with PYTHIA 5.7 and JETSET 7.4*, Comput. Phys. Commun. **82** (1994) 74.

[131] B. Andersson, G. Gustafson, and H. Pi, *The FRITIOF model for very high-energy hadronic collisions*, Z. Phys. **C57** (1993) 485.

[132] H. Pi, *An event generator for interactions between hadrons and nuclei: FRITIOF version 7.0*, Comput. Phys. Commun. **71** (1992) 173.

[133] R. Brun *et al.*, *GEANT3*, Internal report CERN DD/EE/84-1.

[134] M. A. Pleier, *Cloneremove V1.0*, HERA-B Internal Note 01-062.

[135] A. Spiridonov, *Bremsstralung in leptonic onia decays: effects on mass spectra*, HERA-B Internal Note 04-016.

[136] R. Brun and F. Rademakers, *ROOT: An object oriented data analysis framework*, Nucl. Instrum. Meth. **A389** (1997) 81.

[137] G. J. Feldman and R. D. Cousins, *A unified approach to the classical statistical analysis of small signals*, Phys. Rev. **D57** (1998) 3873.

[138] G. Medin, *Low multiplicity HERA-B data and search for a resonance in the $K^0_s p$ mass spectrum*, HERA-B Internal Note 04-012.

[139] A. Sbrizzi and T. S. Bauer, *Have pentaquarks been seen?*, AIP Conf. Proc. **768** (2005) 226.

Summary

"San Giovanni mio carissimo, vedete come trattano e vilipendono il vostro piu' devoto suddito. Vi ho chiesto forse un palazzo al corso? No. Una quaterna? No. Un terno? No. E allora? Che cosa vi ho chiesto io? Una bazzecola, una pinzillacchera, una quisquiglia, una sciocchezzuola."
San Giovanni decollato (1940) - Totò

This thesis reports on the research performed between September 2001 and December 2005 at the HERA-B experiment in pA collisions at $\sqrt{s} = 41.6\ \mathrm{GeV}$. Due to a prolonged commissioning period of the accelerator overall, data taking could not last more than 5 months, when a long shut-down of the accelerator provoked the end of the experiment. Two data samples of about 150 M dilepton triggered and 200 M minimum bias data were collected for physics studies. The large acceptance of the detector, the high spatial resolution for primary and secondary vertices, the selective trigger and the multi-target operation allowed the study of many physics topics [81, 82], where the study of heavy quark production plays a leading role.

Chapter 1 gives an overview of the theoretical description of heavy quark production and subsequent formation of bound states in pA collisions. Due to the large mass of the b quarks, the measurement of the inclusive beauty production cross section ($\sigma_{b\bar{b}}$) in hadron collisions offers the possibility to test the predictive power of perturbative QCD. The calculation of $\sigma_{b\bar{b}}$ at NLO [17, 18] fails to give an accurate prediction near the kinematic threshold, where large contributions come from higher order processes, such as soft gluon emission. In order to account for these effects, Bonciani *et al.*[19] and Kidonakis *et al.*[21] improved the calculations by using two different resummation techniques, but the uncertainties in the predictions are still large. Three measurements of $\sigma_{b\bar{b}}$ are available from fixed target pA experiments, but those performed at the same energy are incompatible [7, 6].

The quark configuration of all experimentally observed hadrons is either $q\bar{q}$ or qqq. The existence of hadrons with exotic quark configuration (so to say different from $q\bar{q}$ and qqq) is not theoretically excluded. Two theoretical models proposed to describe the production of exotic hadrons are presented in chapter 1.

A description of the experiment is presented in chapter 2. The HERA-B detector comprises a vertex detector, a forward spectrometer with an opening angle of about 300 mrad, a ring imaging Čerenkov detector for π/K separation, an electromagnetic calorimeter and a muon detector.

A description of the first level trigger (FLT) can be found in chapter 3. The J/ψ trigger exploits the clear signatures of $\mathrm{J}/\psi \to e^+e^-$ and $\mathrm{J}/\psi \to \mu^+\mu^-$ decays. In data taking the FLT guaranteed a background reduction factor of about 200 and allowed to collect $300,000$ J/ψ (1200 per hour) with an average track efficiency

$$\varepsilon_e = 58.74 \pm 0.12_{stat} \pm 1.0_{sys}\ \% \quad \text{and}$$
$$\varepsilon_\mu = 28.25 \pm 0.12_{stat} \pm 0.7_{sys}\ \%,$$

for electrons and muons respectively. The procedure to generate FLT efficiency maps has been discussed, stressing the motivations which lead to the production of three dimensional maps to account for the observed efficiency dependence on the area of the detector traversed by the particles and their momentum.

In chapter 4 we report on a measurement of the beauty production cross section at HERA-B. In a previous HERA-B measurement (see reference [22]), the beauty cross section was extracted by selecting $b \to \mathrm{J}/\psi \to l^+l^-$ decays. The large lifetime of B hadrons and the boost provided in fixed target experiments allow the identification of b events with the J/ψ mesons detached from the primary vertex. The result of this analysis, combining muon and electron channels, is

$$\sigma_{b\bar{b}} = 14.9 \pm 2.2_{stat} \pm 2.4_{sys}\ \text{nb/nucleon}.$$

In this thesis, we have performed the same measurement by selecting double semi-muonic b decays with two different methods. Firstly, we isolate events which satisfy a set of optimised selection criteria on impact parameters, transverse momentum and vertex detachment. Secondly, the selection is released and the signal is extracted from a likelihood fit of the data to the simulated distributions. Assuming that the prompt J/ψ cross section is $\sigma_{\mathrm{J}/\psi} = 417 \pm 37$ nb/nucleon in the x_F range $[-0.35, 0.15]$, we extract the following $b\bar{b}$ cross sections relative to that of J/ψ,

$$\sigma_{b\bar{b}} = 18.6 \pm 5.2_{stat} \pm 3.2_{sys}\ \text{nb/nucleon} \qquad (\text{Method I}),$$
$$\sigma_{b\bar{b}} = 15.5 \pm 2.4_{stat} \pm 2.3_{sys}\ \text{nb/nucleon} \qquad (\text{Method II}),$$

which are in agreement with the result from $b \to \mathrm{J}/\psi \to l^+l^-$ decays [22]. Among the experimental results in literature, the HERA-B results are the most accurate and are consistent with the theoretical predictions.

In chapter 5 we have performed a search of a possible pentaquark signal in the minimum bias data. An inclusive analysis has been performed to extract upper limits on the production cross section at mid-rapidity. In an exclusive analysis we have tried to isolate a signal by eliminating as far as possible unwanted background through cuts on parameters such as impact parameters, distance of closest approach between tracks, number of reconstructed tracks in the event. No signal could be established. The HERA-B collaboration was the first one to publish an upper limit for the production of pentaquarks in fixed target pA collisions [123].

Samenvatting

Beauty en een Zoiktocht naar Pentaquarks bij HERA-B

Dit proefschrift beschrijft het onderzoek dat is uitgevoerd tussen september 2001 en december 2005 bij het HERA-B experiment in pA botsingen ($\sqrt{s} = 41.6$ GeV). Als gevolg van problemen die buiten het experiment liggen, heeft de data acquisitie periode niet langer geduurd dan vijf maanden, hetgeen geleid heeft tot twee data sets van circa 150 M dilepton getriggeerde events en 200 M minimum bias events. Dit heeft - dankzij de grote acceptantie van de detector en zijn goede ruimtelijke oplossingsvermogen, de selectieve trigger en het gebruik van verschillende botsingsdoelen - verschillende studies naar zware quark productie mogelijk gemaakt.

Hoofdstuk 1 geeft een overzicht van de theoretische beschrijving van zware quark productie en de daaropvolgende formatie van gebonden toestanden in pA botsingen. De meting van de werkzame doorsnede van de inclusieve beauty productie ($\sigma_{b\bar{b}}$) in hadron botsingen geeft, vanwege de hoge massa van de b quarks, de mogelijkheid om de voorspellende kracht van de perturbatieve QCD-theorie te testen. De berekening van $\sigma_{b\bar{b}}$ op NLO niveau [17, 18] faalt in de buurt van de kinematische drempel waar grote bijdragen worden verwacht door hogere orde processen, zoals de emissie van laag energetische gluonen. Om met deze effecten rekening te houden hebben Bonciani *et al.*[19] en Kikonakis *et al.*[21] twee verschillende resummatie technieken toegepast, maar de onzekerheden in de voorspellingen zijn nog altijd groot. Drie vergelijkbare experimenten hebben metingen van $\sigma_{b\bar{b}}$ gepubliceerd, maar, ondanks het feit dat deze bij dezelfde energie zijn uitgevoerd, zijn de resultaten niet met elkaar in overeenstemming [7, 6]. De quark samenstelling van alle experimenteel geobserveerde hadronen is hetzij $q\bar{q}$ of qqq. Het bestaan van hadronen met een andere quark samenstelling is theoretisch echter niet uitgesloten. Hoofdstuk 1 beschrijft twee theoretische modellen waarmee de productie van deze "exotische" hadronen mogelijk verklaard kan worden.

Hoofdstuk 2 geeft een beschrijving van het HERA-B experiment. De detector bestaat uit een vertex detector, een voorwaartse spectrometer met een openingshoek van ≈ 300 mrad, een "Ring Imaging Čerenkov" detector voor deeltjesidentificatie, een electromagnetische calorimeter en een muon detector.

Hoofdstuk 3 beschrijft het eerste trigger niveau (FLT). De J/ψ trigger gebruikt de eenduidige signaturen van de J/$\psi \to e^+e^-$ en J/$\psi \to \mu^+\mu^-$ vervallen. De FLT vermindert de achtergrond ten opzichte van de goede gebeurtenissen met een factor

van ≈ 200 en zorgt ervoor dat zo'n $300,000$ J/ψ (1200 per uur) worden gemeten met een gemiddelde track efficientie $\varepsilon_e = 58.74 \pm 0.12_{stat} \pm 1.0_{sys}$ % voor electronen and $\varepsilon_\mu = 28.25 \pm 0.12_{stat} \pm 0.7_{sys}$ % voor muonen. De procedure voor het aanmaken van 3-dimensionale "FLT efficiency maps" wordt besproken. Deze tabellen bevatten de geobserveerde efficientie waarmee de deeltjes gedetecteerd kunen worden als functie van hun positie in de detector.

In hoofdstuk 4 wordt de meting van de werkzame doorsnede van het beauty quark beschreven. In een vorige meting [22] werd de werkzame doorsnede van het beauty quark bepaald via de selectie van $b \to \mathrm{J}/\psi \to l^+l^-$ vervallen. De grote levensduur van B hadronen, in combinatie met de relativistische snelheid waarmee deze deeltjes worden geproduceerd, maken het mogelijk b gebeurtenissen te identificeren waarin de J/ψ mesonen niet van de primaire vertex komen. Het resultaat van deze analyse, waarin muon en electron kanalen zijn gecombineerd, is:

$$\sigma_{b\bar{b}} = 14.9 \pm 2.2_{stat} \pm 2.4_{sys} \text{ nb/nucleon}.$$

In dit proefschrift is dezelfde meting uitgevoerd door dubbel semi-muonische b vervallen te selecteren, gebruik makend van twee verschillende methoden. In de eerste methode worden de gebeurtenissen geisoleerd die voldoen aan een set van geoptimaliseerde selectie criteria op variabelen zoals de impact parameters, de transversale impuls en de afstand tot de primaire vertex. In de tweede methode word de selectie losgelaten en wordt het signaal verkregen door een waarschijnlijkheidsfit van gesimuleerde distributies op de data. Er vanuit gaande dat de werkzame doorsnede van J/ψ gegeven is door $\sigma_{\mathrm{J}/\psi} = 417 \pm 37$ nb/nucleon op het interval $[-0.35, 0.15]$, kunnen de volgende werkzame doorsnedes voor $b\bar{b}$ verkregen worden relatief aan die van J/ψ,

$$\begin{aligned} \sigma_{b\bar{b}} &= 18.6 \pm 5.2_{stat} \pm 3.2_{sys} \text{ nb/nucleon} \qquad (\text{Method I}), \\ \sigma_{b\bar{b}} &= 15.5 \pm 2.4_{stat} \pm 2.3_{sys} \text{ nb/nucleon} \qquad (\text{Method II}), \end{aligned}$$

welke in overeenstemming zijn met het resultaat van $b \to \mathrm{J}/\psi \to l^+l^-$ vervallen. Binnen de experimentele resultaten in de literatuur heeft de HERA-B de meest nauwkeurige resultaten. Tevens zijn de resultaten in overeenstemming met de theoretische voorspellingen.

Hoofdstuk 5 beschrijft het onderzoek van de zoektocht naar een mogelijk pentaquark signaal. Een inclusieve analyse is uitgevoerd voor het verkrijgen van de bovenlimieten van de werkzame doorsnede van de produktie van het pentaquark bij centrale rapiditeit. In een exclusieve analyse is geprobeerd een signaal te isoleren door zo veel mogelijk de ongewenste achtergrond te elimineren met behulp van snedes op variabelen zoals de impact parameters, de afstand tussen sporen en het aantal gereconstrueerde sporen in de gebeurtenis. Er kon geen pentaquark signaal worden vastgesteld. HERA-B een bovenlimiet voor de productie van pentaquarks in deeltjesbotsingen op een stilstaand doel heeft gepubliceerd [123].

Acknowledgements

First of all, I am grateful to the NIKHEF because it allowed me to continue my studies in physics in a high level scientific environment. I think it is a unique place in Europe for young physicists who want to honorably live out of physics, with bread and roses. During the PhD, I joined the HERA-B collaboration to perform an experiment in Hamburg (Germany), having the possibility to participate to the exciting period of data taking. In this period physicists concentrate their efforts to actually perform the experiment, after a long period passed to prepare it.

The fact that my life, in these years, was pleasant is due to many people I owe something to, and to whom I wish to express my gratitude. My copromotor, Thomas Bauer, was exactly what I needed after my diploma thesis. The way he interpreted the role of a guide was important for a novel particle physicist like me. I appreciated his way of informing me I was wrong without ever embarrassing me. Together with him I performed the research on pentaquarks. His global and radical criticism was essential for my education as a particle physicist. Hernan Wahlberg started the PhD in HERA-B a bit before me. I could profit of his experience working with him on the FLT for two years in complicity and pleasure. If we did a good job, it was because we had so much fun. In the evenings, we shared joys and sorrows of the real work in the streets of Amsterdam, after the relaxed days in the office. I hope one day we could work again together. When Hernan left for Buenos Aires, Besma and Tristan became my office mates. Besma had always something sweet for me, and I specially loved her baklava. If I needed to laugh, than I asked Tristan to speak the dialect of Naples. Mohamed Ouchrif, as a post doc in HERA-B, guided me during my stay in Hamburg. With his italian, vaguely reminding Bologna, he was setting me in good mood every morning. He had always an interesting point of view on all the things happening around the world. I sincerely thank my promotor Jo van den Brand and the entire b physics group, led by Marcel Merk. I wish you a lot of success with your experiment LHCb and certainly more luck than we had in our. Jan Visschers was the first dutch physicist I worked with, during the diploma thesis. His fascinating personality indirectly convinced me to come to the Netherlands to join his efficient, relaxed and funny way of working. Actually, everything started when prof. Paolo Russo sent me at NIKHEF for two weeks during the diploma thesis. Without him, probably, I would have never started a PhD in particle physics.

Among the persons who showed interest and trust in my research, Maaijke Mevius deserve a special place. I was so grateful to her that I even tried to learn

bridge (just to play with her), but I never managed. Mauro Villa gave me support for the study of beauty production, while Antonio Zoccoli did the same for the pentaquark. I want to thank them, and the entire Bologna group, for the possibility they offered me to publish the results of my research.

As a foreigner, I changed many times apartment and flat mates. Vichy, Matthew, Linda and Merija helped me to appreciate living in Reigers Bos. With Scianluca (as Hernan says Gianluca) I lived in Hamburg and he became like a brother for me. He enlarged my musical horizon and introduced me to electronic jazz. With Maaike Limper, Claudine Colnard and Jacopo Nardulli I lived in Watergraafsmeer. We enjoyed excellent dinners in "La Maison" with the sea food of Jacopo, the cakes of Claudine and the tenderness of Maaike. I admit that the trattoria Angelo was almost as good as our cuisine. Jacopo was the pioneer of a migration of people from puglia. Cosimo, "lo Zio" for his experience in life, was a master in cooking "*mpepat' e' cozz*'". Giampiero, il Professore for his deep knowledge of electronics, was not always easy to follow in his Pindaric flight, but he is one of the last gentleman. Toni made my guitar happy after ten years of frustrations under my fingers. The legend says that Antonio Pellegrino was the first italian to come to NIKHEF long time ago. I owe him a feeling of tranquillity. He was ready to help at any moment ("Hai capito a babbuccio"). After Niels, I need to find someone else to play soccer in the office. Thank to Jan Visser I did not miss the crema pasticciera of my sister. Beating Gordon in pool had always a special taste. Many friends came from Italy to visit me, Massi, Belley, Peppino, Roberto e Raffaella, my brother Roberto and my sister Nella, Roberta e Claudia. Checco, I forgive you because you still believe one day we will buy the BeJoNeC. Fulvio came to give the last touches to a spectacular oil on canvas he painted for me.

The only thing, apart from physics, I learned here in Holland is tango, in which Hernan was a maestro. Irma and Pippi were the most enchanting dancing partners. Pippi did not care at all about dancing, laughing was enough for her. Irma was delicious. She took care of me, bringing me in the nicest bars of Amsterdam. In these years I also felt the fundamental presence and support of my family. I thank my parents (specially to my father) for their insisting attempts to find me on the phone, my brother for satisfying all my requests and my sister for making me happy just looking at her.

This manuscript was written with the help of some persons who contributed to improve it. Thomas was patient to read it all times I asked him. I thank Jo for reading it carefully, taking care of the English. Even Hernan made the effort to read it, which is probably the last thing you want to do after you finish your PhD. The comments of Bernhard Schwingeneuer, the master of the FLT, were precious. His eagerness to work was contagious and inspiring.

Irene, sospeso tra i nostri sentimenti, mi consolo all'idea di non rinunciare.